DEVELOPMENT AND CHARACTERISATION OF RECYCLED CARBON FIBRE BASED FILMS/COMPOSITES FOR THERMOELECTRIC APPLICATIONS

PRIYANKA JAGADISH, MEng (Hons)

Thesis submitted to the University of Nottingham for the Degree of Doctor of Philosophy

JULY 2018

ABSTRACT

The increasing usage of carbon fibres in the aerospace, automotive and sports goods industries since the late 20th century has led to an end-of-life concern for the carbon fibre composites. An estimated 3000 tonnes of carbon fibre scrap are generated annually throughout the United States of America (USA) and Europe. The disposal of carbon fibre through incineration or landfill has been deemed infeasible and there have been environmental regulations that have imposed a ban on this material as it is non-biodegradable. For instance, in 1999, the European Union has enforced the Landfill Directive (1999/31/EC) that restricts the disposal of carbon fibre as a chemical waste. Therefore, there is a need for recycling these carbon composites that would not only save disposal cost, but more importantly, provides an avenue for reuse in a more sustainable manner.

In the framework of reuse of recycled carbon fibre (RCF) and alternative product development to close the recycling loop of RCF, this research aims to develop RCF based thermoelectric films and composites.

Electrodeposition method was used to synthesise n-type bismuth telluride (Bi_2Te_3) films on recycled carbon fibre (RCF) under different deposition conditions. Electrodeposition was studied using single parameter and multi-parameter optimisation. From the single parameter optimisation, it was observed that close to stoichiometric n-type Bi_2Te_3 fims have higher Seebeck coefficient (-12.99 μV/K). Multi-parameter optimisation was carried out using D-optimal model under response surface methodology (RSM) to design the experiment and optimise the following deposition parameters: deposition potential (V), deposition time (h), deposition temperature (°C) and electrolyte composition (molar concentration). The Seebeck coefficient of Bi_2Te_3 coated RCF using multi-parameter optimisation (-17.25 μV/K) was 33 % higher than the Seebeck coefficient obtained using single parameter optimisation (-12.99 μV/K).

This research work also focused on the development of a low-cost effective RCF polymer thermoelectric composite.

This study investigated the effect of the concentration of Bi_2Te_3 and Bi_2S_3 fillers respectively on the thermoelectric, morphology, structural and thermal stability of the RCF thermoelectric composites. The power factor of RCF thermoelectric composites was highest at 45 wt% of thermoelectric filler loading at 0.194 $\mu WK^{-2}m^{-1}$ and 0.094 $\mu WK^{-2}m^{-1}$ for RCF-Bi_2Te_3 and RCF-Bi_2S_3 respectively.

In order to further improve the electrical conductivity and the subsequent thermoelectric properties of RCF composites, this study also investigated and studied the effect of varying concentration of multiwall carbon nanotubes (MWCNT) on the thermoelectric properties of RCF-Bi_2Te_3 and RCF-Bi_2S_3 composites. The optimum doping level of MWCNT for RCF-Bi_2Te_3 and RCF-Bi_2S_3 is 0.10 wt% and 0.15 wt% of MWCNTs, respectively. At optimum doping level, MWCNTs enhanced the power factors of RCF-Bi_2Te_3 and RCF-Bi_2S_3 composites by approximately 439 and 800%, respectively. The highest power factor obtained for MWCNT doped RCF-Bi_2Te_3 and RCF-Bi_2S_3 are 1.044 and 0.849 $\mu WK^{-2}m^{-1}$, respectively.

Lastly, to enhance the crystallinity and electronic transport properties of the RCF composites, thermal annealing essentially a heat treatment that alters the physical and chemical properties of a semiconductor was studied. The optimum annealing temperature for Bi_2Te_3 and Bi_2S_3 particles within the RCF composites are 350 and 400 °C respectively. In addition to temperature, the optimum annealing time for both RCF-Bi_2Te_3 and RCF-Bi_2S_3 is 2 hours. At optimum annealing temperature and time, the power factor of RCF-Bi_2Te_3 and RCF-Bi_2S_3 composites are 7.836 and 2.551 $\mu WK^{-2}m^{-1}$ respectively. Both annealed RCF-Bi_2Te_3 and RCF-Bi_2S_3 composites depicted a 4000 and 2600% improvement in power factor as compared to the non-annealed counterparts.

LIST OF PUBLICATIONS

Journal Publications

(a) Jagadish,P.R, Khalid,M., Li,L.P, Hajibeigy,M.T, Amin, M.,Walvekar,R.,Chan,A.,2018. Cost effective thermoelectric composite from recycled carbon fibre: From waste to energy. Journal of Cleaner Production.195

(b) Jagadish,P.R., Siddiqui,M.K.,Amin,A.,Lau,P.L., Chan,A., 2017. Process optimisation for n-type Bi2Te3 films electrodeposited on flexible recycled carbon fibre using response surface methodology. Journal of Materials Science. 52:11467–1148.

(c) Jagadish, P.R., Lau, .PL., Siddiqui, M.K. and Chan, A., 2016. Effect of annealing on virgin and recycled carbon fibre electrochemically deposited with N-type bismuth-telluride and bismuth sulfide. Materials and Manufacturing Processes. 31(9), 1223-1231.

Conference Publications

(a) P. R.,Jagadish, P.L Lau, A.Chan, Khalid,M, 2017. Optimisation of Electrodeposition Parameters for N-type Bismuth Telluride films on Carbon Fibre using Design of Experiments. In: 4th Postgraduate Colloquium for Environmental Research 2017 (POCER). (In Press.)

(b) Lau, P.L., Jagadish, P.R., Chan, A. and Siddiqui, M.K., 2015. Electrodeposition of N-type Bismuth Telluride onto Recycled Carbon Fibre Sheets: Thermoelectric Properties Characterisation. In: Proceedings of the 23rd Annual International Conference on Composites/Nano-Engineering, Chengdu, China, July 12-18.

ACKNOWLEDGEMENT

I would like to extend my gratitude to Prof. Mohammad Khalid Siddiqui, Dr. Lau Phei Li and Prof. Andy Chan for all their insights and supervision throughout my tenure. I highly appreciate the opportunity given to me to pursue this project under their guidance. I would also like to specially thank Prof Dr. Nowshad Amin from the Solar Energy Research Institute (SERI), Universiti Kebangsaan Malaysia (UKM) for giving me the opportunity to work under his guidance in his established laboratory.

My gratitude also extends to all Block N staff that provided continuous assistance and guidance with regards to analytical instrument usage and other related matters.

I am grateful to my family members for their moral support and confidence in me throughout this tenure. Lastly, I would also like to thank my friends and colleagues for their insights and help through these time.

TABLE OF CONTENTS

Contents

ABSTRACT ii

LIST OF PUBLICATIONS iv

ACKNOWLEDGEMENT v

LIST OF FIGURES ix

LIST OF TABLES xiii

LIST OF ABBREVIATIONS xv

LIST OF NOMENCLATURE xvi

Chapter 1: Introduction 1

1.1 Background study 1

1.2 Problem statement 6

1.3 Objectives and scope of study 7

1.4 Significance of research 9

1.5 Thesis outline 9

Chapter 2: Literature Review 11

2.1 Introduction 11

2.2 Fundamentals of Thermoelectricity 11

2.3 Thermoelectric Properties 14

2.4 Categories of Thermoelectric Materials 15

2.5 Chosen Thermoelectric Material 25

2.6 Deposition/Fabrication Techniques 31

2.6.1 Electrodeposition 33

2.6.2 Production of carbon fibre thermoelectric composite 50

2.7 Thermal Annealing 52

2.7.1 Annealing of Bi_2Te_3 52

2.7.2 Annealing of Bi_2S_3 58

2.8 Doping with carbon nanotubes 61

2.8.1 Bi_2Te_3-CNT composites 61

2.8.2 Bi_2S_3-CNT composites 65

2.9 Summary 66

Chapter 3: Methodology 67

3.1 Introduction 67

3.2 Materials 67

3.3 Fabrication Techniques 68
3.3.1 Electrodeposition 68
3.3.2 Recycled carbon fibre polymer composite fabrication 73
3.4 Thermoelectric properties 75
3.4.1 Measurement of Seebeck coefficient 75
3.4.2 Measurement of electrical resistivity 76
3.4.3 Power factor calculation 77
3.5 Thermal properties 77
3.5.1 Thermogravimetric analysis (TGA) 77
3.6 Characterisation 77
3.6.1 X-ray powder diffraction (XRD) 77
3.6.2 Field Emission Scanning Electron Microscope (FESEM) and Energy Dispersive X-ray (EDX) analysis 78
Chapter 4: Optimisation of Seebeck coefficient for electrochemically deposited Bi_2Te_3 on RCF by varying electrodeposition parameters 79
4.1 Introduction 79
4.2 Results and discussion 81
4.2.1 ***Single parameter/univariate optimisation*** 81
4.2.2 Multi-parameter/multivariate optimisation 86
4.3 Summary 99
Chapter 5: Recycled Carbon Fibre Composites with Bi_2Te_3 and Bi_2S_3 thermoelectric fillers 100
5.1 Introduction 100
5.2 Results and discussion 102
5.2.1 Thermoelectric properties of RCF composites coated with Bi_2Te_3 and Bi_2S_3 102
5.2.2 FESEM and EDX study of RCF-Bi_2Te_3 and RCF-Bi_2S_3 composites 111
5.2.3 XRD Analysis of of RCF-Bi_2Te_3 and RCF-Bi_2S_3 composites 113
5.2.4 Thermal stability of RCF-Bi_2Te_3 and RCF-Bi_2S_3 composites 117
5.3 Summary 124
Chapter 6: Effect of Multi Walled Carbon Nanotubes (MWCNTs) on the Thermoelectric Properties of Recycled Carbon Fibre Composites with Bi_2Te_3 and Bi_2S_3 Thermoelectric Fillers 125
6.1 Introduction 125
6.2 Results and discussion 126
6.2.1 Effect of MWCNT on the thermoelectric properties of RCF-Bi_2Te_3 and RCF-Bi_2S_3 126
6.2.2 Morphological study of RCF-Bi_2Te_3 and RCF-Bi_2S_3 composites doped with MWCNT 137
6.2.3 XRD analysis of RCF-Bi_2Te_3 and RCF-Bi_2S_3 composites doped with MWCNT 141
6.2.4 Thermal stability of RCF-Bi_2Te_3 and RCF-Bi_2S_3 composites doped with MWCNT 147

6.3 Summary 151

Chapter 7: Effect of Annealing on the Thermoelectric Properties of Recycled Carbon Fibre Composites with Bi_2Te_3 and Bi_2S_3 Thermoelectric Fillers 152

7.1 Introduction 152

7.2 Results and discussions 153

7.2.1 Effect of annealing temperature on the thermoelectric properties of annealed RCF-Bi_2Te_3 153

7.2.2 Effect of annealing temperature on the thermoelectric properties of annealed RCF-Bi_2S_3 158

7.2.3 Effect of annealing temperature on the morphology of annealed RCF-Bi_2Te_3 composites 162

7.2.4 Effect of annealing temperature on the morphology of annealed RCF-Bi_2S_3 composites 164

7.2.5 Effect of annealing temperature on the XRD analysis of annealed RCF-Bi_2Te_3 composites 166

7.2.6 Effect of annealing temperature on the XRD analysis of annealed RCF-Bi_2S_3 composites 169

7.2.7 Effect of annealing temperature on the thermal stability of annealed RCF-Bi_2Te_3 composites 175

7.2.8 Effect of annealing temperature on the thermal stability of annealed RCF-Bi_2S_3 composites 178

7.2.9 Effect of annealing time on the thermoelectric properties of annealed RCF-Bi_2Te_3 180

7.2.10 Effect of annealing time on the thermoelectric properties of annealed RCF-Bi_2S_3 185

7.2.11 Effect of annealing time on the morphology of annealed RCF-Bi_2Te_3 composites 189

7.2.12 Effect of annealing time on the morphology of annealed RCF-Bi_2S_3 composites 191

7.2.13 Effect of annealing time on the XRD analysis of annealed RCF-Bi_2Te_3 composites 193

7.2.14 Effect of annealing time on the XRD analysis of annealed RCF-Bi_2S_3 composites 196

7.2.15 Effect of annealing time on the thermal stability of annealed RCF-Bi_2Te_3 composites 199

7.2.16 Effect of annealing time on the thermal stability of annealed RCF-Bi_2S_3 composites 201

7.3 Summary 203

Chapter 8: Conclusion and future works 204

8.1 Principal findings 204

8.2 Limitations 208

8.3 Recommendation for future works 209

REFERENCES 211

LIST OF FIGURES

Figure 1- 1: Fossil fuel consumption in energy resources by several countries.(Agency of Natural Resources and Energy, 2016).....1
Figure 1- 2: Global energy consumption from 1990 to 2017 (Enerdata, 2018). 2

Figure 2- 1: Schematic depicting charge carrier flow when subjected to temperature difference for p and n-type semiconductors. 12
Figure 2- 2: Schematic illustrating the difference between Seebeck and Peltier effect (S. Lee et al., 2012). 13
Figure 2- 3: ZT value of common bulk thermoelectric materials (He et al., 2013). 25
Figure 2- 4: Current-potential relation of Ti electrode in a nitric acid solution with 1.5mM of $Bi(NO_3)_3$ and 1.5mM of TeO_2 (Takahashi, 1993)......34
Figure 2- 5: Pourbaix type diagram for Bi and Te in nitric acid electrolyte (Martín-González et al., 2002). 35
Figure 2- 6: Dependence of power factor of the films on the Te content in deposit (Wang et al., 2007). 41
Figure 2- 7: The effect of Te content on (a) Electrical Conductivity (Wang et al., 2007).....42
Figure 2- 8: SEM Images (a) Bismuth rich Bi_2Te_3 (b) Stoichiometric Bi_2Te_3 (c) Tellurium rich Bi_2Te_3 (Golia et al., 2003). 45
Figure 2- 9: SEM images with corresponding Te content (Wang et al., 2007). 46
Figure 2- 10: SEM images of the effect of deposition time on the morphology of Bi_2Te_3 films deposited on stainless steel (a) 2-5 minutes (Ma et al. 2010) *(b) 30 minutes* (Qiu et al., 2010)*(c) 2 hours* (Michel et al., 2005). 48
Figure 2- 11: SEM images of the effect of temperature on the morphology of Bi_2Te_3 films (a) Room temperature (Wang et al., 2007) *(b) 2°C* (Martín-González et al., 2002).....49
Figure 2- 12: SEM surface images of the n-type Bi_2Te_3 samples (a) As-deposited (b) Annealed (Rashid et al., 2013). 52
Figure 2- 13: X-ray diffraction spectra of Bi_2Te_3 film (a) (a) As-deposited (b) 200 ºC, (c) 250 ºC and (d) 300 ºC for 8 min duration (Rashid et al., 2013) 53
Figure 2- 14: Carrier concentration and electron mobility for as-deposited and annealed Bi–Te films (Jeon et al., 2011).....54
Figure 2- 15: SEM surface images of n-type Bi_2Te_3 samples annealed for (a) 2 min, (b) 5 min, (c) 8 min and (d) 10 min at 250 ◦C temperature (Rashid et al., 2013)......57
Figure 2- 16: DSC curve of Bi_2S_3 run in a nitrogen environment (Campos and Sua, 1999).....59
Figure 2- 17: SEM image of (a) Bi_2Te_3 and (b) Bi_2Te_3-MWCNT nanocomposite (Kumar et al., 2017). 62
Figure 2- 18: (a) XRD pattern of single wall carbon nanotube (SWCNT) doped Bi_2Te_3 (sample A,B and C denote samples doped with SWCNT (Zhang et al., 2012) *(b) XRD pattern of Bi_xTe_y and MWCNT film obtained by potentiostatic electrodeposition (MWNT refer to samples doped with MWCNT)* (Xu and Wang, 2013a). 63

Figure 3- 1: Schematic representation of the methodology of the study 67
Figure 3- 2: Schematic of a three cell electrode set up 70
Figure 3- 3: Schematic set up for Seebeck coefficient measurement. 76

Figure 4- 1: Seebeck coefficient of different electrolyte composition for Bi_2Te_3 films. 83
Figure 4- 2: Seebeck coefficient of RCF electrodeposited with Bi_2Te_3 films with respect to deposition potential. 84
Figure 4- 3: FESEM images of (a) Uncoated VCF (b)Uncoated RCF (c) VCF deposited with Bi_2Te_3 (d) RCF deposited with Bi_2Te_3. 85
Figure 4- 4: Zoomed in FESEM images of (a) Presence of charred contaminants on uncoated RCF (b)Clean fibre strands of uncoated VCF. 85
Figure 4- 5: Normal probability plot of residuals. 89
Figure 4- 6: Plot of residuals vs predicted. 89
Figure 4- 7: Predicted values against actual values of Seebeck coefficient. 90
Figure 4- 8: 3D Response surface plot illustrating the effect of deposition potential and deposition time. 91
Figure 4- 9: 3D Response surface plot illustrating the effect of deposition temperature and deposition time. 92
Figure 4- 10: Surface morphologies of Bi_2Te_3 coated RCF (a) At 60 ºC and 0.60 hours (b) At 25 ºC and 0.50 hours both carried out at -0.10 V and 0.2 Bi/(Bi+Te). 93
Figure 4- 11: 3D Response surface plot illustrating the effect of electrolyte composition and deposition time. 94
Figure 4- 12: 3D Response surface plot illustrating the effect of electrolyte composition and deposition temperature. 95
Figure 4- 13: SEM images of (a) Bi_2Te_3 coated RCF (univariate optimisation) (Jagadish et al., 2016) *(b) Bi_2Te_3 coated RCF (multivariate optimisation).* 98

Figure 5- 1: The effect of Bi_2Te_3 concentrations on the Seebeck coefficient of RCF-Bi_2Te_3 and RCF-Bi_2S_3 composites. 102
Figure 5- 2: The effect of Bi_2Te_3 concentrations on the electrical resistivity of RCF-Bi_2Te_3 composites 105
Figure 5- 3: The effect of Bi_2Te_3 concentrations on the power factor of RCF-Bi_2Te_3 composites 106
Figure 5- 4: The effect of Bi_2S_3 concentrations on the Seebeck coefficient of RCF-Bi_2S_3 composites 107
Figure 5- 5: The effect of Bi_2S_3 concentrations on the electrical resistivity of RCF-Bi_2S_3 composites. 108
Figure 5- 6: The effect of Bi_2S_3 concentrations on the power factor of RCF-Bi_2S_3 composites 110
Figure 5- 7: FESEM surface images of RCF-Bi_2Te_3 composite at (a) 15 wt% (b) 30 wt% (c) 45 wt% (d) 60 wt% of Bi_2Te_3. 111
Figure 5- 8: FESEM surface images of RCF-Bi_2S_3 composite at (a) 15 wt% (b) 30 wt% (c) 45 wt% (d) 60 wt% of Bi_2S_3. 112
Figure 5- 9: XRD patterns of RCF-Bi_2Te_3 composite at different Bi_2Te_3 loadings 114
Figure 5- 10: XRD patterns of RCF-Bi_2S_3 composite at different Bi_2S_3 loadings 116
Figure 5- 11: TGA of constituents in RCF-Bi_2Te_3 and RCF-Bi_2S_3 composite. 118
Figure 5- 12: TGA analysis of RCF-Bi_2Te_3 composite. 119
Figure 5- 13: TGA analysis of RCF-Bi_2S_3 composite. 120
Figure 5- 14: DTG curves of constituents in RCF-Bi_2Te_3 and RCF-Bi_2S_3 composites. 121
Figure 5- 15: DTG curve of RCF-Bi_2Te_3 composites. 122
Figure 5- 16: DTG curve of RCF-Bi_2S_3 composites. 123

Figure 6- 1: The effect of MWCNT concentrations on the Seebeck coefficient of RCF-Bi_2Te_3 composites. 127
Figure 6- 2: The effect of MWCNT concentrations on the electrical resistivity of RCF-Bi_2Te_3 composites. 130
Figure 6- 3: The effect of MWCNT concentrations on the power factor of RCF-Bi_2Te_3 composites. 131
Figure 6- 4: The effect of MWCNT concentrations on the Seebeck coefficient of RCF-Bi_2S_3 composites. 133
Figure 6- 5: The effect of MWCNT concentrations on the electrical resistivity of RCF-Bi_2S_3 composites. 135
Figure 6- 6: The effect of MWCNT concentrations on the power factor of RCF-Bi_2S_3 composites. 136
Figure 6- 7: FESEM images of (a) RCF-Bi_2Te_3 composite (b) RCF-Bi_2Te_3 doped with 0.05 wt% of MWCNT. 137
Figure 6- 8: FESEM images of (a) RCF-Bi_2S_3 composite (b) RCF-Bi_2S_3 doped with 0.05 wt% of MWCNT. 138
Figure 6- 9: FESEM images of RCF-Bi_2Te_3 composites doped with (a) 0.05 wt% of MWCNT (b) 0.10 wt% of MWCNT (c) 0.15 wt% of MWCNT (d) 0.20 wt% of MWCNT. 139
Figure 6- 10: FESEM images of RCF-Bi_2S_3 composites doped with (a) 0.05 wt% of MWCNT (b) 0.10 wt% of MWCNT (c) 0.15 wt% of MWCNT (d) 0.20 wt% of MWCNT. 140
Figure 6- 11: XRD patterns of RCF-Bi_2Te_3 composite at different MWCNT loadings. 142
Figure 6- 12: XRD patterns of RCF-Bi_2S_3 composite at different MWCNT loadings. 145
Figure 6- 13: TGA curves of RCF-Bi_2Te_3 composites doped with various loadings of MWCNTs. 147
Figure 6- 14: TGA curves of RCF-Bi_2S_3 composites doped with various loadings of MWCNTs. 148
Figure 6- 15: DTG curves of RCF-Bi_2Te_3 composites doped with various loadings of MWCNTs. 149
Figure 6- 16: DTG curves of RCF-Bi_2S_3 composites doped with various loadings of MWCNTs. 150

Figure 7- 1: The influence of annealing temperature on the Seebeck coefficient of RCF-Bi_2Te_3 composites. 154
Figure 7- 2: The influence of annealing temperature on the electrical resistivity of RCF-Bi_2Te_3 composites. 154
Figure 7- 3: The influence of annealing temperature on the power factor of RCF-Bi_2Te_3 composites. 155
Figure 7- 4: The influence of annealing temperature on the Seebeck coefficient of RCF-Bi_2S_3 composites. 158
Figure 7- 5: The influence of annealing temperature on the electrical resistivity of RCF-Bi_2S_3 composites. 160
Figure 7- 6: The influence of annealing temperature on the power factor of RCF-Bi_2S_3 composites. 161
Figure 7- 7: FESEM surface images of RCF-Bi_2Te_3 composites annealed at (a) non-annealed (b) 300 °C (c) 350 °C (d) 400 °C (e) 450 °C. 162
Figure 7- 8: FESEM surface images of RCF-Bi_2S_3 composites annealed at (a) non-annealed (b) 300 °C (c) 350 °C (d) 400 °C (e) 450 °C. 164
Figure 7- 9: XRD patterns of RCF-Bi_2Te_3 composite annealed at different temperatures for 2 hours. 166
Figure 7- 10: XRD patterns of RCF-Bi_2S_3 composite annealed at different temperatures for 2 hours. 170
Figure 7- 11: Zoomed in view of XRD patterns of RCF-Bi_2S_3 composite annealed at different temperatures. 174

Figure 7- 12: TGA curves of RCF-Bi_2Te_3 composites annealed at different temperatures. 175
Figure 7- 13: DTG curves of RCF-Bi_2Te_3 composites annealed at various temperatures. 177
Figure 7- 14: TGA curves of RCF-Bi_2S_3 composites annealed at different temperatures. 178
Figure 7- 15: DTG curves of RCF-Bi2S3 composites annealed at various temperatures. 179
Figure 7- 16: The influence of annealing time on the Seebeck coefficient of RCF-Bi_2Te_3 composites. 180
Figure 7- 17: The influence of annealing time on the electrical resistivity of RCF-Bi_2Te_3 composites. 183
Figure 7- 18: The influence of annealing time on the power factor of RCF-Bi_2Te_3 composites. 184
Figure 7- 19: The influence of annealing time on the Seebeck coefficient of RCF-Bi_2S_3 composites. 185
Figure 7- 20: The influence of annealing time on the electrical resistivity of RCF-Bi_2S_3 composites. 188
Figure 7- 21: The influence of annealing time on the power factor of RCF-Bi_2S_3 composites. 189
Figure 7- 22: FESEM surface images of RCF-Bi_2Te_3 composites annealed at 350 °C for (a) non-annealed (b) 1 hour (c) 2 hour (d) 3 hour. 190
Figure 7- 23: FESEM surface images of RCF-Bi_2S_3 composites annealed at 400 °C for (a) non-annealed (b) 1 hour (c) 2 hour (d) 3 hour. 192
Figure 7- 24: XRD patterns of RCF-Bi_2Te_3 composite annealed at 350 °C for varying durations. ... 193
Figure 7- 25: XRD patterns of RCF-Bi_2S_3 composite annealed at 400 °C for varying durations. 196
Figure 7- 26: TGA curves of RCF-Bi_2Te_3 composites annealed at different durations. 199
Figure 7- 27: DTG curves of RCF-Bi_2Te_3 composites annealed at various durations. 200
Figure 7- 28: TGA curves of RCF-Bi_2S_3 composites annealed at different durations. 201
Figure 7- 29: DTG curves of RCF-Bi_2S_3 composites annealed at various durations. 202

LIST OF TABLES

Table 2- 1: Thermoelectric properties of clathrates. 17
Table 2- 2: Thermoelectric properties of skutterudites. 18
Table 2- 3: Thermoelectric properties of half-Heusler alloys. 19
Table 2- 4: Thermoelectric properties of ceramics. 20
Table 2- 5: Thermoelectric properties of insulating polymer composites. 22
Table 2- 6: Thermoelectric properties of conducting polymer composites. 23
Table 2- 7: Thermoelectric properties of hybrid polymer inorganic composites. 24
Table 2- 8: Structure, lattice parameters and bond properties of Bi_2Te_3 (Deng and Zhao, 2018). 27
Table 2- 9: Structure, lattice parameters and bond properties of Bi_2S_3 (Deng and Zhao, 2018). 29
Table 2- 10: Advantages and disadvantages of thin film techniques. 32
Table 2- 11: Deposition potentials with respect to composition for the formation of Bi_2Te_3 films. 38
Table 2- 12: Deposition potentials leading to stoichiometric formation of Bi_2Te_3 films using electrodeposition. 39
Table 2- 13: Atomic percentages as a function of the applied potential for depositions on Pt electrodes from 10mM of $HTeO_2^+$ and 7.5 mM of Bi^{3+} in 1 M HNO_3(Martín-González et al., 2002). .. 40
Table 2- 14: Thermoelectric Properties of Bi_2Te_3 films with respect to deposition potential from electrodeposition. 43
Table 2- 15: Resistivity and Hall mobility of Bi_2Te_3 films deposited at increasing deposition time. 47
Table 2- 16: Thermoelectric Properties of Annealed Bi_2Te_3. 55
Table 2- 17: Thermoelectric properties of Bi_2Te_3-CNT composites. 64

Table 3- 1: Varying electrolyte compositions for electrodeposition of Bi_2Te_3 films 69
Table 3- 2: Different compositions of bismuth and tellurium ions in electrolyte 70
Table 3- 3: Parameter ranges chosen for experimental study using D-Optimal 71

Table 4- 1: D-optimal experimental design along with experimental and predicted Seebeck coefficient. 86
Table 4- 2: Analysis of variance (ANOVA) for electrodeposition parameters of Bi_2Te_3 on RCF. 87
Table 4- 3: Parameters yielding the highest Seebeck coefficient for Bi_2Te_3 coated RCF. 95
Table 4- 4: Comparison of Seebeck coefficient and experimental conditions between work done with DOE and without DOE. 97

Table 5- 1: Carrier concentration and carrier mobility of RCF-Bi_2Te_3 composites with respect to increasing Bi_2Te_3 concentrations 104
Table 5- 2: Carrier concentration and carrier mobility of RCF-Bi_2S_3 composites with respect to increasing Bi_2S_3 concentrations. 108
Table 5- 3: FWHM, crystallite size, microstrain and dislocation density of RCF-Bi_2Te_3 composite. 115
Table 5- 4: FWHM, crystallite size, microstrain and dislocation density of RCF-Bi_2S_3 composite. .. 117

Table 6- 1: Carrier concentration and carrier mobility of RCF-Bi_2Te_3 composites with respect to increasing MWCNT concentrations. 128
Table 6- 2: Carrier concentration and carrier mobility of RCF-Bi_2S_3 composites with respect to increasing MWCNT concentrations. 133
Table 6- 3: FWHM, crystallite size, microstrain and dislocation density of RCF-Bi_2Te_3 composites doped with MWCNT. 143
Table 6- 4: FWHM, crystallite size, microstrain and dislocation density of RCF-Bi_2S_3 composites doped with MWCNT. 145

Table 7- 1: Effect of annealing temperature on the Bi and Te content in the RCF-Bi_2Te_3 composites. 155
Table 7- 2: Carrier concentration and carrier mobility of RCF-Bi_2Te_3 composites with respect to annealing temperature. 156
Table 7- 3: Carrier concentration and carrier mobility of RCF-Bi_2S_3 composites with respect to annealing temperature. 159
Table 7- 4: Effect of annealing temperature on the Bi and S content in the RCF-Bi_2S_3 composites. 159
Table 7- 5: FWHM, crystallite size, microstrain and dislocation density of RCF-Bi_2Te_3 annealed at different temperatures. 167
Table 7- 6: FWHM, crystallite size, microstrain and dislocation density of RCF-Bi_2S_3 annealed at different temperatures. 171
Table 7- 7: Effect of annealing time on the Bi and Te content in the RCF-Bi_2Te_3 composites. 181
Table 7- 8: Carrier concentration and carrier mobility of RCF-Bi_2Te_3 composites with respect to annealing time. 181
Table 7- 9: Carrier concentration and carrier mobility of RCF-Bi_2S_3 composites with respect to annealing time. 186
Table 7- 10: Effect of annealing time on the Bi and S content in the RCF-Bi_2S_3 composites. 186
Table 7- 11: FWHM, crystallite size, microstrain and dislocation density of RCF-Bi_2Te_3 annealed at 350 °C with varying durations. 194
Table 7- 12: FWHM, crystallite size, microstrain and dislocation density of RCF-Bi_2S_3 annealed at 400 °C with varying durations. 197

Table 8- 1: Thermoelectric properties of carbon fibre based composites or films. 208

LIST OF ABBREVIATIONS

RCF	Recycled carbon fibre
VCF	Virgin carbon fibre
FESEM	Field emission scanning electron microscope
EDX	Energy dispersive x-ray
TGA	Thermogravimetric analysis
DTG	Derivative thermogravimetric
XRD	X-ray diffraction
DOE	Design of experiment
MWCNTs	Multi walled carbon nanotubes
RSM	Response surface methodology
FWHM	Full width half maximum
PF	Power factor
ANOVA	Analysis of variance
TEG	Thermoelectric generator
wt%	Weight percent
at.%	Atomic percent
PF	Power factor

LIST OF NOMENCLATURE

ZT	Figure of merit
α	Seebeck coefficient
ρ	Electrical resistivity
κ	Thermal conductivity
ΔV	Potential difference
ΔT	Temperature gradient
V_{OC}	Open circuit potential difference
V_H	Potential at hot side
V_C	Potential at cold side
T_H	Temperature on hot side
T_C	Temperature on cold side
α_{CU}	Seebeck coefficient of copper
α_{CF}	Seebeck coefficient of thermoelectric RCF film/composite
D	Crystallite size
ε	Microstrain
δ	Dislocation density

Chapter 1: Introduction

1.1 Background study

In this era of globalization, every industrial and technological endeavours have become highly energy intensive to fulfil the needs of growing global population. Presently, a large fraction of developing and developed countries obtain most of their energy from fossil fuels such as coal, petroleum and natural gas as shown in **Figure 1- 1**. The average global energy consumption is also seen to be rising exponentially as shown in **Figure 1- 2**, with energy consumption in the year 2017 amounting to 13,576 million tonnes of oil equivalent (Mtoe) (Enerdata, 2018). These mass consumption of fossil fuels has led to increased greenhouse gas emissions and global warming with global CO_2 emission increased by 11.3 gigatonne (GT) from the year 1990 to 2011 (Ding et al., 2018). In the recent 2015 United Nations Climate Change Conference (COP 21), all parties agreed in reducing the CO_2 emission and aiming to keep the temperature rise at 1.5 °C in the end of the century.

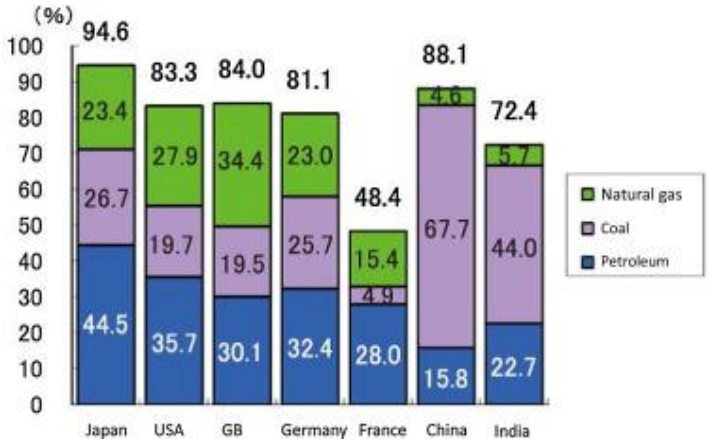


Figure 1- 1: Fossil fuel consumption in energy resources by several countries.(Agency of Natural Resources and Energy, 2016).

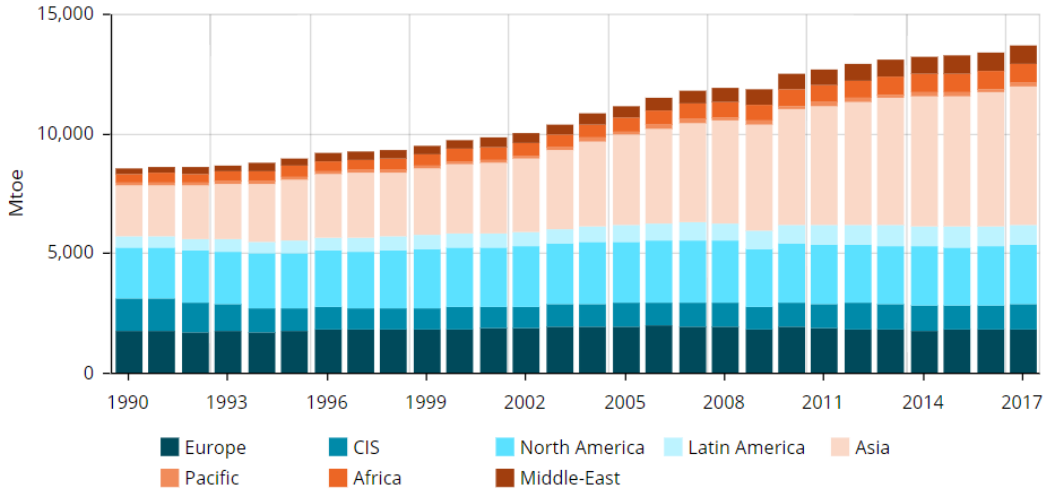


Figure 1- 2: Global energy consumption from 1990 to 2017 (Enerdata, 2018).

Therefore, in order to meet the future energy demand in a sustainable manner it is vital to search for sustainable and environmentally friendly energy sources. The choice of renewable energy is dependent upon the resources that are readily available in a particular place. One such underutilised form of readily available resource is waste heat. It is also noteworthy to point out that when energy sources are used, more than half of the energy is lost to the environment as waste heat and not for the intended purpose (Toshima, 2017). Waste heat, which is undesired, but unavoidable, is the additional energy in the form of heat that is produced from a process of fuel combustion or chemical reaction which is released to the environment and is not reused for useful and economic purposes (Patil et al., 2018).

An apt solution to waste heat re-utilisation is through thermoelectric technology that have received increasing attention in recent years. This waste heat is converted to electricity with the help of thermoelectric materials/modules and will be able to reduce global fuel consumption with re-utilisation of waste heat to produce usable electricity. Thermoelectric modules can be defined as devices that generate an electric potential gradient from a thermal gradient, or vice versa, without any actuating parts. The thermoelectric technology offers a clean,

environmentally friendly, solid state operation, gas emission free, vast scalability and maintenance free operation with no actuating parts and chemical reactions. There are many applications of these thermoelectric devices in the industry as power generators, microcoolers, infrared detectors, wearable devices and etc. (Yoo et al., 2005).

Till date, the compounds X_2Y_3 (where X=Bi, Sb, Pb and Y=S, Se, Te) are regarded as the most promising for thermoelectric applications (Zhao et al., 2008)(Danine et al., 2018). Bi-Te and Sb-Te exhibits the best thermoelectric properties at room temperature whereas Pb-Te exhibits its best at middle temperatures (750-900K).

The efficiency of a thermoelectric module is measured by the value of figure of merit (ZT), the higher the value the better the conversion of energy. The ZT value is given by Eq (1.1) below:

$$ZT = \frac{T\alpha^2}{\rho\kappa} \qquad (1.1)$$

Where α is the Seebeck coefficient; T is the temperature; ρ is the electrical resistivity and κ is the thermal conductivity. The ZT value is majorly influenced by the power factor (PF) due to its largest contribution in Eq (1.1) given by Eq (1.2) below:

$$PF = \frac{\alpha^2}{\rho} \qquad (1.2)$$

For room temperature applications in particular, Bi-Te systems exhibits a much higher figure of merit, ZT of 0.97 as compared to Sb-Te compounds with ZT of 0.56 (Carmo et al., 2010). Bismuth chalcogenides have been widely studied and explored for the last 50 years from the time of its discovery in the early 1950's. Bismuth chalcogenides consist of A_2B_3 whereby (A=Bi; B=S, Se, Te) have attracted a great deal of attention due to its high figure of merit, ZT, the largest reported so far made from p-type bismuth telluride(Bi_2Te_3) super lattice is 2.4 which is the largest reported till date (Venkatasubramanian et al., 2001).

Chalcogenide compounds, those containing sulphur, selenium and tellurium have been considered potential thermoelectric materials due to its high stability in air and high melting points. They also have strong flexibility in hosting other elements and small difference in electronegativity between sulfur, selenium and tellurium, and they have the capability to generate semiconductors with band gap highly desirable for thermoelectric applications (Bing Ling et al., 2014). Hence bismuth in combination with chalcogenide compounds presents desirable attributes for thermoelectric materials.

In the past, Bi_2Te_3 has been coated on various rigid (platinum, gold, stainless steel, nickel and etc.) and flexible substrates (polyimide, Kapton and etc.) using physical and chemical thin film techniques. In addition to thin film techniques, various Bi_2Te_3 nanocomposites was synthesised using powder metallurgy and hydrothermal techniques, which have also been incorporated with electrically conducting polymers to form flexible conductive composite films. However, all of these synthesised powders and films only exhibit a singular semi-conducting behaviour at a time either as n-type or p-type. Thus, requiring the need of a rigid heat sink plate and rigid heat absorber plate external substrates which are made of ceramic mostly, whereby n-type and p-type thermoelectric elements are stacked in the middle of these plates. Ceramic as an external substrate is highly brittle and fragile, and ceramics also get heated up easily, leading to the inability to sustain a temperature difference for effective thermoelectric energy harvesting. For other flexible polymer composite films, it requires the need of another external flexible substrate such as polyimide or Kapton that will serve to attach these n and p-type flexible composite films alternatingly using silver paint. The need of external substrates in both powdered samples and flexible composite films often makes the fabrication process more complicated, cost intensive, not scalable for large area application, and does not have mechanical ruggedness thus being inadequate for practical large scale conversion of thermal to electrical energy.

To overcome this limitation of external substrates and scalability issue, Han and Chung utilised continuous carbon fiber epoxy-matrix composites commonly used for structural purposes and modified it to have energy harvesting features by introducing various thermoelectric interlaminar fillers such as Bi_2Te_3, Te and carbon black into the composite (Han and Chung, 2013a)(Han and Chung, 2013b). In this study, the author has utilised recycled carbon fibre (RCF) in place of virgin carbon fibre and an environmentally friendly formaldehyde free binder, Acrodur DS 3530 to replace epoxy in the composite. The author has studied the thermoelectric properties of the RCF composite with two interlaminar fillers Bi_2Te_3 and bismuth sulphide (Bi_2S_3) (as alternative to toxic tellurium). As carbon fibres is an electrical conductor with a weakly p-type thermoelectric nature, and Bi_2Te_3 and Bi_2S_3 are of n-type thermoelectric nature, the author would like to investigate the plausibility of a singular structure that is able to emulate both n and p-type semiconducting behaviour in a singular structure which has not been reported in literature before.

RCF is used in this study owing to the increasing usage of carbon fibre in the aerospace, automotive and sports goods industries since the late 20^{th} century that have led to an end of life concern for this carbon fibre composites (Pang et al., 2012). It has been reported that an estimated 3000 tonnes of carbon fibre scrap are being generated annually throughout the United States of America (USA) and Europe. It has been forecasted that approximately 6000-8000 commercial planes are expected to reach the end of life and dismantled by the year 2030. The production of virgin carbon fibre is also expected to escalate to 100,000 tonnes to meet demand of major automotive and aerospace players (McConnell, 2010). The disposal of carbon fibre through incineration or landfill has been deemed not optimal due to the environmental regulations that have imposed a ban on this material. In 1999, the European Union has enforced Landfill Directive (1999/31/EC) that has restricted the disposal of carbon fibre as a chemical waste. Therefore, there is a need for recycling these carbon composites that would not only

save disposal cost, but also provide an avenue for the reuse of this material. As it is recycled carbon fibre, it is a much cheaper, economically feasible and environmentally friendly alternative. It will also be able to provide a market for this recycled carbon fibre that is facing disposal issues.

1.2 Problem statement

RCF is often obtained in milled or chopped form after recycling, its fibres are short and are of random distribution. These characteristics often affect its reusability in structural applications as fibre alignment is a key property in the mechanical strength of composites. Despite the improvements made in the techniques for recycling, the tensile strength of carbon fibre after recycling is said to be decreased as compared to the virgin carbon fibres (VCF) by approximately 15 %, 30 % and 50 % for supercritical fluids, pyrolysis and fluidised bed process respectively (Morin and Loppinet-Serani, 2012). The fluffy and the filamentous nature of recycled carbon fibre has also led to possessing half the impact energy as virgin carbon fibre.

Hence, RCF cannot be used as a direct substitute in place of VCF in critical structural applications, as it would not have the same mechanical strength and rigidity. Thus, different routes to use recycled carbon fibre should be explored to close the recycling loop.

A novel alternative is to develop RCF's for the purpose of thermoelectric energy generation, where the mechanical strength is not paramount. RCF has a great potential to be used in the field of thermoelectricity due to its inherent electrically conductive and weakly thermoelectric nature.

1.3 Objectives and scope of study

This study aims to develop RCF based thermoelectric films and composites with the use of thermoelectric materials such as Bi_2Te_3 and Bi_2S_3. Firstly, this study intends to study the feasibility of using RCF as a flexible thermoelectric film with electrodeposited Bi_2Te_3 and fabricate it by employing a single parameter/univariate and multi-parameter/multivariate optimisation approach using Design of Experiments. Secondly, this study intends to develop a cost effective RCF thermoelectric composite by: (a) coating with thermoelectric fillers (i.e Bi_2Te_3 and Bi_2S_3) at varying concentrations, (b) doping thermoelectric fillers with varying concentrations of multi walled carbon nanotubes (MWCNTs) and (c) thermally annealing thermoelectric fillers by varying annealing temperature and time.

Therefore, the aim of this study is met by considering the following objectives:

(1) **To optimise the Seebeck coefficient of Bi_2Te_3 coated RCF by varying electrodeposition parameters**

A univariate approach was used in this objective by varying the electrolyte composition for the electrochemical deposition of Bi_2Te_3 on both RCF and VCF and determining the subsequent effect of this variation on the stoichiometry as well as Seebeck coefficient of RCF and VCF. Then, a multivariate optimisation of the parameters that affects the electrodeposition of Bi_2Te_3 on RCF such as deposition potential, deposition time, deposition temperature, and electrolyte composition were optimised using Design Expert 9 software with D-optimal model. The subsequent effect of these parameters on the Seebeck coefficient of RCF electrodeposited with Bi_2Te_3 were studied.

(2) To fabricate, study and optimise power factors of RCF thermoelectric composites filled with Bi_2Te_3 and Bi_2S_3

This objective focused on the optimisation of the concentration of thermoelectric fillers and its subsequent effect on the thermoelectric properties (i.e. Seebeck coefficient, electrical resistivity and power factor) for both Bi_2Te_3 and Bi_2S_3 filled RCF composite. The morphological, structural and the thermal stability of the RCF composites filled with Bi_2Te_3 and Bi_2S_3 were demonstrated in this objective.

(3) To fabricate, study and optimise power factors of RCF thermoelectric composites filled with Bi_2Te_3 and Bi_2S_3 doped with MWCNTs

This objective focused on the optimisation of MWCNTs and its subsequent effect on the thermoelectric properties (i.e. Seebeck coefficient, electrical resistivity and power factor) for both Bi_2Te_3 and Bi_2S_3 filled RCF composite. The morphological, structural and the thermal stability of the MWCNT doped RCF-Bi_2Te_3 and RCF-Bi_2S_3 composites were demonstrated in this objective.

(4) To fabricate, study and optimise power factors of RCF thermoelectric composites filled with thermally annealed Bi_2Te_3 and Bi_2S_3

This objective focused on the optimisation of annealing temperature and time for both Bi_2Te_3 and Bi_2S_3 and studied its subsequent effect on the thermoelectric properties (i.e. Seebeck coefficient, electrical resistivity and power factor) for both annealed Bi_2Te_3 and Bi_2S_3 filled RCF composite. The morphological, structural and the thermal stability of the annealed RCF-Bi_2Te_3 and RCF-Bi_2S_3 composites were demonstrated in this objective.

1.4 Significance of research

The development of a thermoelectric RCF composite is in line with one of the key areas highlighted in the 11th Malaysia Plan spanning from 2016 to 2020 which is "Pursuing green growth for sustainability and resilience". Within this plan, it has been indicated that there is an evident need for sustainable consumption and production that encompasses creating green markets and also exploring alternative sources of renewable energy. The conversion of waste heat to electricity is directly in line with Malaysia's vision of converting of waste to wealth initiative. The thermoelectric RCF module can definitely contribute to the Sustainable Development Goals (SDG) outlined by countries around the world in partnership with United Nations in particular the following 2 goals: (a) Affordable and clean energy and (b) Sustainable cities and communities which is definitely of great value to Malaysia that is striving to add value to SDG.

1.5 Thesis outline

This thesis contains eight chapters. The outlines of the chapters in the thesis are as follows:

Chapter 1- includes the background study, the problem statement, objectives, scope, and significance of research and chapter outline of this study.

Chapter 2- presents an extensive review of literatures related to fundamentals of thermoelectricity, thermoelectric properties, and classes of thermoelectric materials, fabrication techniques and measures to further enhance thermoelectric properties.

Chapter 3- details the materials and methodology employed in executing the experimental work of this study. It also provides details on thermoelectric property measurement, thermal properties and characterization tests such as FESEM, EDX and XRD.

Chapter 4- addresses the electrodeposition of Bi_2Te_3 on both VCF and RCF using a univariate optimisation process and a multivariate optimisation approach using Design of Experiments

for the electrodeposition of Bi_2Te_3 on RCF. Moreover, the effect of electrodeposition parameters on Seebeck coefficient were discussed.

Chapter 5- reports the thermoelectric properties (i.e Seebeck coefficient, electrical resistivity and power factor) of RCF thermoelectric composites that are filled with two types of thermoelectric fillers (i.e Bi_2Te_3 and Bi_2S_3). The effect of varying concentrations of thermoelectric fillers on the morphological, structural and thermal stability of the composites was reported here.

Chapter 6- reports the thermoelectric properties (i.e Seebeck coefficient, electrical resistivity and power factor) of RCF thermoelectric composites that are filled with two types of thermoelectric fillers (i.e Bi_2Te_3 and Bi_2S_3) that are doped with MWCNTs respectively. The effect of varying concentrations of MWCNT on the morphological, structural and thermal stability of the composites was reported here.

Chapter 7- addresses the effect of annealing and varying annealing parameters (i.e. annealing temperature and time) of the thermoelectric fillers (i.e Bi_2Te_3 and Bi_2S_3). It also reports the thermoelectric properties (i.e Seebeck coefficient, electrical resistivity and power factor) of RCF thermoelectric composites that are filled with annealed thermoelectric fillers. The effect of annealing temperature and time on the morphological, structural and thermal stability of the composites was reported here.

Chapter 8- concludes the main findings based on the objectives of the study as well as makes recommendation for future works.

Chapter 2: Literature Review

2.1 Introduction

This chapter presents a review on the fundamental concepts of thermoelectricity, classes of materials used in thermoelectricity, fabrication/deposition techniques and strategies to further improve thermoelectric power factors.

2.2 Fundamentals of Thermoelectricity

There are 3 different types of thermoelectric effect: (a) Seebeck effect, (b) Peltier effect and (c) Thomson effect.

(a) Seebeck effect

In 1821, Thomas Johann Seebeck discovered that applying a thermal gradient across the junctions of two dissimilar conductors, a flowing electric current will be produced (Goldsmid, 2017). The Seebeck coefficient, also known as thermopower of a material, is a measure of the magnitude of an induced thermoelectric voltage in response to a temperature difference across that material. Its units are volts per Kelvin (V/K), although due to the very small induced voltage, it is more often given in microvolts per Kelvin (μV/K). Defining the Seebeck coefficient in terms of an equation is as in Eq (2.1):

$$\alpha = \frac{\Delta V}{\Delta T} \qquad (2.1)$$

Whereby α is the Seebeck coefficient, ΔV is the potential difference and ΔT is the temperature gradient.

An illustration depicting the charge carrier flow when subjected to a temperature difference for both p-type and n-type semiconductors is as shown in **Figure 2- 1**. The sign of the Seebeck coefficient, α represents the potential of the cold side with respect to the hot side. In a situation

where the electrons travels from the hot side to the cold end, the Seebeck coefficient would be negative here with respect to the hot side.

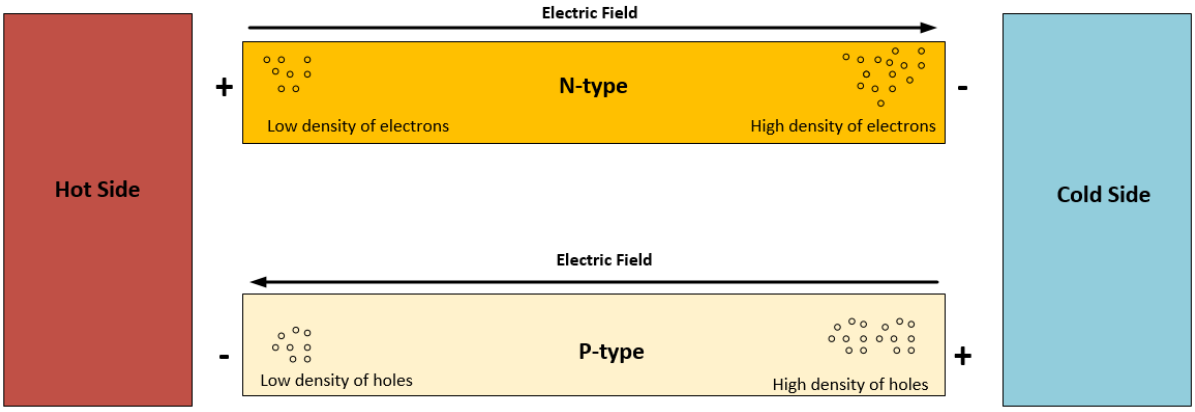


Figure 2- 1: Schematic depicting charge carrier flow when subjected to temperature difference for p and n-type semiconductors.

While this is true for an n-type semiconductor, in contrast, on a p-type semiconductor, the cold side would be positive with respect to the hot side and this makes the Seebeck coefficient a positive quantity (Kasap, 2001). The efficiency of which a thermoelectric material can generate electrical power is largely dependent on the Seebeck coefficient. Higher efficiency can be achieved when a larger induced thermoelectric voltage is produced from a given temperature gradient.

(b) Peltier effect

The Peltier effect was discovered by Charles Athanase Peltier in the year 1834. Peltier found that an electrical current would produce a temperature gradient at the junction of two dissimilar metals. The ratio of the rate of heating or cooling at a junction to the electric current can be expressed by the following equation Eq (2.2):

$$\pi = \frac{q}{I} \qquad (2.2)$$

Where the Peltier coefficient (π), q is is the rate of heating or cooling at a junction and I is the electric current. Peltier effect is essentially the opposite to that of Seebeck effect as depicted in **Figure 2- 2** . It is a principle that is commonly used for the purpose of refrigeration such as that of portable refrigerators, Peltier modules or in laboratory devices for cooling purpose.

Peltier coefficient can also be expressed in terms of Seebeck coefficient as shown in Eq (2.3):

$$\pi = \alpha T \qquad (2.3)$$

Where π is the Peltier coefficient, S is the Seebeck coefficient and T is the thermodynamic temperature.

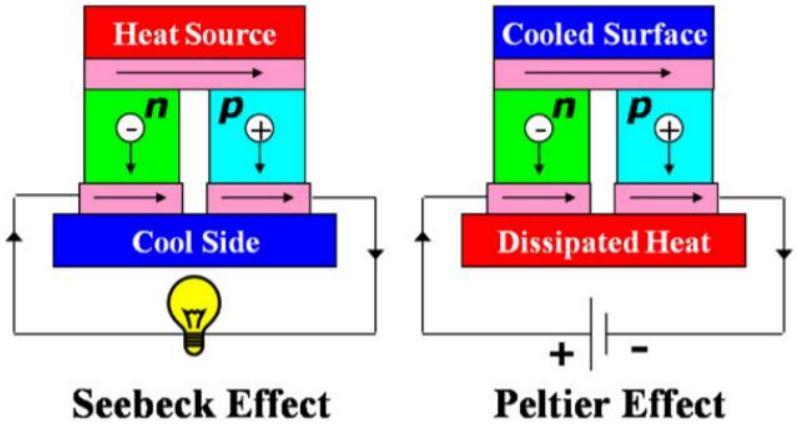


Figure 2- 2: Schematic illustrating the difference between Seebeck and Peltier effect (S. Lee et al., 2012).

(c) *Thomson effect*

Another category of the thermoelectric effect is the Thomson effect. William Thomson discovered in 1854 that there is a reverse cooling or heating process when both temperature difference and a flow of current is present. The Thomson coefficient,β is defined as the rate of heating per unit length resulting from the flow of a unit current along the conductor which is under a temperature gradient as shown in Eq (2.4):

$$q = \beta I \Delta T \qquad (2.4)$$

Where q is the rate of generation of reversible heat resulting from passage of current through a conductor which is subjected to temperature difference, ΔT and I is the current flow. However Thomson effect is not of primary importance in thermoelectric devices and will not be discussed in further detail in this thesis.

In the scope of this thesis, Seebeck effect is the phenomena that will be focused on as the research intends to convert thermal energy to electrical energy.

2.3 Thermoelectric Properties

The efficiency of a thermoelectric material is given by its figure of merit, ZT as shown in Eq (2.5).

$$ZT = \frac{\alpha^2}{\kappa\rho}T \qquad (2.5)$$

Where α is the Seebeck coefficient, κ is thermal conductivity, T is temperature and ρ is electrical resistivity. Therefore, ideal thermoelectric materials must exhibit a large Seebeck coefficient, a low electrical resistivity, and a low thermal conductivity to produce a large potential difference across the junction.

Power factor have also been used to reflect the efficiency of a thermoelectric material due to its largest contribution in calculating the ZT value as shown in Eq (2.6).

$$Power\ factor = \frac{\alpha^2}{\rho} \qquad (2.6)$$

2.4 Categories of Thermoelectric Materials

Thermoelectric materials can be classified in two main groups of (a) inorganic and (b) organic materials. Inorganic materials have generally been more widely used as it has better thermoelectric properties than that of organic materials. There are 3 sub-groups under the inorganic thermoelectric materials branch which are (i) semiconductors, (ii) metal based thermoelectric materials and (iii) ceramics. On the other hand, there are also 3 sub-groups under the organic thermoelectric materials branch which are (i) insulating polymer, (ii) conducting polymer and (iii) hybrid polymer-inorganic thermoelectric composite.

(a) Inorganic thermoelectric materials

(i) Semiconductors

Semiconductors are a favourable class of materials for thermoelectricity as they have large Seebeck coefficient above 100 μV/K (Dughaish, 2002). In order to obtain high values of figure of merit (ZT), it is necessary to have low thermal conductivity, κ without impacting the values of electrical resistivity, ρ and Seebeck coefficient, α. This is plausible by employing semiconductors with high atomic weight such as bismuth telluride (Bi_2Te_3) and its alloys with antimony (Sb), tin (Sn) and lead (Pb). The speed of sound is reduced in materials with high atomic weight thus resulting in decreased thermal conductivity (Majumdar, 2004). A semiconductor electronics component, for example, can perform well and reliably for many years when it is operating at or near the ambient temperature.

The effectiveness of each thermoelectric material is also depended upon its temperature range: (1) cryogenic range from 4 to 250 K, an ideal thermoelectric material for this temperature range is $CsBi_4Te_6$. It exhibits a ZT value of approximately 0.8 at 225 K which is much higher than those of bismuth telluride alloys in the cryogenic range (Chung et al., 2000). (2) Room temperature applications up to 500 K, the most commonly used material in this temperature

range is Bi_2Te_3 and its alloys with Sb, Sn and Pb. Bi_2Te_3 was first discovered by (Haken, 1910), he developed a relationship between thermoelectric power and composition of bismuth-tellurium. It was observed that the maximum thermoelectric power was obtained at the composition of Bi_2Te_3. (Goldsmid and Douglas, 1954) reported that Bi_2Te_3 has a high electrical to thermal conductivity ratio which was perceived to be vital for thermoelectric applications. The highest reported value of ZT at 300 K is 2.4 in p-type Bi_2Te_3/Sb_2Te_3 superlattice and 1.4 in n-type Bi_2Te_3/ $Bi_2Te_{2.83}Se_{0.17}$ (Venkatasubramanian et al., 2001). (3) Middle temperature applications from 500-900 K, thermoelectric materials suitable for this temperature range are lead telluride (PbTe) (Delaire et al., 2011), germanium telluride (GeTe), tin telluride (SnTe) and the alloys $(GeTe)_x(AgSbTe_2)_{100-x}$, commonly known as TAGS-x. A p-type TAGS with $(GeTe)_{0.85}(AgSbTe_2)_{0.15}$ has a ZT value of 1.2-1.4 (Rowe, 1995). (4) High temperatures more than 900 K, the suitable thermoelectric materials for this temperature range is generally silicon germanium (SiGe) that are commonly used in space applications. SiGe has been used in space radioisotope thermoelectric generators by The National Aeronautics and Space Administration (NASA) denoting at ZT value of 0.5 (p-type) and 0.9 (n-type) (Rowe, 1995). By doping with phosphorous and boron, n-type SiGe and p-type SiGe reached a ZT value of 1.0 and 0.75 at 700 °C respectively (Romanjek et al., 2015).

(ii) Metal based thermoelectric materials

Most high performing semiconductor based thermoelectric materials are made from tellurium (Te), lead (Pb) and antimony (Sb) which are toxic in nature and unstable at high temperatures above 1000 K. Therefore, metal based thermoelectric materials which are environmentally friendly and stable for high temperature waste heat energy harvesting were developed. An efficient thermoelectric material should ideally have a high electrical conductivity, high Seebeck coefficient and low thermal conductivity. However, all these variables are independent and cannot be controlled individually as the electrons that carry current also carries heat.

Therefore, in order to achieve a high electrical conductivity and low thermal conductivity simultaneously, a phonon glass electron crystal (PGEC) concept was proposed. PGEC refers to a multilayer composite material in which the component that contribute to electrical conductivity is different/separate from that which is responsible from thermal conductance. There are two classes of PGEC material (a) clathrates and (b) skutterudites.

Clathrates have a cage like crystal structure in which the metal atoms are caged by tetrahedrally coordinated atoms (Iversen et al., 2000). There are three types of clathrates with the following general formulas: (a) A_8E_{46}, (b) $A_{24}E_{136}$ and (c) $A_{30}E_{172}$ whereby A=Na, K, Ba, Rb and E=Al, Ga, Sn, In, Ge and Si (Kleinke, 2010). Clathrates are known to have low thermal conductivities (approximately 1 W/mK) similar to that of glass. This low thermal conductivity is due to the group 13 and group 14 guest atoms that form cages around alkali or alkali earth elements that acts as a phonon scattering centre through rattling (Tritt, 2001). The highest ZT achieved by clathrates is still notably lower than that of semiconductor however its operation temperature is at approximately 700 °C at ZT<1.4, some noteworthy work has been summarized in **Table 2- 1**.

Table 2- 1: Thermoelectric properties of clathrates.

Clathrate General Formula	Seebeck coefficient (µV/K)	Electrical conductivity (S/cm)	Power factor ($\mu W/cmK^2$)	Thermal conductivity (W/mK)	ZT	Ref
$Ba_8Ga_{16}Ge_{30}$	-180	570	18.46	1.25	1.35	(Saramat et al., 2006)
$Yb_{0.3}Ba_{7.7}Ga_{16}Ge_{30}$	-205	280	11.76	1.35	0.82	(Tang et al., 2008)
$Ba_8Ga_{15}Ge_{85}$	-148	550	12.04	0.8	1.25	(Kim et al., 2006)
$Ba_8Ga_{16}In_{1.5}Ge_{28.5}$	-200	166.67	6.67	0.84	0.52	(Liu et al., 2018)

Skutterudites are also another potential PGEC material that has low thermal conduction due to its complex structure. MX_3 is the chemical formula for skutterudites, where M is Co, Rh or Ir and X is P, As or Sb. Examples of skutterudite structures are CoP_3, $CoAs_3$, $CoSb_3$, RhP_3, $RhAs_3$, $RhSb_3$, IrP_3, $IrAs_3$ and $IrSb_3$ (Nolas et al., 1999). It has an octahedral structure with a void in its centre, the void filling atom can function as an electron donor or electron acceptor thus altering the electron concentration. In addition to altering the electron concentration, this void filling atoms also functions as a phonon scattering centre that is responsible for its lower thermal conductivity property (Sootsman et al., 2009). Filled skutterudites have shown promising thermoelectric properties in the temperature range of 500-800 K with ZT as large as 1.71, noteworthy work involving skutterudites have been summarized in **Table 2- 2**.

Table 2- 2: Thermoelectric properties of skutterudites.

Skutterudite General Formula	Seebeck coefficient (μV/K)	Electrical conductivity (S/cm)	Power factor ($\mu W/cmK^2$)	Thermal conductivity (W/mK)	ZT	Ref
$CoSb_3$	-180	200	6.5	6	0.1	(Nolas et al., 2000)
$Ba_{0.08}La_{0.05}Yb_{0.04}Co_4Sb_{12}$	-192	1428	52.6	2.6	1.71	(Nolas et al., 2000)
$In_{0.12}Yb_{0.20}Co_{4.00}Sb_{11.84}$	-195	1500	57.0	3.5	1.48	(Lee et al., 2018)
$Yb_{0.35}Co_4Sb_{12}$(with Ag)	-180	1500	48.6	3.1	1.0	(Chen et al., 2018)

Half-heusler are intermetallic class of compounds with possible high temperature thermoelectric application owing to their high temperature stability (up to 1000 °C) and abundance (Tritt, 2001). Half-heusler alloys consists of three components whereby two of them consists of transition metals and the third component consists of metals and metalloids. The chemical formula for half-heusler is ABC whereby A is Sc, Y, La, Ti, Zr, Hf, V, Nb, Ta, Cr and Mn, B is Fe, Ru, Co, Rh, Ni, Pd, Cu and Zn and C is Al, Ga, Si, Ge, Sn, Pb, As, Sb and Bi (Liu et al., 2012). Half-Heusler alloys demonstrated a high Seebeck coefficient (approximately 300 μV/K) and a high electrical conductivity (10^3-10^4 S/cm) but are limited by their high thermal conductivity (10 W/mK) (Lee and Chao, 2010). In most cases, half-Heusler alloys only obtain a maximum ZT value of 1.5 at a temperature of 800 K. Some noteworthy work using half-Heusler alloys are as shown in **Table 2- 3**.

Table 2- 3: Thermoelectric properties of half-Heusler alloys.

Half-Heusler General Formula	Seebeck coefficient (μV/K)	Electrical conductivity (S/cm)	Power factor (μW/cmK^2)	Thermal conductivity (W/mK)	ZT	Ref
$Ti_{0.5}(Zr_{0.5}Hf_{0.5})_{0.5}NiSn_{1-Y}Sb_Y$ (Y ~ 0.002)	-280	666	52.21	2.9	1.5	(Shutoh and Sakurada, 2005)
Nanostructured $Zr_{0.25}Hf_{0.75}NiSn$	-187	1110	38	2.6	1.1	(Bhardwaj et al., 2012)
$(ZrNiSn)_{0.925}(ZnO)_{0.075}$	-200	1000	40	3	1.0	(Chauhan et al., 2018)

(iii) Ceramics

Ceramic is an important class of thermoelectric material for waste heat energy conversion at high temperatures such as that from incinerators or combustion engines. When compared to that of commercial thermoelectric alloys such as Bi_2Te_3 and SiGe, ceramics such as metal oxides have better chemical stability, lower oxidation and lower toxicity (Ohta, 2018). Some notable n-type ceramics used are zinc oxide (ZnO), strontium titanate ($SrTiO_3$), and indium oxide (In_2O_3) and p-type ceramic are $Ca_3CO_4O_9$, BiCuSeO and nickel oxide (NiO). The thermoelectric performance of most n-type ceramics are lower than that of the p-type owing to the higher thermal conductivity (S. Wang et al., 2013) as shown in **Table 2- 4**.

Table 2- 4: Thermoelectric properties of ceramics.

Ceramic General Formula	Seebeck coefficient (μV/K)	Electrical conductivity (S/cm)	Power factor ($\mu W/cmK^2$)	Thermal conductivity (W/mK)	ZT	Ref
$Ca_3CO_4O_9$	-206	100	4.243	-	-	(Madre et al., 2013)
$Ca_{2.55}Ag_{0.3}La_{0.15}Co_4O_9/Ag$	-56.3	3968.3	12.58	3.5	0.39	(Gong et al., 2018)
$Bi_{0.88}Ba_{0.06}Pb_{0.06}CuSeO$	200	175	7.00	0.65	1.01	(Feng et al., 2018)

(a) Organic thermoelectric materials

(i) Insulating polymer

Thermoelectric devices made of solely inorganic materials are generally heavier, non-flexible, more toxic and non-environmentally friendly than that organic devices. Polymers are light weight, flexible, require simpler manufacturing processes (i.e. spin coating, screen printing, inkjet printing and paint brush technique) that are economically feasible (Bharti et al., 2018). Organic materials are composed of atoms that have natural abundance such as carbon (C), nitrogen (N), sulphur (S) and hydrogen (H) as compared to the less abundant metals such as tellurium and germanium commonly used in inorganic materials (McGrail et al., 2015). The low thermal conductivity of polymers is also an interesting attribute that encourages the development of polymer based thermoelectric devices. The thermal conductivity of polymers are commonly below 1 W/mK which is less than those of metals and semiconductors. For example, the thermal conductivity of polyaniline is 0.1-0.4 W/mK at room temperature with an electrical conductivity of 10^{-7}- 10^{2} S/cm which is independent of the thermal conductivity (Yan et al., 2002).

Insulating polymers though electrically insulating with a coil like structure with no electronically active backbone can also be used to form organic thermoelectric materials with the help of nanoparticles with thermoelectric properties. These insulating polymers with thermoelectric particles can be processed using highly cost effective techniques such as extrusion, melt blending and electrospinning. Examples of insulating polymers used for thermoelectric purpose is polyethylene (PE), polypropylene (PP), poly(vinylidene fluoride) (PVDF) and epoxy. The thermoelectric performance of some thermoelectric materials with insulating polymer matrices are as shown in **Table 2- 5**.

Table 2- 5: Thermoelectric properties of insulating polymer composites.

Polymer	Dopant	Seebeck coefficient (μV/K)	Electrical conductivity (S/cm)	Power factor (μW/cmK^2)	Thermal conductivity (W/mK)	ZT	Ref
Polyethylene oxide (PEO)	Molybdenum sulphide (MOS_2)	1.5	0.1	2.25 X 10^{-7}	-	-	(Bissessur et al., 1993)
Poly(vinyl acetate) (PVAc)	Single wall carbon nanotube (SWCNT)	40	48	0.0192	0.34	0.006	(Yu et al., 2008)
Poly(vinyl acetate) (PVAc)/aryclic copolymer	Multi-wall carbon nanotube (MWCNT)	78	71.1	0.4325	-	-	(Moriarty et al., 2012)
Polyvinylidene fluoride (PVDF)	Graphene	17	170	0.0491	-	-	(Hewitt et al., 2013)

(ii) *Conducting polymer*

Most polymers are electrically insulating in nature, however conjugated polymers are conductive in nature due to charge delocalization across the polymer backbone. Conjugated polymer depict an extremely low thermal conductivity (0.1 to 1 W/mK), large range of electrical conductivity (10^{-8} to 10^4 S/cm) and Seebeck coefficient (ranging from 1 to 100 μV/K)(Du et al., 2012a). Some prominent examples of conducting polymer that are significant for thermoelectric applications are polypyrrole (PPy), poly

(3,4-ethylenedi-oxythiophene):poly(styrenesulfonate) (PEDOT:PSS), polyaniline (PANI) and poly(3-hexylthiophene) (P3HT). The thermoelectric performance of some conducting polymer composite are as shown in **Table 2- 6**.

Table 2- 6: Thermoelectric properties of conducting polymer composites.

Polymer	Dopant	Seebeck coefficient (μV/K)	Electrical conductivity (S/cm)	Power factor ($\mu W/cmK^2$)	Thermal conductivity (W/mK)	ZT	Ref
PPy	Reduced graphene oxide (RGO)	33.8	75.1	0.0857	-	-	(Zhang et al., 2015)
PEDOT: PSS	Formic acid	20.6	1900	0.8063	0.2	0.32	(Mengistie et al., 2015)
PANI	Hydrochloric acid and graphene	33.8	123	0.1405	-	-	(Abad et al., 2013)
PANI	Camphor sulfonic acid (CSA)	21	5.4×10^{-4}	2.381×10^{-7}	0.5-0.7	0.77	(Nath et al., 2014)
P3HT	Single wall carbon nanotube (SWCNT)	40.3	524	0.851	0.38	-	(Lee et al., 2015)

(iii) *Hybrid polymer-inorganic thermoelectric composite*

In recent times, inorganic nano-sized thermoelectric materials have exhibited relatively high ZT values, however due to concern of heavy metal pollution as well as its poor processability limits its wider application (Li et al., 2010). On the other hand, conductive polymers are environmentally friendly, cost effective and has easy processing capabilities. However, the power factor/ZT values of most organic conductive polymer composites are approximately three orders lower than that of inorganic thermoelectric materials (Lévesque et al., 2007)(Liu et al., 2002). An emerging approach to capitalize both the high ZT values of inorganic materials and the electrical conductivity as well as the easy processing capability of polymers, is a two component polymer-inorganic thermoelectric nanocomposite. Recently, various researchers have attempted to prepare hybrid heterostructure consisting of inorganic thermoelectrics with conducting polymers, some obtained results are as shown in **Table 2- 7**.

Table 2- 7: Thermoelectric properties of hybrid polymer inorganic composites.

Polymer	Inorganic Thermoelectric Filler	Seebeck coefficient (µV/K)	Electrical conductivity (S/cm)	Power factor (µW/cmK2)	Thermal conductivity (W/mK)	ZT	Ref
PANI	Bi_2Te_3	125	80	1.25	0.1	0.18	(Toshima et al., 2011)
PANI	PbTe	578	0.022	0.0073	-	-	(Wang et al., 2011)
PEDOT: PSS	Te nanorods	50	100	0.25	-	-	(Li et al., 2017)
PEDOT: PSS	Silicon carbide (SiC) nanowires	20.9	1550	0.677	0.23	0.17	(Wang et al., 2018)

2.5 Chosen Thermoelectric Material

The focus of this research work will be thermoelectric energy harvesting from low grade waste heat. Thus, it will be utilising thermoelectric materials suitable for room temperature applications. Till date, the compounds X_2Y_3 (where X=Bi, Sb, Pb and Y=S, Se, Te) are regarded as the most promising for thermoelectric applications (Zhao et al., 2008). Bi-Te and Sb-Te exhibits the best TE properties at room temperature whereas Pb-Te exhibits its best at middle temperatures (750-900K). For room temperature applications in particular, Bi-Te systems exhibits a much higher figure of merit, ZT at 0.97 as compared to Sb-Te compounds at 0.56 (Carmo et al., 2010). Amongst all bulk thermoelectric materials, Bi_2Te_3 based alloys depicts the highest ZT value for room temperature application as shown in *Figure 2- 3***Figure 2- 3** below:

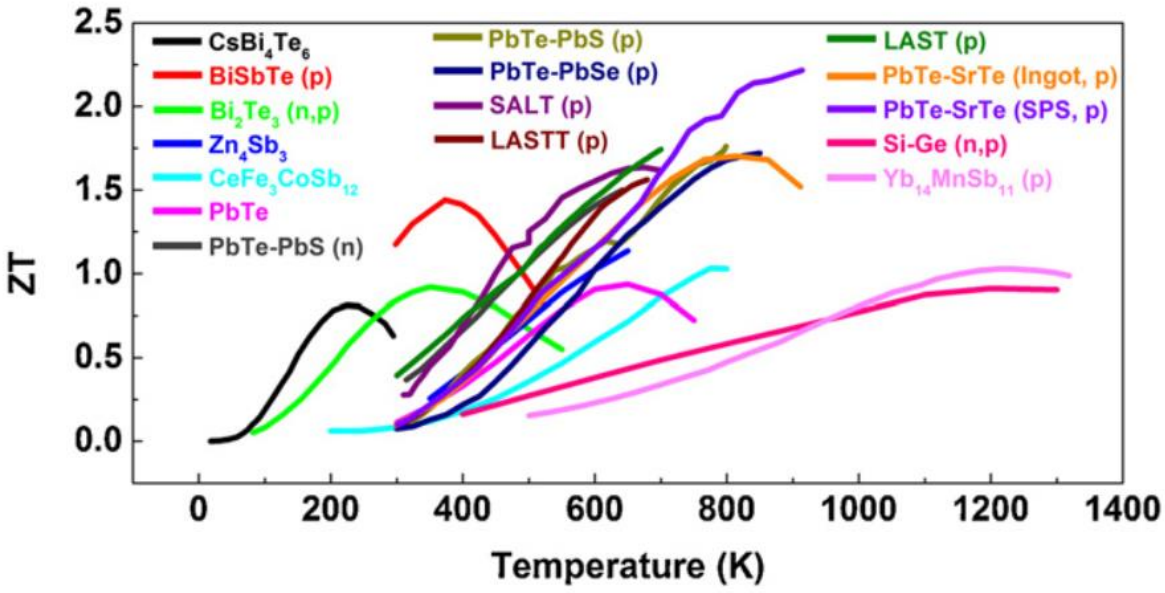


Figure 2- 3: ZT value of common bulk thermoelectric materials (He et al., 2013).

Bismuth chalcogenides have been widely studied and explored for the last 50 years from the time of its discovery in the early 1950's. Bismuth chalcogenides consist of A_2B_3 whereby (A=Bi; B=S, Se, Te) have attracted a great deal of attention due to its high figure of merit, ZT, the largest reported so far made from p-type bismuth telluride (Bi_2Te_3) super lattice is 2.4 which is the largest reported till date (Venkatasubramanian et al., 2001).

Chalcogenide compounds are also considered potential thermoelectric materials due to its high stability in air and high melting points. They also have strong flexibility in hosting other elements and small difference in electronegativity between sulfur, selenium and tellurium, they have the capability to generate semiconductors in the energy gap of 0.1 to 0.8ev which is highly desirable for thermoelectric applications (Bing Ling et al., 2014). Hence bismuth in combination with chalcogenide compounds presents desirable attributes for thermoelectric materials.

Within the group of bismuth chalcogenides, bismuth telluride (Bi_2Te_3) has shown better thermoelectric properties as compared to its counter parts bismuth sulfide (Bi_2S_3) and bismuth selenide (Bi_2Se_3) and has been more widely studied.

Bi_2Te_3

Bi_2Te_3 based alloys has a lamellar structure perpendicular to the c-axis which is commonly used for low temperature applications up to 227 °C. Bi_2Te_3 has a rhombohedral crystal structure, in which the atoms are arranged in a hexahedral layered sandwich structure. It consists of five monoatomic sheets, at which in each layer Bi_2Te_3 is ordered in Te^1-Bi-Te^2-Bi-Te^1 sequence along the c axis (Goldsmid, 2016). Te^1 and Te^2 denotes two different chemical states for the anions. Bi and Te^1 atom are combined by covalent and ionic bond whereas Bi and Te^2 atom are combined with covalent bond. The Te^1 and Te^1 atoms are combined via van der Waals interactions. The lattice constant parameters of the unit cell,

atomic bond and bond average net charge of Bi_2Te_3 from Mulliken's population analysis is as shown in **Table 2- 8**. At room temperature, the band gap of Bi_2Te_3 is from 0.131-0.16 eV (Goldsmid, 2016) and it is direct band gap semiconductor. It has a low melting temperature of 585 °C. It has a molar mass of 800.76 g/mol and density of 7.74 g/cm^3. Bi_2Te_3 displays unique properties such as a high Seebeck coefficient (~220 µV/K), good electrical conductivity (~400 S/cm), and low thermal conductivity (~1.5 W/m K).

Table 2- 8: Structure, lattice parameters and bond properties of Bi_2Te_3 (Deng and Zhao, 2018).

Symmetry		Trigonal
Space group		$R\bar{3}mD_{2d}^5$
Lattice constant		$a = 4.378$ Å $b = 4.378$ Å $c = 30.389$ Å $\alpha = \beta = 90°, \gamma = 120°$
Crystal volume/Å^3		504.398
Density/g cm^{-3}		7.909
Binding energy/eV atom^{-1}		4.129
Bond length/ Å		3.065-3.223
Bond angle/degree	Bi-Te-Bi	85.563-180
	Te-Bi-Te	85.5-176.101

Though Bi_2Te_3 is a widely commercialised thermoelectric alloy, the scarcity and toxicity of tellurium has always been of pivotal concern (Yu et al., 2011). Tellurium is one of the rarest stable solid element that only makes up 0.0000001 % of the Earth's crust (Seeking Alpha, 2017). It only has a crystal abundance of 1µg/kg (Investorintel, 2014).

Alternatives to tellurium based alloys: Bi_2S_3

Due to the poor crystal abundance of tellurium as mentioned in the previous section, it is vital that we look for alternatives to replace tellurium. Tellurium can be replaced with other element such as sulphur that is abundantly present which makes up 0.042 % of the Earth's crust.

Bi_2S_3 has an orthorhombic crystal structure with 4 molecules per unit cell. Each molecule consists of 2 bismuth atoms and 3 sulphur atoms mounting to 20 atoms per unit cell. Within the Bi_2S_3 structure atoms are bound by covalent bonds and weak Coulombic interactions between bismuth cations and sulphur anions (Deng and Zhao, 2018). The lattice constant parameters of the unit cell, atomic bond and bond average net charge of Bi_2S_3 from Mulliken's population analysis is as shown in **Table 2- 9**.

Bi_2S_3 is an indirect band gap semiconductor and at room temperature it displays a band gap of 1.3-1.7 eV (Yang et al., 2013). It has a melting temperature of 850 °C. It has a molar mass of 514.16 g/mol and density of 6.78 g/cm^3. Bi_2S_3 has naturally low carrier concentrations 2 X 10^{18} cm^{-3} which contributes to its high Seebeck coefficient, and a low thermal conductivity which makes it a suitable replacement for telluride based alloys in thermoelectric applications. However, it is mostly limited by its low electrical conductivity which can be overcome by extrinsically doping Bi_2S_3 or by introducing sulphur vacancies.

Bi_2S_3 occurs naturally as bismuthinite in nature, the average abundance of bismuth being is 0.00002% and sulphur is 0.042 % in the Earth's crust. With its natural abundance leading to lower cost and lower toxicity, Bi_2S_3 is a good alternative to telluride based thermoelectric alloys.

Table 2- 9: Structure, lattice parameters and bond properties of Bi_2S_3 (Deng and Zhao, 2018).

Symmetry		Orthorhombic
Space group		P*nma* (D_{2h}^{16})
Lattice constant		$a = 11.445$ Å $b = 3.921$ Å $c = 10.911$ Å $\alpha = \beta = \gamma = 90°$
Crystal volume/Å^3		489.595
Density/g cm^{-3}		6.975
Binding energy/eV atom^{-1}		4.858
Bond length/ Å		2.671-2.996
Bond angle/degree	Bi-S-Bi	94.522-100.388
	S-Bi-S	80.123-89.923

Bi_2S_3 powders has been fabricated using hydrothermal, mechanical alloying and spark plasma sintering. The thermoelectric properties of these powders have been characterised in the form of sintered blocks and no form of substrate/structure/fibre composite has been used. Bi_2S_3 is known to achieve high Seebeck coefficient due to its inherently low intrinsic carrier concentration (2 X 10^{18} cm^{-3}) which two orders lower than that of Bi_2Te_3 (10^{20} cm^{-3}), however this results in increased resistivity and poor ZT values (Chmielowski et al., 2015). Thus, to improve its ZT values, it is necessary to extrinsically dope Bi_2S_3 (Yu et al., 2011)(X. Du et al., 2014) or by introducing sulphur vacancies in its lattice system (Mizoguchi et al., 1995).

Zhao et al. observed that inducing sulphur vacancies in sintered $Bi_2S_{2.90}$ increased both the carrier concentration and carrier mobility that further reduced its electrical resistivity resulting in a ZT value of 0.08 and a power factor of 250 μW/Km^2 (300 K) (Zhao et al., 2008). A few dopants such as bismuth (Bi), bismuth chloride ($BiCl_3$) and silver (Ag) have been used in the

past to help reduce the electrical resistivity of Bi_2S_3 and improve its ZT values. Ge et al. observed that addition of Bi to a Bi_2S_3 nanowire improved the electrical conductivity by 3 orders of magnitude with a ZT value of 0.05 (Ge et al., 2017). A similar observation was made by Wong et al. who synthesised a percolated bismuth rich bismuth sulphide while maintaining the Seebeck coefficient and improving the electrical conductivity with a ZT value of 0.15 (Wong et al., 2016). Du et al. and and Yu et al. used $BiCl_3$ and Ag as electron dopants to tune the carrier concentration of Bi_2S_3 and resulted in a ZT value of 0.1 and 0.05 respectively (X. Du et al., 2014)(Yu et al., 2011).

2.6 Deposition/Fabrication Techniques

Thin film technologies are largely used in producing n and p-type semiconductor by forming a thin layer of material on rigid/flexible substrates. Thermoelectric thin films has potential for use in diverse applications such as micro thermoelectric generators, micro thermoelectric coolers and micro thermoelectric sensors (Goto et al., 2017). Thin film thermoelectric devices have higher efficiency than that of bulk materials due to quantum and classical size effects of phonons and electrons.

There are two groups used under the branch of thin film technology which is chemical deposition and physical deposition.

In chemical deposition, the source material to be deposited is mixed with a volatile precursor in fluid form that acts as a carrier. Chemical reaction takes place on the substrate between the precursors that results in the deposition of thin films. Chemical deposition can be achieved by electrodeposition/chemical bath deposition, electrochemical atomic layer epitaxy (ECALE) and metal organic chemical vapour deposition (MOCVD).

Physical deposition involves the transfer of atoms or molecules from a source by physical means to generate the vapour species on a substrate. This could be done with thermal evaporation processes or by bombarding the source by energetic beam of electrons, photons or ions (Arthur, 1998). Unlike chemical deposition, there is no chemical reaction that takes place on the surface of the substrate/in the entire process and the source material used are close to 99.999% purity with no volatile precursors that act as carries.

Physical deposition for Bi_2Te_3 films consists of evaporative deposition and sputter deposition. This review will be looking into flash evaporation, co-evaporation, ion beam sputtering and radio frequency (RF) magnetron sputtering.

The advantages and disadvantages of each thin film technique is discussed as shown in **Table 2- 10** below.

Table 2- 10: Advantages and disadvantages of thin film techniques.

No	Technique	Advantages	Disadvantages
1	Electrodeposition	-Room temperature and atmospheric pressure operation -Does not require special environment to operate such as sputtering gas -Simple and easy setup of equipment -Provides large area for deposition -Relative ease in modulating film composition and thickness -Cost effective technique -High growth rate -Low processing time	-Disposal of electrolyte
2	Metal Organic Chemical Vapour Deposition (MOCVD)	-Production of high quality films with good composition control -Able to control the partial pressures of several metal sources -Higher throughput compared to other vapor deposition techniques	-High temperature operation -Need to use expensive and high purity volatile organic compounds as precursors of Bi and Te -Low vacuum operation -Possible carbon contamination due to the usage of organic vapours -Expensive reactor chamber
3	Flash evaporation	-Simple system setup -No waste material generated	-There is a difference in vapor pressure for different elements leading to compositional gradient along the film thickness -Deviation from the stoichiometric composition due to the re-evaporation of Te element from a deposited film.
4	Co-evaporation	-Independent temperature and partial pressure control for individual elements -Simple system setup	- High temperature operation - High vacuum environment -No direct contact between precursors and substrate, possible mass loss of precursors during evaporation.
5	Radio Frequency (RF) Magnetron sputtering	-Difference in vapour pressure of Bi and Te elements does not affect the process -Ion bombardment before deposition removes surface impurities	-Vacuum environment -Above room temperature operation -Requires highly purified inert gas to prevent contamination of films -Impurities from the fixtures in the chamber may also be sputtered and deposited in the films
6	Ion Beam Sputtering	-Arriving of sputtered atoms have high kinetic energies at the substrate perhaps enhance deposition coverage	-Ion bombardment may damage substrate at energies higher than 50 eV

		-Power radiated heating is less damaging to substrate than direct heating in evaporation	-Sputtered films may contain an element of the sputtering gas

For the purpose of this research work, recycled carbon fibres will be coated with n-type bismuth telluride using the electrodeposition technique. Referring to **Table 2- 10**, it can be noted that electrodeposition is the most cost effective process as it is carried out in room temperature, atmospheric pressure with no requirement of any special environments. In addition to that, electrodeposition have been widely studied since 1994 till date and it is also it is almost the most studied technique compared to all other technique due to the mentioned advantages. Electrodeposition also has very high growth rates that is suitable for fabrication of thick film thermoelectric devices at 34-50 μm/h approximately 5 times higher than other techniques reported in literature (Wang et al., 2007)(Glatz et al., 2008).

The parameters and thermoelectric properties of electrodeposited Bi_2Te_3 thin films will be discussed in more detail in the section below.

2.6.1 Electrodeposition

Electrodeposition is essentially a chemical redox reaction using aqueous or non-aqueous solvents with a three electrode system set up. The source material will be reduced on the surface of the substrate by the applied reduction potentials. The mechanism of electrodeposition is dependent on a multitude of parameters such as deposition potential, electrolyte composition, deposition temperature and deposition time which will be discussed further in the sub-sections below:

2.6.1.1 Effect of deposition potential

Electrodeposition of Bi_2Te_3 was first discovered by Takahashi that proved Bi_2Te_3 thin films could be produced using electrodeposition with a nitric acid solution (Takahashi, 1993). In this earlier research, Takahashi et al. concluded that cathodic currents showed an increasing trend at potentials more negative than 0.05 V as shown in **Figure 2- 4**, an acidic electrolyte containing 1.5 mM $HTeO_2^+$ and 1.5 mM Bi^{3+} resulted in black deposits on the substrate surface confirming the presence of Bi_2Te_3 (Takahashi, 1993).

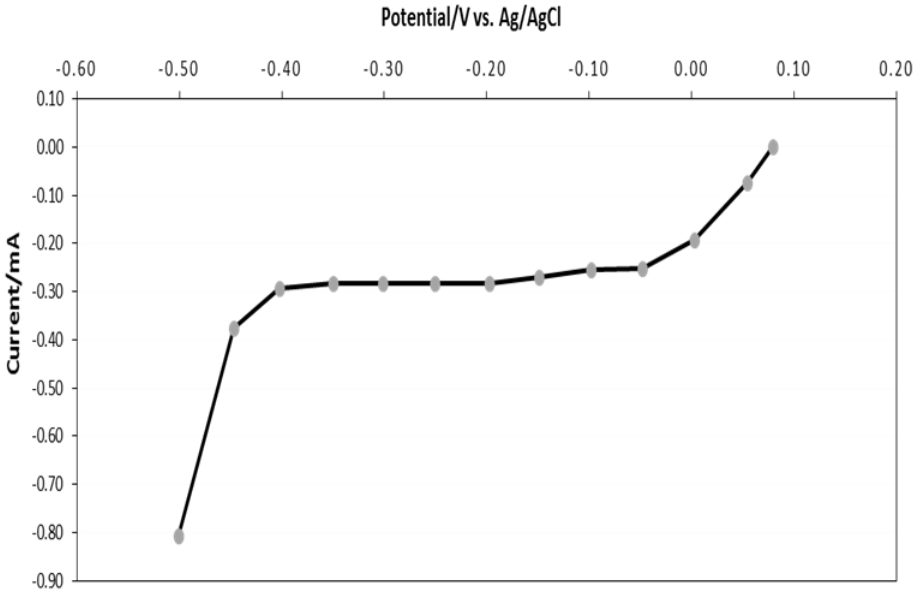


Figure 2- 4: Current-potential relation of Ti electrode in a nitric acid solution with 1.5mM of $Bi(NO_3)_3$ and 1.5mM of TeO_2 (Takahashi, 1993).

Later, in 2002, a Pourbaix-type diagram was constructed for the electrodeposition of Bi and Te which mentioned that the suitable deposition potentials for Bi_2Te_3 is potentials more negative than 0.50 V as shown in **Figure 2- 5** (Martín-González et al., 2002).

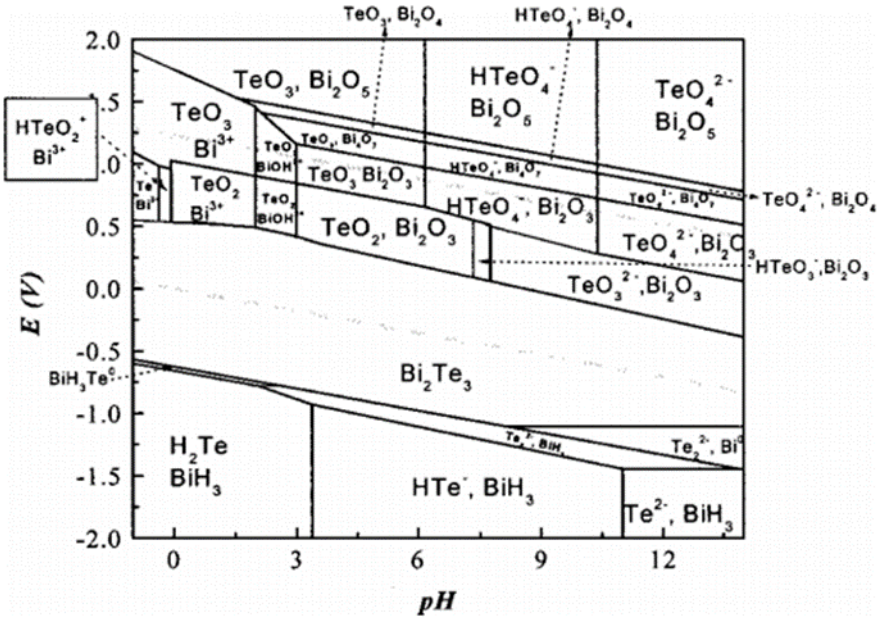


Figure 2- 5: Pourbaix type diagram for Bi and Te in nitric acid electrolyte (Martín-González et al., 2002).

A similar observation was reported by Magri et al. at -0.05 V with much higher concentrations of 3.5 mM Bi^{3+} and 7.5 mM $HTeO_2^+$ with one reduction wave in cyclic voltammetry (Magri et al., 1996). . In another study by (Ma et al. 2010), a -0.062 V was reported with 7.5mM Bi^{3+} and 10mM $HTeO_2^+$ electrolyte. However (Miyazaki and Kajitani ,2001), obtained a slightly positive reduction potential at 0.02V with an electrolyte concentration of 10mM Bi^{3+} and 10mM $HTeO_2^+$. An interesting observation obtained from (Takahashi, 1993),(Magri et al., 1996) and (Miyazaki and Kajitani ,2001) is that as the Bi^{3+} concentration increases, the deposition potentials tend to be more positive values. This is because the individual deposition potential of Bi^{3+} is more positive than that of $HTeO_2^+$ resulting in more positive deposition values for the combined electrolyte.

The reduction potentials of bismuth, tellurium and bismuth tellurium in nitric acid (HNO_3) was studied by both (Qiu et al., 2010) and (Martín-González et al., 2002)using 1 M of HNO_3, 7.5-8mM of Bi^{3+} and 10mM of $HTeO_2^+$. Their results show very similar reduction potentials for

both bismuth and tellurium in a HNO_3 electrolyte of -0.062 to -0.060 V similar to the earlier observation made by (Takahashi, 1993) with a much lower amount of Bi^{3+} and $HTeO_2^+$ ions.

The deposition potentials is also found to majorly affect the conduction band in thermoelectric materials, Miyazaki et al. observed that p-type Bi_2Te_3 were obtained for potentials less than 0.02V while n-type Bi_2Te_3 is observed from 0.02V to 0.08V. Hence, it is possible to alter the conduction band of a thermoelectric material by easily controlling the potential (Miyazaki and Kajitani ,2001). The crystallographic orientations and compositions of the deposited films were also affected by the deposition potentials.

Despite knowing the potentials viable for the reduction of Bi^{3+} and $HTeO_2^+$ in nitric acid which is less than 0.05 V as shown in **Table 2- 11** as obtained by most researchers as mentioned above, it is imperative to know the exact range of potentials that will lead to the stoichiometric formation of Bi_2Te_3 phase as shown in **Table 2- 12**. The potentials that led to a stoichiometric Bi_2Te_3 phase was in the range of -0.12 to -0.145 V with close to 40 at.% of Bi and 60 at.% of Te and also the presence of {110} orientation in its XRD peaks (Martín-González et al., 2002). A similar reduction potential was also observed by Yoo et al. that obtained stoichiometric Bi_2Te_3 at -0.17 V relatively high Seebeck coefficient (Yoo et al., 2005). Both Yoo et al. and Gonzalez et al. observed that there is a decreasing Te trend between -0.1 V to -0.25 V and later observed an increasing Te trend above -0.25 V as shown in **Table 2- 13**. This could be due to the fact that reduction of $HTeO_2^+$ to Te occurs in acidic electrolytes around -240 to -330 mV, hence an increasing Te is observed in this reduction potential region. Both also observed that the region of 60 at.% of Te is observed at close to -0.145 V leading to the stoichiometric formation of Bi_2Te_3. Ma et al. observed a stoichiometric Bi_2Te_3 at a slightly positive cathodic potential at -0.08 V for a similar composition of electrolyte, this could be attributed to the stainless steel substrate used that kinetically deters the Te deposition in an overpotential of 0.7 V (Ma et al. 2010). A much more positive reduction potential is observed at 0.02 V by Miyazaki

et al., due to larger amount of Bi^{3+} used in electrolyte with the same amount of $HTeO_2^+$; as the individual deposition potential of Bi^{3+} is slightly more positive as compared to $HTeO_2^+$.

On the contrary, (Qiu et al., 2010) concluded that composition of Bi_2Te_3 films are not dependent upon the deposition potentials as the range investigated from -0.025 V to -0.25 V did not produce any substantial changes in Bi and Te atomic percentage and all were close to stoichiometric proportions. Despite having said that, the least deviation from stoichiometry among the potentials investigated by Qiu et al. is within -0.1 V to -0.15 V which is in line with the observations made by both Yoo et al. and Gonzalez et al. A lower cathodic potential is observed by Kim and Oh,2009 but with a much higher concentration of Bi^{3+} and $HTeO_2^+$ that leads to the formation of stoichiometric Bi_2Te_3 (Kim and Oh ,2009).

Table 2- 11: Deposition potentials with respect to composition for the formation of Bi_2Te_3 films.

No	Bath Composition	pH	Deposition Potential (V)	Substrate Used	Remarks	Ref
1	1.5mM of TeO_2 1.5mM of $Bi(NO_3)_3$ Diluted HNO_3	0.90	< 0.05	Ti sheet	Black deposites were formed on the Ti sheet at potentials more negative than 0.05 V.	(Takahashi, 1993)
2	10 mM $HTeO_2^+$ 7.5 mM Bi^{3+} 1 M HNO_3	< 0	-0.062	Platinum Disk	The reduction potential for electrolytes containing both $HTeO_2^+$ and Bi^{3+} is more positive at -0.062 V than the reduction potential of electrolytes containing only $HTeO_2^+$ (-0.240 V) or only Bi^{3+} (-0.080 V) for comparable concentrations. At potentials more negative than -0.50 V, the atomic percentage of Te increases again	(Martín-González et al., 2002)
3	7mM $HTeO_2^+$ 3.5mM Bi^{3+} 1M HNO_3	0	-0.05	Platinum	The reduction potential for electrolytes containing both $HTeO_2^+$ and Bi^{3+} is more positive at -0.05 V than the reduction potential of electrolytes containing only $HTeO_2^+$ (-0.350 V) or only Bi^{3+} (-0.150 V) for comparable concentrations.	(Magri et al., 1996)
4	10 mM $HTeO_2^+$ 7.5 mM Bi^{3+} 1 M HNO_3	0	-0.080	Stainless Steel	The potential at which reduction is observed when both $HTeO_2^+$ and Bi^{3+} are present in solution at -0.080 V is more positive compared with the reduction of solutions containing only $HTeO_2^+$ (-0.375 V) or only Bi^{3+} (-0.120 V) for comparable concentrations.	(Ma et al., 2010)
5	10mM of TeO_2 10mM of Bi_2O_3 Diluted HNO_3	0.50	0.02	Titanium sheet	The films deposited at E<+0.02 V were found to show p-type conduction while those prepared at E >+ 0.02 V were n-type conductors	(Miyazaki and Kajitani, 2001)
6	10mM of $HTeO_2^+$ 8mM of Bi^{3+} 1M of HNO_3	1.0	-0.060	Stainless Steel	The potential at which reduction is observed when both $HTeO_2^+$ and Bi^{3+} are present in solution (E_{pc} . -0.060 V) is more positive compared with the reduction of solutions containing only $HTeO_2^+$ (E_{pc} . -0.330 V) or only Bi^{3+} (E_{pc} . -0.108 V) for comparable concentrations.	(Qiu et al., 2010)

Table 2- 12: Deposition potentials leading to stoichiometric formation of Bi_2Te_3 films using electrodeposition.

No	Bath Composition	pH	Deposition Potential (V)	Substrate Used	Remarks	Ref
1	10 mM $HTeO_2^+$ 7.5 mM Bi^{3+} 1 M HNO_3	< 0	-0.12 to -0.145	Platinum Disk	The films formed at deposition potentials of -0.12 to -0.145 resulted in films with 60 at % of Te and 40 at % of Bi.	(Martín-González et al., 2002)
2	10 mM $HTeO_2^+$ 8 mM Bi^{3+} 1 M HNO_3	0.1	-0.17 V	SiO_2/Si	Te content in Bi_2Te_3 films was seen to deccrease from 60.8 at.% (−0.12 V) to 43.6 at.% (−0.26 V), and increased again to 55.9 at.% (−0.52 V). Highest Seebeck of −188.5 μV/K was achieved at −0.17 V that yielded stoichiometric Bi_2Te_3 films.	(Yoo et al., 2005)
3	10 mM $HTeO_2^+$ 7.5 mM Bi^{3+} 1 M HNO_3	0	-0.080	Stainless Steel	Stoichiometric Bi_2Te_3 film on steel formed at -0.08 V.	(Ma et al., 2010)
5	10mM of TeO_2 10mM of Bi_2O_3 Diluted HNO_3	0.50	0.02	Titanium sheet	Nearly stoichiometric Bi_2Te_3films at potentials <+0.02 V, and films prepared at potentials >+0.02 V lack Bi	(Miyazaki and Kajitani, 2001)
6	10mM of $HTeO_2^+$ 8mM of Bi^{3+} 1M of HNO_3	1.0	-0.025 to -0.25	Stainless Steel	Composition of the films was not strongly dependent on the deposition potentials.	(Qiu et al., 2010)
7	50 mM (Bi^{3+}+ $HTeO_2^+$) 1 M HNO_3 Bi/Bi+Te=0.3 to 0.7	X	-0.05	Ti/glass	Electrolyte with a Bi/(Bi + Te) mole ratio of 0.54 led to stoichiometric Bi_2Te_3 films.	(Kim and Oh, 2009)

Table 2- 13: Atomic percentages as a function of the applied potential for depositions on Pt electrodes from 10mM of $HTeO_2^+$ and 7.5 mM of Bi^{3+} in 1 M HNO_3(Martín-González et al., 2002).

Applied Deposition Potentials (V)	**Bi (at%)**	**Te (at%)**
-0.12	**39.2**	**60.8**
-0.145	**39.6**	**60.4**
-0.17	43.9	56.1
-0.195	45.3	54.7
-0.22	47.7	52.3
-0.26	57.4	*43.6
-0.42	45.9	*54.1
-0.52	44.1	*55.9

*Increasing trend observed for Te at potentials more negative than -0.25V

Deposition potential is also known to affect the stoichiometry of electrodeposited Bi_2Te_3 films. Stoichiometry of a film plays key role on the thermoelectric properties of electrodeposited films (Cai et al., 2013). A stoichiometric bismuth telluride films should encompass a Bi:Te ratio of 2:3 or consists of 40 at.% of bismuth and 60 at.% of tellurium. This was observed by Magri et al., as the stoichiometric composition was closer to Te/Bi=1.5, it was observed that the carrier concentrations decreased and the Hall mobility of carriers increased which eventually improves the ZT value (Magri et al., 1996). The stoichiometric effect on Seebeck coefficient was also observed by Yoo et al, as stoichiometric Bi_2Te_3 with 60 at.% of Te was deposited at -0.17 V it exhibited a high Seebeck coefficient at -188.5 µV/K (Yoo et al., 2005) . Meanwhile, a nearly stoichiometric Bi_2Te_3 obtained by Miyazaki et al. at 0.02 V exhibited a Seebeck coefficient of -63 µV/K. This is because bismuth telluride films with the stoichiometric composition of Bi_2Te_3 have a preferred orientation, which is an ideal thermoelectric device configuration as cleavage planes are perpendicular to the surface (Szymczak et al., 2014).

Wang et al. discovered an interesting relationship between Seebeck coefficient and Te content, where the Seebeck coefficient was directly proportional to the increment of Te until 68.5 at % of Te (-104.6 µV/K). But as the Te content increased to 78.9at.% of Te the Seebeck coefficient dropped to -20 µV/K (Wang et al., 2007). Despite that increasing Te content way beyond stoichiometry leads to large carrier concentrations and low Hall mobility which leads to electrodeposited films with lower ZT. On the contrary, Wang et al. observed that films with the highest power factor at 7x 10^{-4} W/mK^2 at Te content close to 60 at.% as shown in **Figure 2- 6** which proves the claim stoichiometric films have the best thermoelectric properties.

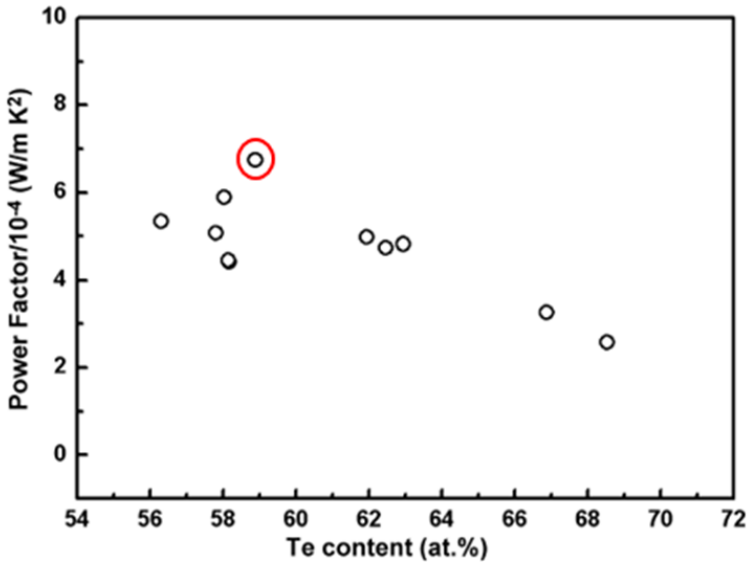


Figure 2- 6: Dependence of power factor of the films on the Te content in deposit (Wang et al., 2007).

Besides Seebeck coefficient, electrical resistivity of Bi_2Te_3 films was also found to be dependent on the Te content. Wang et al. observed the highest electrical conductivity of 1416 Scm^{-1} in films with Te content close to 60 at.% as shown in **Figure 2- 7(a)**. The films with stoichiometric Bi_2Te_3 have higher crystallinity hence better electrical conductivity (Wang et al., 2007). In addition to that, more Te content leads to higher resistivity as pure Te films have very high electrical resistivity(Lee et al., 2011). Referring to **Figure 2- 7(b)**, it can be observed that as the deposition potential is reduced from -0.40 V to -0.20 V, the Te content gets closer to 60 at.% and the electrical resistivity also decreased tremendously at -0.20 V (Yoo et al., 2005). The highest resistivity of 45.8 μΩm was observed between -0.3 to -0.4 V that resulted in a needle like structure because the porosity of the structure increases electrical resistivity. A lower cathodic potentials of -0.06 V resulted in more granular structures leading to lower resistivity at 18 μΩm (Yoo et al., 2005). The thermoelectric properties of Bi_2Te_3 films with respect to deposition potential is as shown in **Table 2- 14**.

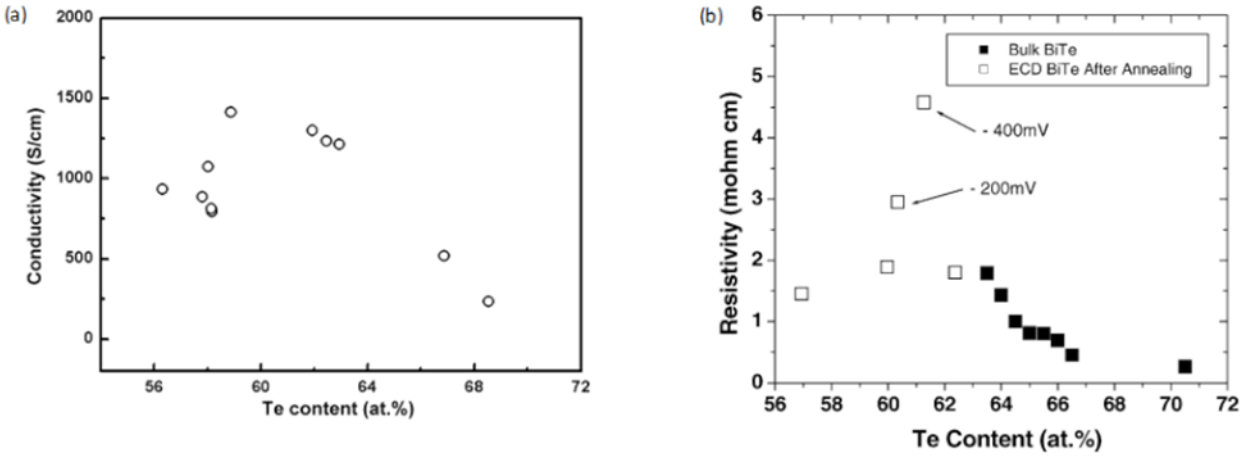


Figure 2- 7: The effect of Te content on (a) Electrical Conductivity (Wang et al., 2007)

(b) Electrical resistivity and deposition potential (Yoo et al., 2005).

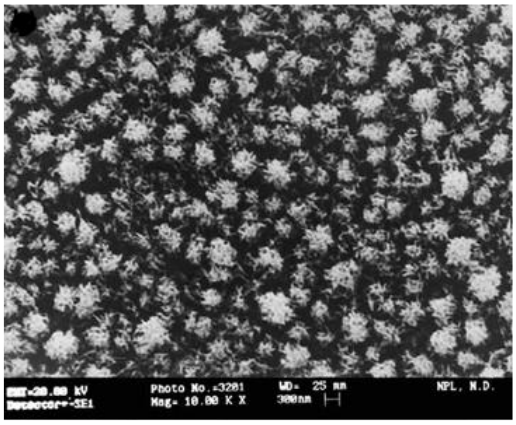
Table 2- 14: Thermoelectric Properties of Bi_2Te_3 films with respect to deposition potential from electrodeposition.

No	Bath Composition	pH	Temperature (°C)	Deposition Time (min)	Substrate Used	Deposition Potential (V)	Seebeck Coefficient (μV/K)	Electrical Resistivity (μΩm)	Power Factor (mW/K^2m)	Remarks	Ref
1	10mM of $HTeO_2^+$ 2.5,5,7.5,10mM of Bi^{3+} 1M HNO_3	0.6	Room temperature	10	Platinum	-0.14	-70	7.06	0.70	Films rich in Te have Te content above 60 at.% while films rich in Bi have Te content below 60 at.%. At -0.14V , [015] is a more prominent peak. The highest power factor of obtained from the film containing 58.9 at.% Te.	(Wang et al., 2007)
2	10 mM $HTeO_2^+$ 8 mM Bi^{3+} 1 M HNO_3	0.1	23	X	SiO_2/Si	-0.17	-188.5	18	1.97	Highest Seebeck of −188.5 μV/K was achieved at −0.17 V that yielded stoichiometric Bi_2Te_3 films.	(Yoo et al., 2005)
3	50 mM (Bi^{3+}+ $HTeO_2^+$) 1 M HNO_3 Bi/Bi+Te=0.3 to 0.7	X	X	X	Ti/glass	-0.05	-51.6	4	0.67	The stoichiometric Bi2Te3 film would be obtained by electrodeposition in an electrolyte with a Bi/(Bi + Te) mole ratio of 0.54	(Kim and Oh, 2009)
4	10 mM TeO_2 2.5-10 mM of $Bi(NO_3)_3$ 1.5M HNO_3	X	Room temperature	X	Au/Ni/Si	-0.10	-70	15	0.33	Highest power factor obtained from 7.5 mM of Bi^{3+} and 10 mM of $HTeO_2^+$	(Yoo et al., 2013)
5	10mM of TeO_2 10mM of Bi_2O_3 Diluted HNO_3	0.50	X	X	Titanium sheet	0.02	-63	X	X	X	(Miyazaki and Kajitani, 2001)
6	10mM $HTeO_2^+$ 7.5mM Bi^{3+} 1M HNO_3	0	Room temperature	X	Stainless Steel	-0.08	-51.9	23.2	0.12	X	(Ma et al., 2011)
7	10mM $HTeO_2^+$ 7.5mM Bi^{3+} 1M HNO_3	X	Room temperature	X	Gold coated silicon wafer	-0.13	-66.07	11.55	0.38	X	(Ma et al., 2012)

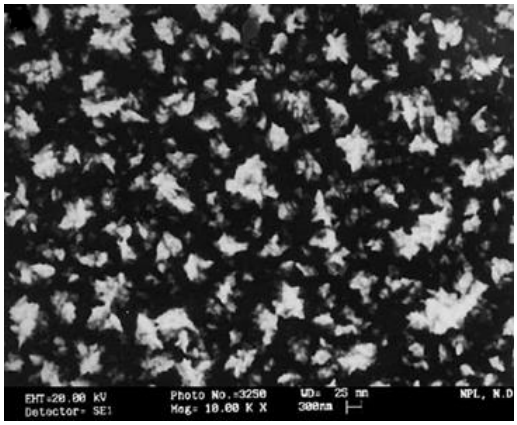
2.6.1.2 Effect of electrolyte ionic composition

The amounts of Bi^{3+} and $HTeO_2^+$ present in the electrolyte also affects the crystallographic orientation as well as the morphology of the deposits. Te rich samples of Bi_2Te_3 with above 60 at.% of Te exhibits a {110} orientation where else the Bi rich samples of Bi_2Te_3 with below 60 at.% of Te exhibits two orientations of {110} and {1010} (Michel et al., 2006). The morphology of the films are also affected by the amount of bismuth and tellurium, as shown in **Figure 2- 8**. The bismuth rich bismuth telluride film results in needle shaped structure while tellurium rich films have a granular structure (Golia et al., 2003). The morphology of films with a decreasing Te content was studied by Wang et al., he discovered that as Te content decreases from 68.54% to 57.67% the films exhibited a coarser needle like structure as it is becoming more Bi rich (**Figure 2- 9**)which is in line with Golia et al. as shown in **Figure 2- 8**. The Te content also affects the crystallographic orientation of films as observed by Michel et al., he observed the {100} orientation for Te>65 at.% and 60<Te<65 at.%. Where else the preferential {110} and another orientation {1010} was observed 56<Te<60 (Michel et al., 2006). The presence of the {110} can be observed to be on the c-axis when the compound is close to 60 at.% of Te which is stoichiometric amount of Te in a Bi_2Te_3 compound. This observation made by Michel et al. 2006, is also validated by Wang et al.2007 when he obtained the highest figure of merit at 58.9 at.% of Te. The {015} diffraction peak is also commonly observed for randomly oriented polycrystalline films (Martín-González et al., 2002) (Wang et al., 2007) alongside the {110} peak. The {110} and {015} orientations are given much importance in the field of electrochemistry because it resembles the c-axis plane in deposit. The c-axis resembles the growth of the deposit occurs with the basal plane perpendicular to the substrate which enhances the electrical conductivity, thus desirable for the transfer of electrons in an electrochemical process (Michel et al., 2006).

(a)



(b)



(c)

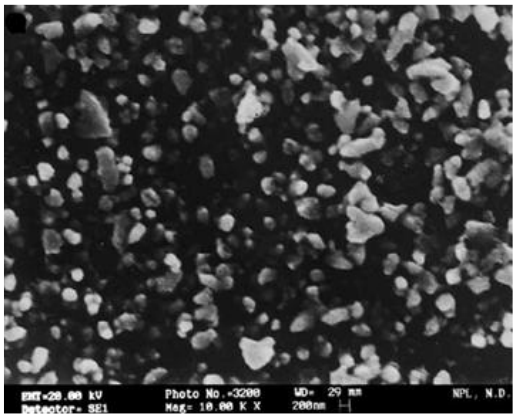
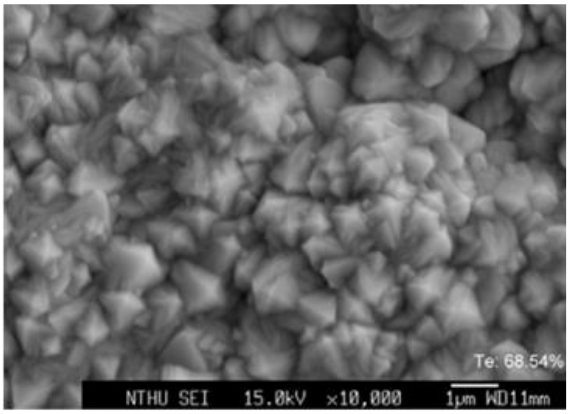
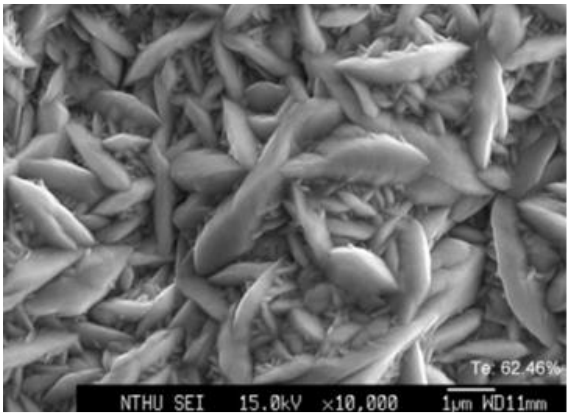


Figure 2- 8: SEM Images (a) Bismuth rich Bi_2Te_3 (b) Stoichiometric Bi_2Te_3 (c) Tellurium rich Bi_2Te_3 (Golia et al., 2003).

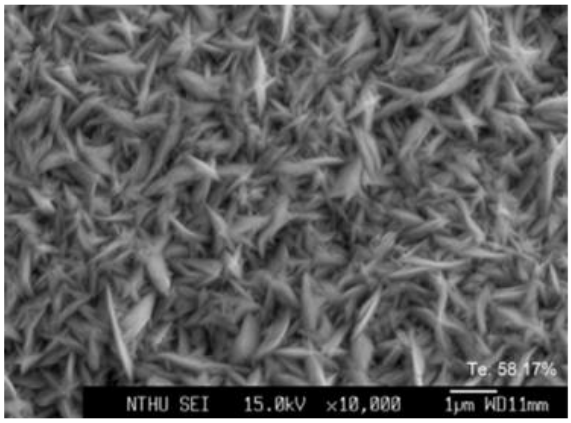
(a) Te: 68.54 at.%



(b) Te: 62.46 at.%



(c) Te: 58.17 at.%



(d) Te: 57.67 at.%

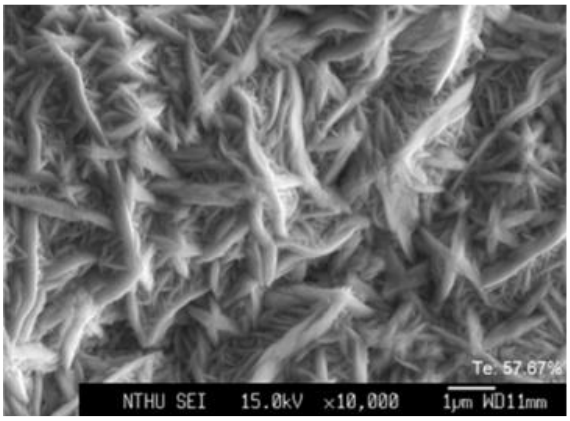


Figure 2- 9: SEM images with corresponding Te content (Wang et al., 2007).

2.6.1.3 Effect of deposition time

In 1996, Magri et al. carried out the deposition at 2, 3 and 4 hours yielding a thickness of 38, 56 and 74 μm respectively (Magri et al., 1996). As the deposition time prolongs a thicker film is obtained as mentioned above. It is also noteworthy that the electrical resistivity decreases and the mobility of electrons improves with prolonging deposition time as shown in **Table 2-15**. This could be attributed to the fact that the deposition layer is more homogenous with increasing time and better conductivity of carriers with larger grain size. The effect of time on the morphology of the deposited films can be observed in **Figure 2- 10**. It can be observed in **Figure 2- 10 (a)** that films deposited at shorter time of 2-5 minutes (Ma et al., 2010) are less homogenous as compared to **Figure 2- 10 (b)** that was deposited at 30 minutes (Qiu et al., 2010) and **Figure 2- 10 (c)** 2 hours (Michel et al., 2005). The morphology of that at 30 minutes and 2 hours are almost similar indicating that longer deposition time does not affect the morphology but the effect on thermoelectric properties was not studied by all three researchers.

Hence, the effect of deposition time on the morphology and thermoelectric properties could be further optimised to obtain better performance of these films.

Table 2- 15: Resistivity and Hall mobility of Bi_2Te_3 films deposited at increasing deposition time.

Thickness (μm)	Temperature (K)	Resistivity (μΩm)	R_H (10^{-3} cm^3C^{-1})	Carrier Concentration (10^{-19}-cm^{-3})	Hall Mobility ($cm^2V^{-1}s^{-1}$)
38	301.3	11.92	-11.77	-53.10	-9.88
56	304.2	10.87	-10.84	-57.67	-9.97
74	303.8	10.27	-10.38	-60.43	-10.12

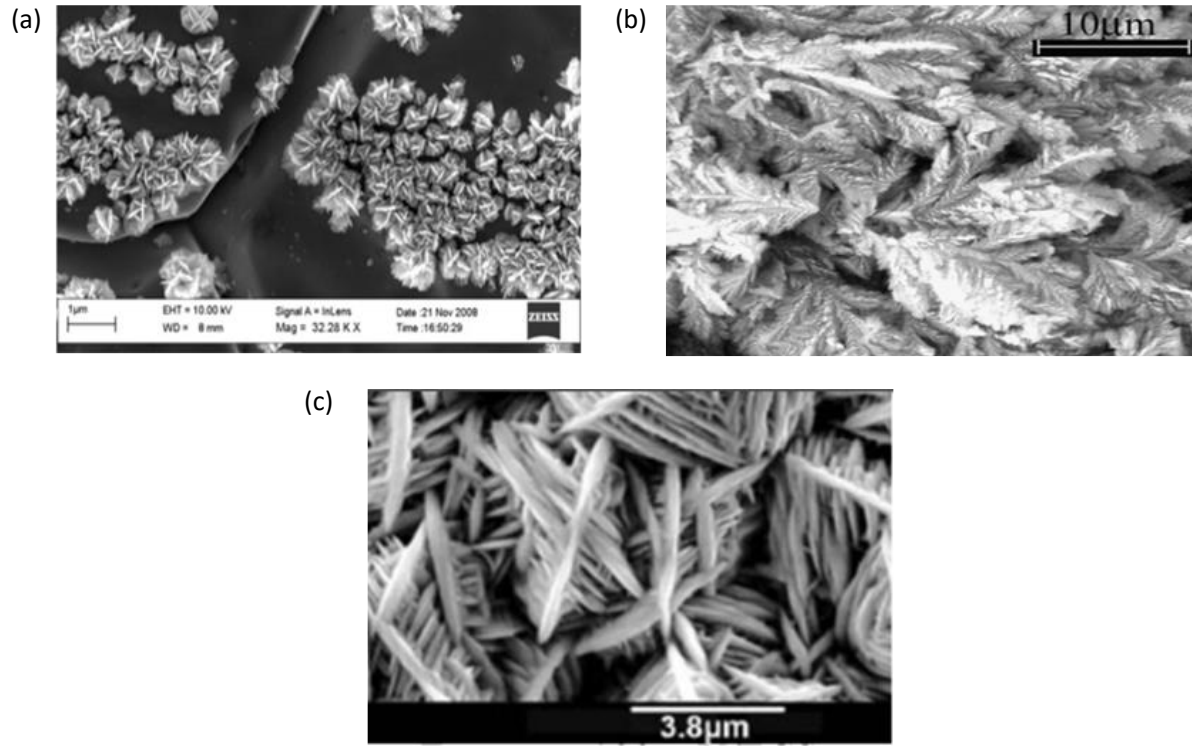


Figure 2- 10: SEM images of the effect of deposition time on the morphology of Bi_2Te_3 films deposited on stainless steel (a) 2-5 minutes (Ma et al. 2010) *(b) 30 minutes* (Qiu et al., 2010)*(c) 2 hours* (Michel et al., 2005).

2.6.1.4 Effect of deposition temperature

Predominantly a majority of Bi_2Te_3 films from nitric acid electrolytes are deposited at room temperature as it is believed on an industrial scale it is thought to be more cost effective. The effect of the electrolyte temperature on the thermoelectric properties is yet to be investigated. Having said that, Gonzalez et al carried out the deposition of Bi_2Te_3 at a lower temperature of 2°C and discovered that films deposited at this temperature are more homogenous as compared to that of room temperature (Martín-González et al., 2002). Despite the claim made by Gonzalez et al. a comparison of the morphology with Wang et al observed no obvious difference between that deposited at 2°C (**Figure 2- 11 (b)**) and of room temperature (**Figure 2- 11 (a)**). A slightly higher electrodeposition temperature at 70°C was attempted by Golia et

al. that showed more granular structures of Bi_2Te_3 films as observed in **Figure 2- 8 (b)** (Golia et al., 2003). Both Gonzalez et al. and Golia et al. did not investigate the effect of electrolyte temperature on the thermoelectric properties of Bi_2Te_3 films. As there is no concrete observation made by both, this parameter would need further investigation to provide a conclusive evidence.

(a) (b)

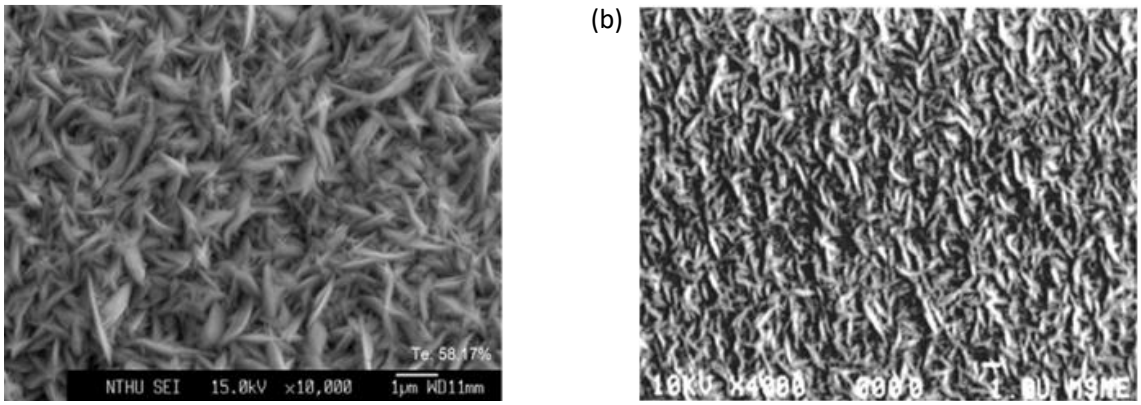


Figure 2- 11: SEM images of the effect of temperature on the morphology of Bi_2Te_3 films (a) Room temperature (Wang et al., 2007) *(b) 2°C* (Martín-González et al., 2002).

2.6.2 Production of carbon fibre thermoelectric composite

Though thin film thermoelectric devices can attain large ZT values due to the quantum confinement effect on carriers, however for large scale applications thin films may not be able to sustain a substantial temperature difference for thermoelectric energy harvesting (Han and Chung, 2013a). Therefore, for practical applications it is imperative to have thermoelectric materials that can be scaled up to large cost effective thermoelectric devices that can effectively capture a large amount of thermal energy.

Although there are conductive polymers available in the market, however economically sustainable polymers are mostly non-conductive. Thus, with carbon fibre composites due to its waviness and imperfect coverage of the fibres by the polymer matrix, there is fibre to fibre contact points that enables this composite to be electrically conductive even in the presence of insulating polymer matrix (Chung, 2017)(Han and Chung, 2013b). The advantages of a fibre composite are its low cost, mechanical durability, ease of processing and that the thermoelectric material in itself is the structure/thermoelectric device.

Both Kim et al. and Sung et al. have demonstrated the thermal energy harvesting capabilities of virgin carbon fibre-epoxy composites by attaining Seebeck coefficients in the range 3.5-4.5 μV/K (Kim et al., 2016)(Sung et al., 2016). Virgin carbon fibre-epoxy composites exhibited a p-type thermoelectric behaviour attaining a ZT of 3.0×10^{-5} and 2×10^{-9} from in plane and through thickness measurements respectively (Sung et al., 2016). Wang and Chung also depicted improved Seebeck coefficient of virgin carbon fibre-epoxy composites to 36-44 μV/K through intercalation with bromine and sodium (Wang and Chung, 1999).

Carbon fibre is an electrical conductor that is weakly thermoelectric, the incorporation of thermoelectric particles will enhance the power factor of these carbon fibre-epoxy composites. Thermoelectric particles such as tellurium, Bi_2Te_3 and carbon black have been used in the past

to improve the Seebeck coefficient of these carbon fibre composites (Yao and Xia, 2014)(Han and Chung, 2013a)(Han and Chung, 2013b). The presence of these thermoelectric fillers is thought to add more contact points between the fibre strands in a composite, enabling electron to hop from one fibre to the other for efficient electron transportation.

Han and Chung demonstrated improved Seebeck coefficient up to 110 µV/K by utilising tellurium as the sole interlaminar filler in carbon fibre-epoxy composites (Han and Chung, 2013b). A combination of tellurium and Bi_2Te_3 in an 8:1 ratio depicted a high Seebeck coefficient of 163.3 µV/K with a ZT value of 0.086 (Han and Chung, 2013a). Bi_2Te_3 was also observed by Yao and Xia to improve the Seebeck coefficient of carbon fibre reinforced cement composites to 33.5 µV/K, consequently enhancing the thermoelectric properties of the composite (Yao and Xia, 2014).

All the reviewed work above exhibited the plausibility of utilising a virgin carbon fibre-epoxy composite as a thermoelectric energy harvesting structure. All previous works have also demonstrated improved thermoelectric properties with the addition of thermoelectric particles as fillers in the carbon fibre composite. Thus, this research work will explore the plausibility of replacing virgin carbon fibre with recycled carbon fibre to form recycled fibre based thermoelectric composites with telluride and non-telluride based thermoelectric fillers.

As there has been no prior work done using Bi_2S_3 as a thermoelectric filler for carbon fibre composites, therefore there was no literature to be reviewed for Bi_2S_3. However, a general overview of its thermoelectric properties obtained are shown under Section 2.5.

2.7 Thermal Annealing

Thermal annealing is essentially a heat treatment that alters the physical and chemical properties of a material. Thermal annealing is commonly used as a post deposition treatment in order to further improve the power factors of bismuth chalcogenides. During annealing, the reorganization of atoms occur which then forms the crystalline nature of materials while reducing the amorphous phase (Huang et al., 2009).

2.7.1 Annealing of Bi_2Te_3

The reduction of amorphous phase in the Bi_2Te_3 deposit will also improve its electrical conductivity, due to enlarged grain size and more uniformly sized grains after annealing. A similar observation was made by Kotkata and Kandil, as the selenium mixtures moved from 90% amorphous-10% crystalline samples to 100 % crystalline samples, the electrical conductivity was seen to increase from 5.5 X 10^{-13} Ω^{-1} cm^{-1} to 5.27 X 10^{-7} Ω^{-1} cm^{-1} (Kotkata and Kandil ,1987). In addition to the reduction of amorphous phase, annealing also increases the grain size of Bi_2Te_3 films as shown in **Figure 2- 12** due to the diffusion and agglomeration of Bi and Te atoms at higher temperatures (Rashid et al., 2013)

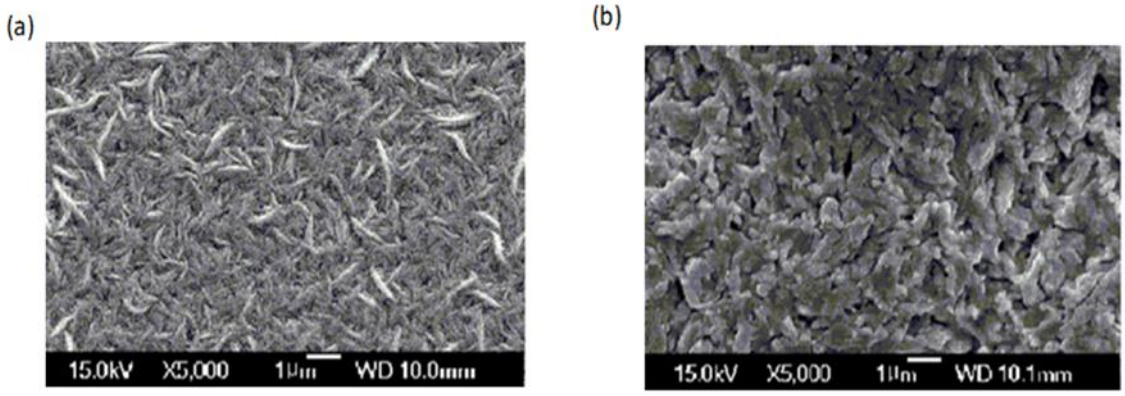


Figure 2- 12: SEM surface images of the n-type Bi_2Te_3 samples (a) As-deposited (b) Annealed (Rashid et al., 2013).

Both Rashid et al. and Huang et al. observed that by the annealing process strengthened the c-axis perpendicular planes such as {110} and {015} as shown in **Figure 2- 13**.

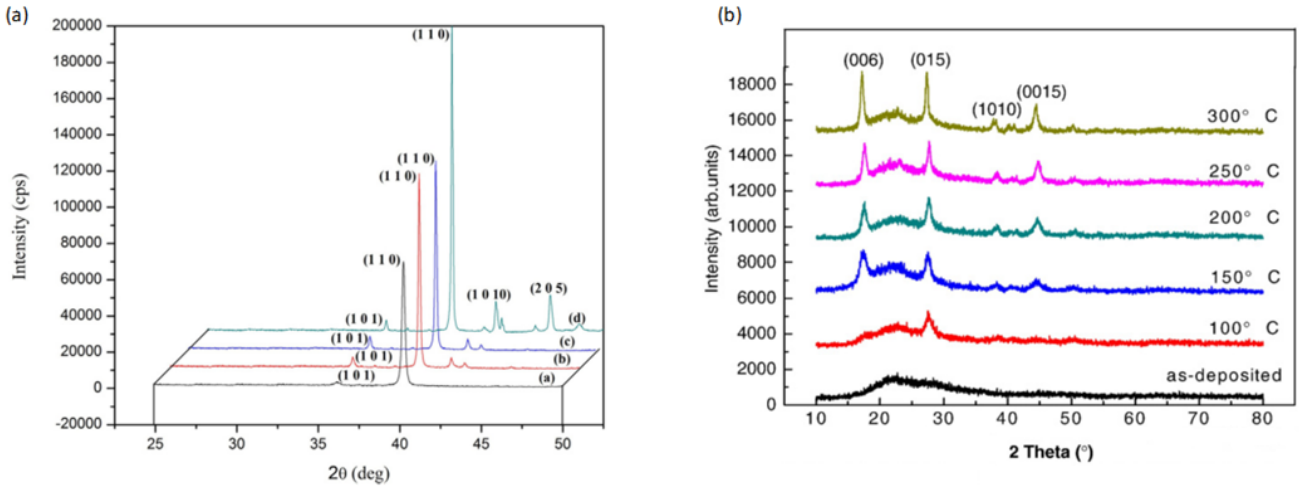


Figure 2- 13: X-ray diffraction spectra of Bi_2Te_3 film (a) (a) As-deposited (b) 200 ºC, (c) 250 ºC and (d) 300 ºC for 8 min duration (Rashid et al., 2013)

(b) X-ray diffraction spectra of as-deposited film and films annealed at 100 °C, 150 °C, 200 °C, 250 °C, 300 °C

(Huang et al., 2009).

The increase in grain size results in smaller grain boundaries that results in an increase of carrier mobility with a subsequent decrease in carrier concentration, leads to an increase in electrical conductivity thus improving the power factor of Bi_2Te_3 films as shown in **Figure 2- 14** (Jeon et al., 2011).

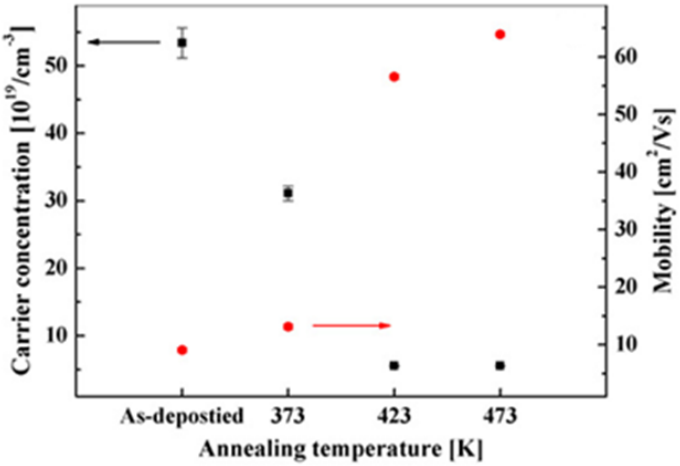


Figure 2- 14: Carrier concentration and electron mobility for as-deposited and annealed Bi–Te films (Jeon et al., 2011).

The annealing process is affected by the annealing temperature and duration of annealing. The highest power factors were obtained for Bi_2Te_3 films annealed in the temperature range of 250 ºC to 450 ºC as shown in **Table 2- 16**. Cai et al. observed 3.6 times improvement in Seebeck coefficient and 1.75 times increase in electrical conductivity after annealing at 400 ºC leading to a larger power factor than the as-deposited Bi_2Te_3 film (Cai et al., 2013). The highest annealing temperature was reported by Jun et al. at 450 ºC (Jun et al., 2006), despite the theory of Te rich phase melting occurs at 413 ºC in binary Bi-Te alloys as reported by most in literature (Kim and Lee, 2006)(J. Lee et al., 2012). Most researchers obtained highest power factors with an annealing temperature of 250 to 350 ºC as beyond this temperature range is believed to evaporate the Te content leading to an imbalance in the stoichiometric composition of films (Huang et al., 2009; J. Lee et al., 2012; Lin et al., 2013; Rashid et al., 2013).

Table 2- 16: Thermoelectric Properties of Annealed Bi_2Te_3.

No	Annealing Temperature (°C)	Annealing Time (minutes)	Annealing Gas	Power Factor (mW/K^2m) Before Annealing	Power Factor (mW/K^2m) After Annealing	Remarks	Ref
1	250,300,350,400,450	60	Ar	0.069	0.821	The highest power factor obtained for Bi_2Te_3 films annealed at 400°C At 450°C, there was a decrease in electrical conductivity due to great enhancement of impurity scattering affecting the charge carriers.	(Cai et al., 2013)
2	200 to 300 Rapid thermal annealing	2-10	Ar (Halogen lamps)	0.3	1.7	The highest power factor for N-type Bi_2Te_3 films are obtained at 300°C for 8 minutes. Longer duration than 8 minutes, the decreasing trend of At% Te with longer annealing duration at high temperature could be attributed to the expected re-evaporation of Te.	(Rashid et al., 2013)
3	100,150,200,250,300	60	N_2	0.27	0.42	The highest power factor was observed for Bi_2Te_3 films annealed at 300° C.	(Huang et al., 2009)
4	100,150,200	480	N_2	0.33	2.41	The highest power factor was observed for Bi_2Te_3 films annealed at 200° C.	(Jeon et al., 2011)
5	400 and 450	240	50%H_2+ 50% Ar	0.68	3.3	The highest power factor was observed for Bi_2Te_3 films annealed at 450° C.	(Jun et al., 2006)
6	100-250	30 and 60	N_2	0.489	0.605	The heat treatment temperature was kept lower than 300 °C to avoid the evaporation of the composition of films. The highest power factor obtained for Bi_2Te_3 films annealed at 250°C for 30 minutes.	(Lin et al., 2013)
7	450	240	50%H_2+ 50% Ar	0.31	1.65	Annealing in hydrogen and argon mixture results in high power factor than pure argon due to its reductive nature.	(Kim et al., 2007a)
8	300-400	10	Ar with 10% H_2 (Halogen lamps)	0.38	0.90	Stoichiometric specimen has relatively larger values of power factor. Largest value of power factor could be obtained for the stoichiometric specimen annealed at 400 °C.	(Kim and Lee, 2006)

9	150-400	240	N_2	-	-	Annealing at 250 and 350 °C showed no tellurium evaporation and uniform distribution of Bi and Te. Highest Seebeck coefficient obtained at 350 °C	(J. Lee et al., 2012)
						Annealing above 400 °C led to non-stoichiometry of Bi_2Te_3.	
10	300	120 and 300	H_2	0.22	0.68 (120 minutes) 0.58 (300 minutes)	Needle like structure observed at 120 minutes whereas a granular structure after prolonged annealing at 300 minutes.	(Li et al., 2008)
						Increase in grain size observed as annealing time was prolonged.	
						Films annealed at 300 °C show a higher average Seebeck coefficient (ca. -130 µV K-1 for 120 minutes and -120 µV K-1 for 300 minutes)	
						Film annealed for 120 minutes is less homogeneous with the abundance distribution showing a half width of around 3 µV K-1, and film annealed for 300 minutes is even less homogeneous with the abundance distribution showing a half width of around 10 µV K-1.	
11	300	60	vacuum	0.58	1.10	When the annealing temperature increases from 100 °C to 300 °C, the XRD intensity enhances. This indicates that the grain gets larger and the crystalline quality improved after annealing.	(Zheng et al., 2010)
						The film annealed at 300 °C obviously has the (0 1 5) preferred phase, which can yield better thermoelectric performance	
						The sample annealed at 300 °C has a maximum PF value of 1.10 X 10^{-3} Wm^{-1} K^{-2} with the highest Seebeck coefficient and a moderate electrical conductivity.	
12	450	240	50 % H_2+ 50 % Ar and 100 % Ar	0.35	1.7 (100 % Ar) 1.9 (50 % H_2+ 50 % Ar)	Hydrogen annealing causes a reduction of the dislocation density, the oxygen content, and the TeBi anti-site defect density, resulting in an improved figure-of-merit with optimization of the carrier concentration.	(Kim et al., 2007a)
13	150-350	-	-	-	-	Annealing temperature below 250 ◦C do not supply enough energy to complete crystallization of the films, , which agree with the low strength of the XRD peaks of the films annealed below.	(X. Wang et al., 2013)
						Annealing-induced reduction in the deficiency facilitates the enhancement of carrier mobility, which peaks at 300 °C.	
14	100-250	30	N_2	0.12	0.22	Highest power factor obtained at 250 °C for 30 minutes.	(Lin et al., 2015)
15	250-400	60	N_2, vacuum	0.09	0.35	Highest power factor obtained at 400 °C for 60 minutes.	(Singkaselit et al., 2017)
16	150-350	60	Ar	-	-	It is found that the Te/Bi ratio decreases upon thermal annealing, indicating the loss of Te as a result of evaporation.	(Shuai et al., 2015)

Li et al. studied the effect of annealing duration at 300ºC for 2 and 5 hours respectively. It was observed that annealing at 2 hours gave a slightly higher Seebeck coefficient at -130 μV/K as compared to that of 5 hours with -120 μV/K. This phenomenon could be due to the re-evaporation of Te element that leads to higher impurity scattering leading to a less homogenous structure as the annealing time increases (Li et al., 2008). A similar outcome was also observed by Rashid et al. for rapid thermally annealed Bi_2Te_3, he observed that longer annealing time led to less defined crystallites as shown in **Figure 2- 15**. The duration of annealing generally ranges from 0.5 hours to 8 hours with majority work done from 1 hour to 4 hours as shown in **Table 2- 16**.

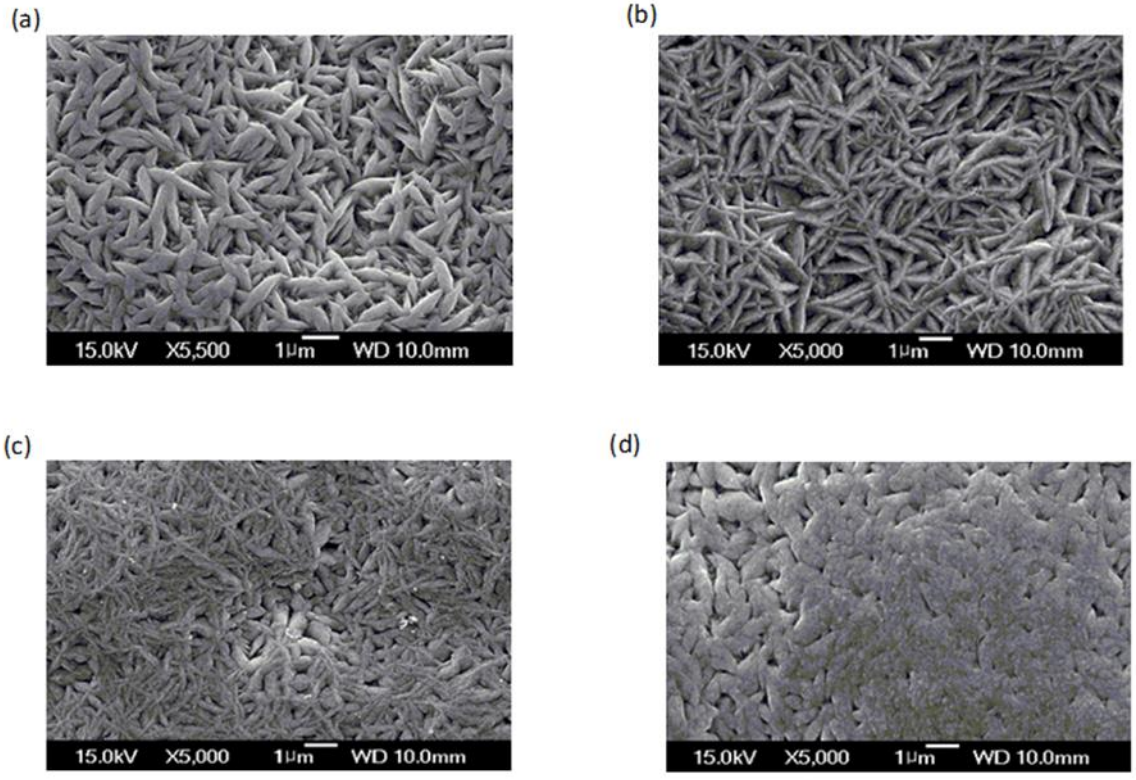


Figure 2- 15: SEM surface images of n-type Bi_2Te_3 samples annealed for (a) 2 min, (b) 5 min, (c) 8 min and (d) 10 min at 250 ◦C temperature (Rashid et al., 2013).

2.7.2 Annealing of Bi_2S_3

All previous work on thermal annealing of bismuth sulphide have focused on the improvement in optical (Balasubramanian et al., 2011)(Zhu et al., 2017)(Hussain et al., 2014)(Riahi et al., 2017), photoconductivity (Rincón and Nair, 1996), photosensitivity (Desale et al., 2013) and dark conductivity properties (Campos and Sua, 1999). No prior literature studied the effect of annealing Bi_2S_3 on its thermoelectric properties, however selected literature have investigated the effect of annealing on structural, morphological and electrical properties which will be reviewed in this section.

Rincon et al. studied the thermal profile of Bi_2S_3 using differential scanning calorimeter (DSC) in a nitrogen environment as shown in **Figure 2- 16** (Campos and Sua, 1999). The crystallisation temperature of Bi_2S_3 can be obtained from heating run 1 denoted as EXT 1 and EXT 2. EXT 1 and EXT 2 are referring to exothermic reactions that take place during the breaking of bonds in crystallisation. EXT 1 is responsible for the nucleation and growth of Bi_2S_3 and the corresponding transformation of amorphous Bi_2S_3 to crystalline Bi_2S_3. EXT 2 on

the other hand occurs in the presence of bismuth rich or sulphur rich defects at which the following reaction mechanism occurs as shown in Eq (2.5)

$$(Bi_nS_m) \rightarrow 2BiS_2 \rightarrow Bi_2S_3 + S \rightarrow (Bi_4S_3)_{cry} \rightarrow Bi_2S_3 + Bi_2 \qquad (2.5)$$

Thus, the nucleation and recrystallization of Bi_2S_3 is expected to occur within 200-260 °C.

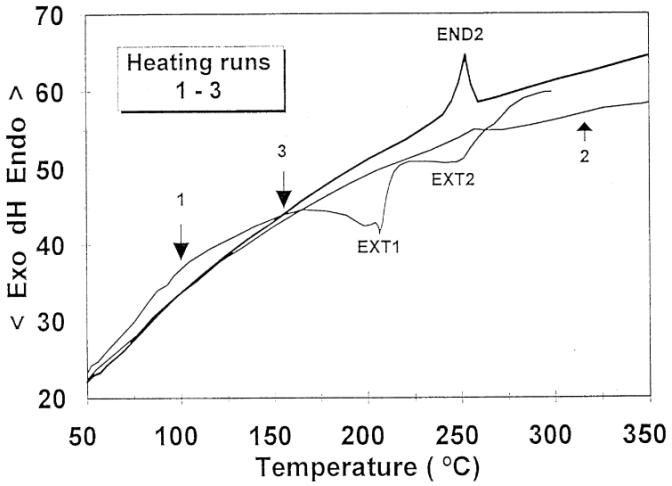


Figure 2- 16: DSC curve of Bi_2S_3 run in a nitrogen environment (Campos and Sua, 1999).

Dachraoui et al. observed a much better crystallinity in its XRD peaks of Bi_2S_3 films when annealed at 190 °C when compared to that annealed at 150 °C and 180 °C (Dachraoui et al., 2018), as 190 °C is closer to the recrystallization temperature range.

A similar observation was also observed by Balasubramanian et al. with chemically deposited Bi_2S_3 thin films, which showed maximum improvement in crystallinity of XRD peaks, least dislocation density and microstrain when annealed at 250 °C compared to 150 and 200 °C. These structural changes from annealing also impacted positively on its optical band gap reduction. The optical band gap decreases from 2.73 eV to 2.34 eV as annealed temperature varied from 150 to 250 °C (Balasubramanian et al., 2011). In a later work Balasubramanian et al. also exhibited improvement in carrier mobility and electrical

conductivity as a result of decreased carrier concentration when annealed from 150 to 250 °C, with the highest conductivity obtained at 250 °C (Balasubramanian et al., 2015).

Bi_2S_3 thin films grown by successive ionic layer adsorption and reaction method (SILAR) demonstrated grain size enlargement in morphology, improved I-V characteristics under dark and light illumination giving good photoresponse, decreased optical energy band gap and increased thermo emf voltage of annealed Bi_2S_3 at 250 °C compared to its non-annealed counterpart (Desale et al., 2013). A similar improvement in morphology and structural properties was also observed by Riahi et al.,when electrodeposited Bi_2S_3 films was sulphur annealed from 250-400 °C, the largest crystallite size, least dislocation density and microstrain was observed at 400 °C, however at 400 °C there was a lack of structure (Riahi et al., 2017). Hussain et al. also observed increased grain size in morphology, decreased microstrain and dislocation density, increased electrical conductivity and optical absorbance when air annealed from room temperature to 250 °C, with optimum properties observed at 250 °C (Hussain et al., 2014).

Rincon and Nair discovered improvement in dark conductivity when Bi_2S_3 films were vacuum annealed in argon and hydrogen environment from 230 to 400 °C, however above 400 °C there was a decrease in the conductivity films owing film sublimation or evaporation at temperature higher than 400 °C (Rincón and Nair, 1996).

Thus, from the above mentioned previous works in literature it can be conclude that annealing has a positive impact on the morphology, structural and electrical properties of Bi_2S_3. Therefore, we would like to hypothesize that annealing would also bring about similar positive impact on thermoelectric properties of Bi_2S_3. In this research work, the temperature range from 300-450 °C will be studied as most previous work have only shown improvement in properties around when crystallization starts at approximately 250 °C. This research work would like to

investigate the morphological, structural, thermoelectric and thermal properties of Bi_2S_3 at a higher annealing temperature range.

2.8 Doping with carbon nanotubes

The discovery of carbon nanoparticles such as carbon nanotubes (CNT) with remarkable electrical properties such as high electrical conductivity and carrier mobility have broadened the range of applications and unleased a new revolution in the electronic device industry.

2.8.1 Bi_2Te_3-CNT composites

To further enhance the thermoelectric performance as shown in Eq (2.5) it is necessary to have a high Seebeck coefficient, low electrical resistivity and low thermal conductivity. However, Seebeck coefficient, electrical resistivity and thermal conductivity are parameters that are interdependent upon each other, thus making it difficult to attain high ZT values in bulk materials (Aswal et al., 2016). However, this interdependence can be decoupled by introducing nanostructures within the thermoelectric composites and have shown potential in improving the thermoelectric performance (Yucheng et al., 2010). With the doping these conductive nanofillers in thermoelectric materials, the carrier concentration can be optimised by decoupling both S and ρ by using interfaces (Narducci et al., 2012). With interfaces introduced by these conductive nanostructures, it will help filter out low energy charge carriers and and transport high energy charge carriers across thereby increasing carrier mobility that help improve S and decrease ρ (Y. Du et al., 2014)(S. Zhang et al., 2017).

In recent year, multiwall carbon nanotubes (MWCNT) have been considered as excellent dopants for thermoelectric materials due to its nanoscale, low dimensional, holey structure features and its quantum confinement effect on charge carriers that is beneficial to improving ZT values (Kunadian et al., 2009).

Kumar et al. observed that hydrothermally synthesised Bi_2Te_3-MWCNT composites showed a 31%, 17% and 45% improvement in electrical conductivity, carrier mobility and ZT value upon the addition of 1 wt% of MWCNTs (Kumar et al., 2017). The addition of MWCNT in Bi_2Te_3 matrix enhanced ZT values because it generated a higher surface area of contact between the Bi_2Te_3 resulting in improved pathway for electrons as depicted in **Figure 2- 17**.

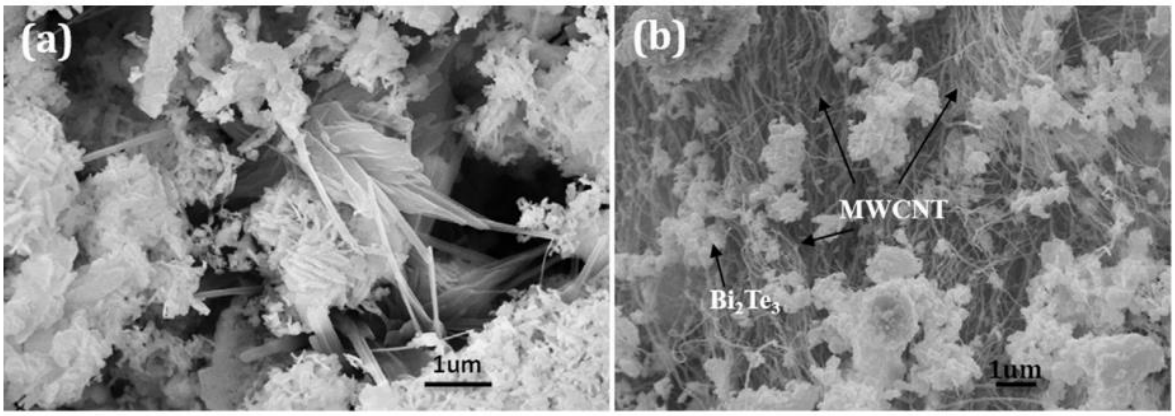


Figure 2- 17: SEM image of (a) Bi_2Te_3 and (b) Bi_2Te_3-MWCNT nanocomposite (Kumar et al., 2017).

Kim et al. also observed improvement in ZT values by approximately 66% upon incorporation of MWCNTs in Bi_2Te_3 and $Bi_2(SeTe)_3$ composites accompanied by a 30% decrease in thermal scattering owing to phonon scattering that occurs as a result of adding MWCNT (Kim et al., 2015a). The doping of MWCNT in a Bi_2Te_3 matrix also demonstrated improved crystallinity in its XRD peaks implying good electrical conductivity (Zhang et al., 2012)(Xu and Wang, 2013a) as shown in **Figure 2- 18**. However, most literature reports that there is an absence of graphite peak in the XRD due to small concentrations of MWCNT/SWCNT used.

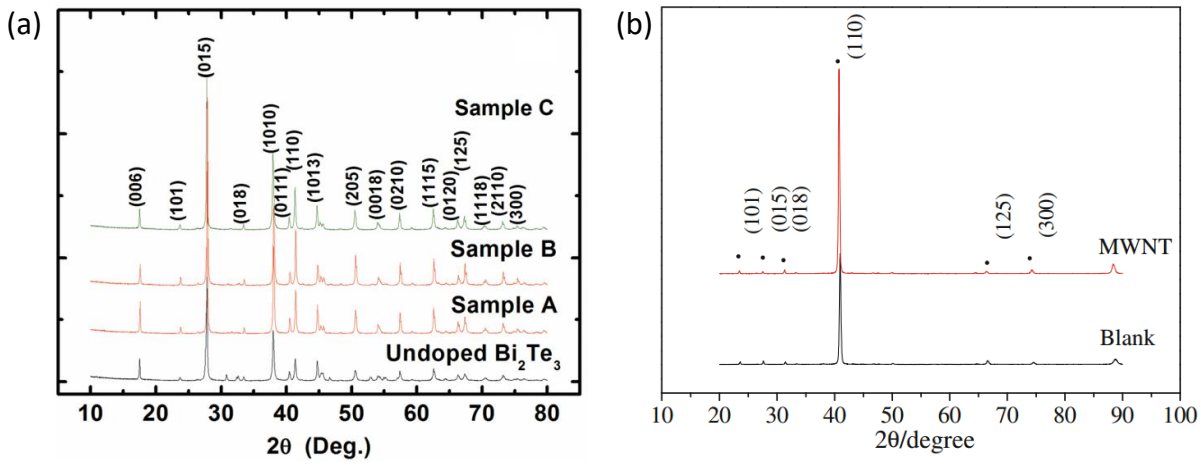


Figure 2- 18: (a) XRD pattern of single wall carbon nanotube (SWCNT) doped Bi_2Te_3 (sample A,B and C denote samples doped with SWCNT (Zhang et al., 2012) *(b) XRD pattern of Bi_xTe_y and MWCNT film obtained by potentiostatic electrodeposition (MWNT refer to samples doped with MWCNT)* (Xu and Wang, 2013a).

Pang et al. also demonstrated the possibility of fabricating a segregated conductive polymer composite with insulating polymer (ultrahigh molecular weight polyethylene (UHMWPE)) by doping it with MWCNT and Bi_2Te_3. A segregated conductive polymer composite as such is thought to be cost effective, has easy fabrication method that is scalable, lightweight and flexible compared to conventional thermoelectric materials however has very low ZT value of approximately 3×10^{-5} (Pang et al., 2013).

Some studies have also demonstrated a change in the magnitude of Seebeck coefficient, addition of MWCNT or SWCNT has shown improvements in Seebeck coefficient owing to the tremendous improvement in carrier mobility (Lognone and Gascoin, 2015). However, higher loadings of CNT has also shown parasitic effect on Seebeck coefficient and electrical resistivity of Bi_2Te_3 due to a p-type doping that occurs as the number of CNTs that cover Bi_2Te_3 particles increases thus playing the role of impurities that prevent Bi_2Te_3 particles from connecting with each other (Bark et al., 2013)(Lognone and Gascoin, 2015)(Zhang et al., 2012).

Some notable literature done on doping Bi_2Te_3 with MWCNT and its corresponding thermoelectric properties are reviewed and tabulated in **Table 2- 17**. Overall, doping with CNT has a positive impact on the thermoelectric properties of Bi_2Te_3.

Table 2- 17: Thermoelectric properties of Bi_2Te_3-CNT composites.

Inorganic thermoelectric material	Optimum CNT doping concentration	Methodology	Seebeck coefficient (μV/K)	Electrical conductivity (S/cm)	Power factor ($\mu W/cmK^2$)	Thermal Conductivity (W/mK)	ZT	Remarks	Ref
Bi_2Te_3	20 vol% of MWCNT	Ball milling and ultrasonication	130	85	1.44	-	-	The increasing amount of carbon nanotubes decreased the electrical conductivity and Seebeck coefficient due to hindered carrier mobility.	(Bark et al., 2013)
Bi_2Te_3	0.5 wt% of SWCNT	Ball milling, physical grinding and sintering	231.2	200	10.69	1.5	1.2 (normalised)	The sign for Seebeck coefficient can be tuned from n-type to p-type by varying the SWCNT concentration.	(Zhang et al., 2012)
$Bi_2Te_{2.4}Se_{0.6}$	0.1 wt% of MWCNT	Ball milling and spark plasma sintering	-192	476.19	17.5	1.0	0.52	All MWCNT doped composite exhibited lower thermoelectric performance than pure $Bi_2Te_{2.4}Se_{0.6}$ owing to reduced grain size promoted during ball milling.	(Lognone and Gascoin, 2015)
Bi_2Te_3	0.15 wt% of MWCNT	Ball milling	-115	670	8.8	1.1	0.25	-	(Trawiński et al., 2018)
Bi_2Te_3	2 wt% of MWCNT	Ball milling	115	1370	18.11	1.12	0.53	MWCNTs enhances phonon scattering from the grain boundaries.	(Pundir et al., 2016)
Bi_2Te_3	0.7 wt% of MWCNT	Hydrothermal, ball milling and spark plasma sintering	-113	787.4	10.05	0.65	0.50	The carrier concentration decreased from $8.1X10^{19}$ cm^{-3} (non-doped) to $1.4X10^{18}$ cm^{-3} (doped with MWCNT). The carrier mobility increased from 100 $cm^2V^{-1}s^{-1}$ (non-doped) to 3400 $cm^2V^{-1}s^{-1}$ (doped with MWCNT).	(K. T. Kim et al., 2013)
Bi_2Te_3 and (UHMWPE)	2.6 vol% of MWCNT	Ultrasonication and compression molding (segregated polymer composite)	29	0.45	3.78×10^{-4}	0.43	3×10^{-5}	Segregated polymer structures are cost effective, lightweight and easy to process compared to inorganic materials.	(Pang et al., 2013)
$(Bi_{0.2}Sb_{0.8})_2Te_3$	0.12 wt% of MWCNT	Ball milling and hot pressing	220	714.29	34.5	0.46	1.40	-	(Yeo and Oh, 2014)

2.8.2 Bi_2S_3-CNT composites

There was no prior literature found on the application of CNT-Bi_2S_3 composites in thermoelectricity. However, CNT-Bi_2S_3 composites have been employed in other electronic devices such as lithium and sodium ion batteries (Yang et al., 2016)(Zhao et al., 2014)(Ni et al., 2014), dye sensitised solar cells (DSSCs) (Memon et al., 2018) and pressure sensors (Ali et al., 2017) and exhibited outstanding electrical performance.

Yang et al. demonstrated that inclusion of CNT in Bi_2S_3 composite served as a highly conducting network that promoted electron transport in sodium ion battery anode material. This improved electron transport in CNT-Bi_2S_3 showed better electrochemical performance than that of bare Bi_2S_3 (Yang et al., 2016). Zhao et al. have also employed Bi_2S_3-CNT hybrids as efficient electrode materials for lithium (Li) storage. The Bi_2S_3-CNT hybrid exhibited reversible capacity (671 mA h g^{-1}), robust rate capability (399 mA h g^{-1} at 3000 mA g^{-1}), and stable cyclability (534 mA hg^{-1} after 90 cycles at various rates) (Zhao et al., 2014).

Besides batteries, Memon et al. have also used Bi_2S_3-CNT composites for the synthesis of highly electro-catalytic active counter electrode (CE) for the application in DSSCs. These Bi_2S_3-CNT composites exhibited enhanced electro-catalytic activity, low charge resistance of 0.9 Ω and impressive cyclic stability compared with that of pristine Bi_2S_3 (Memon et al., 2018). The usage of CNT in pressure sensors also showed decrease in DC resistance under the external applied uniaxial pressure was observed in both Ag/CNT-Bi_2S_3/Ag composite and pure Ag/CNT/Ag-based sensors (Ali et al., 2017).

The improved electrical transport properties in all the above electronic applications upon addition of CNT in Bi_2S_3 composites may also prove to be useful for thermoelectric applications. Thus, this research work will explore the structural, morphological,

thermoelectric and thermal properties of Bi_2S_3-CNT composites for thermoelectric applications.

2.9 Summary

Based on the literature reviewed in this chapter, it is worth noting that most work have focused on enhancing the thermoelectric properties of powdered thermoelectric materials. Most works have carried out thermoelectric characterisations on sintered blocks of these powdered samples or on thin films that is not usable for practical applications. Most powdered and film based thermoelectric materials requires an external substrate to form a thermoelectric generator. For practical energy harvesting applications it is vital to have a substrate/structure in which this powdered thermoelectric materials can be incorporated into such as that in the form of carbon fibre composites. It is also worth to highlight that most of the reviewed work have focused on improving the thermoelectric property of Bi_2Te_3 alloys, there are very few reported literature on Bi_2S_3 based thermoelectric materials. Hence, this study will explore the possibility of using two bismuth chalcogenides (Bi_2Te_3 and Bi_2S_3) in recycled carbon fibre composites to form a thermoelectric material in which itself is a thermoelectric structure capable of emulating both n and p-type behavior.

Chapter 3: Methodology

3.1 Introduction

This chapter lists the materials and sample preparation methods used in this study. **Figure 3- 1** represents the overall schematic of the methodologies, properties and characterisation employed in this study.

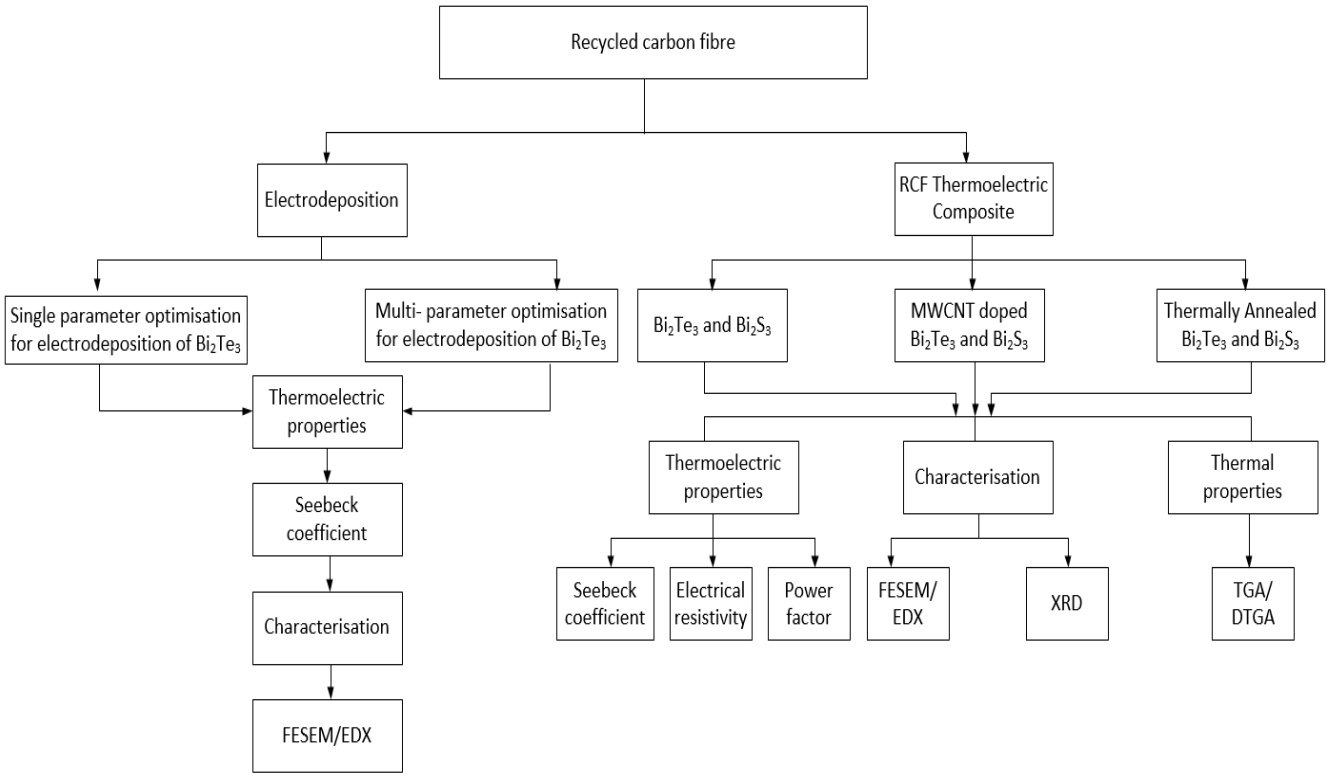


Figure 3- 1: Schematic representation of the methodology of the study

3.2 Materials

The following materials were used for electrodeposition of Bi_2Te_3: (a) bismuth nitrate pentahydrate ($Bi(NO_3)_3.5H_2O$) with purity >98% and relative density of 2.83 g/cm^3 from Sigma Aldrich Sdn. Bhd, (b) tellurium dioxide (TeO_2) with purity >97% and relative density of 5.67 g/cm^3 Sigma Aldrich Sdn. Bhd (c) 65% nitric acid (HNO_3) from R&M Chemicals. The carbon fibres used in this study are virgin carbon fibres manufactured by Yoho Tenax Co. Ltd

with model HTS-406K and recycled Toray T600 carbon fibre recovered via fluidised bed process by Recycled Carbon Fibre Limited (RCF) Coseley, United Kingdom. The following materials were used for recycled carbon polymer composite: (a) bismuth (III) telluride (Bi_2Te_3) powders with a relative density of 7.6 g/cm^3 and purity of 99.99% was purchased from Sigma Aldrich Sdn. Bhd, (b) bismuth (III) sulphide (Bi_2S_3) powders with a relative density of 7.7 g/cm^3 and purity of 99% was purchased from Sigma Aldrich Sdn. Bhd, (c) water-based formaldehyde-free cross-linked acrylate binding polymer, Acrodur DS 3530 was supplied by BASF Malaysia Sdn. Bhd and (d) ethylene glycol from R&M Chemicals and (e) multiwall carbon nanotubes (MWCNTs) with outer diameter 20-30 nm, length of ~30 µm and purity of 95 wt% were supplied by Chengdu Organic Chemicals Co.Ltd.

3.3 Fabrication Techniques

3.3.1 Electrodeposition

3.3.1.1 Single parameter optimisation for electrodeposition of Bi_2Te_3

3.3.1.1.1 Preparation of electrolyte

The electrolytes were used to deposit Bi_2Te_3 on both virgin and recycled carbon fibres (RCF).The Bi_2Te_3 films were deposited from electrolyte solutions consisting of 1 M of 65% aqueous nitric acid bath with three different compositions of $Bi(NO_3)_3.5H_2O$ and TeO_2 as shown in **Table 3- 1**.

Table 3- 1: Varying electrolyte compositions for electrodeposition of Bi_2Te_3 films

Batch Number	Batch Composition	
	$Bi(NO_3)_3.5H_2O$ (mM)	TeO_2 (mM)
A	8	10
B	1	10
C	8	11

3.3.1.1.2 Electrochemical deposition

Electrodeposition was carried out using a potentiostat (VersaStat-3, Princeton Applied Research) at room temperature. The potentiostat was used with a standard three-cell electrode configuration whereby the working electrode is the virgin/RCF sheet with a dimension of 8 cm x 0.5 cm, the reference electrode is a silver/silver chloride (Ag/AgCl) in 1 M of potassium chloride (KCl) and the counter-electrode is a platinum rod. The schematic for the electrodeposition set up is depicted in **Figure 3- 2**. The electrodeposition is carried out in potentiometry mode. In the potentiommetry mode, constant agitation is provided at 300 RPM to the electrolyte at a constant deposition potential for 1 hour and this is the stage at which the actual deposition occurs. After electrodeposition was completed, the electrodeposited carbon fiber was dried in an oven for 15 minutes at 70 °C.

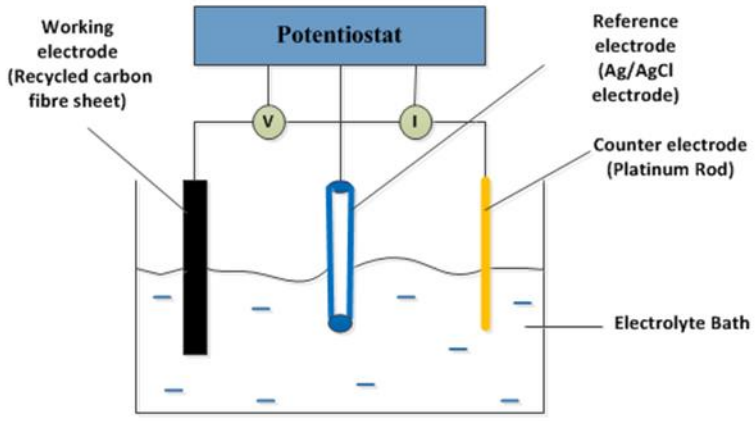


Figure 3- 2: Schematic of a three cell electrode set up

3.3.1.2 Multi-parameter optimisation for electrodeposition of Bi_2Te_3 using response surface methodology

3.3.1.2.1 Preparation of electrolyte

The electrolytes were used to deposit Bi_2Te_3 on RCF.The Bi_2Te_3 films were deposited from electrolyte solutions consisting of 1 M of 65% aqueous nitric acid bath with three different compositions of $Bi(NO_3)_3.5H_2O$ and TeO_2 as shown in **Table 3- 2**.

Table 3- 2: Different compositions of bismuth and tellurium ions in electrolyte

Electrolyte Composition in molar concentration ratio(Bi/(Bi+Te))	**Concentration of Bi and Te ions (mM)**	
	$Bi(NO_3)_3.5H_2O$ (mM)	TeO_2 (mM)
0.20	2.5	10
0.40	6.7	10
0.60	15	10

3.3.1.2.2 Electrochemical deposition

A similar setup as in **Figure 3- 2** with glass wool insulation was used in this section. In the potentiommetry mode, constant agitation is provided at 300 RPM to the electrolyte at varying

deposition time from 0.5 to 3 hours, deposition potential from -0.10 V to -0.60 V and deposition temperature from 25 °C to 60 °C.

3.3.1.2.3 Experimental design and statistical analysis

Response Surface Methodology (RSM) was used to design the sets of experiments for this study. In RSM, the primary objective is to optimise a response that is influenced by various experimental parameters and also helps to quantify the relationship between a response and the vital experimental parameters (Raissi and Farsani, 2009). The D-Optimal model under RSM was used to investigate the effects of four different experimental parameters in electrodeposition of Bi_2Te_3 on one response output (i.e., Seebeck coefficient) based on 23 sets of experiments. The four experimental parameters were deposition potential (A), deposition time (B), deposition temperature (C) and electrolyte composition, Bi/(Bi+Te) (D). Parameters A, B and C are numeric continuous type factors varied over two levels (low and high) while parameter D was numeric discrete type factor varied over three levels as shown in **Table 3- 3**.

Table 3- 3: Parameter ranges chosen for experimental study using D-Optimal

Coded Name	**Variable Name**	**Type**	**Parameter Range**		**Parameter Unit**
A	Deposition Potential	Continuous	Level 1/Low	-0.6	V
			Level 2/High	-0.1	
B	Deposition Time	Continuous	Level 1/Low	0.5	hours
			Level 2/High	3	
C	Deposition Temperature	Continuous	Level 1/Low	25	ºC
			Level 2/High	60	
D	Electrolyte Composition	Discrete	Level 1	0.2	mM
			Level 2	0.4	
			Level 3	0.6	

The experimental parameters were varied based on previous studies. The deposition potentials were varied from -0.60 V to -0.10 V, as (Martín-González et al., 2002) mentioned that all potentials more negative than 0.50 V were suitable for the deposition of Bi_2Te_3. Martin-Gonzalez et al. (2002) observed that potentials between -0.10 V to -0.20 V led to stoichiometric

Bi_2Te_3, however, a close to stoichiometric Bi_2Te_3 was also observed close to -0.50 V. Many studies (Qiu et al., 2010) (Yoo et al., 2005) (Pang et al., 2012) have concluded that -0.10 to -0.20 V is ideal for the stoichiometric deposition of Bi_2Te_3. A stoichiometric Bi_2Te_3 is often associated with better thermoelectric properties (Jagadish et al., 2016) (Szymczak et al., 2014) (Kim and Lee, 2006). Thus, in this study the effect of deposition potential on the Seebeck coefficient of Bi_2Te_3 will be studied and verified using D-optimal model. The effect of deposition time on Seebeck coefficient of Bi_2Te_3 has not been reported in literature thus far as most studies were carried out for a fixed duration of an hour, in this study the effect of electrodeposition duration on Seebeck coefficient of Bi_2Te_3 will be clearly demonstrated. In addition to time, temperature is also another parameter that has not been investigated despite bath temperature playing a vital role in electrochemical kinetics (Goux et al., 2005). Thus, the bath temperature in this study will be carried out up to 60 ºC, due to the limitation of the Ag/AgCl electrode that is only able to withstand a maximum temperature of 75 ºC. In addition to deposition potential, electrolyte composition consisting of varying amounts of Bi^{3+} and $HTeO_2^+$ also affects the stoichiometry and thermoelectric properties of electrodeposited bismuth telluride films. As the atomic percentage of bismuth and tellurium atoms in electrodeposited films is postulated to be similar to ratios of bismuth and tellurium in the electrolyte (Glatz et al., 2008)(Del Frari et al., 2005)(Kim and Oh, 2009). Many studies in the past have studied the change in stoichiometry of bismuth telluride films by varying the deposition potential, however only few studies (Wang et al., 2007) (Kim and Oh, 2009)(Yoo et al., 2013) have studied the effect of varying electrolyte composition on the stoichiometry and subsequent Seebeck coefficient of electrodeposited films. In this research, the effect of both deposition potential and electrolyte composition will be investigated in tandem on the Seebeck coefficient of electrodeposited bismuth telluride films unlike past research that have only studied the effects of these parameters individually. The composition of electrolyte is

varied into 3 types such as tellurium rich (0.2), stoichiometric (0.4) and bismuth rich (0.6) and the corresponding stoichiometry and its effect on Seebeck coefficient is investigated.

The response output for the D-Optimal RSM design is the Seebeck coefficient measured. The four experimental parameters and the response output is fitted together in a reduced quadratic polynomial model as shown in Eq (3.1):

$$Y = B_0 + \sum B_i X_i + \sum B_{ij} X_i X_j + \sum B_{ii} {X_i}^2 \qquad (3.1)$$

Where Y is the response output, B_0 is independent constant effect, B_i is the linear/individual effect, X_i are the independent experimental parameters (i=A,B,C,D), B_{ij} is the interaction effect (i=A,B,C,D and j=A,B,C,D), B_{ii} is the squared effect.

The data collected were analysed using multiple regressions to fit the quadratic model through Analysis of variance (ANOVA) to study the significance of each experimental parameter and their interactions during the electrodeposition of Bi_2Te_3 on RCF. The response surface models developed were then optimised to determine the required conditions for energy efficient deposition of Bi_2Te_3 on RCF.

3.3.2 Recycled carbon fibre polymer composite fabrication

3.3.2.1 RCF composite

Layers of randomly oriented RCF were placed in a binder-water suspension with a 1: 10 (volume ratio). The RCF was soaked in the suspension for approximately 15 minutes. The soaked RCF was sandwiched between two metal plates that were covered with laboratory wipes on the top and bottom plate to remove the residual water. The top metal plate was then manually subjected to a brick load of 10 kg to produce a uniform RCF composite with a thickness of 1 mm. The laboratory wipes were replaced with new ones once it was wet and the RCF were

subjected to the same load for approximately three times until it was dried. The dried RCF with an applied top load of 5 kg was then placed in a Memmert oven at 200 °C for 1 hour for moisture evaporation and also curing and formation of the RCF composite.

3.3.2.2 Thermoelectric filler coating on RCF composite

Two thermoelectric fillers are used in this work, namely Bi_2Te_3 and Bi_2S_3 particles. The thermoelectric filler particles are mixed with ethylene glycol and Acrodur DS 3530 binder and are subjected to ultrasonication for one hour, this ultrasonicated solution will thereafter be referred to as thermoelectric filler coating. The thermoelectric filler coating is then applied to the surface of the RCF composite using a brushing technique (using paint brush). The coated RCF composite is then placed into the oven at 200 °C for 1 hour. The weight percent of both thermoelectric fillers were varied from 15 to 60 weight percent (wt%) within the composite.

3.3.2.3 MWCNT doped thermoelectric filler coating on RCF composite

The MWCNTs were suspended in ethylene glycol and subjected to ultrasonication for one hour. Then, the thermoelectric filler particles and Acrodur 3530 binder will be added to the ultrasonicated MWCNT suspension and is subjected again to another one hour of ultrasonication. Thereafter, this suspension will be referred to as MWCNT doped thermoelectric coating. The MWCNT doped thermoelectric filler coating is then applied to the surface of the RCF composite using a brushing technique (using paint brush). The coated RCF composite is then placed into the oven at 200 °C for 1 hour. The weight percent of MWCNT is varied from 0.05 to 0.20 wt% with respect to the optimised weight of thermoelectric filler loading.

3.3.2.4 Annealing of thermoelectric fillers

The thermoelectric fillers was placed in a crucible boat before being inserted into the quartz furnace. The crucible boat is placed in the middle of the annealing chamber using a pair of tongs to ensure that the sample was heated uniformly. Annealing was carried out in a 100% argon environment under a vacuum pressure of 1.7 ± 2 Torr. The tubular furnace was programmed to have a ramping of 10 °C/min. The annealing temperature was varied at 300, 350, 400 and 450 °C as well as annealing time that was varied for 1, 2 and 3 hours respectively for each annealing temperature. Annealing temperature was varied from 300-450 °C for both Bi_2Te_3 and Bi_2S_3 fillers because crystallisation for both only takes place at temperatures higher than 250 °C and at temperatures higher than 350 °C there is re-evaporation of tellurium that occurs owing to its lower evaporation energy for Bi_2Te_3 and Bi_2S_3 sublimes easily at temperatures higher than 400 °C. The temperature variation during annealing within the quartz furnace was controlled at ± 1.5 °C.

3.3.2.5 Annealed thermoelectric filler coating on RCF composite

The annealed thermoelectric filler coating was applied on RCF composite using the same methodology as described in Section 3.3.2.2.

3.4 Thermoelectric properties

3.4.1 Measurement of Seebeck coefficient

The Seebeck coefficient was measured using an in-house measurement system as shown in **Figure 3- 3**.

The Seebeck coefficient is calculated using the formula shown in Eq (3.2):

$$\alpha = \frac{\Delta V}{\Delta T} = \frac{V_H - V_C}{T_H - T_C} \qquad (3.2)$$

ΔV in millivolts is the open circuit potential difference (V_{OC}) generated between V_H, the potential at the hot side and V_C, the potential at cold side, ΔT in Kelvin is the temperature induced between the T_H, temperature on the hot side and T_c, temperature on the cold side. The test was conducted with an average measuring temperature of 40 °C on the hot side and cold side subjected to room temperature. Whereby, α is the combined measured value of the Seebeck coefficient of copper (α_{CU}) and RCF thermoelectric composite/film (α_{CF}), therefore the Seebeck coefficient of RCF thermoelectric composite is given by Eq (3.3).

$$\alpha_{CF} = \alpha_{Cu} - \alpha \qquad (3.3)$$

The Seebeck coefficients of the carbon fibres were calculated using Eq (3.3) by taking an average of all six readings.

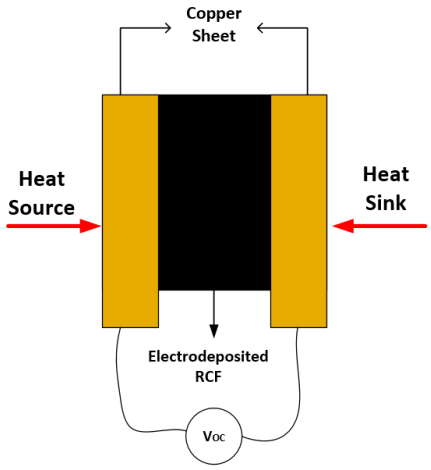


Figure 3- 3: Schematic set up for Seebeck coefficient measurement.

3.4.2 Measurement of electrical resistivity

The electrical parameters such as electrical resistivity, carrier concentration and carrier mobility was measured using a Hall Effect measurement system, HMS ECOPIA 3000 with a magnetic field 0.57T and probe current of 15mA for all samples.

3.4.3 Power factor calculation

The performance/efficiency of a thermoelectric material is given by the power factor (PF) with the formula shown in Eq (3.4) (Kim and Oh, 2009).

$$PF = \frac{\alpha^2}{\rho} \qquad (3.4)$$

PF is calculated based on measured values of both α and ρ.

3.5 Thermal properties

3.5.1 Thermogravimetric analysis (TGA)

Thermal degradation and stability of the RCF thermoelectric composites were measured using a thermogravimetric analyser (Perkin Elmer STA 6000). A sample of approximately 10-15 mg in weight was placed in an open alumina pan under an air flow rate of 20 ml/min and heated from ambient 30 °C to 900 °C at a heating rate of 10 °C/min. The onset degradation temperature (T_{onset}) is defined as the temperature at 5% weight loss. Maximum degradation temperature (T_{max}) is defined as temperature at which the thermoelectric composite losses its maximum weight, that is identified by the peak of derivative (dW/dT) curve. These temperatures were used to indicate the thermal degradation and stability of the RCF thermoelectric composites.

3.6 Characterisation

3.6.1 X-ray powder diffraction (XRD)

The phase structure and crystallinity property analysis of the RCF thermoelectric composites was determined by X-ray powder diffraction (XRD) (Cu-Kα, Bruker D8 Advance) operating

at 40kV and 40 mA. XRD patterns were recorded in the 2θ range from 10 to 80° with a step size of 0.025° using Cu Kα radiation wavelength of 1.540 Å.

Crystallite size (D) can be calculated using the Scherrer equation as shown in Eq (3.5):

$$D = \frac{0.9\lambda}{\beta cos\theta} \qquad (3.5) \qquad \text{(Hasan and Shallal, 2014)}$$

Where θ is the Bragg diffraction angle, λ is the wavelength of x-ray (1.540 Å), β is the full width at half maximum (FWHM) of the main peak in the XRD pattern.

The microstrain (ε) of the thermoelectric composites are calculated using the formula in Eq (3.6):

$$\varepsilon = \frac{\beta}{4\tan\theta} \qquad (3.6) \qquad \text{(Yücel and Yücel, 2017a)}$$

Dislocation density (δ) is defined as the length of dislocation lines per unit volume of the crystal space is calculated using Eq (3.7):

$$\delta = \frac{1}{D^2} \qquad (3.7) \qquad \text{(Yücel and Yücel, 2017b)}$$

3.6.2 Field Emission Scanning Electron Microscope (FESEM) and Energy Dispersive X-ray (EDX) analysis

The RCF thermoelectric composite/electrodeposited RCF was cut into 1 cm x 1 cm and placed onto a double-sided sticky tape that was positioned on sample pins before being placed into the FESEM machine. The FESEM images were taken using the FEI Quanta 400 to obtain the morphological structure of the composites. The EDX analysis was carried out to determine the percentage distribution of bismuth, tellurium and sulphur in the composites/electrodeposited RCF.

Chapter 4: Optimisation of Seebeck coefficient for electrochemically deposited Bi_2Te_3 on RCF by varying electrodeposition parameters

4.1 Introduction

This chapter addresses the first aim of the study which is to develop a flexible thermoelectric film from RCF with electrodeposited Bi_2Te_3 by employing a univariate and multivariate optimisation approach using Design of Experiments.

The conventional and commercial thermoelectric power generators consists of a rigid ceramic substrate that acts as the sink plate and absorber plate with thermoelectric elements stacked in the middle (Sugiyama, 2005). However, the lack of flexibility and the sheer size of these conventional devices have proven to be the Achilles Heel, thus limiting its potential applications. Hence in order to enhance thermal contact with heat sources of different geometry and prevent large thermal energy losses (Kim et al., 2014), there is a need for a thermoelectric generator (TEG) that easily conforms to any surface (Kusagaya and Takashiri, 2015). The cost of a TEG can be reduced by employing recycled materials as flexible substrate, one such suitable candidate is RCF. Thus, in this study RCF is chosen as a viable substrate to replace the conventional ceramics due to its flexible, lightweight nature and as a means to close the recycling loop for RCF.

Electrodeposition was chosen to deposit Bi_2Te_3 on RCF as it is a cost effective, room temperature operation, provides a large area for deposition which is suitable for industrial application and the composition of the films can be easily monitored by altering the electrodeposition parameters (Ma et al., 2010). Though electrodeposition of Bi_2Te_3 using nitric acid electrolytes have been widely studied from the year 1993 (Takahashi, 1993), a majority of work focussed on varying deposition potentials with different substrates (Ma et al., 2010; Magri

This chapter has been published in Journal of Materials and Manufacturing Processes, DOI: 10.1080/10426914.2015.1090590 and Journal of Materials Science, DOI: 10.1007/s10853-017-1284-2

et al., 1996; Martín-González et al., 2002; Miyazaki and Kajitani, 2001; Qiu et al., 2010). There were also some work done by varying the amount of bismuth and tellurium precursors to observe its effects on thermoelectric properties (Kim and Oh, 2009; Wang et al., 2007; Yoo et al., 2013). Both parameters showed substantial effects on thermoelectric properties; however, those are not the only parameters that affect electrodeposition. Faraday's Law have also identified deposition time as a crucial parameter that affects the amount of semiconductor deposited (Paunovic, Milan;Schlesinger, 2006) on a substrate that have yet to be investigated in any study pertaining Bi_2Te_3. Electrolyte bath temperature is also another vital parameter in electrodeposition which was thought to improve electrochemical kinetics and led to grain size increment (Goux et al., 2005; Rakhshani and Varghese, 1988). However, the effects of parameters such as deposition time and deposition temperature have yet to be investigated for the electrodeposition of Bi_2Te_3.

There are two parts to this objective. For the first part of this study a univariate optimisation by only varying the electrolyte composition was carried out on both VCF and RCF, and its subsequent effect on stoichiometry and Seebeck coefficient was studied. In the second part of the study, Design of Experiments (DOE) was employed to study the combined effect of experimental parameters such as deposition potential, electrolyte composition, deposition time, and deposition temperature on the Seebeck coefficient of Bi_2Te_3 coated RCF.

Most research work pertaining electrodeposition of Bi_2Te_3 have been studied by varying one deposition parameter at a time whilst maintaining the others. This univariate approach may not result in optimum experimental conditions that will yield the highest properties due to the neglected experimental domain. However, with the multivariate approach using DOE, this study will be able to explore a larger experimental domain thus resulting in higher optimum values.

A D-optimal model under Response Surface Methodology (RSM) was used to study the inter-parameter interactions, leading to the subsequent optimisation of parameters that yield the optimum Seebeck coefficient of Bi_2Te_3. The D-optimal approach was preferred in this case compared to that of Central Composite Design (CCD), Box-benken method and factorial method as it yielded the least amount of experimental runs but with comprehensive information on each parameter and its subsequent effect on Seebeck coefficient (Triefenbach, 2008) (Anderson and Whitcomb, 2014). D-optimal has a flexible design structure that allows the researcher to vary numeric factors either in discrete or continuous manners, which is not plausible with other rigid designs such as CCD, Box-benken that vary parameters based on fixed levels.

This study ultimately aims to determine the combination of experimental parameters that will yield the optimum Seebeck coefficient with the least amount of chemicals and energy. In addition to that, the data obtained in the multivariate optimisation will be compared to that of univariate optimisation to highlight the improvement brought about by DOE on the Seebeck coefficient.

4.2 Results and discussion

4.2.1 *Single parameter/univariate optimisation*

4.2.1.1 Deposition of n-type Bi_2Te_3 and Seebeck Coefficient

Bi_2Te_3 films with different compositions of Bi and Te were deposited on RCF and VCF with the same electro-deposition parameters. Bi_2Te_3 is a well-known efficient thermoelectric material at room temperature, but a very large part of its efficiency is dependent on the stoichiometry of the semiconductor. The thermoelectric properties of Bi_2Te_3 are directly linked to the stoichiometry of the Bi_2Te_3 films formed; hence it is important to determine the atomic percentage of Bi and Te present in this film (Cai et al., 2013) .

In this study, bismuth telluride was deposited on both VCF and RCF from three different batches of electrolytes that have different composition of Bi^{3+} and $HTeO_2^+$ ions which produced different stoichiometric formulas of bismuth telluride is shown in **Figure 4- 1**.

Based on **Figure 4- 1**, Batch A produces bismuth telluride films closest to stoichiometric composition for both RCF and VCF, which could probably be attributed to the arrangement of Bi and Te atoms in the films that impact the crystal structure and orientation and subsequently the carrier concentrations. There is a decreasing trend in Seebeck coefficient from Batch A to Batch C for VCF, whereas for RCF the trend varies slightly with a small increase in Seebeck coefficient for Batch C. This discrepancy in Seebeck coefficient trend for RCF is stemming from the difference in stoichiometry of the films deposited on VCF and RCF respectively, as in Batch C for RCF the atomic ratio of Bi: Te is 2:2.48 is closest to the original stoichiometry of 2:3. It is also important to emphasize that electrolyte composition with stoichiometric Bi/Bi+Te molar ratios of closer to 0.4 also resulted in electrodeposited films closer to stoichiometry. A similar observation on the proportional relationship between molar ratios in electrolyte and atomic ratios in electrodeposited films was also observed by (Glatz et al., 2008)(Del Frari et al., 2005)(Kim and Oh, 2009). The results also highlight that bismuth telluride films that are closest to the stoichiometry of Bi_2Te_3 for both VCF and RCF show a much higher improvement in Seebeck coefficient. As shown in **Figure 4-1**, A similar phenomena was also observed with close to stoichiometric bismuth telluride films grown by co-sputtering, as stoichiometric films have the least carrier concentration and the largest carrier mobility (Kim and Lee, 2006).

The Seebeck coefficient of RCF is comparatively lower than that of VCF in most cases; this could be attributed to the random orientation of RCF, which does not allow uniform adhesion of the coatings on to the fibre. Furthermore, the soft texture of the RCF caused it to frail upon

contact with the electrolyte. However, in this study the VCF is used only as a control to compare the difference in the Seebeck coefficient that arises from its fibre properties.

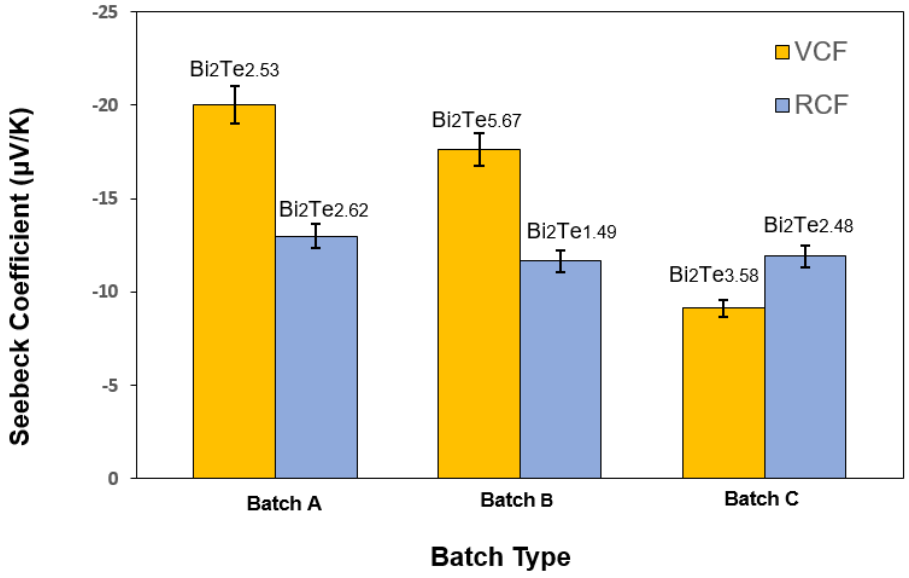


Figure 4- 1: Seebeck coefficient of different electrolyte composition for Bi_2Te_3 films.

In addition to electrolyte composition, the stoichiometry of electrodeposited films is also plausibly altered by the applied deposition potential. The effect of deposition potential on the Seebeck coefficient of RCF for Batch A was also studied briefly as depicted in **Figure 4- 2**. The deposition potential yielding the highest Seebeck coefficient is at -0.50 V, this is slightly higher than the conventional range of -0.10 to -0.20 V perhaps owing to the rough and haphazard surface of RCF posing resistance for the deposition of bismuth telluride films thus requiring a higher potential to overcome the interface energy between the substrate and deposited films. The composition as well as morphology of electrodeposited films are sensitive to the substrate material.

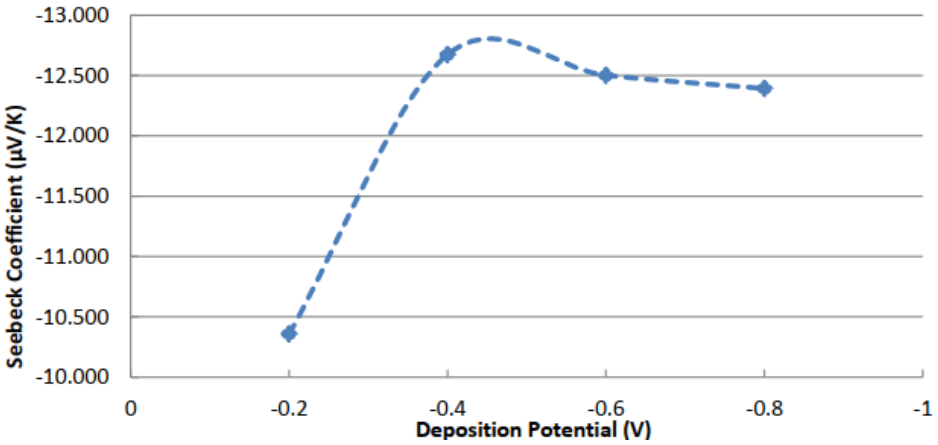


Figure 4- 2: Seebeck coefficient of RCF electrodeposited with Bi_2Te_3 films with respect to deposition potential.

4.2.1.2 Surface Morphologies of electrodeposited VCF and RCF

The surface FESEM images of the raw uncoated and electrodeposited VCF and RCF are shown in **Figure 4- 3**. It can be clearly observed from the FESEM images that the fibre strands of RCF (**Figure 4- 3 (b)**) are of random orientation as compared to the orderly orientation of VCF (**Figure 4- 3 (a)**). For the deposition of Bi_2Te_3, the RCF has a less uniform coating on its strands as compared to that of VCF. The fibre orientation of RCF is haphazardly arranged and the surface of RCF is rougher than that of VCF, it is believed to offer more resistance to the mobility of electrons leading to lower Seebeck coefficients. A difference in Seebeck coefficient as a result of substrate was also observed by Jin and Wang, a smoother surface of gold (Au) led to a slightly higher Seebeck coefficient than a rougher surface of Bi (Jin and Wang, 2010)(Mele et al., 2013). Besides that, the effect of recycling may have resulted in some charred contaminants present on the surface of RCF as highlighted by the red circle in **Figure 4- 4 (a)** leading to less homogenous coatings on RCF. However, EDX analysis was unable to confirm the presence of this charred contaminant as it is predominantly carbon.

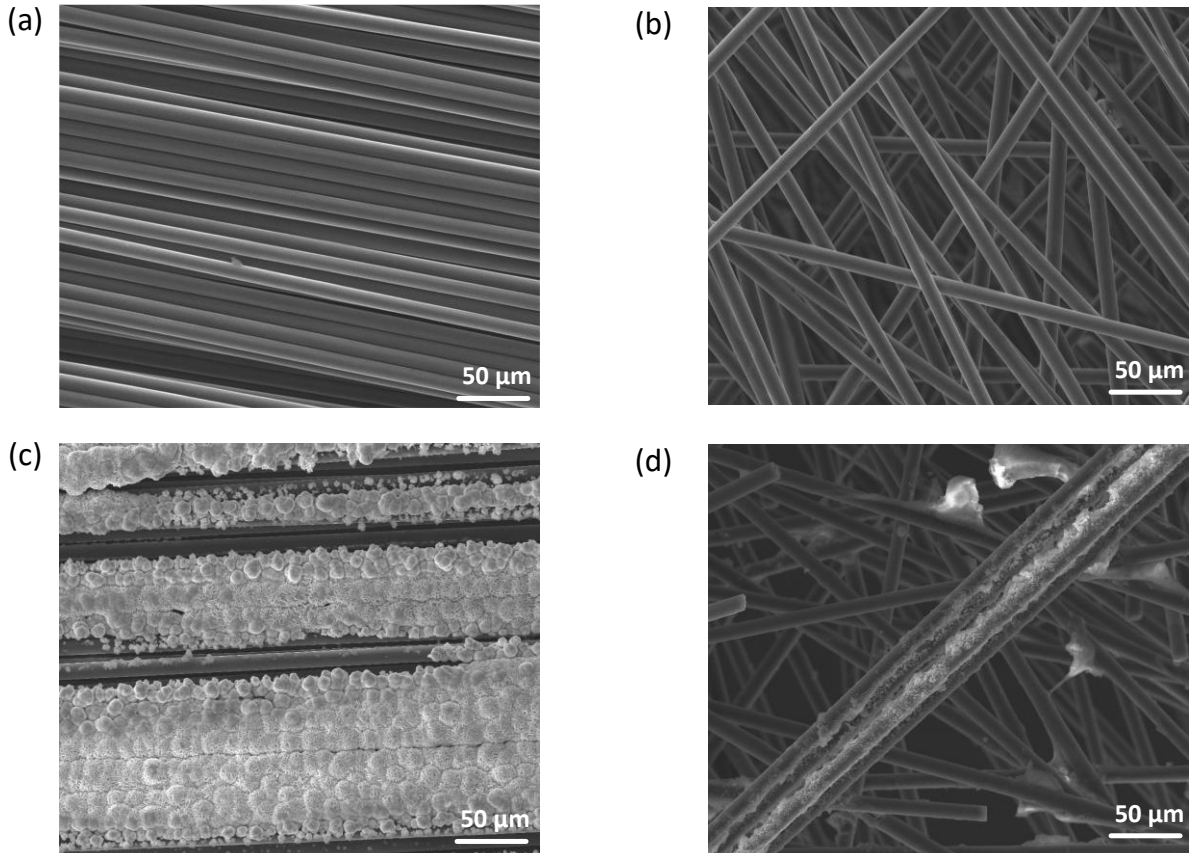


Figure 4- 3: FESEM images of (a) Uncoated VCF (b)Uncoated RCF (c) VCF deposited with Bi_2Te_3 (d) RCF deposited with Bi_2Te_3.

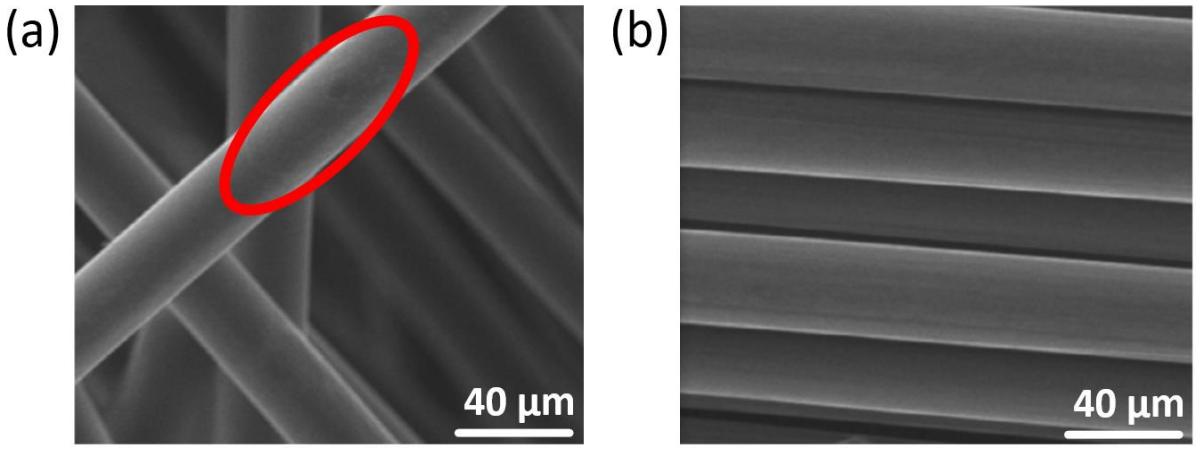


Figure 4- 4: Zoomed in FESEM images of (a) Presence of charred contaminants on uncoated RCF (b)Clean fibre strands of uncoated VCF.

4.2.2 Multi-parameter/multivariate optimisation

Under this section, Design of Experiments (DOE) was employed to study the combined effect of multiple electrodeposition parameters such as deposition potential, electrolyte composition, deposition time, and deposition temperature on the Seebeck coefficient of Bi_2Te_3 coated RCF.

4.2.2.1 Model fitting and analysis of variance (ANOVA)

The design of experiments generated by D-Optimal response surface methodology (RSM) design with varying electrodeposition conditions along with the experimental and predicted values of Seebeck coefficient are as shown in **Table 4- 1**.

Table 4- 1: D-optimal experimental design along with experimental and predicted Seebeck coefficient.

Run	A	B	C	D	Seebeck Coefficient (μV/K)		Percentage Difference between experimental and predicted(%)
	Deposition Potential (V)	Deposition Time (hours)	Deposition Temperature (^{0}C)	Bi/(Bi+Te)	Experimental	Predicted	
1	-0.60	0.5	43.6	0.2	-10.48	-10.40	0.76
2	-0.10	2.7	25.0	0.6	-12.55	-12.65	0.79
3	-0.10	0.6	60.0	0.2	-10.32	-11.18	8.33
4	-0.60	0.5	43.6	0.2	-9.55	-10.40	8.90
5	-0.42	3.0	41.7	0.6	-14.05	-14.78	4.94
6	-0.10	0.6	60.0	0.2	-12.04	-11.18	7.14
7	-0.60	0.5	25.0	0.6	-10.79	-10.49	2.78
8	-0.35	1.6	29.0	0.6	-10.77	-10.46	2.88
9	-0.60	3.0	60.0	0.2	-11.82	-11.94	1.02
10	-0.36	1.7	51.3	0.2	-11.19	-10.72	4.20
12	-0.41	0.5	60.0	0.4	-12.22	-11.68	4.40
13	-0.60	1.7	60.0	0.6	-12.07	-11.63	3.65
14	-0.10	3.0	25.0	0.2	-10.80	-10.69	1.02
15	-0.10	0.5	25.0	0.6	-10.66	-11.05	3.66
16	-0.10	0.5	25.0	0.2	-13.52	-13.05	3.50
17	-0.60	1.7	60.0	0.6	-11.14	-11.63	4.40
18	-0.10	0.5	56.5	0.6	-10.97	-11.18	1.91
19	-0.10	1.8	43.4	0.4	-14.60	-15.08	3.29
20	-0.60	3.0	25.0	0.4	-10.66	-10.72	0.56
21	-0.43	1.8	25.0	0.2	-9.29	-9.48	2.05
22	-0.10	3.0	53.0	0.2	-16.06	-16.03	0.19

The experimental outcome of the D-Optimal design above is fitted to a quadratic polynomial equation as shown below in Eq (4.1)

$$Y = -13.33 - 1.50A - 1.44B - 1.21C - 0.71D - 0.72AB - 0.49AC - 2.16BC - 1.18BD - 0.53CD - 1.05B^2 + 2.13D^2 \quad (4.1)$$

Where Y is the Seebeck coefficient (μV/K); A, B, C and D are deposition time, deposition potential, deposition temperature and electrolyte composition respectively.

The F-value and P-value in the Analysis of Variance (ANOVA) determines the significance of the model, model parameters and model parameter interactions. P values smaller than 0.05 indicate that the model terms are significant thus greatly contributing to the Seebeck coefficient (Coşkun et al., 2014). The F and P values obtained in this study are as shown in **Table 4- 2**.

Table 4- 2: Analysis of variance (ANOVA) for electrodeposition parameters of Bi_2Te_3 on RCF.

Source	Sum of Squares	Degree of Freedom df	Mean Square	F Value	p-value	Significance
Model	66.75	11	6.07	11.43	0.0003	Significant
A-Deposition Potential	27.86	1	27.86	52.45	< 0.0001	Significant
B-Deposition Time	27.38	1	27.38	51.55	< 0.0001	Significant
C-Deposition Temperature	17.66	1	17.66	33.26	0.0002	Significant
D-Bi/(Bi+Te)	8.32	1	8.32	15.67	0.0027	Significant
AB	5.47	1	5.47	10.31	0.0093	Significant
AC	2.11	1	2.11	3.97	0.0744	Insignificant
BC	27.03	1	27.03	50.90	< 0.0001	Significant
BD	14.90	1	14.90	28.05	0.0003	Significant
CD	2.80	1	2.80	5.28	0.0444	Significant
B^2	4.08	1	4.08	7.68	0.0198	Significant
D^2	9.55	1	9.55	17.99	0.0017	Significant
Residual	5.31	10	0.53			
Lack of Fit	1.70	6	0.28	0.32	0.8996	Insignificant
Pure Error	3.61	4	0.90			
Cor Total	72.06	21				

Std. Dev.	0.73	R-Squared	0.9263
Mean	-11.87	Adj R-Squared	0.8452
Coefficient of Variation (C.V. %)	6.14	Pred R-Squared	0.6823
Predicted Residual Sum of Squares (PRESS)	22.89	Adeq Precision	12.155

a Significant at ‘‘p-value” less than 0.05.

b Insignificant at ‘‘p-value’’ more than 0.05.

Thus, from the table above all parameters A, B, C, D, AB, BC, BD, CD, B^2 and D^2 have significant effect on the Seebeck coefficient as they have a p value less than 0.05 which indicates 95% of confidence. The model is significant which is also complemented with the high non- significance of the lack of fit approximately 90%. This ensures that the D-Optimal quadratic model fits the experimental data well, thus giving a better robustness to the design for predicting the response of electrodeposited samples.

The determination coefficient (R^2) for Seebeck coefficient of 92.63% implies that the variations could be explained well by the fitted model. The adjusted and predicted R-squared are also in reasonable agreement with difference less than 0.2, ensuring the model provides good predictions for the outcomes.

The model was further confirmed with the normal probability plot as shown in **Figure 4- 5**. The data forms an approximate straight line on a normal probability plot that ensures no abnormality in data population. It can be observed in **Figure 4- 6** that the practical results are distributed randomly within the range of internally studentized residuals of ±3.00 that confirms the 95% confidence limit, implying that the fitted model is appropriate and the availability of variance assumption.

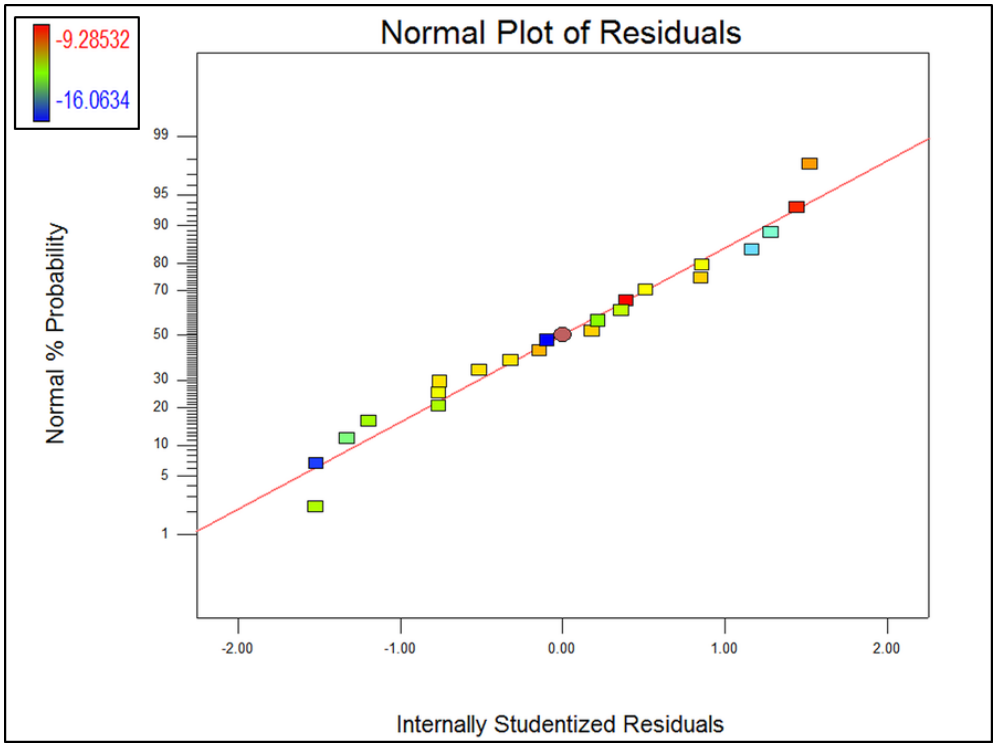


Figure 4- 5: Normal probability plot of residuals.

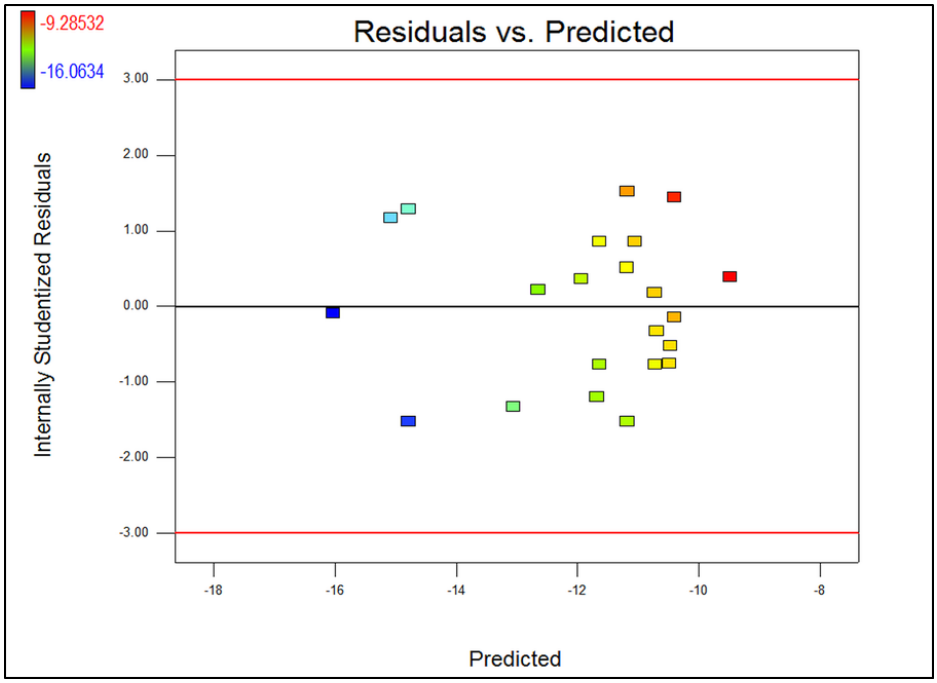


Figure 4- 6: Plot of residuals vs predicted.

Figure 4- 7 presents the comparison between the predicted and experimental measured Seebeck coefficient, which shows that they are in good agreement.

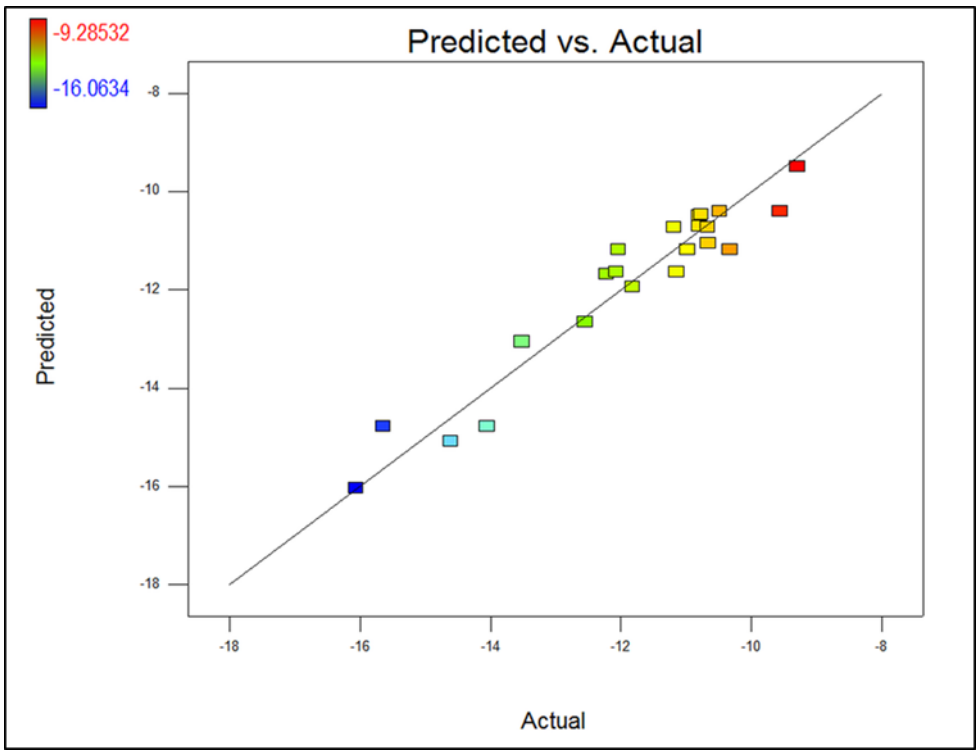


Figure 4- 7: Predicted values against actual values of Seebeck coefficient.

4.2.2.2 Screening of parameters and response surface analysis

The interaction between electrodeposition parameters and the Seebeck coefficient of Bi_2Te_3 coated recycled carbon fibres was investigated by 3D response surface plots. Based on the formulated quadratic model (Eq 4.1), the response surface plots for the interaction effects of deposition time, deposition potential, deposition temperature, electrolyte composition and their interactions is depicted respectively.

The interaction between deposition potential and deposition time, and their combined effect on Seebeck coefficient is shown in **Figure 4- 8**. It is clear from **Figure 4- 8** that longer deposition time and lower deposition potential individually leads to higher Seebeck coefficient. The highest Seebeck coefficient of -18.03 μV/K is obtained at a deposition potential of -0.10 V and 3 hours deposition time. A similar deposition potential for the reduction of bismuth and

tellurium ions was observed by (Ma et al., 2010; Takahashi, 1993) at -0.062 V which is close to the observed potential in this study using DOE. Martín-González et al. (2002) also discovered that stoichiometric Bi_2Te was deposited at potentials close to -0.12 V, this could have resulted in the high Seebeck coefficient that was observed in this study. Magri et al. discovered that deposition time affects the Bi_2Te_3 film thickness, concluding that electrical resistivity decreases and the mobility of electrons improves with prolonging deposition time (Magri et al., 1996). Thus, it is justified in this study that the Seebeck coefficient improves linearly with deposition time.

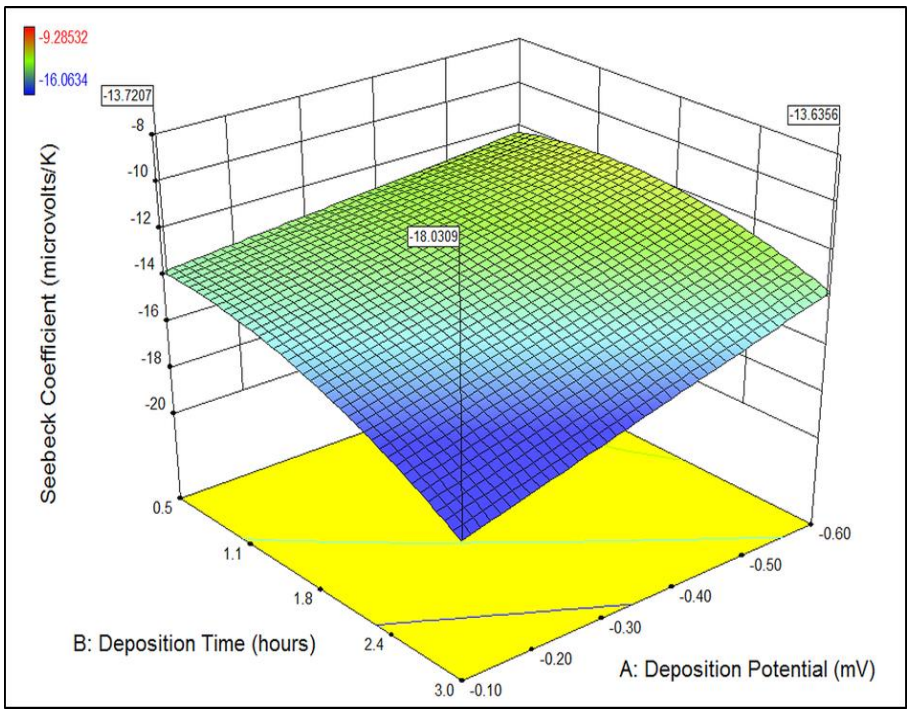


Figure 4- 8: 3D Response surface plot illustrating the effect of deposition potential and deposition time.

Figure 4- 9 illustrates the combined effect of deposition temperature and deposition time on Seebeck coefficient. It is observed that higher deposition temperature and longer deposition time leads to a higher Seebeck coefficient. It was observed that a sample deposited at 60 ºC and 0.6 hours has 59 wt.% of Te and 39 wt.% of Bi leading to stoichiometric Bi_2Te_3. Whereas

another sample deposited at 25 ºC and 0.5 hours has 80 wt.% of Te and 20 wt.% of Bi that is far from stoichiometric composition. The difference in the atomic percentage could be attributed to the change in surface adsorption temperature as the electrolyte temperature increases, thus allowing a redistribution of atoms attributed to the temperature rise. In addition to that, Bi_2Te_3 coats RCF better at higher temperatures than at lower temperatures owing to the increase in grain size that results from higher electrolyte temperature as shown in **Figure 4-10**. A similar relationship between electrolyte temperature and amount of coating on substrate was observed by (Gautier et al., 2016; Sanchez et al., 2012).

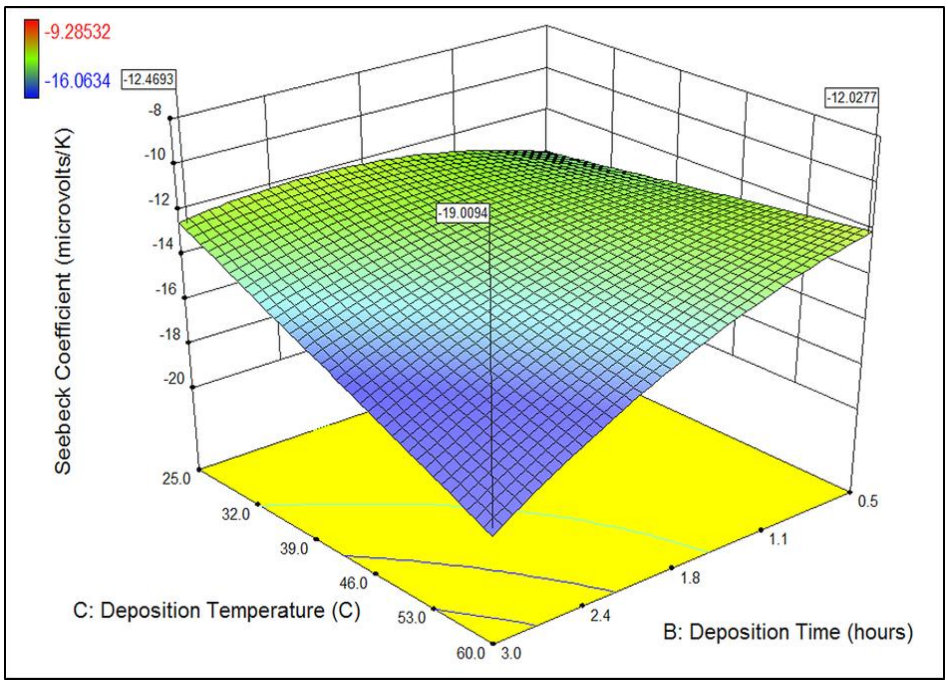


Figure 4- 9: 3D Response surface plot illustrating the effect of deposition temperature and deposition time.

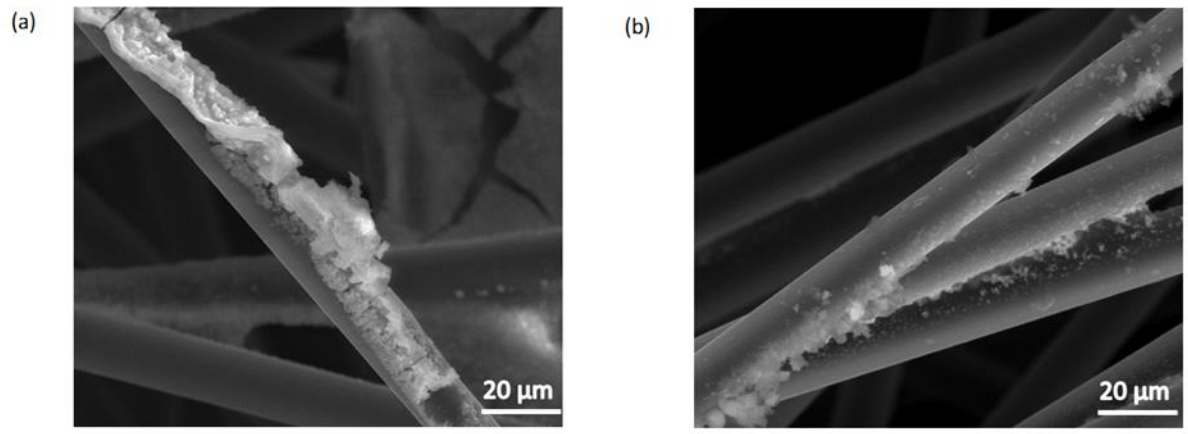


Figure 4- 10: Surface morphologies of Bi_2Te_3 coated RCF (a) At 60 ºC and 0.60 hours (b) At 25 ºC and 0.50 hours both carried out at -0.10 V and 0.2 Bi/(Bi+Te).

The combined effect of electrolyte composition and deposition time on Seebeck coefficient is shown in **Figure 4- 11**. The ideal electrolyte composition for the highest Seebeck coefficient, -16.14 µV/K is between 0.4 to 0.5 ratio of Bi/(Bi+Te). This could essentially be attributed because stoichiometric Bi_2Te_3, yields a 0.4 ratio. A longer deposition time yields a higher Seebeck coefficient, the observed trend may be due to time-dependent mass transfer between Bi^{3+} and $HTeO_2^+$ ions with the working electrode (Zhu et al., 2016).

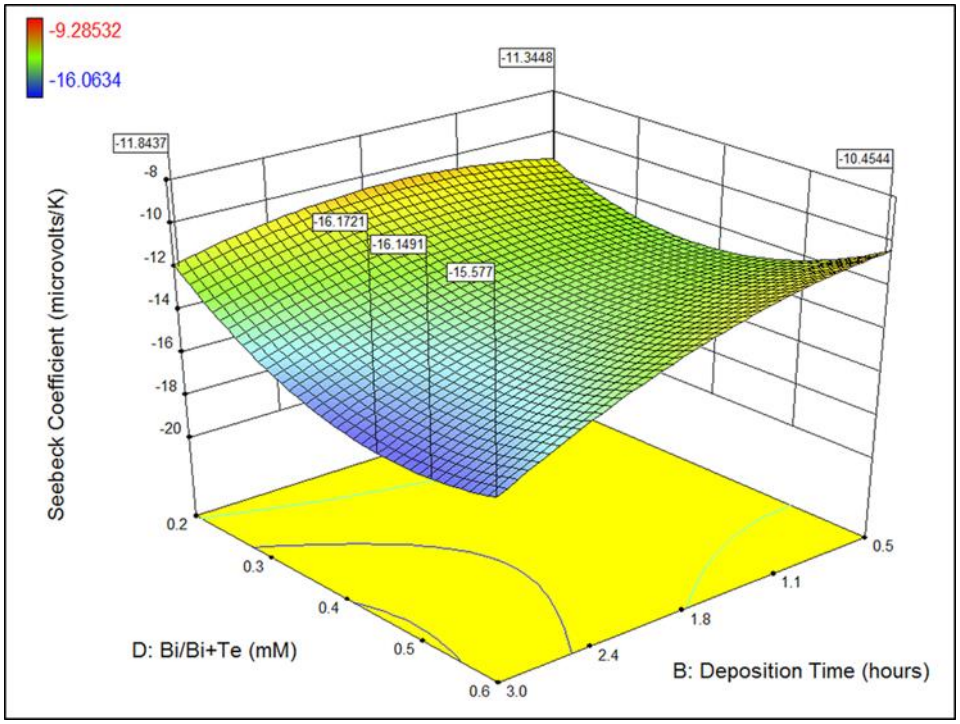


Figure 4- 11: 3D Response surface plot illustrating the effect of electrolyte composition and deposition time.

There is also a clear correlation between deposition temperature and electrolyte composition on Seebeck coefficient as shown in **Figure 4- 12**. There is a linear relationship between deposition temperature and Seebeck coefficient; whereas Seebeck coefficient increases with electrolyte composition until a ratio of 0.4 then it begins to deteriorate. The highest Seebeck coefficient of -14.71 μV/K is achievable at 60 ºC and 0.4 Bi/(Bi+Te) electrolyte ratio.

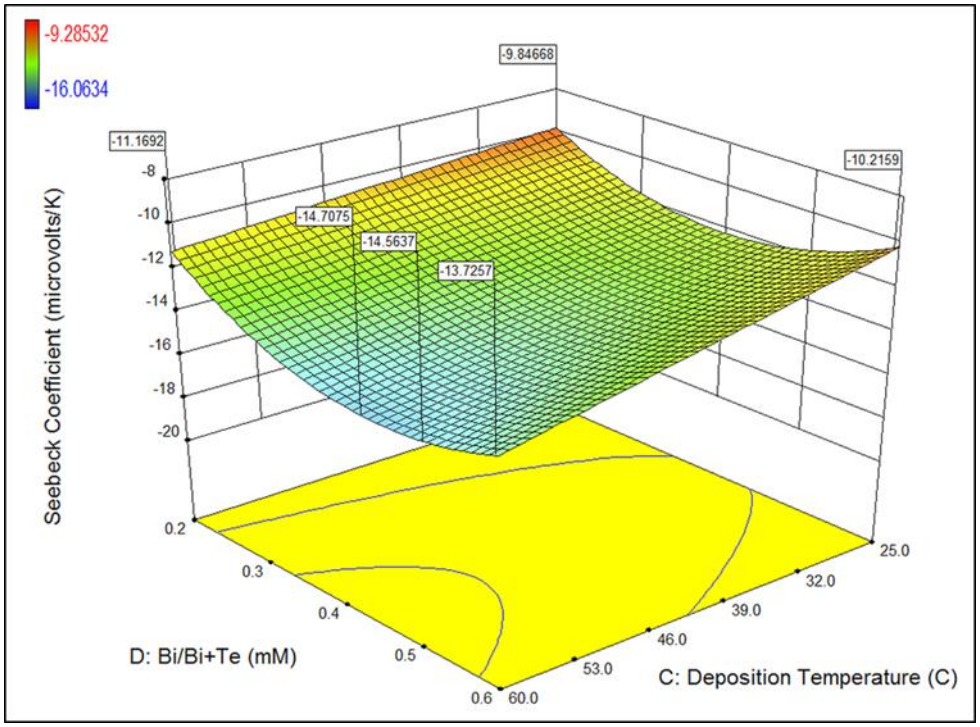


Figure 4- 12: 3D Response surface plot illustrating the effect of electrolyte composition and deposition temperature.

4.2.2.3 Optimisation and validation of the RSM-derived predictive model

In this study, the highest Seebeck coefficient of Bi_2Te_3 coated RCF obtained is -17.25 μV/K with the following parameters as shown in **Table 4- 3**.

Table 4- 3: Parameters yielding the highest Seebeck coefficient for Bi_2Te_3 coated RCF.

Deposition Potential (V)	-0.175
Deposition Time (hours)	2.22
Deposition Temperature (^{0}C)	57.54
Electrolyte Composition (Bi/(Bi+Te))	0.395

The Seebeck value obtained through the Design of Experiment (DOE) in this study has shown a 33% improvement as compared to univariate optimisation (-12.99 μV/K) of electrochemically deposited Bi_2Te_3 on RCF (Jagadish et al., 2016). This drastic improvement in Seebeck coefficient may have arised due to the multiparameter interaction that was studied in this work. Conventionally, most research pertaining electrodeposition of Bi_2Te_3 have been studied using the univariate approach in which most of the deposition parameters are

maintained at constant values while one parameter is varied in the chosen pattern. However, the optimum conditions studied previously are only determined by varying one parameter at a time that may not accurately represent the real time process as it neglects the possibility of parameter interaction that is highly likely. In addition to that, the univariate approach may result in optimum conditions that are dependent on a particular starting condition and may not represent a whole experimental domain leaving some parts unanalysed due to the univariate approach.

This is clearly proven that a multivariate approach brings about an improvement in the properties due to the larger domain investigated, interactions are identified between deposition parameters thus resulting in property enhancement as compared to a univariate approach. Besides that, by using a multivariate approach with DOE, we are able to investigate a large pool of experimental parameters based on only 23 experimental runs, whereas the same in univariate approach may have resulted in a large number of experimental runs.

The results discussed above suggest that a higher Seebeck coefficient is attainable at longer deposition time, higher deposition temperature and moderate amount of Bi and Te precursors. However, the increase in value of these parameters results in a longer and more expensive deposition system that may not be economically feasible for industrial purposes. Thus, this study attempts to find the optimum Seebeck coefficient by minimising deposition time, temperature and the amount of precursor chemicals used in the electrolyte. This was aided by the desirability function in Design Expert 9 software so that the optimum Seebeck coefficient at low deposition temperature, short deposition time and least expensive electrolyte composition could be determined. The analysis suggested that a combination of 0.5 hours of deposition time, 25 ^{o}C deposition temperature, 0.240 Bi/(Bi+Te) electrolyte composition and -

0.10 V of deposition potential had a high desirability of 0.871. This combination of parameters was expected to yield a -13.62 μV/K Seebeck coefficient of Bi_2Te_3 coated RCF.

An experiment to replicate the obtained optimum conditions was carried out to validate the predicted response. The experimental result obtained was -13.42 μV/K, which is in close agreement with the predicted value above with only 1.45 % difference.

4.2.2.4 Performance of Bi_2Te_3 coated RCF under optimum conditions

In this section, the performance of Bi_2Te_3 coated RCF with multivariate optimisation obtained in this study was compared to univariate optimisation of Bi_2Te_3-coated RCF (Jagadish et al., 2016). The Seebeck coefficient of Bi_2Te_3 coated RCF (with multivariate optimisation) was 3.3% higher than the Seebeck coefficient reported for univariate optimisation as shown in **Table 4- 4**.

Table 4- 4: Comparison of Seebeck coefficient and experimental conditions between work done with DOE and without DOE.

	Bi_2Te_3 coated RCF (univariate optimisation)(Jagadish et al., 2016)	**Bi_2Te_3 coated RCF (multivariate optimisation)**
Seebeck coefficient (μV/K)	-12.99	-13.42
Deposition Potential (V)	-0.50	-0.10
Deposition Time (hours)	1	0.50
Deposition Temperature (^{0}C)	25	25
Electrolyte Composition (Bi/(Bi+Te))	0.444	0.240

Moreover, a higher Seebeck coefficient was attained in this study despite using lower electrolye concentration of 0.240 which is approximately 45% lesser electrolyte concentration than that used for univariate optimisation. In addition to that, this Seebeck coefficient was also attained at 50% less deposition time (0.5 hours) than the 1 hour deposition time of univariate optimisation. The high Seebeck coefficient is also complimented by the better Bi_2Te_3 coverage on RCF as shown in **Figure 4- 13**. It can be clearly observed from the FESEM images that the

RCF in **Figure 4- 13 (b)** has a more uniform and widespread deposition of Bi_2Te_3 on its strands as compared to that of **Figure 4- 13 (a)** that have site specific Bi_2Te_3 deposited on certain areas of the fibre. Though the coverage of Bi_2Te_3 on RCF has improved, the coating was still not uniform throughout the strands of RCF to measure the coating thickness.

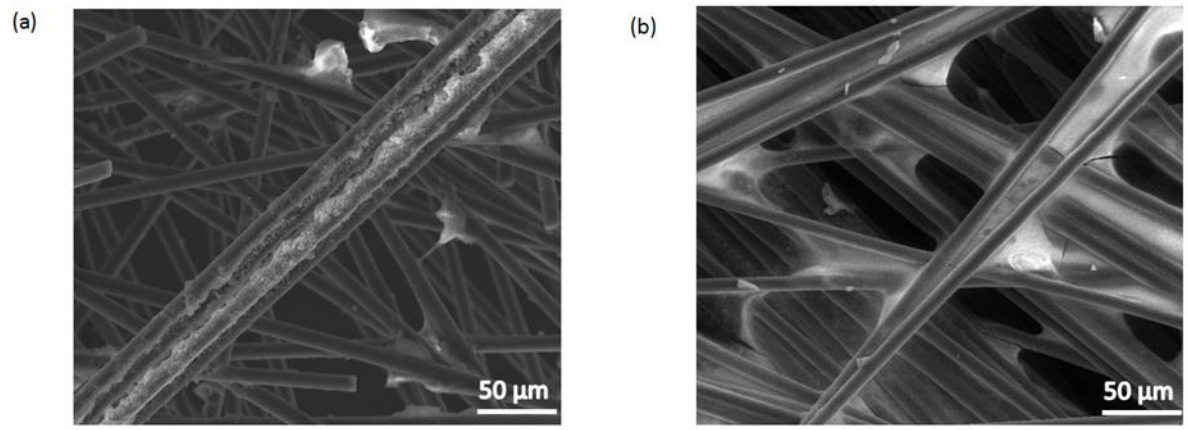


Figure 4- 13: SEM images of (a) Bi_2Te_3 coated RCF (univariate optimisation) (Jagadish et al., 2016) *(b) Bi_2Te_3 coated RCF (multivariate optimisation).*

The increase in Seebeck coefficient in this study can be attributed to the contribution of the simultaneous interaction effects between deposition parameters that improved the overall deposition of Bi_2Te_3 on RCF. The univariate optimisation only focused on single parameter variation at a time, namely the electrolyte concentration, however this univariate approach may not be able to predict the real process and interplay between the various parameters, thus unable to produce the global optimum response. A univariate approach does not take into consideration the individual effect of each deposition parameter and their combined interaction effects on the investigated response, hence missing an experimental domain that may have potentially resulted in higher optimum values.

4.3 Summary

From the univariate optimisation study, it can be concluded that nearly stoichiometric n-type Bi_2Te_3 was obtained from an electrolyte with 8mM of of $Bi(NO_3)_3.5H_2O$ and 10mM of TeO_2 has the highest Seebeck coefficient (-12.99 μV/K) which proves that stoichiometric specimens have a higher figure of merit. VCF has shown higher properties than that of RCF, however VCF is used as a mere control to compare the difference in Seebeck coefficient that arises from its fibre properties.

From the multivariate optimisation study, it can be concluded that it is one among the first to report the statistical evaluation of important deposition parameters for the electrodeposition of Bi_2Te_3 on RCF using Design of Experiments (DOE). Deposition potential, deposition time, deposition temperature and electrolyte composition was identified as vital process parameters that affects the Seebeck coefficient of Bi_2Te_3. It can be concluded that a multi-parameter interaction yields a 33 % higher optimum response value (-17.25 μV/K) than univariate experimental design (-12.99 μV/K) due to the simultaneous effects of more than one deposition parameter as proven in this study. Even under optimum conditions of 45% lesser than the electrolyte concentration and 50% less deposition time, the Seebeck coefficient of multivariate optimisation (-13.42 μV/K) is still 3.3% higher than that of univariate optimisation (-12.99 μV/K). The optimum parameters obtained are deposition potential: -0.10 V, deposition time: 0.5 hours, deposition temperature: 25 ^{0}C, and electrolyte composition: 0.240 that yielded a decent Seebeck coefficient of -13.42 μV/K. The predicted and experimental results were in close agreement with only 1.45% of difference, which indicates the robustness of the experimental design by DOE.

Chapter 5: Recycled Carbon Fibre Composites with Bi_2Te_3 and Bi_2S_3 thermoelectric fillers

5.1 Introduction

The previous chapter have focused on electrochemical/electrodeposition of Bi_2Te_3 on RCF. The electrodeposition of Bi_2Te_3 have definitely improved the Seebeck coefficient of raw RCF fibre from -6.52 μV/K to -12.99 μV/K (without DOE) and -13.42 μV/K (with DOE). The deposition of Bi_2Te_3 has improved the Seebeck coefficient of RCF by approximately 2 times. However, as electrodeposition is a thin film technique that is based on liquid electrolytes, the fibrous nature of RCF tends to frail apart upon contact with this liquid during the electrodeposition process as compared to its rigid substrate counterparts reported in literature before such as glass and stainless steel. As RCF continuously moves and its unsteady during the electrodeposition process, the deposition of Bi_2Te_3 is not uniform throughout the fibre strands of RCF. Moreover, each stack of RCF is made of many layers of RCF which tends to come apart after being in contact with the liquid electrolyte, thereby Bi_2Te_3 is deposited only on one layer of RCF which becomes too thin for the electrical resistivity characterisation. Due to the thin and porous nature of one layer of RCF, the probes of the Hall Measurement system does not sit on the fibres and tends to tear through the fibre, thereby giving inaccurate electrical resistivity readings.

Thus, due to the nature of the RCF fibres, this chapter will explore an alternative technique to fabricate RCF thermoelectric composite. Most research in the field of thermoelectrics have focused on utilising thin film techniques such as electrodeposition (Burton et al., 2017), sputtering (Goto et al., 2017; Shang et al., 2017), thermal evaporation (D. H. Kim et al., 2013; Takashiri and Hamada, 2016) and etc. Thin film thermoelectric materials are known to achieve

This chapter has been published in Journal of Cleaner Production, DOI: 10.1016/j.jclepro.2018.05.238

higher values of figure of merit, ZT due to the quantum confinement effect on the carriers (Han and Chung, 2013a). However, thin film techniques are expensive, time consuming and energy intensive which makes it unfriendly for a large scale thermoelectric energy conversion. In most cases the thickness of the thin films range from a few nanometres up to micrometres which is insufficient to sustain a substantial temperature difference. Thus, it is vital to find a technique that is able to fabricate thermoelectric materials that are capable of performing on a larger scale of thermal to electrical energy conversion.

In this study, the inorganic thermoelectric filler chosen is n-type bismuth telluride (Bi_2Te_3) as it has the highest reported value of ZT≈ 1.4 at a room-temperature range of 200–400 K which is suitable for portable power generators (Venkatasubramanian et al., 2001; Kusagaya and Takashiri, 2015).

Although telluride based thermoelectric materials especially Bi_2Te_3 have high figure of merit (ZT) values at approximately 1.2 (Venkatasubramanian et al., 2001; Wang et al., 2015) showing superior thermoelectric properties and hold dominant market share in thermoelectric industry, it is imperative to develop alternative materials because of the rare nature of availability and toxicity of tellurium (Zhao et al., 2008). Bi_2S_3 has recently acquired much attention due to its environmentally friendly nature and its potential application in the thermoelectric field (Yu et al., 2011; Wong et al., 2016). Bismuth sulphide (Bi_2S_3) is promising in this respect because of its abundance, high Seebeck coefficient and low thermal conductivity. Thus, the second part of this study also investigated the thermoelectric properties of Bi_2S_3 coated RCF composite.

In this chapter, the RCF composites are formed using a polymeric binder, Acrodur DS 3530 and thermoelectric fillers (Bi_2Te_3 and Bi_2S_3) using a hot compression technique. This work focused on the optimisation of the concentration of thermoelectric fillers and its subsequent

effect on the thermoelectric properties (i.e. Seebeck coefficient, electrical resistivity and power factor) for both Bi_2Te_3 and Bi_2S_3. The morphological, structural and also the thermal stability of the RCF composites filled with Bi_2Te_3 and Bi_2S_3 were also demonstrated in this chapter.

5.2 Results and discussion

5.2.1 Thermoelectric properties of RCF composites coated with Bi_2Te_3 and Bi_2S_3

Seebeck coefficient, electrical resistivity and power factor of RCF composites coated with different weight concentrations of Bi_2Te_3 are shown in **Figure 5- 1** to **Figure 5- 3**. Based on **Figure 5- 1**, it is observed that RCF composites exhibit weakly p-type thermoelectric nature with a Seebeck coefficient of + 4.52 µV/K. Upon the incorporation of Bi_2Te_3 coating on the surface of RCF composite, the thermoelectric nature of the RCF composite shifts from p-type to n-type as shown in **Figure 5- 1**. This shift is because Bi_2Te_3 used in this study is an n-type semiconductor which is electron dominant (J. Kim et al., 2013).

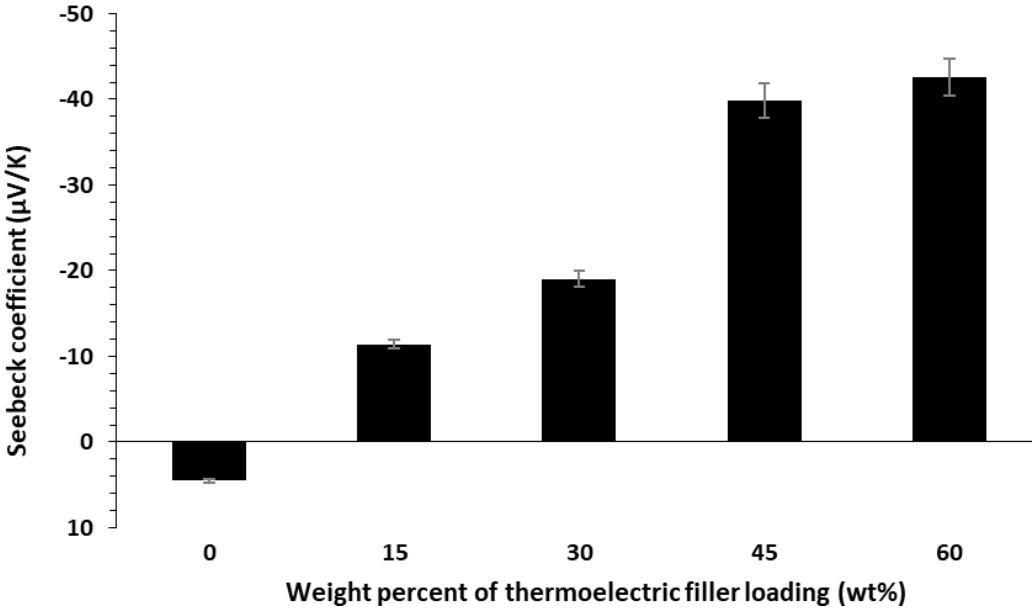


Figure 5- 1: The effect of Bi_2Te_3 concentrations on the Seebeck coefficient of RCF-Bi_2Te_3 and RCF-Bi_2S_3 composites.

As both Seebeck coefficient, α and electrical resistivity, ρ are highly dependent on the carrier concentration, their changes are well explained by the variation in carrier concentration as shown in Eq 5.1 and Eq 5.2 below (Li et al., 2011).

$$\rho = \frac{1}{ne\mu} \qquad (5.1)$$

$$\alpha = \pm\frac{k_B}{e}\left[(r+2) + \ln\frac{2(2\pi m^* k_B T)^{3/2}}{h^3 n}\right] \qquad (5.2)$$

Where, n is carrier concentration, e is the electron charge ($1.60217662 \times 10^{-19}$ coulombs), μ is carrier mobility, k_B is Boltzmann's constant, r is the scattering factor, m^* is effective mass, h is Planck constant and T is temperature.

The thermoelectric performance of the composite was measured using a simplified formula of ZT which is power factor (PF) with the formula shown in Eq 5.3 below (Kim and Oh, 2009):

$$PF = \frac{\alpha^2}{\rho} \qquad (5.3)$$

PF is calculated based on measured values of α and ρ.

The Seebeck coefficient was observed to increase linearly with respect to the concentration of Bi_2Te_3 particles as shown in as shown in **Figure 5- 1**. An increase in Seebeck coefficient is a result of decreased carrier concentration as deduced from Eq (5.2) above. The carrier concentration for RCF-Bi_2Te_3 composites decreased by approximately 68% from 1.43×10^{21} cm^{-3} (15 wt%) to 4.50×10^{20} cm^{-3} (60 wt%) as shown in **Table 5- 1**. RCF are inherently conductive due to its carbon content, thus having a higher amount of carrier concentrations. However, with the increased incorporation of semiconductors such as Bi_2Te_3 on RCF, the composites transition from a conductive to semi-conductive nature, suppressing the density of its carrier concentration. A similar increase in Seebeck coefficient was observed by Li et al., as

the concentration of Bi_2Te_3 was increased in a high performance $(Bi_2Te_3)_x(Sb_2Te_3)_{1-x}$ bulk materials due to the large difference in electronegativity between Bi and Te atoms that suppresses the carrier concentrations (Li et al., 2011).

Table 5- 1: Carrier concentration and carrier mobility of RCF-Bi_2Te_3 composites with respect to increasing Bi_2Te_3 concentrations

Weight percent of thermoelectric filler (wt%)	Carrier Concentration (cm^{-3})	Carrier Mobility ($cm^2V^{-1}s^{-1}$)
15	1.43×10^{21}	4.62×10^{-3}
30	9.70×10^{20}	7.31×10^{-3}
45	6.01×10^{20}	1.27×10^{-2}
60	4.50×10^{20}	1.49×10^{-2}

The influence of the concentration of Bi_2Te_3 particles on the electrical resistivity of the composites are shown in **Figure 5- 2**. All RCF-Bi_2Te_3 composites exhibited higher electrical resistivity than that of pure RCF composites (0 wt%), attributed to the decreased carrier concentrations. RCF-Bi_2Te_3 depicted an initial increase in resistivity from 0 wt% to 15 wt% as shown in **Figure 5- 2**, this behaviour is observed due to the presence of polymeric binder in the coating on the surface of RCF. However a decreasing trend in the electrical resistivity was observed from 15 wt% to 45 wt%, this decreasing trend is owing to the improvement in carrier mobility by one order from 4.62×10^{-3} $cm^2V^{-1}s^{-1}$ (15 wt%) to 1.27×10^{-2} $cm^2V^{-1}s^{-1}$ (45 wt%) in RCF-Bi_2Te_3 as shown in **Table 5- 1**. Bi_2Te_3 particles acts as a bridge between the haphazardly arranged RCF strands, thereby improving carrier mobility and facilitating electron transport throughout the composite.

Rahman et al. also observed a similar decrease in electrical resistivity when poly(3.4-ethylenedioxythiophene)-poly(styrenesulfonate) (PEDOT: PSS) was doped with Bi_2Te_3 until a maximum of 0.8 wt% whereby beyond that there was intense dopant aggregation that resulted in increased electrical resistivity (Rahman et al., 2015). However increased loading of Bi_2Te_3 beyond 45 wt%, exhibited a detrimental effect on the electrical resistivity as shown in **Figure 5- 2**, due to the continuous decrease in carrier concentration and only marginal improvement in carrier mobility at higher loadings.

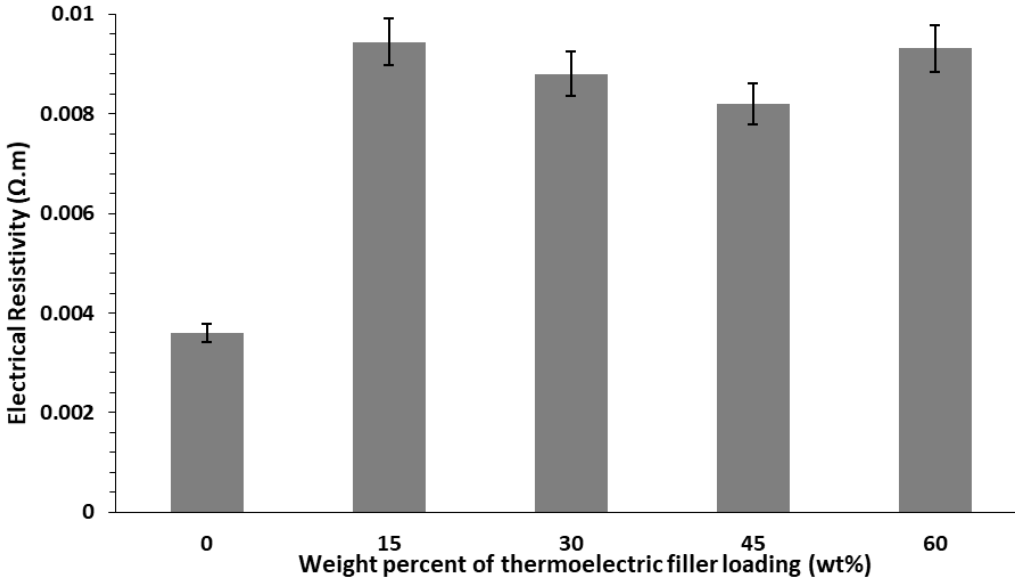


Figure 5- 2: The effect of Bi_2Te_3 concentrations on the electrical resistivity of RCF-Bi_2Te_3 composites

The power factor of RCF-Bi_2Te_3 composites is calculated taking into consideration both Seebeck coefficient and electrical resistivity and the corresponding values is as shown in **Figure 5- 3**. The highest power factor obtained for RCF-Bi_2Te_3 is 0.194 $\mu WK^{-2}m^{-1}$ at 45 wt% of thermoelectric filler loading.

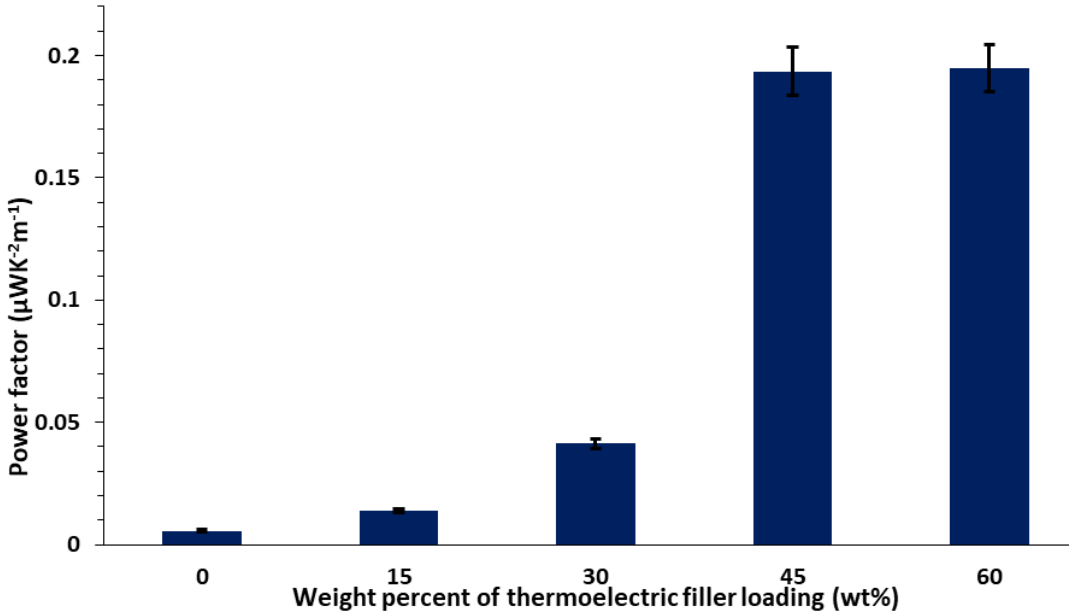


Figure 5- 3: The effect of Bi_2Te_3 concentrations on the power factor of RCF-Bi_2Te_3 composites

Although, telluride based thermoelectric materials especially Bi_2Te_3 have high ZT values at approximately 1.2 showing superior thermoelectric properties and hold dominant market share in thermoelectric industry, it is imperative to develop alternative materials because of the rare nature of availability and toxicity of tellurium (Zhao et al., 2008). Bi_2S_3 has recently acquired much attention due to its environmentally friendly nature and its potential application in the thermoelectric field (Yu et al., 2011). Thus, the second part of this study will investigate the thermoelectric properties of Bi_2S_3 coated RCF composite. Bi_2S_3 is also an n-type semiconductor similar to that of Bi_2Te_3 in which the majority carrier is electron dominant. Seebeck coefficient, electrical resistivity and power factor of RCF composites coated with different concentrations of Bi_2S_3 are shown in **Figure 5- 4** to **Figure 5- 6**.

The Seebeck coefficient of RCF composites changed from + 4.52 µV/K to -45.36 µV/K (15 wt%) as shown in **Figure 5- 4**. It is also important to emphasize that the Seebeck coefficient of RCF-Bi_2S_3 composites are higher than that of RCF-Bi_2Te_3 composites at all loadings. This

is because Bi_2S_3 has intrinsic carrier concentrations around 10^{18} cm^{-3} that are two orders lower than that of Bi_2Te_3 (10^{20} cm^{-3}) (Rowe, 1995). As shown in Eq (5.2), Seebeck coefficient is highly affected by the concentration of carriers, thus the difference in carrier concentration between Bi_2S_3 and Bi_2Te_3 plays a significant role on the obtained Seebeck coefficient values.

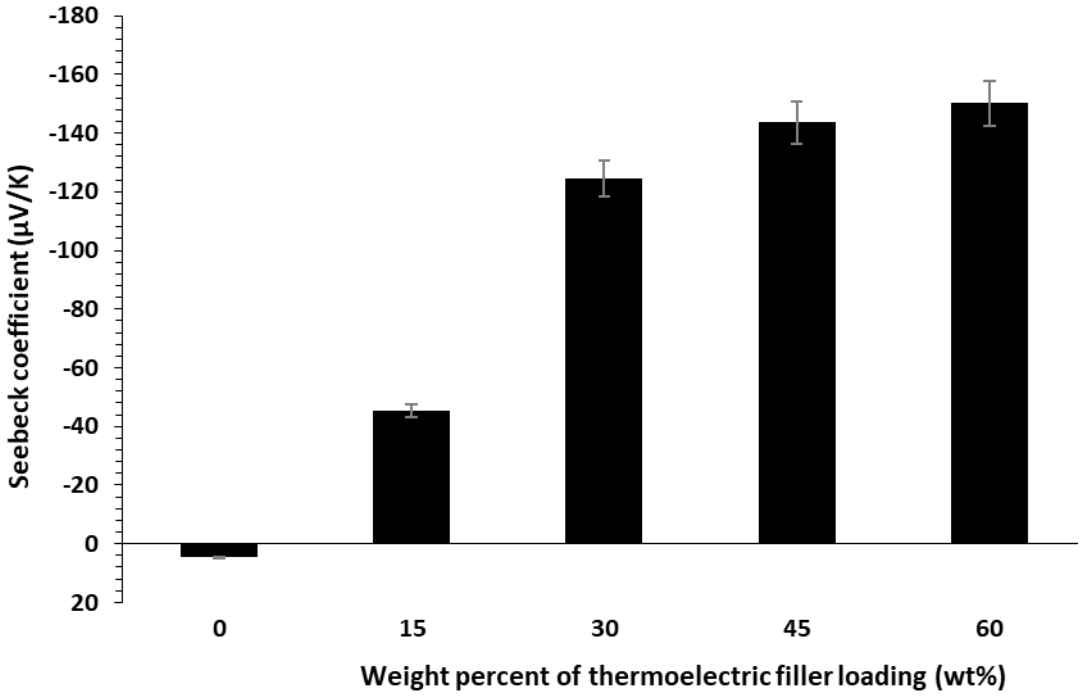


Figure 5- 4: The effect of Bi_2S_3 concentrations on the Seebeck coefficient of RCF-Bi_2S_3 composites

As shown in **Figure 5- 4**, there is a continuous improvement in the Seebeck coefficient of RCF composites with increasing concentrations of Bi_2S_3 until 45 wt%. However as that of Bi_2Te_3, the rise in Seebeck coefficient is no longer significant beyond 45 wt% indicating saturation. The Seebeck coefficient of 45 wt% is -143.56 µV/K and at 60 wt% is -150.12 µV/K, indicating that further increment in the concentration beyond 45 wt% does not contribute greatly to increasing its thermoelectric performance.

On the other hand, electrical resistivity is also seen to initially increase from 0 wt% to 15 wt% upon incorporation of Bi_2S_3 due to change from a conductive nature of RCF to a semiconducting nature of the fillers as shown in **Figure 5- 5**. From 15 wt% to 30 wt%, there is

a decrease in the electrical resistivity due to a one order improvement in its carrier mobility as shown in **Table 5- 2**. A similar behaviour was also observed with RCF-Bi_2Te_3 composites due to facilitation of facile electron transport in between the fibre strands due to Bi_2S_3.

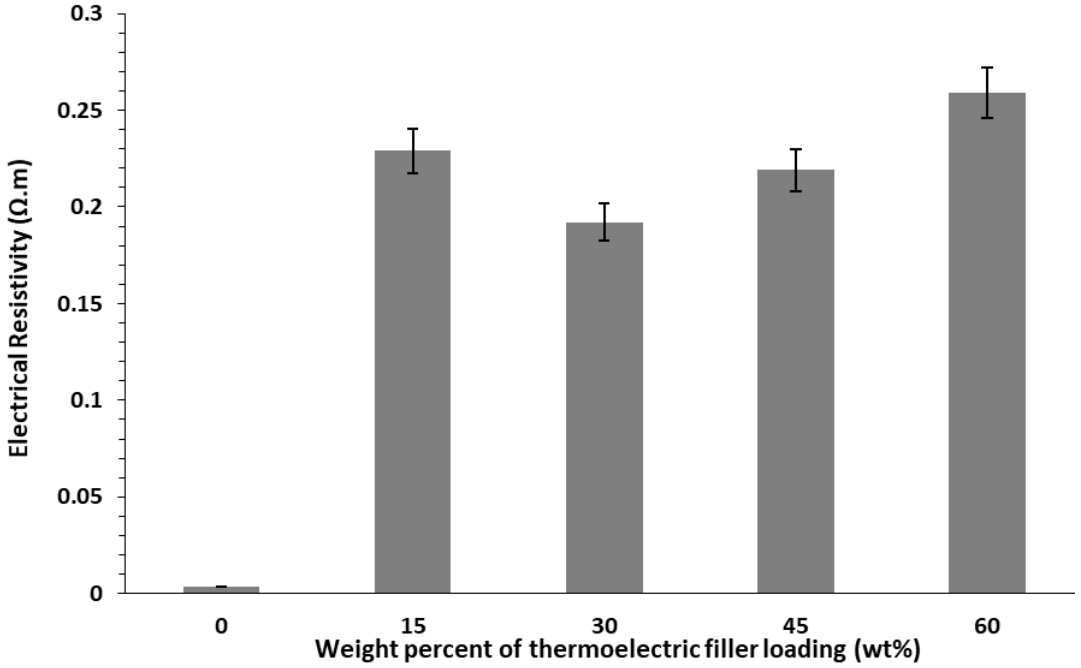


Figure 5- 5: The effect of Bi_2S_3 concentrations on the electrical resistivity of RCF-Bi_2S_3 composites.

Table 5- 2: Carrier concentration and carrier mobility of RCF-Bi_2S_3 composites with respect to increasing Bi_2S_3 concentrations.

Weight percent of thermoelectric filler (wt%)	Carrier Concentration (cm^{-3})	Carrier Mobility ($cm^2V^{-1}s^{-1}$)
15	4.59×10^{19}	5.94×10^{-3}
30	9.55×10^{18}	3.40×10^{-2}
45	4.27×10^{18}	6.67×10^{-2}
60	3.27×10^{18}	7.37×10^{-2}

It is also observed that RCF-Bi_2S_3 displayed a higher resistivity than that of RCF-Bi_2Te_3 at all concentrations. The highest resistivity of RCF-Bi_2S_3 composites is 0.259 Ω.m whereas that of Bi_2Te_3 is 0.009 Ω.m which renders Bi_2S_3 more resistive than that of Bi_2Te_3. This is due to the difference in band gap between these two semiconductors, Bi_2S_3 has a band gap of 1.3 eV (Liufu et al., 2007) whereas that of Bi_2Te_3 is at 0.17 eV (Kioupakis et al., 2010). Band gap influences the intrinsic carrier concentration and this relationship is described in Eq (5.4) below:

$$n_i = \sqrt{N_C N_V}\exp(^{-E_g}/_{2kT}) \quad (5.4) \quad \text{(F.Keuch, 2015)}$$

Where, n_i is the intrinsic carrier concentration, N_C is the effective density of states in the conduction band, N_V is the effective density of states in the valence band, E_g is the band gap, k is Boltzmann's constant and *T* is temperature. Therefore, as the band gap of Bi_2S_3 is wider than that of Bi_2Te_3, intrinsically it has fewer carrier concentrations thus rendering it more resistive.

Taking into consideration both Seebeck coefficient and electrical resistivity, the power factor of Bi_2S_3 composites is highest at 0.094 $\mu WK^{-2}m^{-1}$ for 45 wt% thermoelectric filler loading as shown in **Figure 5- 6**. The environmentally friendly RCF-Bi_2S_3 thermoelectric composite is approximately 52% lower in power factor compared to that of RCF-Bi_2Te_3 composites. The lower thermoelectric performance of RCF-Bi_2S_3 composites could be attributed to its resistivity. The highest resistivity of RCF-Bi_2S_3 composites is 0.259 Ω.m whereas that of RCF-Bi_2Te_3 is 0.009 Ω.m, which renders Bi_2S_3 more resistive than Bi_2Te_3. The resistive nature of Bi_2S_3 is due to its low carrier concentrations, the lowest carrier concentration of RCF-Bi_2S_3 composite is 3.27×10^{18} cm^{-3} whereas that of RCF-Bi_2Te_3 composite is 4.50×10^{20} cm^{-3} which is approximately two orders lower than Bi_2Te_3. However, the naturally low carrier

concentrations in Bi_2S_3 resulted in higher Seebeck coefficient of RCF-Bi_2S_3 (-150.1 µV/K) composites approximately 252% higher than that of RCF-Bi_2Te_3 (-42.6 µV/K) composites.

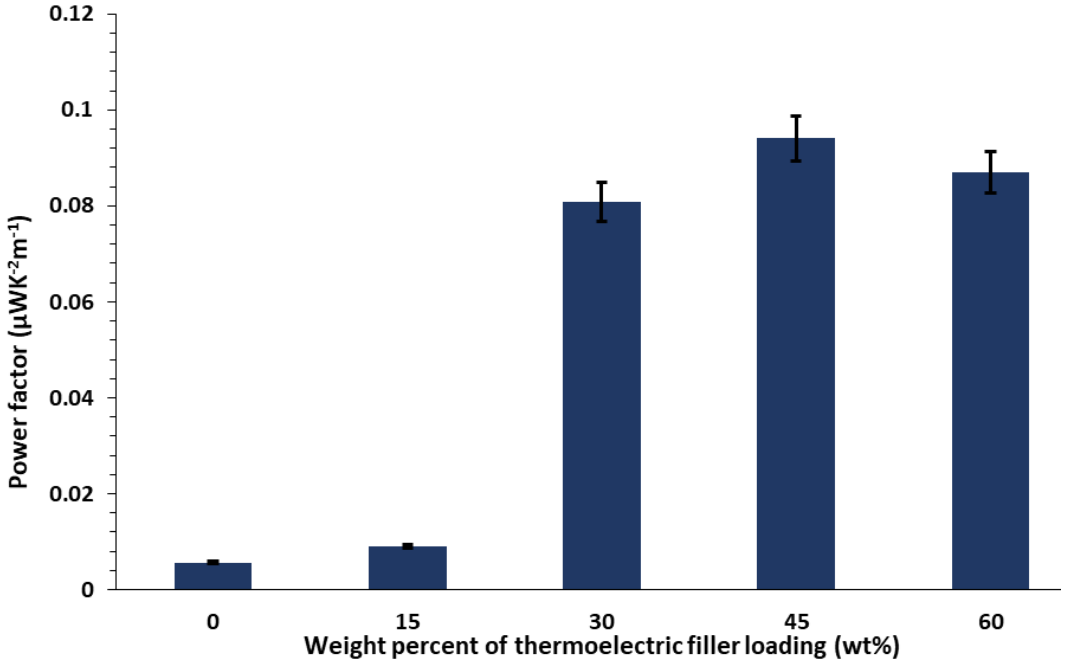


Figure 5- 6: The effect of Bi_2S_3 concentrations on the power factor of RCF-Bi_2S_3 composites

5.2.2 FESEM and EDX study of RCF-Bi_2Te_3 and RCF-Bi_2S_3 composites

Figure 5- 7 shows the effect of increasing Bi_2Te_3 concentration within the RCF-Bi_2Te_3 composite. At lower loadings of Bi_2Te_3 in the composite (15 and 30 wt%), it can be seen that there is not sufficient amount of Bi_2Te_3 particles filling up the gaps between the RCF strands and having low coverage, thus leading to lower power factors as observed in **Figure 5- 3**. However, from 45 wt% onwards there seems to be sufficient Bi_2Te_3, no visible gaps were observed in the FESEM image and reaching saturation at 60 wt%. Thus, the values of power factors plateaued with no further increase.

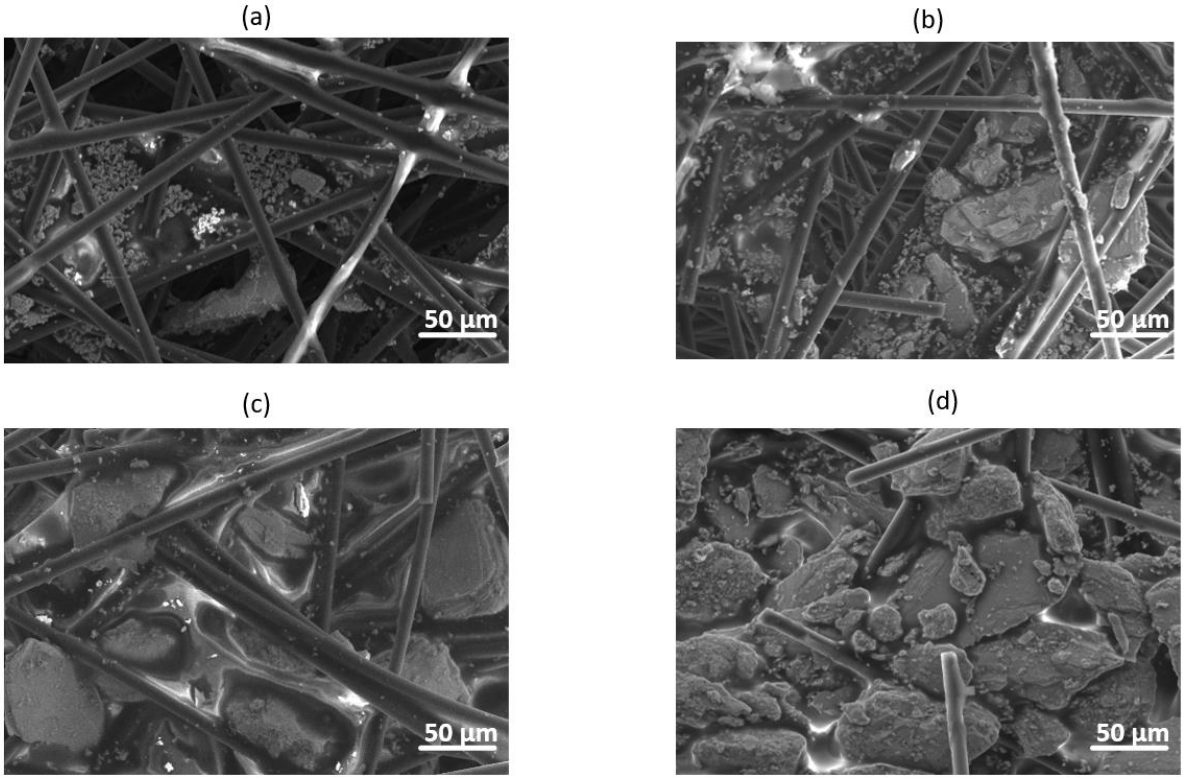


Figure 5- 7: FESEM surface images of RCF-Bi_2Te_3 composite at (a) 15 wt% (b) 30 wt% (c) 45 wt% (d) 60 wt% of Bi_2Te_3.

Referring to **Figure 5- 8**, it can be seen that the gap between RCF strands have been filled with Bi_2S_3 particles from 30 wt% onwards which corresponds to increasing power factor values as shown in **Figure 5- 6**. At 60 wt% (see **Figure 5- 8 (d)**), it can be seen that the RCF strands are

not completely embedded in the polymer-Bi_2S_3 coating when compared to **Figure 5- 8 (a-c)**. There is a separation of polymeric binder phase from the Bi_2S_3 particles perhaps owing to the high loading of Bi_2S_3 particles, thus also leading to a drop in power factor as shown in **Figure 5- 6**.

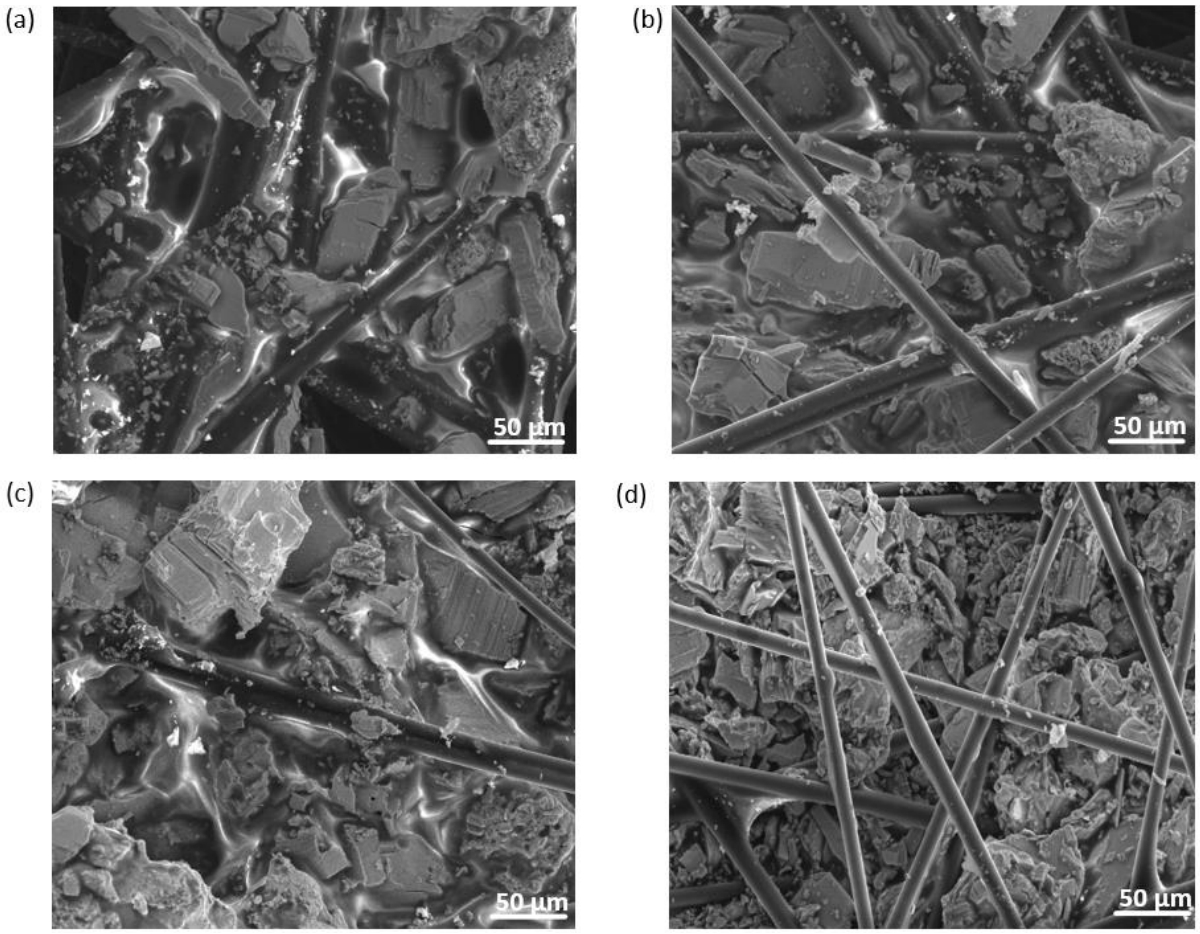


Figure 5- 8: FESEM surface images of RCF-Bi_2S_3 composite at (a) 15 wt% (b) 30 wt% (c) 45 wt% (d) 60 wt% of Bi_2S_3.

With optimum loading of Bi_2Te_3 and Bi_2S_3, the thermoelectric fillers acts as a bridge to fill in the gaps between the RCF strands. Thus, allowing for better transport of electrons across the composite which is proven by the improved carrier mobility in both RCF-Bi_2Te_3 composites and RCF-Bi_2S_3 composites as shown in **Table 5- 1** and **Table 5- 2** respectively.

Thus, it can be concluded based on surface morphology and thermoelectric properties, 45 wt% is the highest optimum filler concentration for both RCF-Bi_2Te_3 and RCF-Bi_2S_3 composite.

5.2.3 XRD Analysis of of RCF-Bi_2Te_3 and RCF-Bi_2S_3 composites

The obtained XRD patterns for RCF-Bi_2Te_3 composites from X-ray diffractometer are shown in **Figure 5- 9**. The following 12 diffraction peaks of Bi_2Te_3 located at 2θ, 17.59°, 27.78°, 37.93°, 40.42°, 41.27°, 44.64°, 50.37°, 54.00°, 57.17°, 62.31°, 66.04° and 67.17° with orientations of (006), (015), (1010), (0111), (110), (0015), (205), (1016), (0210), (1115), (0120) and (125) were observed for all the RCF-Bi_2Te_3 composite.

At all loadings of Bi_2Te_3, all 12 diffraction peaks mentioned above are observed. These values are in good agreement with standard data of Joint Committee on Powder Diffraction Standards (PDF 00-015-0863) data and the observed peak positions are consistent with the rhombohedral structure of Bi_2Te_3 and observed peak positions are represented by their corresponding Miller indices in the spectra. The most prominent peak is (015) was used to calculate all XRD related parameters for RCF-Bi_2Te_3 composites.

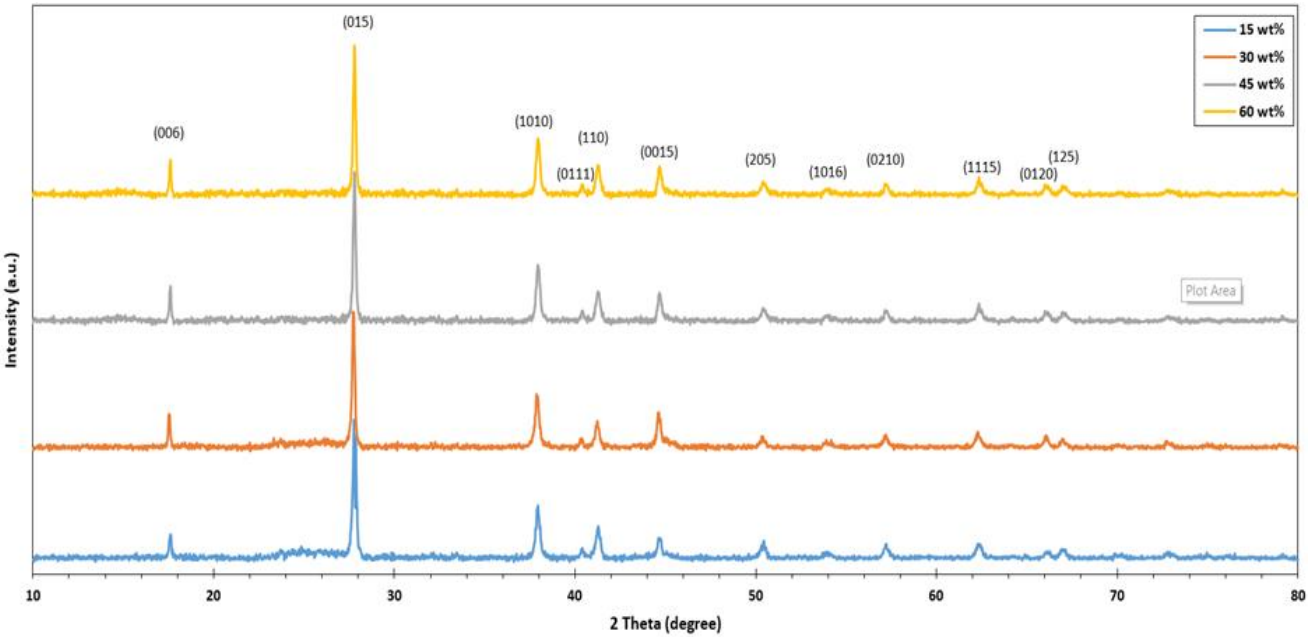


Figure 5- 9: XRD patterns of RCF-Bi_2Te_3 composite at different Bi_2Te_3 loadings

With increasing amount of Bi_2Te_3, there is a slight increase in crystallite size from 15 wt% to 30 wt%, however from 30 wt% to 60 wt% the crystallite size is kept constant around 46-47 nm as shown in **Table 5- 3**. This is probably because at 15 wt% there is not much thermoelectric particles, thus the x-rays may have passed through the gaps between the RCF strands hence recording a smaller crystallite size. However, from 30 wt% there is an increased packing of Bi_2Te_3 particles on the surface of RCF thus resulting in a slightly larger crystallite size. In addition to the crystallite size, there is also a small decrease in the FWHM as shown in **Table 5- 3** values indicating slightly improved crystallinity with increasing incorporation of Bi_2Te_3 particles.

Table 5- 3: FWHM, crystallite size, microstrain and dislocation density of RCF-Bi_2Te_3 composite.

Bi_2Te_3 Concentrations (wt%)	**FWHM (radian)**	**Crystallite size, D (nm)**	**Microstrain (ε x 10^{-3}) (lines^{-2} m^{-4})**	**Dislocation density (δ x 10^{14}) (lines/m^2)**
15	0.0032	44.46	3.2	5.06
30	0.0031	46.74	3.1	4.58
45	0.0030	47.01	3.1	4.52
60	0.0031	45.69	3.2	4.79

A lower microstrain and dislocation density is commonly preferred in order to lower electrical resistivity values (Grasso et al., 2013; Jariwala et al., 2015). With increasing Bi_2Te_3 concentration, the microstrain and dislocation density is seen to have decreased from 15 wt% to 45 wt% as shown in **Table 5- 3**. The decreased microstrain and dislocation density is because Bi_2Te_3 particles filled in the gaps between RCF strands, which also led to a decrease in electrical resistivity as shown in **Figure 5- 2**. Beyond 45 wt%, the increased packing of Bi_2Te_3 particles results in the propagation of small micro cracks on the surface of the RCF-Bi_2Te_3 composite that may have resulted in increased dislocation density and microstrain with a corresponding increase in electrical resistivity at 60 wt%.

For the RCF-Bi_2S_3 composite, the XRD spectra is as shown in **Figure 5- 10.** The following 27 diffraction peaks of Bi_2S_3 was observed on all the RCF-Bi_2S_3 composite were located at 2θ, 15.75°, 17.62°, 22.43°,24.99°, 25.23°, 27.49°, 28.65°, 31.84°, 33.04°, 33.96°, 35.65°, 36.68°, 39.09°, 39.95°, 45.60°, 46.51°, 47.05°, 48.48°, 49.21°, 52.63°, 53.86°, 54.77°, 62.68°, 64.57°, 72.04°,73.05° and 76.21° with orientations of (200), (201), (202),(301),(103), (210), (112), (212), (013), (303), (402), (312), (410), (411), (020), (314), (511), (600), (512), (321), (610), (611), (711), (712), (606), (417) and (408).

At all loadings of Bi_2S_3, all 27 diffraction peaks mentioned above are observed. These values are in good agreement with standard data of Joint Committee on Powder Diffraction Standards (PDF 01-074-9437) data and the observed peak positions are consistent with the orthorhombic

structure of Bi_2S_3 and observed peak positions are represented by their corresponding Miller indices in the spectra. The most prominent peak is (301) was used to calculate all XRD related parameters for RCF-Bi_2S_3 composites.

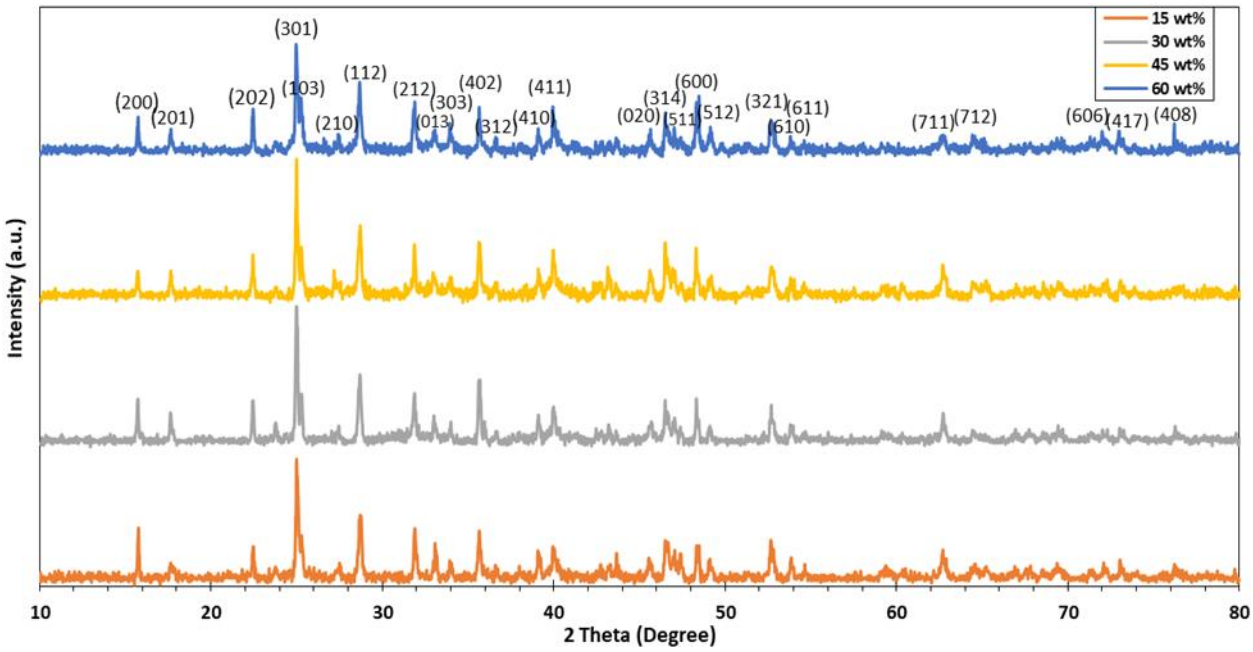


Figure 5- 10: XRD patterns of RCF-Bi_2S_3 composite at different Bi_2S_3 loadings

With increasing amount of Bi_2S_3, there is an increase in crystallite size from 15 wt% to 30 wt%, however, from 30 wt% to 45 wt% the crystallite size is kept constant around 52-53 nm as shown in **Table 5- 4**. This is probably because at 15 wt% there are not much thermoelectric particles, thus the x-rays may have passed through the gaps between the RCF strands hence recording a smaller crystallite size. However, from 30 wt% there is an increased packing of Bi_2S_3 particles on the surface of RCF thus resulting in a slightly larger crystallite size. In addition to the crystallite size, there is also a decrease in the FWHM as shown in **Table 5- 4** values indicating slightly improved crystallinity with increasing incorporation of Bi_2S_3 particles.

Table 5- 4: FWHM, crystallite size, microstrain and dislocation density of RCF-Bi_2S_3 composite.

Bi_2S_3 Concentrations (wt%)	**FWHM (radian)**	**Crystallite size, D (nm)**	**Microstrain (ε x 10^{-3}) ($lines^{-2}\,m^{-4}$)**	**Dislocation density (δ x 10^{14}) ($lines/m^2$)**
15	0.0031	45.69	3.50	4.79
30	0.0026	53.86	2.97	3.45
45	0.0027	52.14	3.08	3.68
60	0.0034	41.07	3.90	5.93

Similar to that of Bi_2Te_3, the microstrain and dislocation density as depicted in **Table 5- 4** decreased from 15 wt% to 30 wt% as Bi_2S_3 particles filled in the gaps between RCF strands that facilitated electron transport, thereby decreasing the electrical resistivity as shown in **Figure 5- 5**. From 45 wt% onwards owing to saturation there is a slight increase in the dislocation density and microstrain structurally which is reflected on the increase in electrical resistivity, however, there is still a continuity between the RCF strands and polymer-Bi_2S_3 coating as shown in **Figure 5- 8 (c)** thus still improving the power factors of the composite. However, at 60 wt% there is a significant increase in microstrain and dislocation density even higher than 15 wt%, due to the discontinuity that occur due to the separation of the polymeric phase from the Bi_2S_3 particles as shown in **Figure 5- 8 (d)**, thus leading to a significant increase in electrical resistivity and subsequent drop in power factor as shown in **Figure 5- 6**.

5.2.4 Thermal stability of RCF-Bi_2Te_3 and RCF-Bi_2S_3 composites

The thermal stabilities of both RCF-Bi_2Te_3 and RCF-Bi_2S_3 were evaluated using thermogravimetric analysis (TGA) and derivative thermogravimetric (DTG) studies. As thermoelectric composites are subjected to temperature differences, it is vital to determine the temperature range in which it is thermally stable.

The thermal stability of each constituent within the RCF-Bi_2Te_3 and RCF-Bi_2S_3 composite such as RCF, Bi_2Te_3, Bi_2S_3 and binder in the air are shown in **Figure 5- 11**. The polymeric binder experienced major degradation after 180 °C owing to the decomposition of some

polyester components such as CO, CO_2, CH_4, ethylene and acetylene (Khalfallah et al., 2014). The RCF started to degrade from 290-300 °C, owing to residual epoxy that may still be present on its strands from previous applications. Bi_2Te_3 particles exhibited a thermally stable behaviour until 400 °C, beyond 400 °C the particles experienced oxidation that results in a sharp weight gain as shown in **Figure 5- 11**. This weight gain was also observed by Brostow et al., that attributed it to the escape of tellurium due to its low vapour pressure and subsequent oxidation of bismuth at 400 °C (Brostow et al., 2012). On the other hand, Bi_2S_3 particles exhibited a thermally stable behaviour in air as depicted in **Figure 5- 11** until 530 °C, beyond that it experienced a slight oxidation (540 °C) (due to the oxidation of its main constituents such as Bi and Bi_2S_3 in the presence of oxygen in air (Rincbn, 1996), a subsequent mass degradation (from 600 °C to 800 °C) and oxidized (beyond 800 °C).

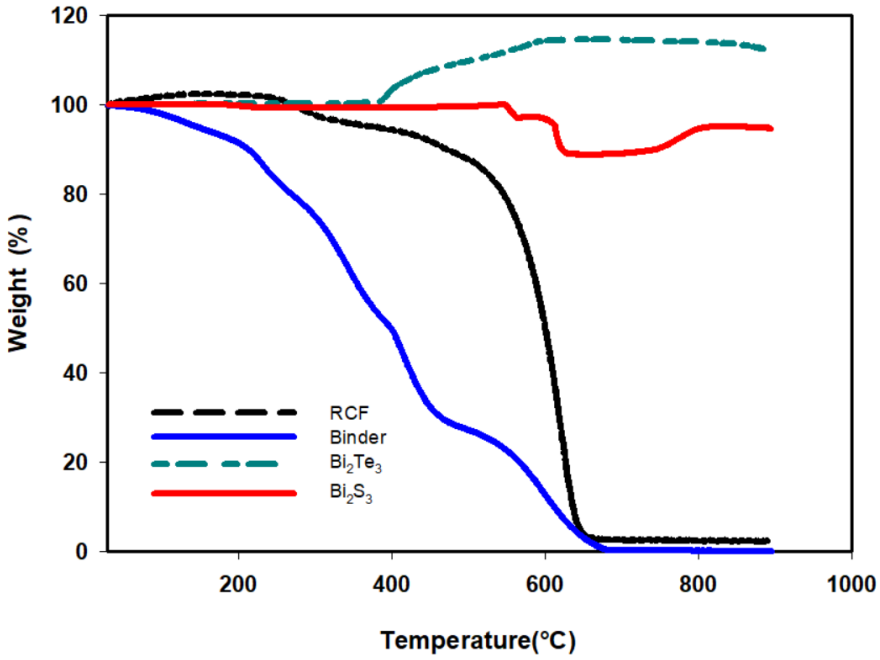


Figure 5- 11: TGA of constituents in RCF-Bi_2Te_3 and RCF-Bi_2S_3 composite.

Based on **Figure 5- 12**, increasing amounts of Bi_2Te_3 had no significant change on the onset degradation temperature (T_{onset}) at 5% weight loss. T_{onset} varied slightly from 308.46°C (at lower loadings of Bi_2Te_3) to 316.2°C (at higher loadings of Bi_2Te_3). All RCF-Bi_2Te_3 composites started degrading at around 294 °C as shown in **Figure 5- 12**. The composites tend to degrade at 294 °C owing to thermal degradation of the polymeric constitutes in the composite such as residual epoxy resin on RCF from recycling and the cured Acrodur binder. A similar thermal degradation around 300 °C were observed by (Khalili et al., 2017) and (Khalfallah et al., 2014) for palm empty fruit bunch and flax fibre composites with Acrodur binders.

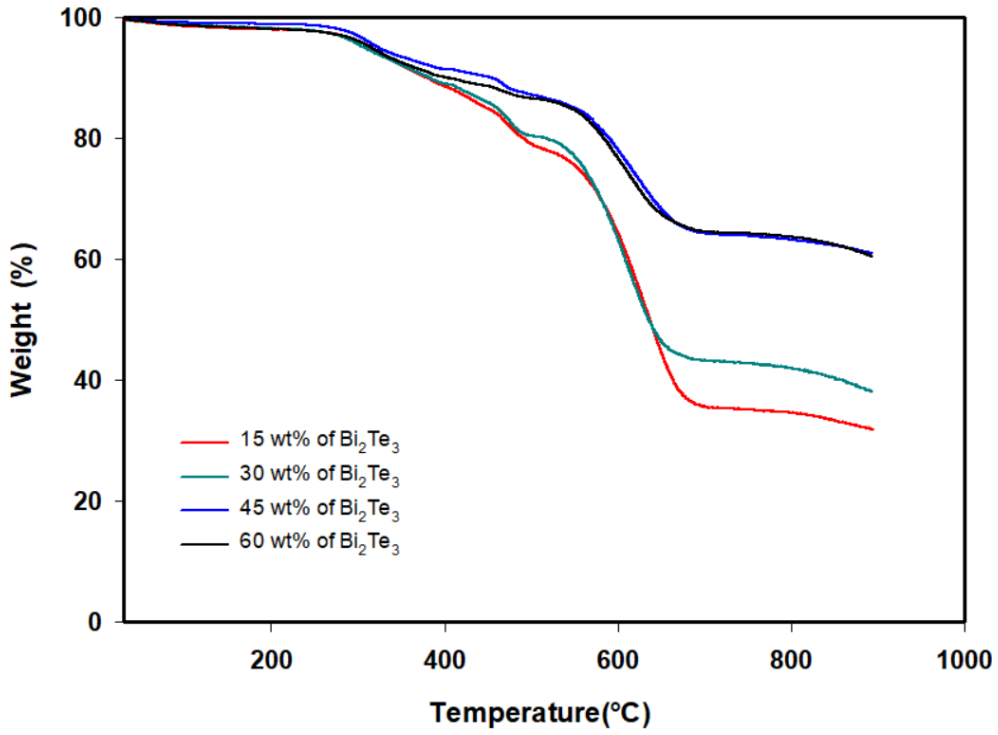


Figure 5- 12: TGA analysis of RCF-Bi_2Te_3 composite.

A similar pattern in the TGA analysis was also observed for RCF-Bi_2S_3 composites until 45 wt% as shown in **Figure 5- 13**. The T_{onset} varied from 306.13°C to 316.32°C, at 60 wt% there is a slight drop in T_{onset} at 308.86°C. At 60 wt%, due to high filler loading resulting in the

separation of the polymer from the thermoelectric fillers, may have resulted in lower thermal stabilities. As that of RCF-Bi_2Te_3 composites, all RCF-Bi_2S_3 composites exhibited degradation from approximately 294°C.

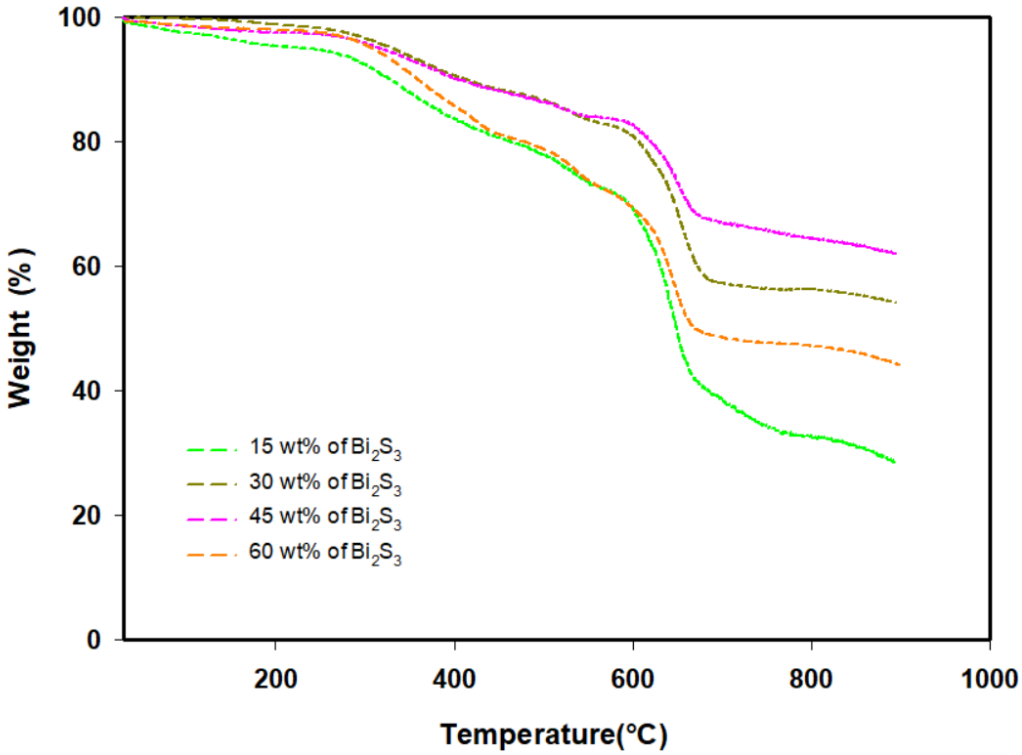


Figure 5- 13: TGA analysis of RCF-Bi_2S_3 composite.

Figure 5- 14 shows the DTG curve of all the constituents in the RCF-Bi_2Te_3 and RCF-Bi_2S_3 composites. It can be seen that both RCF and binder started degrading at lower temperatures around 250 °C due to the lower thermal stability of polymeric compounds. On the other hand, both the thermoelectric fillers only exhibited degradation after 400 °C and 480 °C for Bi_2Te_3 and Bi_2S_3 respectively. The maximum degradation temperature (T_{max}) for all the constituents is at 600 °C as shown in **Figure 5- 14**.

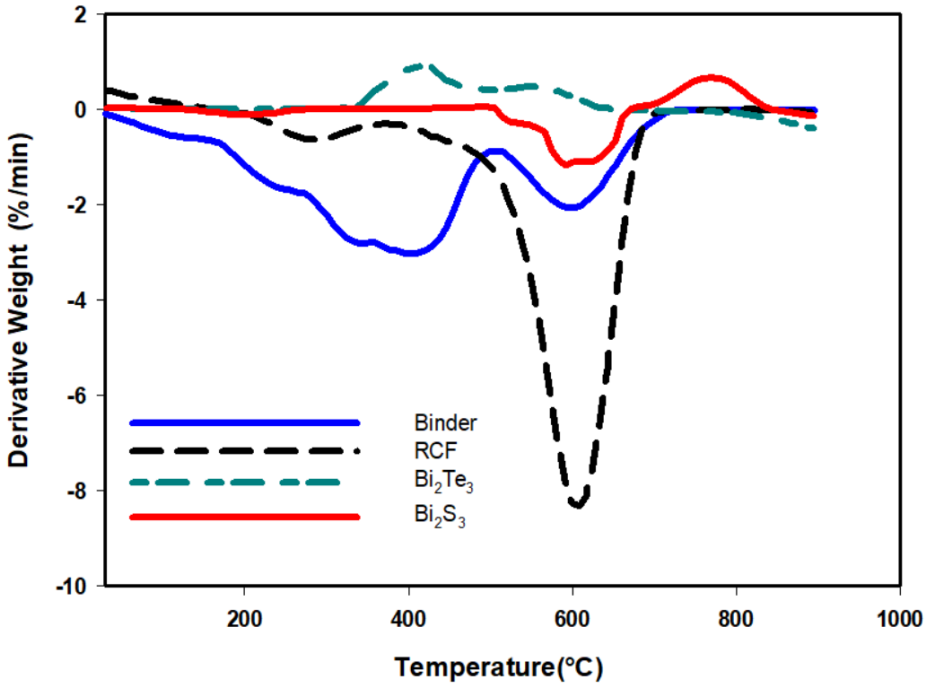


Figure 5- 14: DTG curves of constituents in RCF-Bi_2Te_3 and RCF-Bi_2S_3 composites.

For all RCF-Bi_2Te_3 composites, the T_{max} is at approximately 602.19 °C as shown in **Figure 5-15**. There was no significant improvement in T_{max} with respect to increasing concentration of Bi_2Te_3. With increasing amount of Bi_2Te_3, the mass loss rate reduced as Bi_2Te_3 has higher thermal stability as mentioned before. However at higher loadings of 45 wt% and 60 wt% though it has lower mass loss rate, it seems to have plateaued as shown in **Figure 5- 15**.

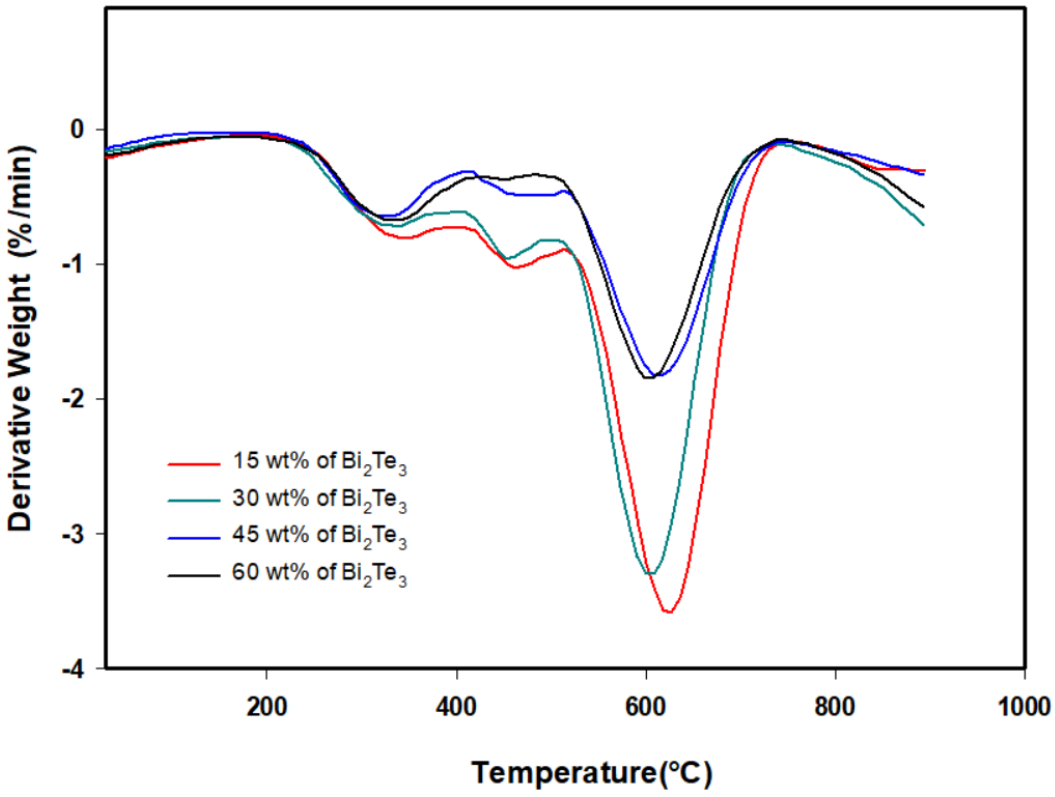


Figure 5- 15: DTG curve of RCF-Bi_2Te_3 composites.

All RCF-Bi_2S_3 composites exhibited a T_{max} of approximately 638.88 °C as shown in **Figure 5-16**. However, there was insignificant improvement in T_{max} with respect to increasing concentration of Bi_2S_3. The mass loss rate reduced with increasing concentrations of Bi_2S_3 until 45 wt%. However, at 60 wt%, the mass loss rate was accelerated showing that it becomes less thermally unstable owing to the agglomeration and separation from the polymeric binder.

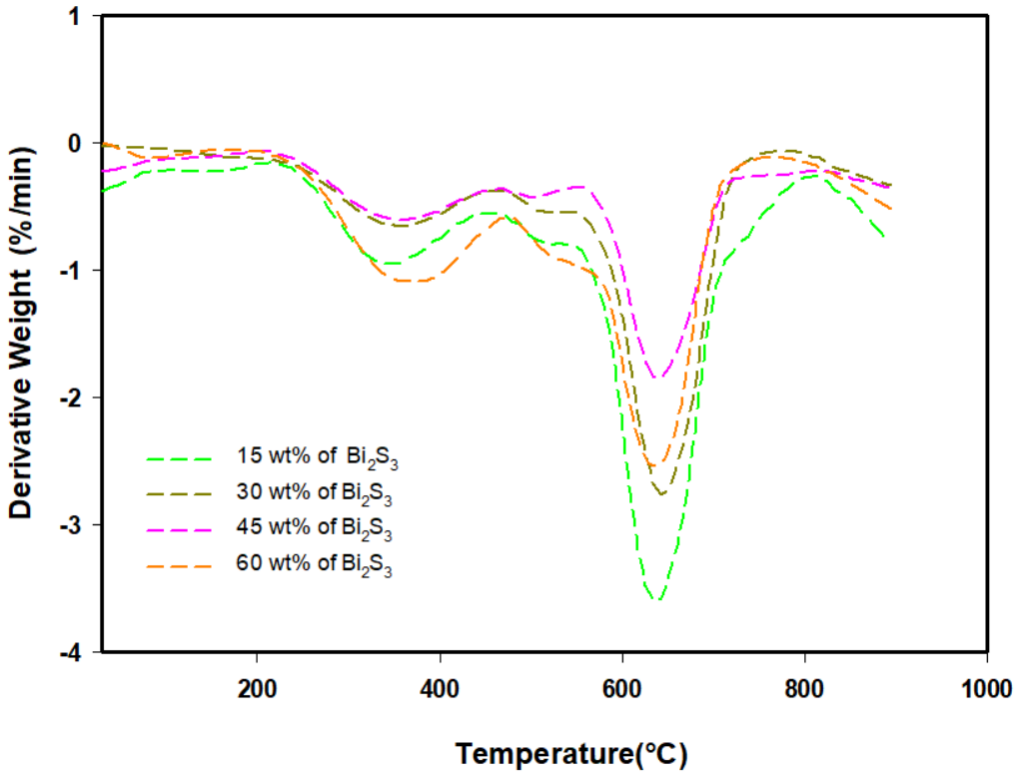


Figure 5- 16: DTG curve of RCF-Bi_2S_3 composites.

5.3 Summary

The power factor of RCF composite improved by 34 and 17 times upon the incorporation of thermoelectric fillers (Bi_2Te_3 and Bi_2S_3) respectively. The power factor of RCF composites increased with respect to increasing concentrations of Bi_2Te_3 and Bi_2S_3, however, it reached a maximum of 0.194 $\mu WK^{-2}m^{-1}$ and 0.094 $\mu WK^{-2}m^{-1}$ for RCF-Bi_2Te_3 and RCF-Bi_2S_3 at 45 wt% respectively. The thermoelectric properties of both RCF-Bi_2Te_3 and RCF-Bi_2S_3 were remarkably higher than that of bare RCF as proved by the Seebeck coefficient, electrical resistivity, carrier property measurement, FESEM, EDX, XRD and TGA analysis. This is because the presence of the thermoelectric fillers not only suppressed the carrier concentration but also improved the carrier mobility between the gaps of RCF strands, thus enhancing its thermoelectric capabilities.

The environmentally friendly RCF-Bi_2S_3 thermoelectric composite is approximately 52% lower in power factor compared to that of RCF-Bi_2Te_3 composites due to its innate material property that has high electrical resistivity. The thermoelectric composites are proven to be a cost effective and feasible alternative to producing efficient thermoelectric materials, which is economically efficient as well as industrially scalable with minimal infrastructure requirement.

Chapter 6: Effect of Multi Walled Carbon Nanotubes (MWCNTs) on the Thermoelectric Properties of Recycled Carbon Fibre Composites with Bi_2Te_3 and Bi_2S_3 Thermoelectric Fillers

6.1 Introduction

In this chapter, the third aim of the study is addressed, whereby the improvement of the thermoelectric properties of RCF-Bi_2Te_3 and RCF-Bi_2S_3 composites was achieved through the doping of MWCNTs. The power factors of bulk thermoelectric materials can be further increased through synthesising of low dimensional nanostructures from bulk materials or by introducing low dimensional nanoscale phase into the bulk thermoelectric matrix (Cui et al., 2007; Zhao et al., 2005). In the past several metallic dopants such as lead (Zhou et al., 2014), copper (Lim et al., 2016), silver (Yang et al., 2006) and etc. have been used to alter the power factors of bulk bismuth chalcogenides. However as metallic elements are electrical conductors with a high carrier concentrations which results in excellent electrical properties, however they have a zero band gap nature resulting in poor Seebeck coefficient as well as high thermal conductivity values which is detrimental to its thermoelectric properties. On the other hand, the electrical conductive nature of MWCNTs varies from metallic to semiconducting depending on its chirality, thus effectively it can be used as a dopant with semiconductor band gap(Hewitt and Carroll, 2014). Due to this semiconducting capability, MWCNTs also exhibits higher Seebeck coefficient (40 μV/K) that is approximately 8-10 times higher than the Seebeck coefficient of metal such as lead, silver and copper while exhibiting exceptional electrical conductivity. MWCNTs are also light weight, flexible and environmentally friendly dopants compared to its metallic counter parts. MWCNTs are renowned for their superior electrical, mechanical and thermal properties and is being widely used as a dopant to enhance mechanical

properties and enhance/optimise electrical conductivity (K. T. Kim et al., 2013; Q. Zhang et al., 2017).

Low dimensional nanostructures is thought to improve the power factor of bulk thermoelectric materials through a mechanism called energy filtering (Narducci et al., 2012). In the presence of these nanostructures, carriers with low kinetic energy are stopped by the energy barrier at nanostructure boundaries while high energy carrier pass through them (Zou et al., 2001). Thus, Seebeck coefficient and electrical conductivity can be simultaneously improved in the presence of this potential barrier eliminating low energy carriers and increasing carrier mobility (Ma et al., 2017).

In this chapter, to further improve the electrical conductivity and the subsequent thermoelectric properties of RCF composites, this chapter investigated and studied the effect of varying concentration of MWCNT on the thermoelectric properties of RCF-Bi_2Te_3 and RCF-Bi_2S_3 composites. The morphological, structural and also the thermal stability of the MWCNT doped RCF-Bi_2Te_3 and RCF-Bi_2S_3 composites will also be studied in this chapter.

6.2 Results and discussion

6.2.1 Effect of MWCNT on the thermoelectric properties of RCF-Bi_2Te_3 and RCF-Bi_2S_3

The Seebeck coefficient, electrical resistivity, and power factor of RCF-Bi_2Te_3 composites with varying concentrations of MWCNT are shown in **Figure 6- 1** to **Figure 6- 3**. As shown in **Figure 6- 1**, there is a significant rise in the Seebeck coefficient of RCF-Bi_2Te_3 composites upon the incorporation of MWCNTs. The introduction of nanostructures such as MWCNTs at appropriate concentrations into bulk materials such as Bi_2Te_3 is known to introduce interfaces

within the thermoelectric matrix (Kumar et al., 2017). At these interfaces within the bulk of thermoelectric matrix, low energy carriers are filtered out and high energy charge carriers travel through the conducting path within the composites (Dresselhaus et al., 2007). Seebeck coefficient of RCF-Bi_2Te_3 composites improved by approximately 80 % at the optimum doping of 0.10 wt% of MWCNT compared to that of 0 wt% of MWCNT due to the above mentioned filtering effect.

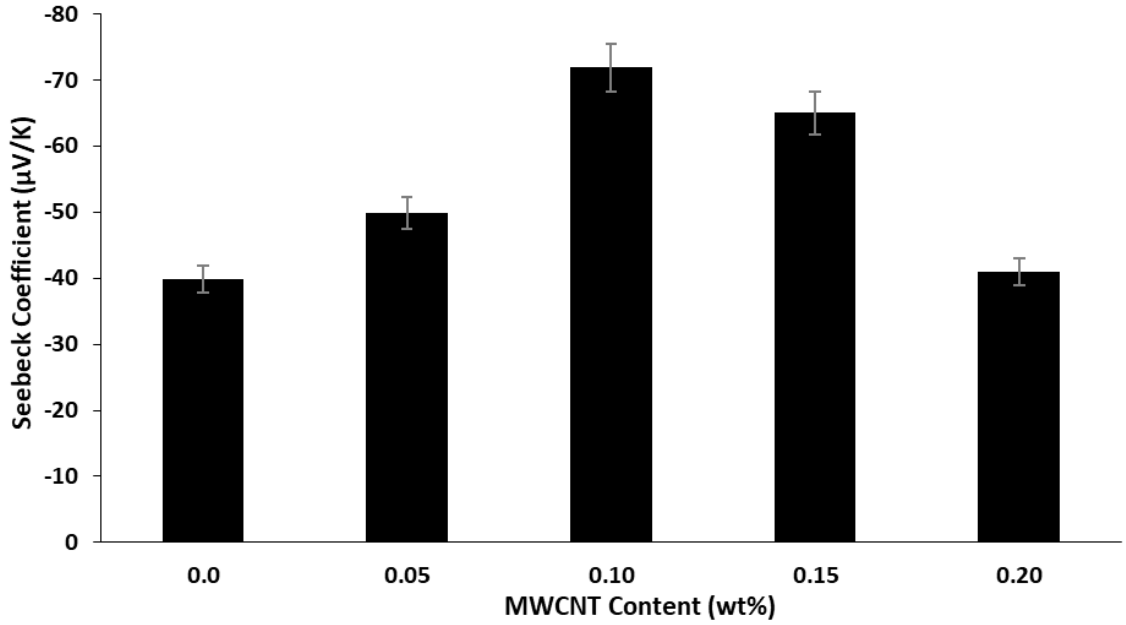


Figure 6- 1: The effect of MWCNT concentrations on the Seebeck coefficient of RCF-Bi_2Te_3 composites.

Table 6- 1: Carrier concentration and carrier mobility of RCF-Bi_2Te_3 composites with respect to increasing MWCNT concentrations.

MWCNT Concentrations (wt%)	Carrier Concentration (cm^{-3})	Carrier Mobility ($cm^2V^{-1}s^{-1}$)
0.00	6.01×10^{20}	1.27×10^{-2}
0.05	0.83×10^{20}	10.30×10^{-2}
0.10	0.96×10^{20}	13.20×10^{-2}
0.15	1.29×10^{20}	11.30×10^{-2}
0.20	2.10×10^{20}	6.75×10^{-2}

Doping with MWCNTs resulted in decreased carrier concentrations as shown in **Table 6- 1**, thus leading to increased Seebeck coefficient of RCF-Bi_2Te_3 composites upon MWCNT doping. This decreased carrier concentration is a validation of the energy filtering effect mechanism occurring within the composite by removing low energy carriers. In addition to decreased carrier concentrations, as MWCNTs are highly conductive, they have high levels of carrier mobility (Ebbesen et al., 1996; Zhang et al., 2012), which also contributes majorly to the improvement of charge transport within the inorganic matrix (Bi_2Te_3) and a non-conducting polymer matrix (polymeric binder) that led to higher Seebeck coefficients.

However at higher concentrations of MWCNT's (0.15 wt% and 0.20 wt%) as shown in **Figure 6- 1**, there was a gradual decrease in its Seebeck coefficient with the subsequent increase in carrier concentrations as shown in **Table 6- 1**. As MWCNTs are p-type with Seebeck coefficients normally in the range of +40-50 μV/K (Yu et al., 2008), the drop in Seebeck coefficient at higher concentrations of MWCNTs may be due to the dominating p-type doping effect over the n-type Bi_2Te_3 particles (Bark et al., 2013). At higher concentrations, MWCNT

may be playing the role of impurity and preventing Bi_2Te_3 particles from connecting with each other. A similar doping effect that decreased Seebeck coefficient of Bi_2Te_3 at higher concentration of carbon nanotubes was also observed and reported by Bark et al. using MWCNT (Bark et al., 2013), Zhang et al. using single wall carbon nanotubes (SWCNTs)(Zhang et al., 2012) and Lognone and Gascoin using MWCNTs on n-type $Bi_2Te_{2.4}Se_{0.6}$ (Lognone and Gascoin, 2015).

As illustrated in **Figure 6- 2**, the electrical resistivity of RCF-Bi_2Te_3 composites was seen to decrease with increasing concentrations of MWCNTs. Though there was an 86 % decrease in carrier concentrations upon the incorporation of 0.05 wt% MWCNTs when compared to 0 wt% MWCNT as shown in **Table 6- 1**, this did not result in an increase in the electrical resistivity. This is because of the massive improvement in carrier mobility as shown in **Table 6- 1** (711 % improvement) that was brought about by the presence of MWCNTs in the RCF-Bi_2Te_3 composites. The continuous decrease of resistivity with increasing amount of MWCNTs is because MWCNTs are thought to form conducting channels to transport electrons between Bi_2Te_3 particles and the insulating polymer. A decreasing trend of electrical resistivity was observed from 0.05 to 0.15 wt% of MWCNT, the resistivity of the RCF-Bi_2Te_3 composite was reduced by approximately 40 % at 0.10 wt% of MWCNT. However at 0.20 wt% of MWCNT, a slight increase in resistivity (3.27% increase compared to 0.15 wt% of MWCNT) but still lower than that of 0 wt% MWCNT is observed as it is plausible that at larger concentrations MWCNT may play the role of impurities that prevent Bi_2Te_3 particles from connecting with each other resulting in decreased carrier mobility (Bark et al., 2013).

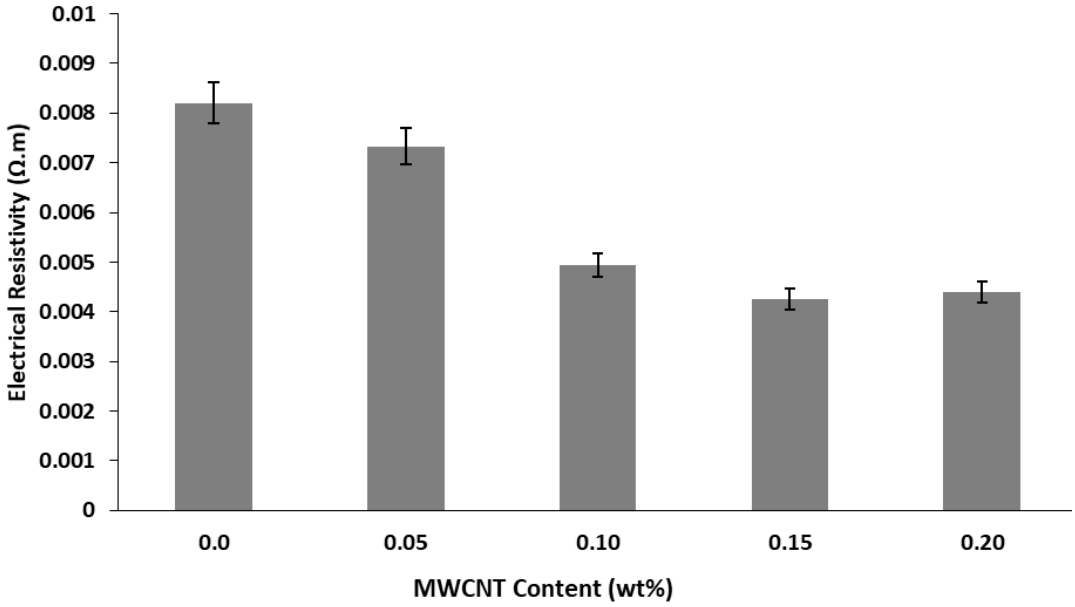


Figure 6- 2: The effect of MWCNT concentrations on the electrical resistivity of RCF-Bi_2Te_3 composites.

Most research work pertaining CNT-Bi_2Te_3 composite was fabricated via ball milling/mechanical alloying complemented with spark plasma sintering reported an increase in the electrical resistivity of Bi_2Te_3 alloy upon the incorporation of MWCNT (K. T. Kim et al., 2013; Kim et al., 2015b; Lognone and Gascoin, 2015; Ren et al., 2013; Yeo and Oh, 2014; Zhang et al., 2012). This increase in resistivity maybe due to the defects introduced on carbon nanotubes during the milling process that may have altered its conductive networks (Lognone and Gascoin, 2015). On the other hand, few studies have reported a decrease in electrical resistivity upon incorporation of MWCNTs in Bi_2Te_3 alloys. These few research works incorporated MWCNT into Bi_2Te_3 alloy using ultrasonic (Bark et al., 2013; Pang et al., 2013), hydrothermal(Kumar et al., 2017) and electrodeposition (Xu and Wang, 2013a, 2013b) and all of them reported a decrease in the electrical resistivity of Bi_2Te_3 alloy composites similar to that observed in this study.

The power factor as shown in **Figure 6- 3**, is one of the most important factors that monitor thermoelectric properties. The power factor of RCF-Bi_2Te_3 composites increased by a staggering 75- 440 % upon the varying incorporation of MWCNTs. The power factor was observed to increase from 0 wt% to 0.10 wt% of MWCNT, and then gradually decrease from 0.15 wt% to 0.20 wt% of MWCNT. The increase in power factor was greatly contributed by both the enhanced electrical conductivity and Seebeck coefficient upon the incorporation of MWCNT from 0.05 wt% to 0.15 wt% of MWCNT. This may have resulted from the energy filtering effect at MWCNT/Bi_2Te_3 and also MWCNT/insulating polymer interfaces that forms potential barriers that allow only carriers with energy to pass, thus increasing the mean carrier energy in the flow. This proposed phenomena is supported by the drastic decrease in carrier concentration while the carrier mobility increased parabolically as shown in **Table 6- 1**. A similar observation was made by Du et al. (Du et al., 2012b) in which a simultaneous improvement in Seebeck coefficient and electrical conductivity was reported due to inclusion of graphene that induced the energy filtering effect.

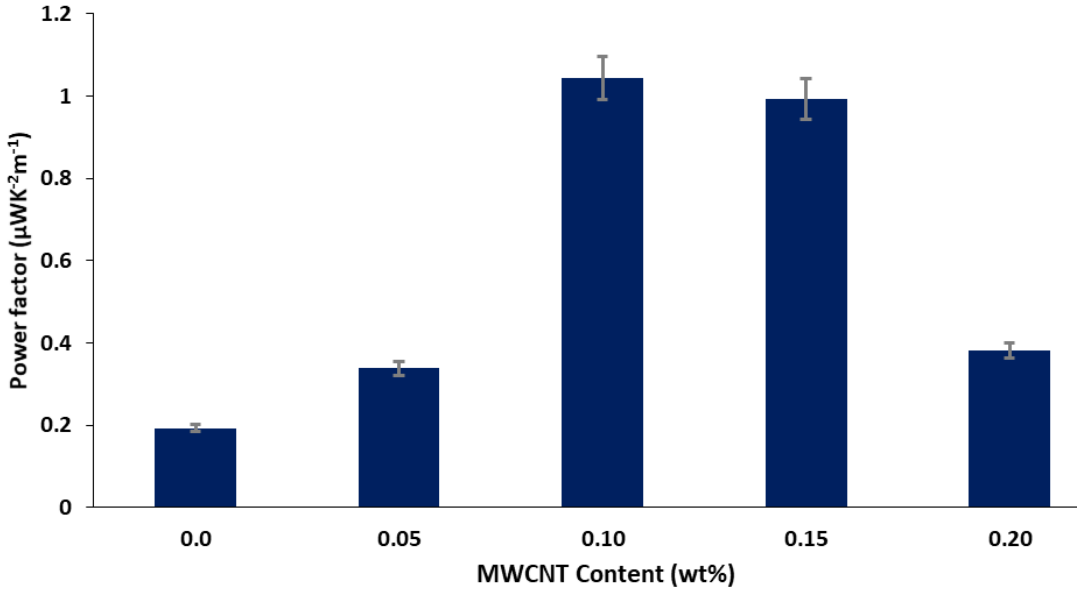


Figure 6- 3: The effect of MWCNT concentrations on the power factor of RCF-Bi_2Te_3 composites.

Although Bi_2S_3-CNT hybrid structures were used in enhancing the energy storage of lithium-ion batteries (Ni et al., 2014; Yang et al., 2016; Zhao et al., 2014), to the best of author's knowledge, no studies have been reported in literature thus far on the thermoelectric properties of Bi_2S_3-CNT composites.

The Seebeck coefficient, electrical resistivity and power factor of RCF-Bi_2S_3 composites with varying concentrations of MWCNT are shown in **Figure 6- 4** to **Figure 6- 6**. As shown in **Figure 6- 4**, the Seebeck coefficient of RCF-Bi_2S_3 composites were seen to show an increasing trend upon the incorporation of MWCNTs until 0.10 wt% of MWCNT. The Seebeck coefficient of RCF-Bi_2S_3 composites doped with 0.10 wt% of MWCNT was 33 % higher than 0 wt% of MWCNT coefficient. A similar increase in Seebeck coefficient was also observed with RCF-Bi_2Te_3 composites doped with MWCNT explained previously. The incorporation of MWCNTs within the RCF-Bi_2S_3 composites introduced two interfaces: (a) MWCNT/Bi_2S_3 interface and (b) MWCNT/insulating polymer. These interfaces are thought to induce an energy filtering effect that form potential boundaries that are capable of filtering out lower energy carriers while higher energy carriers are allowed to pass through them thus increasing mean energy of carriers in the path (Kumar et al., 2017; Narducci et al., 2012). The decrease in carrier concentrations (by 87 %) and the improvement in carrier mobility (by 3618 %) as shown in **Table 6- 2** could be attributed to the energy filtering mechanism.

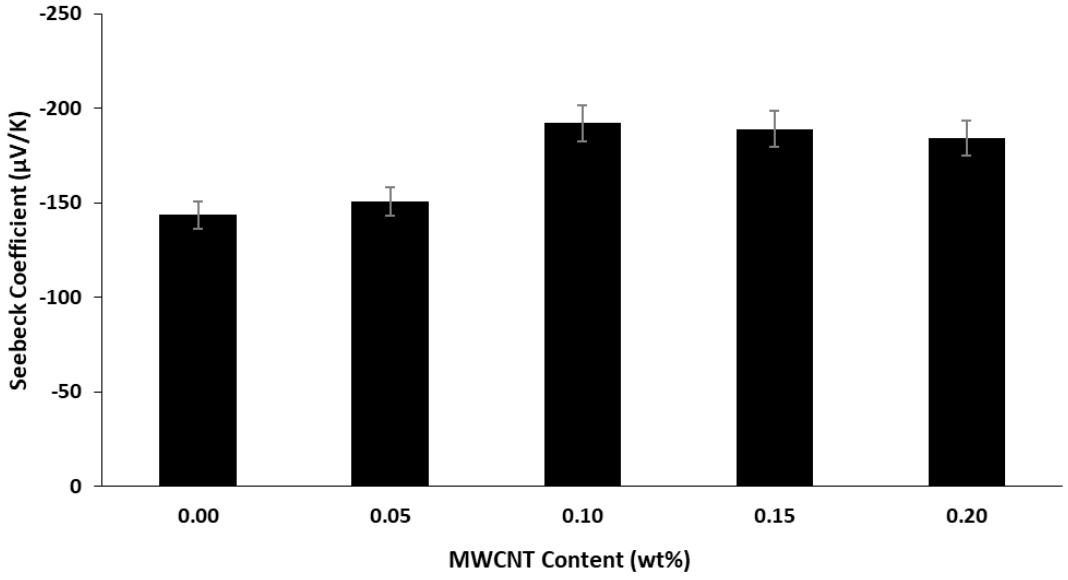


Figure 6- 4: The effect of MWCNT concentrations on the Seebeck coefficient of RCF-Bi_2S_3 composites.

Table 6- 2: Carrier concentration and carrier mobility of RCF-Bi_2S_3 composites with respect to increasing MWCNT concentrations.

MWCNT Concentrations (wt%)	Carrier Concentration (cm^{-3})	Carrier Mobility ($cm^2V^{-1}s^{-1}$)
0	4.27×10^{18}	6.67×10^{-2}
0.05	4.07×10^{18}	22.7×10^{-2}
0.10	0.541×10^{18}	248×10^{-2}
0.15	0.543×10^{18}	273×10^{-2}
0.20	0.590×10^{18}	252×10^{-2}

However, at higher loadings of 0.15 wt% MWCNT and 0.20 wt% MWCNT, the Seebeck coefficient slowly decreased as shown in **Figure 6- 4**, perhaps owing to a dominant p-type doping effect of MWCNTs that increased carrier concentrations but also hindered its carrier mobility as shown in **Table 6- 2**. The energy filtering effect in most cases is only observed to be present at intermediate doping levels when the dopant is filling in interstitial spaces between

Bi_2S_3 particles and insulating polymer (Moriarty et al., 2012; Narducci et al., 2012). A similar decrease in Seebeck coefficient at higher loadings of MWCNT was also observed in RCF-Bi_2Te_3 composites mentioned above.

As depicted in **Figure 6- 5**, the electrical resistivity of RCF-Bi_2S_3 composites is seen to decrease upon the incorporation of MWCNTs at all concentrations however at higher loadings of 0.15 wt% and 0.20 wt% of MWCNT, the resistivity remained constant. The substantial improvement in carrier mobility at 0.15 wt% of MWCNT (by approximately 3992 %) has helped to reduce the electrical resistivity of RCF-Bi_2S_3 composites by approximately 81% when compared to 0 wt% of MWCNT. Although there was an 87 % decrease in carrier concentration as shown in **Table 6- 2**, the staggering improvement of 3992 % in carrier mobility helped to decrease the electrical resistivity by 81 %. A similar decrease in resistivity with increasing concentration of MWCNTs was also observed by Yu et al. (2008) and Moriarty et al. (2012) that doped a non-conducting polymer poly (vinyl acetate) (PVAc) with CNT (Moriarty et al., 2012; Yu et al., 2008). Both the cited studies mentioned that significant enhancement in electrical conductivity is plausible with MWCNT fillers as MWCNT forms conductive networks through the insulating polymer.

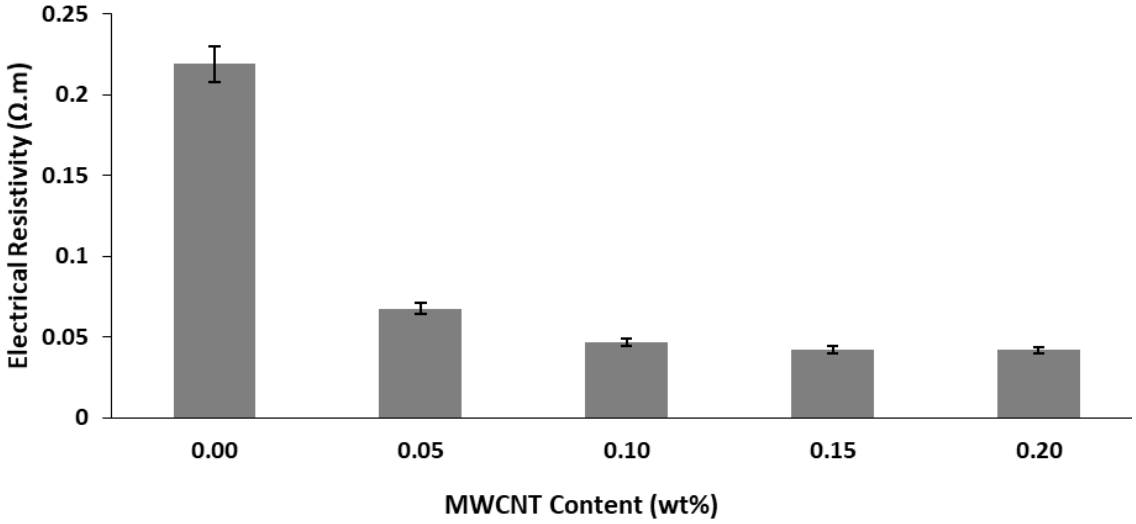


Figure 6- 5: The effect of MWCNT concentrations on the electrical resistivity of RCF-Bi_2S_3 composites.

The power factors of RCF-Bi_2S_3 composites doped with MWCNTs are as shown in **Figure 6-6**. The power factors of RCF-Bi_2S_3 composites improved by approximately 800 % upon incorporation of 0.15 wt% of MWCNT due to the simultaneous improvement in electrical conductivity and Seebeck coefficient. The power factor showed significant improvement from 0.05 to 0.10 wt% MWCNT, however from 0.15 to 0.20 wt% MWCNT there was minimal improvement. This indicates that at lower doping concentrations MWCNT can effectively enhance carrier transportation owing to the energy filtering mechanism. However at higher concentrations (0.20 wt%) of MWCNT an opposite effect is observed whereby the MWCNT acts as a degenerate (highly doped) semiconductor that exhibits a metallic behaviour. Thus, increasing its carrier concentration and leading to decreased Seebeck coefficient.

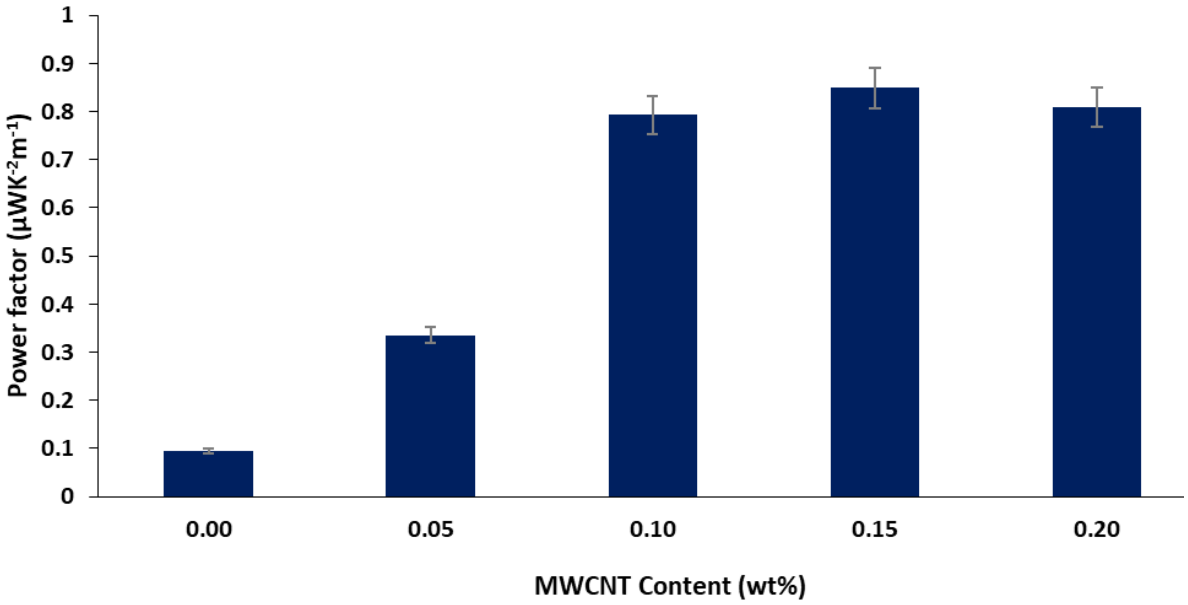


Figure 6- 6: The effect of MWCNT concentrations on the power factor of RCF-Bi_2S_3 composites.

Thus, the optimum doping level of MWCNT for RCF-Bi_2Te_3 and RCF-Bi_2S_3 is 0.10 wt% and 0.15 wt% of MWCNTs with a power factor of 1.044 and 0.849 $\mu WK^{-2}m^{-1}$ respectively.

6.2.2 Morphological study of RCF-Bi_2Te_3 and RCF-Bi_2S_3 composites doped with MWCNT

Figure 6- 7 shows the FESEM images of RCF-Bi_2Te_3 and RCF-Bi_2Te_3 doped with MWCNT composite. The granular structures shown in **Figure 6- 7 (b)** (as indicated by the blue arrows) are referring to the Bi_2Te_3 particles while the worm-like structures (as indicated by the yellow arrows) are referring to the MWCNTs. The MWCNTs are well dispersed in the polymer-Bi_2Te_3 matrix and filled the inter-spaces between Bi_2Te_3 particles leading to the formation of conductive network within the matrix. A similar morphology was also observed in the RCF-Bi_2S_3 composites doped with MWCNT as shown in **Figure 6- 8 (b)**. A higher magnification was used to study the interaction of MWCNT within the RCF-Bi_2S_3 composite as this was the lowest magnification that could clearly visualise the interaction. The MWCNTs is also seen to form a conductive pathway between the Bi_2S_3 particles within the insulating polymer matrix. The 81% reduction in electrical resistivity of MWCNT doped RCF-Bi_2S_3 composites mentioned in Section 6.2.1 is due to the presence of this conductive network.

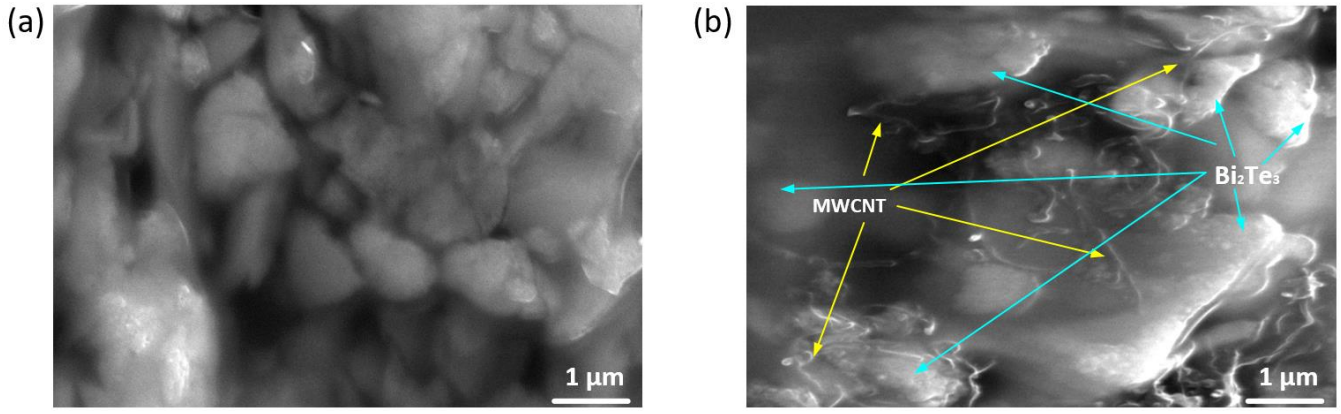


Figure 6- 7: FESEM images of (a) RCF-Bi_2Te_3 composite (b) RCF-Bi_2Te_3 doped with 0.05 wt% of MWCNT.

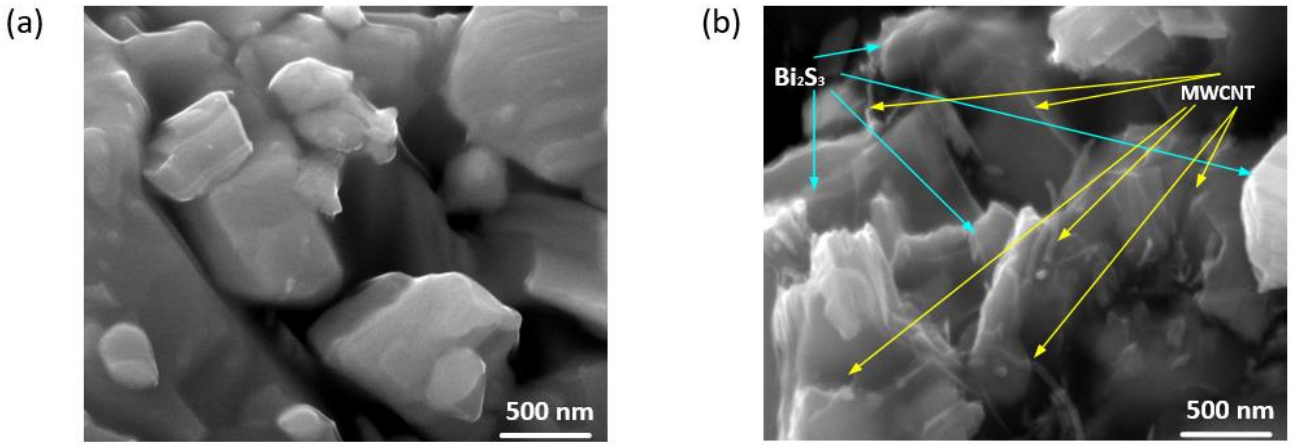


Figure 6- 8: FESEM images of (a) RCF-Bi_2S_3 composite (b) RCF-Bi_2S_3 doped with 0.05 wt% of MWCNT.

The morphology of RCF-Bi_2Te_3 composites with increasing concentrations of MWCNTs are shown in **Figure 6- 9**. The MWCNTs are seen to be well dispersed within the polymer-Bi_2Te_3 matrix at 0.05 and 0.10 wt% of MWCNT, however at 0.15 wt% it can be seen that MWCNTs are beginning to concentrate in a particular portion of the Bi_2Te_3 polymer matrix as highlighted by the yellow circle in **Figure 6- 9 (c)**. These concentration of MWCNTs may have possibly hindered carrier mobility leading to decreased carrier mobility as shown in **Table 6- 1**, thus leading to lower Seebeck coefficient at 0.15 wt% than that at 0.10 wt% of MWCNT. At 0.20 wt% of MWCNT as shown in **Figure 6- 9 (d)**, agglomerates of MWCNT (as highlighted by the yellow circle) is formed and there is also a separation of the granular structures of Bi_2Te_3 and the worm like structures of MWCNTs (as highlighted by the red circle). These agglomeration and separation could be the reason for the increased electrical resistivity at 0.20 wt% of MWCNT.

For the RCF-Bi_2S_3 composites doped with MWCNT as shown in **Figure 6- 10**, the MWCNT is seen to be well dispersed at all doping concentrations within the Bi_2S_3-polymeric matrix. Though no agglomerates of MWCNT was observed in the case of RCF-Bi_2S_3 composites, a

small well of concentrated MWCNT (as highlighted by the yellow circle) in **Figure 6- 10 (d)** was observed within the matrix at 0.20 wt%, which may have contributed to reduced mobility as shown in **Table 6- 2**. At higher concentrations of MWCNTs, it is observed that the power factors of both RCF-Bi_2Te_3 and RCF-Bi_2S_3 composites decreased, this could possibly be due the decreased interfaces between that of MWCNT and the thermoelectric particles, as shown in the FESEM images, which is responsible for the energy filtering mechanism.

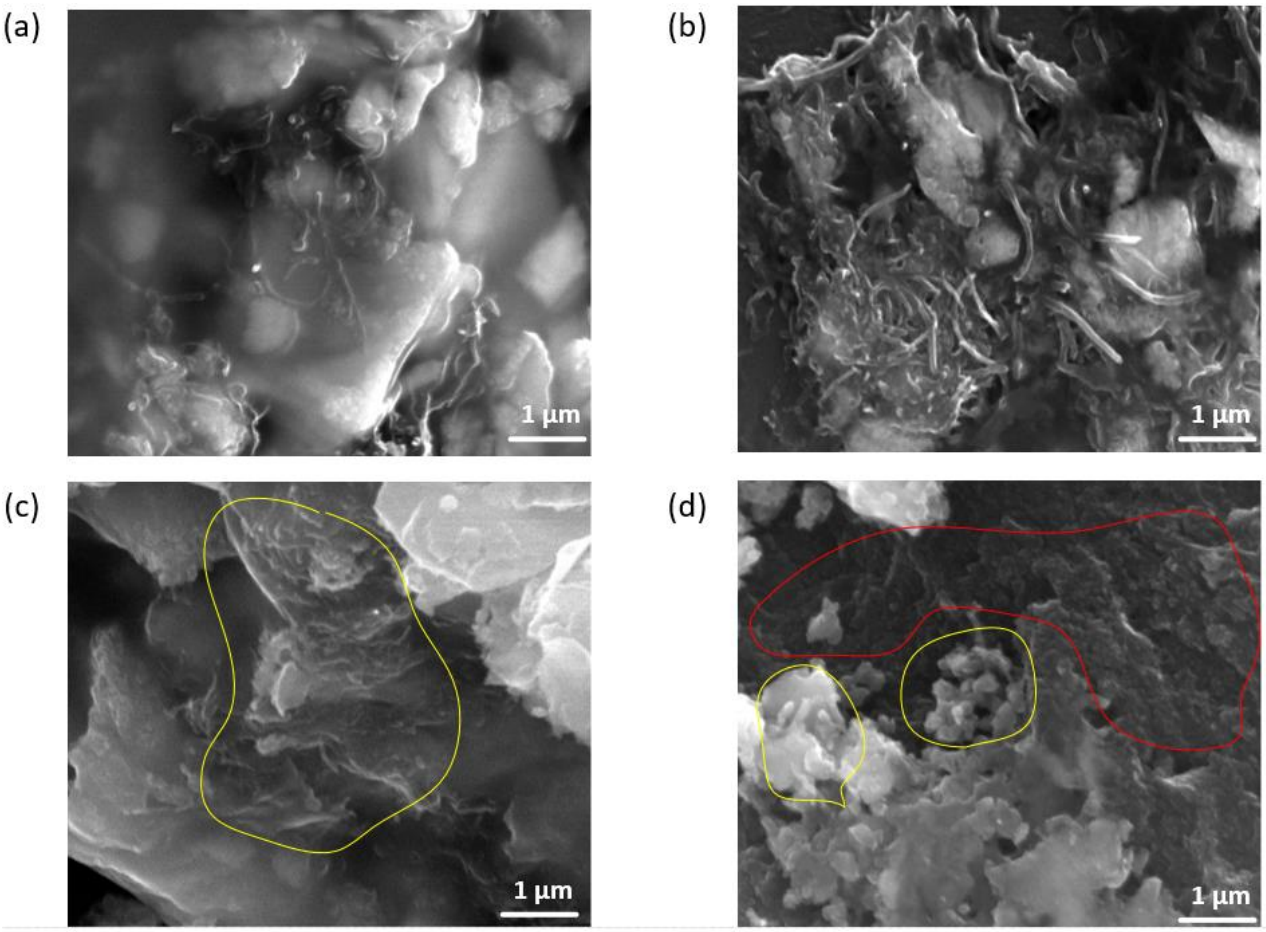


Figure 6- 9: FESEM images of RCF-Bi_2Te_3 composites doped with (a) 0.05 wt% of MWCNT (b) 0.10 wt% of MWCNT (c) 0.15 wt% of MWCNT (d) 0.20 wt% of MWCNT.

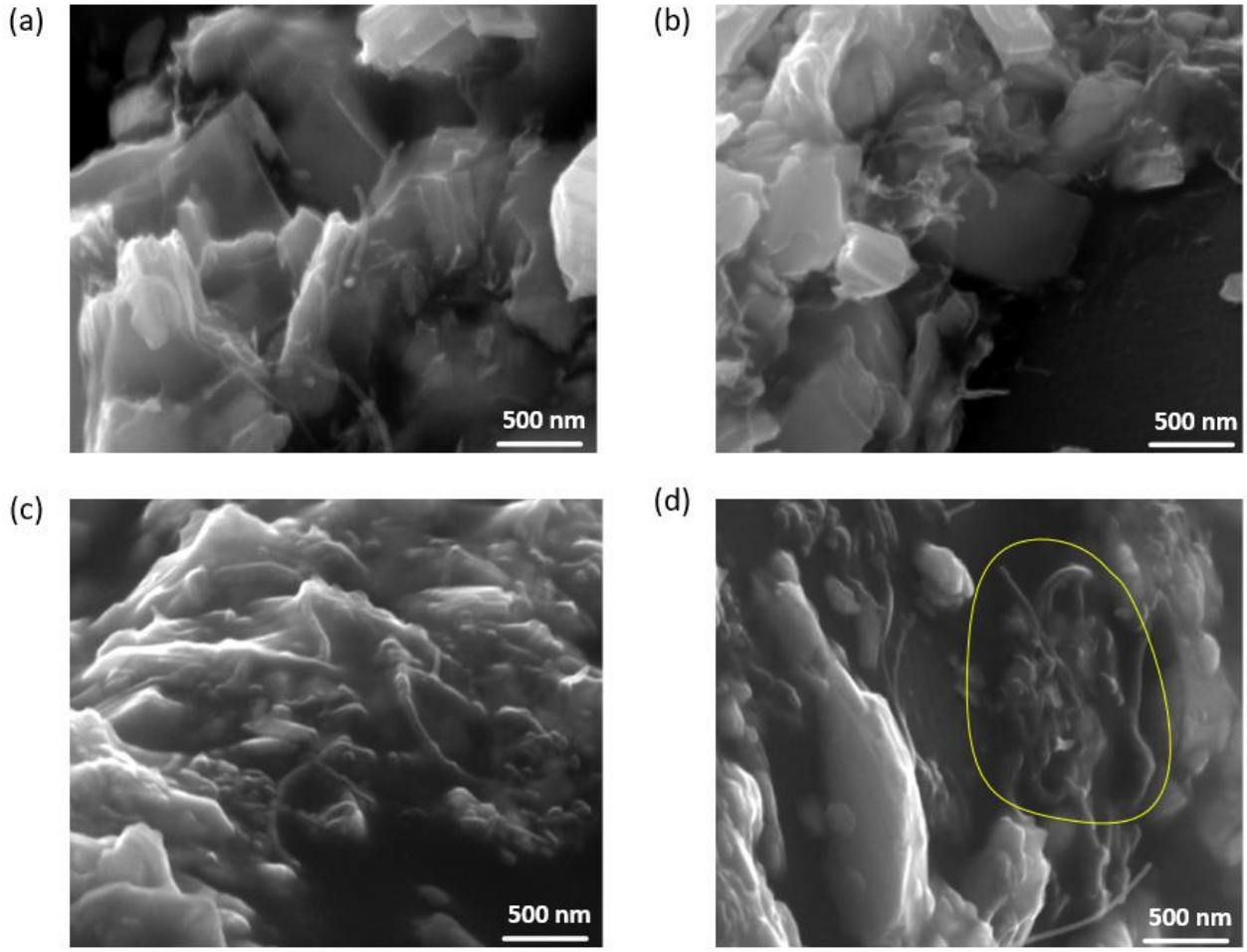


Figure 6- 10: FESEM images of RCF-Bi_2S_3 composites doped with (a) 0.05 wt% of MWCNT (b) 0.10 wt% of MWCNT (c) 0.15 wt% of MWCNT (d) 0.20 wt% of MWCNT.

6.2.3 XRD analysis of RCF-Bi_2Te_3 and RCF-Bi_2S_3 composites doped with MWCNT

XRD patterns of RCF-Bi_2Te_3 and RCF-Bi_2Te_3 doped with MWCNT composites are shown in **Figure 6- 11**. All XRD patterns shown in **Figure 6- 11** have the following 12 diffraction peaks located at 2θ, 17.59°, 27.78°, 37.93°, 40.42°, 41.27°, 44.64°, 50.37°, 54.00°, 57.17°, 62.31°, 66.04° and 67.17° with orientations of (006), (015), (1010), (0111), (110), (0015), (205), (1016), (0210), (1115), (0120) and (125). In general, the obtained XRD patterns of all samples were similar to that of Bi_2Te_3. No visible peak corresponding to MWCNT in RCF-Bi_2Te_3 doped MWCNT composites was observed due to the low amount of MWCNT in the composites. A lack of MWCNT peak in XRD was also observed in several other Bi_2Te_3-MWCNT composite studies owing to its low doping amount (Bark et al., 2013; Kumar et al., 2017; Xu and Wang, 2013a; Zhang et al., 2012). The most prominent peak in the case of all XRD patterns is (015) which were used to calculate all XRD related parameters.

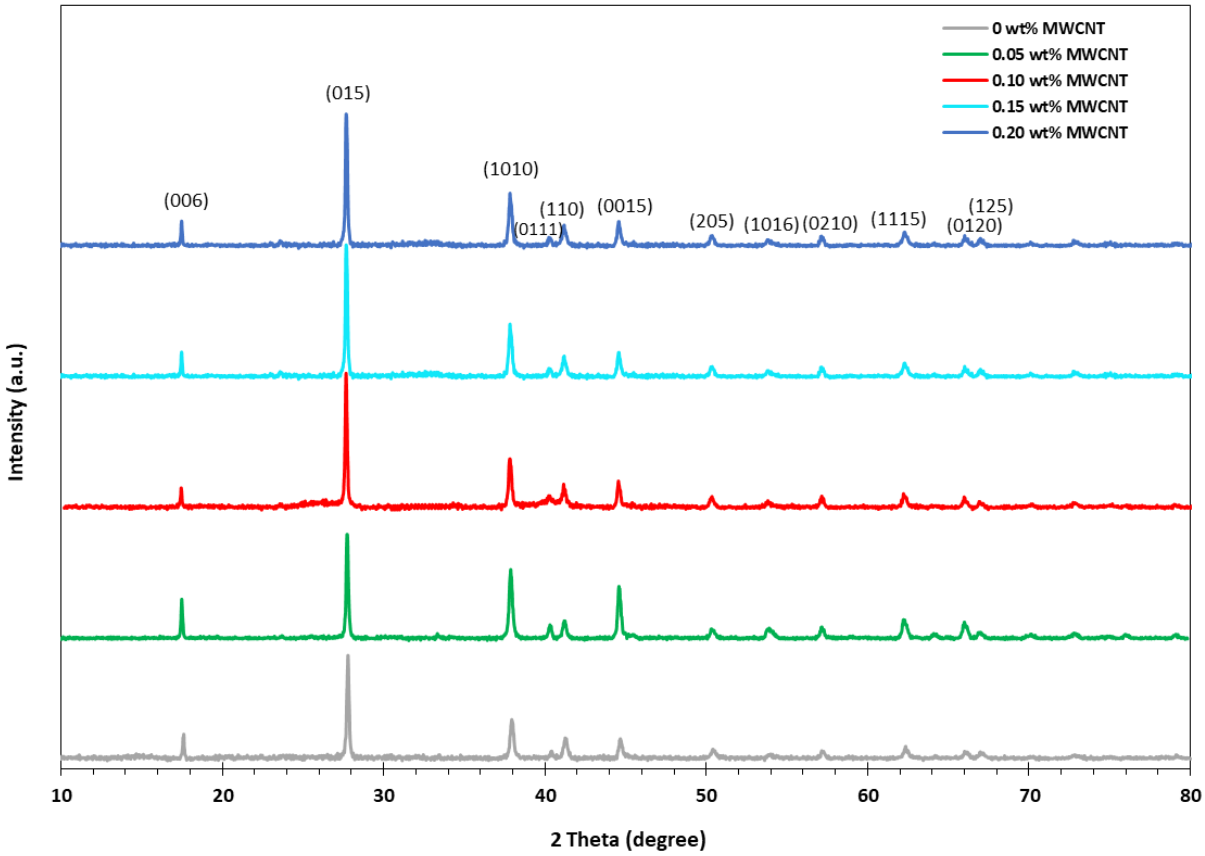


Figure 6- 11: XRD patterns of RCF-Bi_2Te_3 composite at different MWCNT loadings.

The D, ε and δ of the RCF-Bi_2Te_3 and MWCNT doped RCF-Bi_2Te_3 composites are as shown in **Table 6- 3**.

Table 6- 3: FWHM, crystallite size, microstrain and dislocation density of RCF-Bi_2Te_3 composites doped with MWCNT.

MWCNT Concentrations (wt %)	FWHM (radian)	Crystallite size, D (nm)	Microstrain (ε x 10^{-3}) (lines^{-2} m^{-4})	Dislocation density (δ x 10^{14}) (lines/m^2)
0.00	0.0030	47.01	3.1	4.52
0.05	0.0028	51.12	2.8	3.83
0.10	0.0026	55.26	2.6	3.27
0.15	0.0025	57.60	2.5	3.01
0.20	0.0025	57.20	2.5	3.06

The intensity of XRD patterns increased with increasing concentrations of MWCNT as shown in **Figure 6- 11**, showing that incorporation of MWCNT can enhance the crystallisation of Bi_2Te_3. The improvement in crystallinity is also complemented by the decrease in the FWHM values as shown in **Table 6- 3** upon incorporation of MWCNT. A similar increase in crystallinity was also observed by (Bark et al., 2013; L. Wang et al., 2013; Xu and Wang, 2013a) upon incorporation of MWCNTs.

The crystallite size, D was also seen to increase with increasing concentrations of MWCNT, however seemed to remain almost constant after 0.15 wt%. The increase in crystallite size could be attributed to MWCNTs attaching itself to the Bi_2Te_3 particles as the conductive networks are formed throughout the matrix as shown in **Figure 6- 9**. A similar increase of crystallite size was also observed by Luo et al. when CNTs were added to zirconia nanoparticles (Luo et al., 2004) and also by Kaganj et al. when MWCNTs were added to a conductive poly (propylene) composite(Kaganj et al., 2009).

The microstrain and dislocation density as shown in **Table 6- 3** are also seen to decrease until 0.15 wt% of MWCNT, these structural properties also reflected in decreased electrical resistivity of the RCF-Bi_2Te_3 composites with MWCNTs as shown in **Figure 6- 2**. However as agglomerates of MWCNTs are formed at 0.20 wt% it resulted in slight rise in dislocation density and a subsequent increase in electrical resistivity followed by decreased power factor.

XRD patterns of RCF-Bi_2S_3 and RCF-Bi_2S_3 doped with MWCNT composites are shown in **Figure 6- 12**. All XRD patterns shown in **Figure 6- 12** have the following 27 diffraction peaks of Bi_2S_3 was observed on all the RCF-Bi_2S_3 composite were located at 2θ, 15.75°, 17.62°, 22.43°,24.99°, 25.23°, 27.49°, 28.65°, 31.84°, 33.04°, 33.96°, 35.65°, 36.68°, 39.09°, 39.95°, 45.60°, 46.51°, 47.05°, 48.48°, 49.21°, 52.63°, 53.86°, 54.77°, 62.68°, 64.57°, 72.04°,73.05° and 76.21° with orientations of (200), (201), (202),(301),(103), (210), (112), (212), (013), (303), (402), (312), (410), (411), (020), (314), (511), (600), (512), (321), (610), (611), (711), (712), (606), (417) and (408). Similar to that of RCF-Bi_2Te_3 composites, the obtained XRD patterns of all samples were similar to that of Bi_2S_3. No visible peak corresponding to MWCNT in RCF-Bi_2S_3 doped MWCNT composites was observed due to the low amount of MWCNT in the composites. A lack of MWCNT peak in XRD was also observed in several other Bi_2S_3-MWCNT composite studies owing to its low doping amount (Ni et al., 2014; Zhao et al., 2014). The most prominent peak in the case of all XRD patterns is (301) which were used to calculate all XRD related parameters.

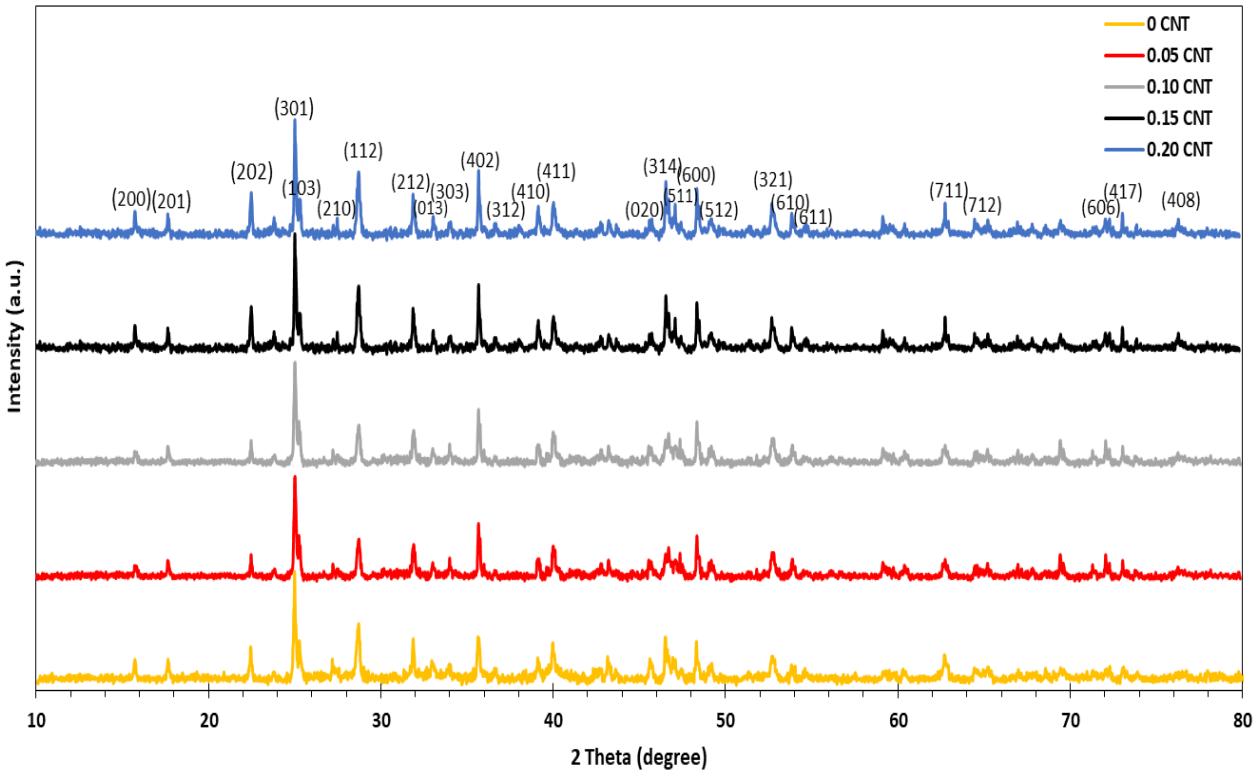


Figure 6- 12: XRD patterns of RCF-Bi_2S_3 composite at different MWCNT loadings.

Table 6- 4: FWHM, crystallite size, microstrain and dislocation density of RCF-Bi_2S_3 composites doped with MWCNT.

MWCNT Concentrations (wt %)	FWHM (radian)	Crystallite size, D (nm)	Microstrain (ε x 10^{-3}) (lines^{-2} m^{-4})	Dislocation density (δ x 10^{14}) (lines/m^2)
0.00	0.00272	52.14	3.1	3.68
0.05	0.00267	53.16	3.0	3.54
0.10	0.00261	54.23	2.9	3.40
0.15	0.00248	57.28	2.8	3.05
0.20	0.00246	57.69	2.8	3.00

Similar to that of MWCNT doped RCF-Bi_2Te_3, RCF-Bi_2S_3 also exhibited a decreasing pattern of the FWHM values, as shown in **Table 6- 4**, upon incorporation of MWCNTs which denotes an improvement in the crystallinity. It can be seen that crystallite size, D also increased from 52.14 nm to a maximum of 57.69 nm with increasing concentration of MWCNT. This may be due to the conductive network of MWCNT that is attaching itself to the crystals of Bi_2S_3 particles as shown in **Figure 6- 10**. However at higher concentrations of MWCNTs (0.20 wt%), there is no observable change in D perhaps because the interaction between Bi_2S_3 particles and MWCNTs are lower with an observable concentration/accumulation of MWCNTs in the polymer phase at 0.20 wt% with not much connection to that of Bi_2S_3 as shown in **Figure 6- 10 (d)**.

With the increase in D, the decrease in microstrain, ε and dislocation density, δ is a widely known phenomena (Manohari et al., 2014). The continuous decrease in both ε and δ resulted in an 81% decrease in electrical resistivity for 0.15 wt% MWCNT as compared to that of 0 wt% MWCNT as shown in **Figure 6- 5**.

6.2.4 Thermal stability of RCF-Bi_2Te_3 and RCF-Bi_2S_3 composites doped with MWCNT

The TGA measurement results for RCF-Bi_2Te_3 (0 wt% MWCNT) and MWCNT doped RCF-Bi_2Te_3 composites with 0.05-0.20 wt% MWCNTs are shown in **Figure 6- 13**.

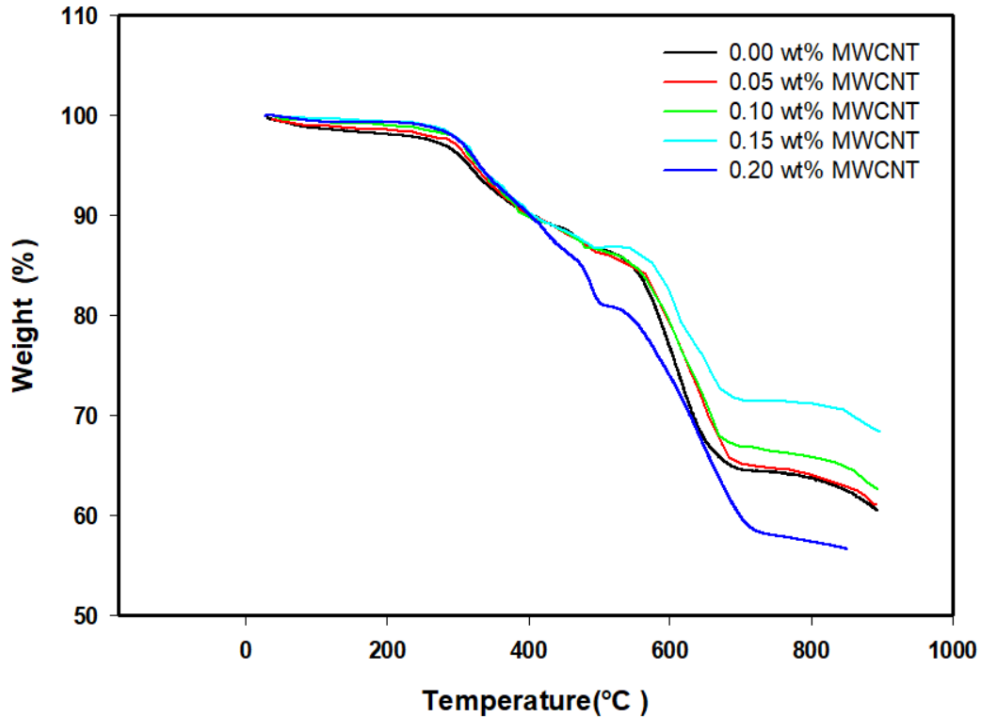


Figure 6- 13: TGA curves of RCF-Bi_2Te_3 composites doped with various loadings of MWCNTs.

Based on **Figure 6- 13**, MWCNTs improved the onset degradation temperature (T_{onset}) at 5% weight loss of RCF-Bi_2Te_3 composites from 316.2 °C (0 wt% MWCNT) to 330.75°C (0.20 wt% MWCNT). The weight loss of composites decreased with increasing MWCNT content until 0.15 wt%, at 0.20 wt% of MWCNT the weight loss was seen to suddenly increase perhaps owing to the agglomeration of MWCNTs in the composite as explained in Section 6.2.2. Nevertheless, it can be concluded that doping of MWCNTs improved the thermal stability of RCF-Bi_2Te_3 composites if it is uniformly dispersed within the matrix. A similar improvement in weight loss and thermal stability of the composites were also observed in electrically

conductive polymers doped with MWCNTs (Du et al., 2012b; Wang et al., 2014; L. Wang et al., 2013).

An improved onset degradation temperature (T_{onset}) at 5% weight loss was also observed for RCF-Bi_2S_3 composites doped with MWCNTs as shown in **Figure 6- 14**.

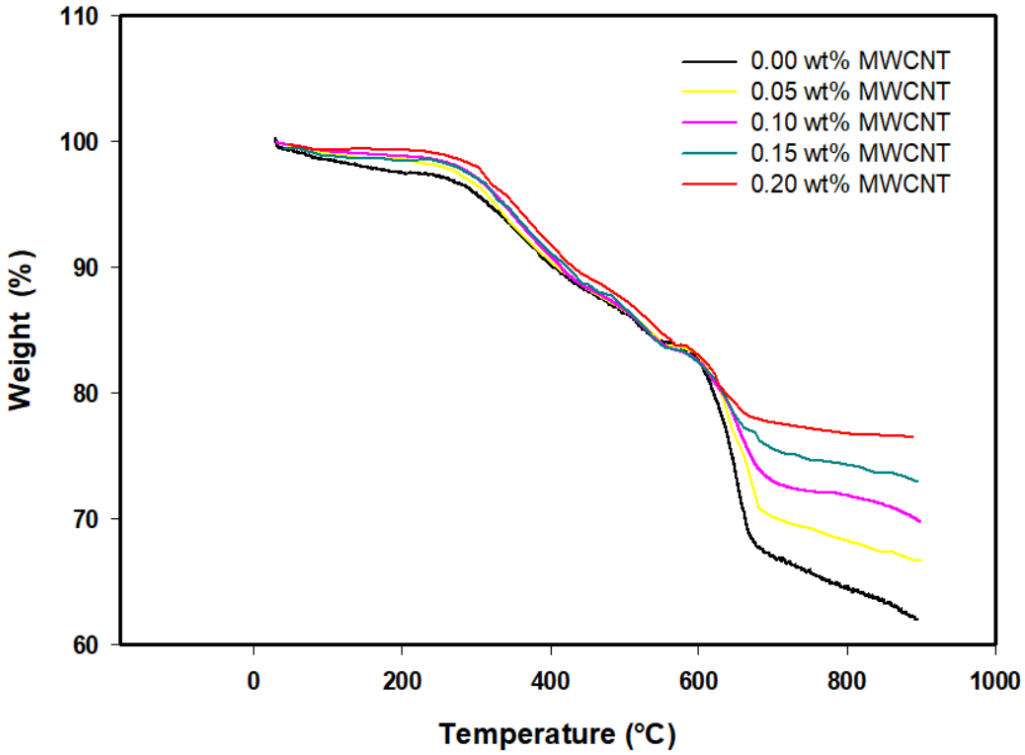


Figure 6- 14: TGA curves of RCF-Bi_2S_3 composites doped with various loadings of MWCNTs.

The TGA curves for MWCNT doped RCF-Bi_2S_3 composites were similar to those of RCF-Bi_2S_3. The T_{onset} at 5% mass loss improved from 316.32 (0.00 wt% MWCNT) to 350.67 °C (0.20 wt% MWCNT).

The improvement in thermal stability of MWCNT doped RCF-Bi_2Te_3 composite is also highlighted in the improvement of the maximum degradation temperature (T_{max}) of the composites upon incorporation of MWCNT as shown in **Figure 6- 15**. All the DTG curves

upon incorporation of MWCNT shifted to the right showing an increase in the T_{max} from 602.19 °C (0.00 wt% MWCNT) to 643.91°C (0.20 wt% MWCNT).

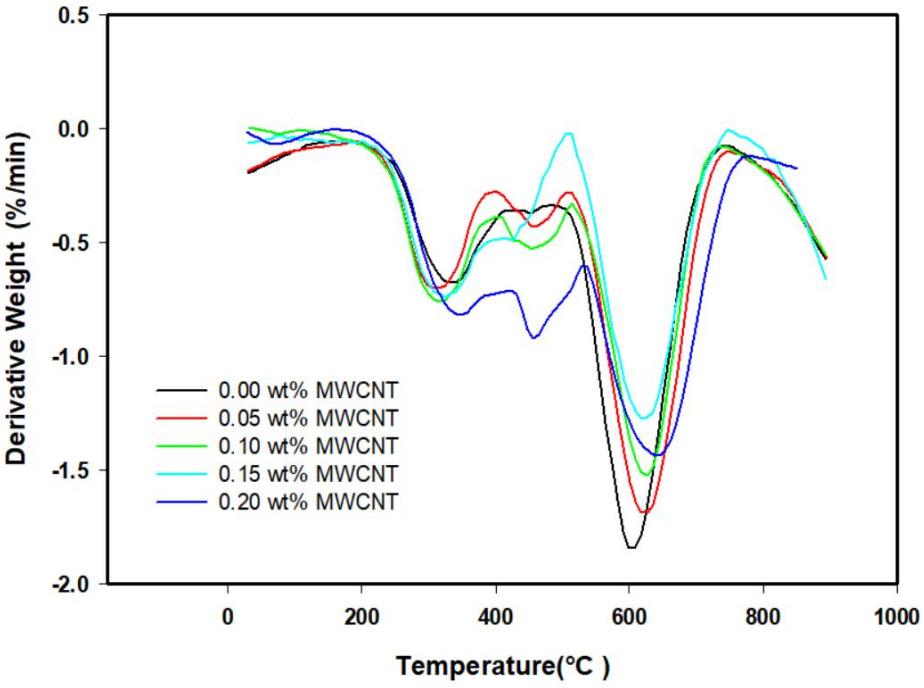


Figure 6- 15: DTG curves of RCF-Bi_2Te_3 composites doped with various loadings of MWCNTs.

MWCNT doped RCF-Bi_2S_3 composite also showed a similar improvement in its T_{max} as shown in **Figure 6- 16**. The T_{max} improved from 638.88 °C (0.00 wt% MWCNT) to 660.45 °C (0.20 wt% MWCNT) indicating that MWCNT has brought an improvement in its thermal stability.

When MWCNT is uniformly dispersed within the matrix, it is seen to improve the thermal stability (i.e. T_{onset} and T_{max}) of both RCF-Bi_2Te_3 and RCF-Bi_2S_3 composites due to remarkable thermal properties of MWCNT (Chen et al., 2006). The thermal stability is the key parameter for polymer materials, which determines the application temperature range of the polymers (Wang et al., 2014). As thermoelectric composites are subjected to constant temperature variation cycles, it is imperative to have a thermoelectric composite that has robust thermal

stability and MWCNT as a dopant is proven to be valuable in improving the thermal stability of RCF composites.

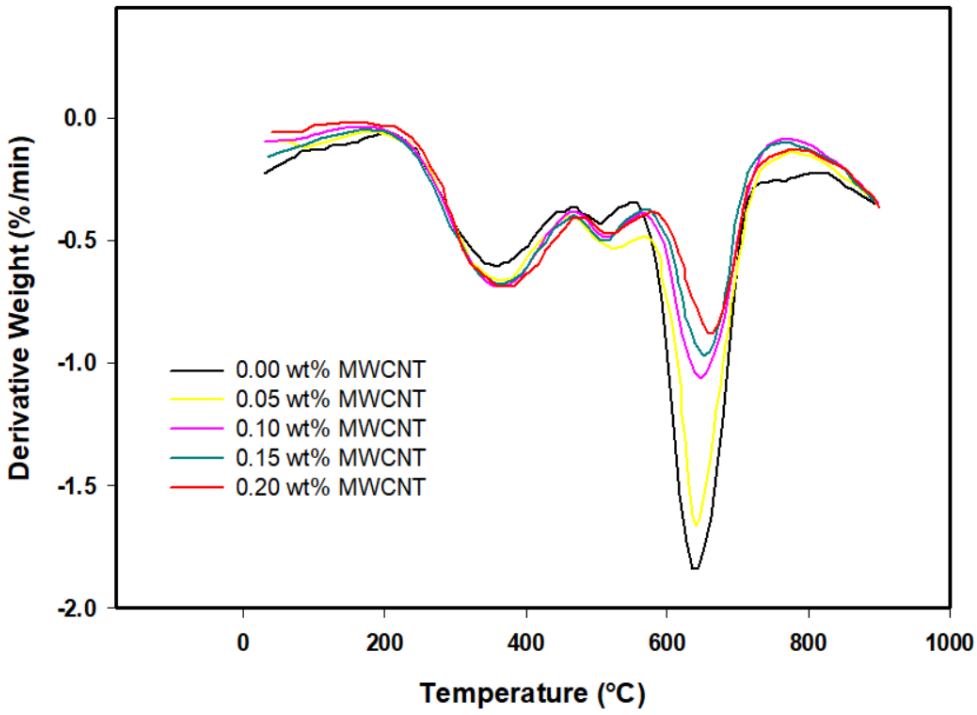


Figure 6- 16: DTG curves of RCF-Bi_2S_3 composites doped with various loadings of MWCNTs.

6.3 Summary

In summary, the optimum doping level of MWCNT for RCF-Bi_2Te_3 and RCF-Bi_2S_3 is 0.10 wt% and 0.15 wt% of MWCNTs, respectively. The highest power factor obtained for MWCNT doped RCF-Bi_2Te_3 and RCF-Bi_2S_3 were 1.044 and 0.849 $\mu WK^{-2}m^{-1}$, respectively. At optimum doping level, MWCNTs enhanced the power factors of RCF-Bi_2Te_3 and RCF-Bi_2S_3 composites by approximately 438 and 800%, respectively. With the addition of MWCNT, the difference in power factor between RCF-Bi_2Te_3 and RCF-Bi_2S_3 was approximately 19% whereas the difference in power factor without the addition of MWCNT between RCF-Bi_2Te_3 and RCF-Bi_2S_3 was approximately 52%. This is a validation of the capability of MWCNT to improve the power factor of the environmentally friendly Bi_2S_3 thermoelectric composites to a comparable value with that of Bi_2Te_3. At optimum doping levels, MWCNT also improved the crystallinity and thermal stability of the RCF-Bi_2Te_3 and RCF-Bi_2S_3 composites.

Chapter 7: Effect of Annealing on the Thermoelectric Properties of Recycled Carbon Fibre Composites with Bi_2Te_3 and Bi_2S_3 Thermoelectric Fillers

7.1 Introduction

In this chapter, the fourth objective of the study was addressed, whereby the effect of annealing on the thermoelectric properties of RCF-Bi_2Te_3 and RCF-Bi_2S_3 composites were studied. Thermal annealing is essentially a heat treatment that alters the physical and chemical properties of a material. Thermal annealing is commonly used as a post deposition treatment in order to further improve the power factors of Bi_2Te_3 and Bi_2S_3. During annealing, the reorganization of atoms occur which then forms the crystalline nature of materials while reducing the amorphous phase (Huang et al., 2009).

Annealing is known to critically impact semiconductor material and can alter its electrical transport characteristics. The thermoelectric properties of semiconductor materials are improved by the annealing process by means of altering their surface defects, grain size and carrier concentration (Kim et al., 2007b).

The annealing process is primarily affected by the temperature and time of annealing. Many researchers till date have used annealing as a post deposition treatment for Bi_2Te_3 films deposited using thin film techniques such as electrodeposition (Jun et al., 2006; J. Lee et al., 2012; Li et al., 2008; Rashid et al., 2013; Yoo et al., 2013), thermal evaporation (Lin et al., 2015, 2013; Takashiri et al., 2007), radio frequency magnetron sputtering (Huang et al., 2009; Jeon et al., 2011; Liu et al., 2016; Zeng et al., 2013; Zhu et al., 2014), etc. Most of these researchers have primarily focused on the effect of annealing temperature, however only very few research have studied the effect of varying time of annealing on the thermoelectric

properties of Bi_2Te_3. Thus, this chapter studied the effect of both annealing temperature and time on the thermoelectric properties of RCF-Bi_2Te_3 composites. To the best of the author's knowledge, there has been no prior work reported on the effect of annealing temperature and time on the thermoelectric properties of Bi_2S_3. Thus, this chapter also studied the effect of both annealing temperature and time on the thermoelectric properties of RCF-Bi_2S_3 composites.

Lastly, to the best of the author's knowledge there has been no prior work done on annealed semiconductor fillers in polymer thermoelectric composites. Thus, this work will be one of the first to report the effects of annealing in a polymer thermoelectric composite.

7.2 Results and discussions

7.2.1 Effect of annealing temperature on the thermoelectric properties of annealed RCF-Bi_2Te_3

The Seebeck coefficient, electrical resistivity, and power factor of RCF-Bi_2Te_3 composites with varying annealing temperatures are shown in **Figure 7- 1** to **Figure 7- 3**. As shown in **Figure 7- 1**, the Seebeck coefficient increased by approximately 437% from non-annealed to 350 °C, the increase in Seebeck coefficient is associated with the reorganization of bismuth (Bi) and tellurium (Te) atoms. During the annealing process that Te atomic percent (at.%) increased from 58.42 at.% (non-annealed) to 59.41-59.46 at.% of Te (300 and 350 °C) as shown in **Table 7- 1**. The increase in Te at.% closer to stoichiometric proportions decreased the carrier concentrations from 6.01×10^{20} cm^{-3} (non-annealed) to 1.07×10^{19} cm^{-3} (350 °C) as shown in **Table 7- 2**. In addition to the increase in Te content, the larger grain and or the crystallite sizes of Bi_2Te_3 particles upon annealing (will be discussed more extensively in Section 7.2.3 and 7.2.5) also led to a larger carrier mean free path that enhanced carrier mobility of electrons in

Bi_2Te_3 particles from 1.27×10^{-2} $cm^2V^{-1}s^{-1}$ (non-annealed) to 9.91×10^{-1} $cm^2V^{-1}s^{-1}$ (350 °C) as shown in **Table 7- 2**, thus leading to enhanced Seebeck coefficients.

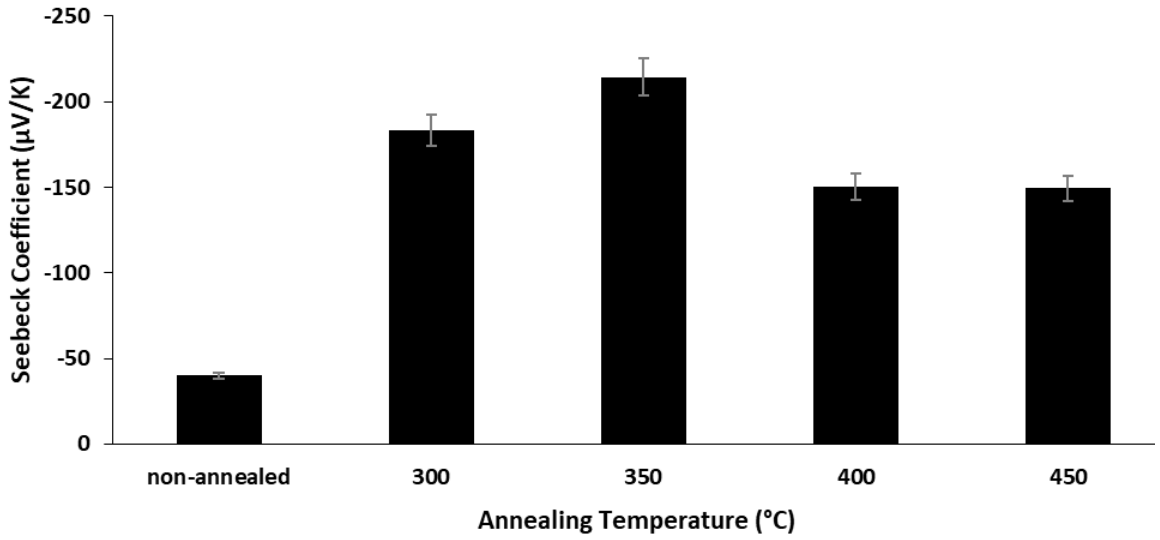


Figure 7- 1: The influence of annealing temperature on the Seebeck coefficient of RCF-Bi_2Te_3 composites.

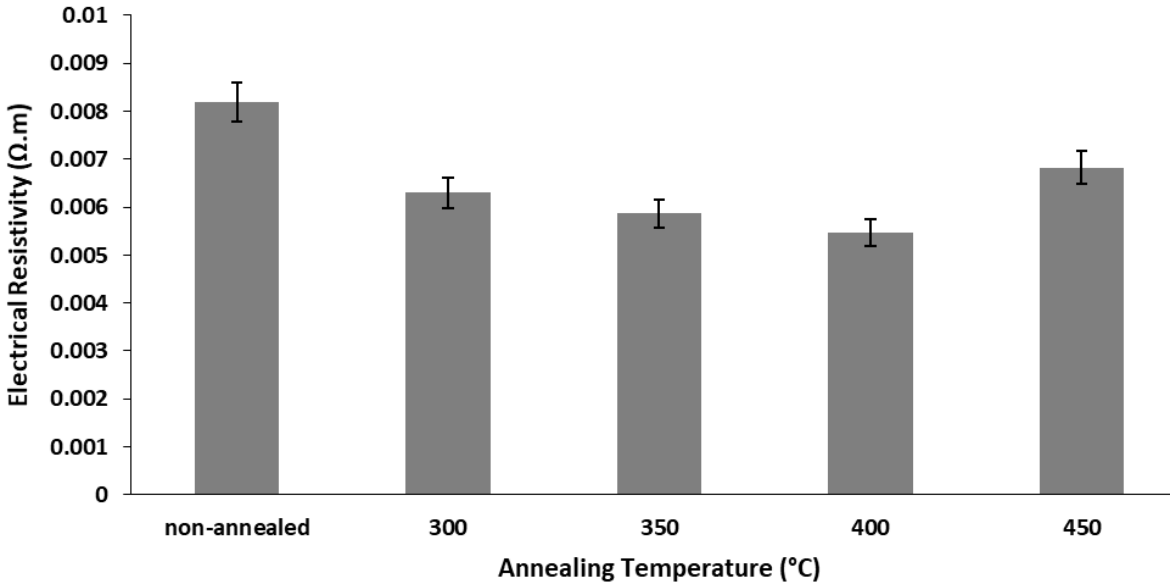


Figure 7- 2: The influence of annealing temperature on the electrical resistivity of RCF-Bi_2Te_3 composites.

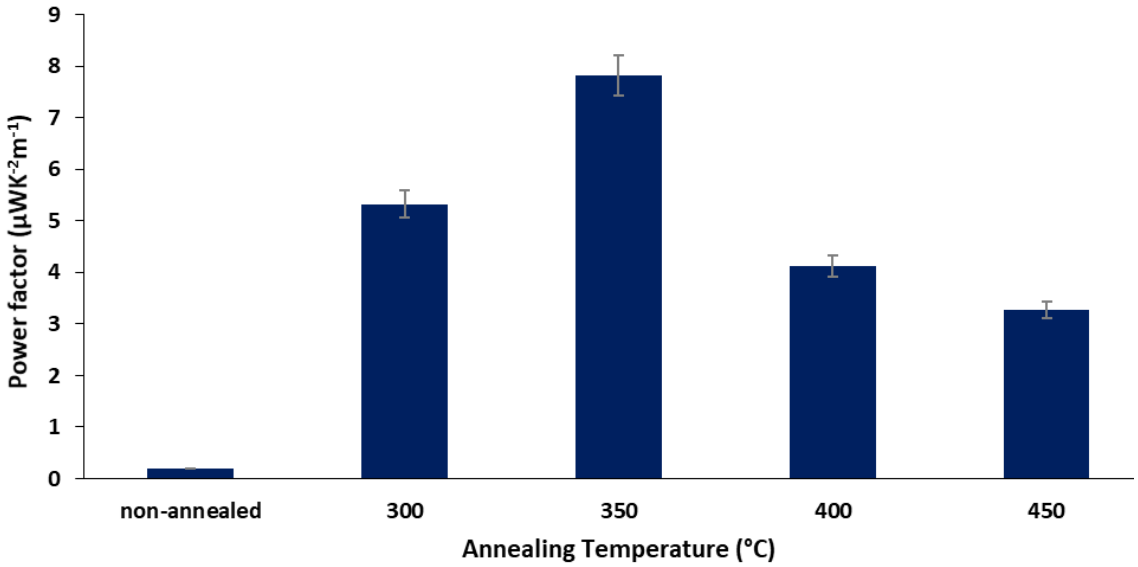


Figure 7- 3: The influence of annealing temperature on the power factor of RCF-Bi_2Te_3 composites.

Table 7- 1: Effect of annealing temperature on the Bi and Te content in the RCF-Bi_2Te_3 composites.

Annealing Temperature (°C)	Te (at %)	Bi (at %)
non-annealed	58.42	41.58
300	59.41	40.59
350	59.46	40.54
400	58.14	41.86
450	57.61	42.39

Table 7- 2: Carrier concentration and carrier mobility of RCF-Bi_2Te_3 composites with respect to annealing temperature.

Annealing Temperature (°C)	Carrier Concentration (cm^{-3})	Carrier Mobility ($cm^2V^{-1}s^{-1}$)
non-annealed	6.01×10^{20}	1.27×10^{-2}
300	2.43×10^{19}	4.08×10^{-1}
350	1.07×10^{19}	9.91×10^{-1}
400	1.67×10^{19}	6.90×10^{-1}
450	4.42×10^{19}	2.07×10^{-1}

However at higher annealing temperatures of 400 and 450 °C, the re-evaporation of Te occurs as its melting point is approximately 450 °C, this re-evaporation is proved in the EDX study (see **Table 7- 1**) as the Te content decreased from 59.46 at.% (350 °C) to 57.61 at.% (450 °C). This decrease in Te content also resulted in an increased carrier concentration and decreased carrier mobility at 400 and 450 °C respectively as shown in **Table 7- 2**, thus leading to a decrease in Seebeck coefficient beyond 350 °C as depicted in **Figure 7- 1**.

The annealing process greatly improved the crystalline quality of the Bi_2Te_3 particles resulting in reduced defect vacancies and grain boundaries (Rashid et al., 2013; X. Wang et al., 2013). This reduction in surface defects has improved the carrier mobility within the RCF-Bi_2Te_3 composites, thus decreasing the electrical resistivity from 0.0082 Ω.m (non-annealed) to 0.0055 Ω.m (400 °C) by approximately 33% as shown in **Figure 7- 2**. The carrier mobility improved by one order from 1.27×10^{-2} $cm^2V^{-1}s^{-1}$ (non-annealed) to 9.91×10^{-1} $cm^2V^{-1}s^{-1}$ (350 °C) as shown in **Table 7- 1**. A similar decrease in electrical resistivity upon annealing is also observed in Bi_2Te_3 films obtained by electrodeposition (Rashid et al., 2013) and RF magnetron sputtering (X. Wang et al., 2013) owing to the annealing induced reduction in defect vacancies.

However at 450 °C, there was an increase in electrical resistivity of RCF-Bi_2Te_3 composites as compared to at 400 °C perhaps owing to surface defects that was induced due to lack of stoichiometry at higher annealing temperatures thus reducing the carrier mobility,

The power factor of RCF-Bi_2Te_3 composites were greatly enhanced from 0.194 $\mu WK^{-2}m^{-1}$ (non-annealed) to 7.821 $\mu WK^{-2}m^{-1}$ (350 °C) by approximately 3930% as shown in **Figure 7-3**. This increment in power factor is owing to the improvement in grain growth that occurs during annealing thus altering its electron transport behaviour (Jeon et al., 2011). Beyond 350 °C, the power factors are seen to decrease at higher annealing temperatures of 400 and 450 °C. At higher annealing temperatures, the atomic percentage of Te decreased as shown in **Table 7-1** owing to the evaporation of Te. This occurs because the evaporation energy of Te (1)(52.55 kJ/mol) is approximately two times lower than that of Bi (104.80 kJ/mol) in the rhombohedral layered structure of -Te(1)-Bi-Te(2)-Bi-Te(1)-, thus making it easier for Te to evaporate (Liu et al., 2011; Shuai et al., 2015). Therefore, due to the imbalance in stoichiometry of Bi_2Te_3 at higher temperatures it may have resulted in decreased power factors at 400 and 450 °C. The optimum annealing temperature for RCF-Bi_2Te_3 composites is 350 °C.

7.2.2 Effect of annealing temperature on the thermoelectric properties of annealed RCF-Bi_2S_3

The Seebeck coefficient, electrical resistivity, and power factor of RCF-Bi_2S_3 composites with varying annealing temperatures are shown in **Figure 7- 4** to **Figure 7- 6**. **Figure 7- 4** shows the Seebeck coefficient of RCF-Bi_2S_3 composites as a function of annealing temperature. The Seebeck coefficient increased from non-annealed to 400 °C by approximately 65%, this is because the Bi_2S_3 grains coalesce and increased in grain size during thermal treatment that reduced grain boundaries thus decreased carrier concentration and improved carrier mobility as shown in **Table 7- 3**. At 450 °C, a decrease in Seebeck coefficient was observed as Bi_2S_3 sublimes easily at temperatures higher than 400 °C (Rincón and Nair, 1996) and as sulphur is highly volatile a large drop in its atomic percent is observed in the EDX study at this temperature (see **Table 7- 4**).

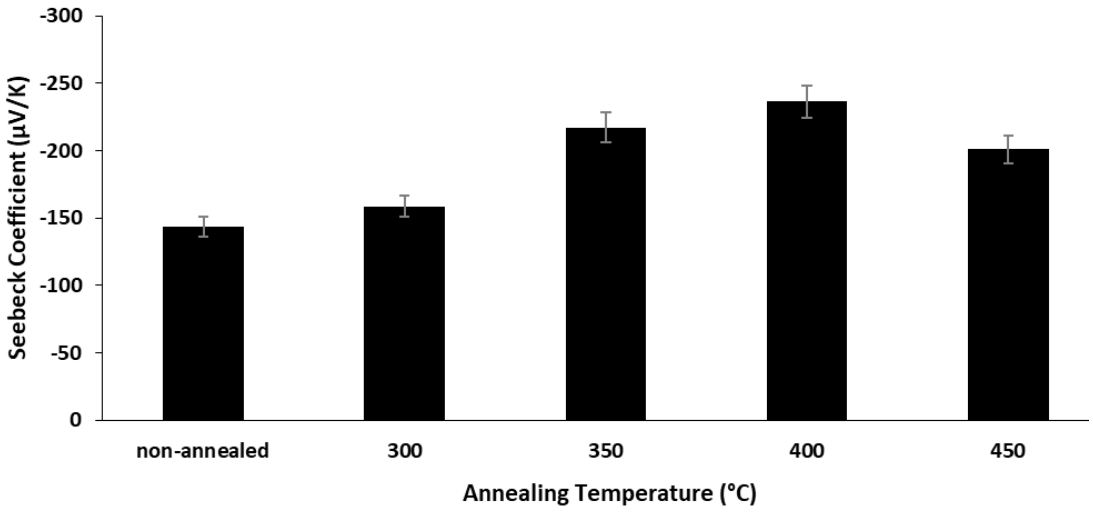


Figure 7- 4: The influence of annealing temperature on the Seebeck coefficient of RCF-Bi_2S_3 composites.

Table 7- 3: Carrier concentration and carrier mobility of RCF-Bi_2S_3 composites with respect to annealing temperature.

Annealing Temperature (°C)	Carrier Concentration (cm^{-3})	Carrier Mobility ($cm^2V^{-1}s^{-1}$)
non-annealed	4.27×10^{18}	6.67×10^{-2}
300	2.24×10^{18}	1.24×10^{0}
350	5.38×10^{17}	5.95×10^{0}
400	4.41×10^{17}	6.45×10^{0}
450	7.45×10^{17}	2.06×10^{0}

Table 7- 4: Effect of annealing temperature on the Bi and S content in the RCF-Bi_2S_3 composites.

Annealing Temperature (°C)	S (at %)	Bi (at %)
non-annealed	62.54	37.46
300	61.67	38.33
350	60.90	39.10
400	60.98	39.02
450	53.71	46.29

Figure 7- 5 depicts the electrical resistivity of RCF-Bi_2S_3 composites as a function of annealing temperatures. The electrical resistivity decreased by approximately 91% from 0.219 Ω.m (non-annealed) to 0.020 Ω.m (350 °C) although there was a 87% decrease in carrier concentration, the improvement in carrier mobility by approximately 2 orders contributed to the tremendous drop in electrical resistivity. The sulphur (S) at.% as shown in **Table 7- 4** decreased from 62.54 at.% (non-annealed) to 60.90 at.% (350 °C), this loss of sulphur to stoichiometric ratios generated a lower defect band gap that allowed improvement in electrons carrier mobility thus decreased the electrical resistivity (Zhao et al., 2008). From 300-400 °C, there was no significant variation in electrical resistivity with respect to annealing temperature, however there was a remarkable 90% decrease in electrical resistivity of all samples annealed from 300-450 °C when compared to that of non-annealed sample. Beyond 450 °C, there is an increase in electrical resistivity though still lower than non-annealed sample as the stoichiometry of Bi_2S_3 is distorted with 53.71 at.% of S and 46.29 at.% of Bi as shown in **Table 7- 4**, thus increasing the impurity states near the Fermi level (Zhan et al., 2014).

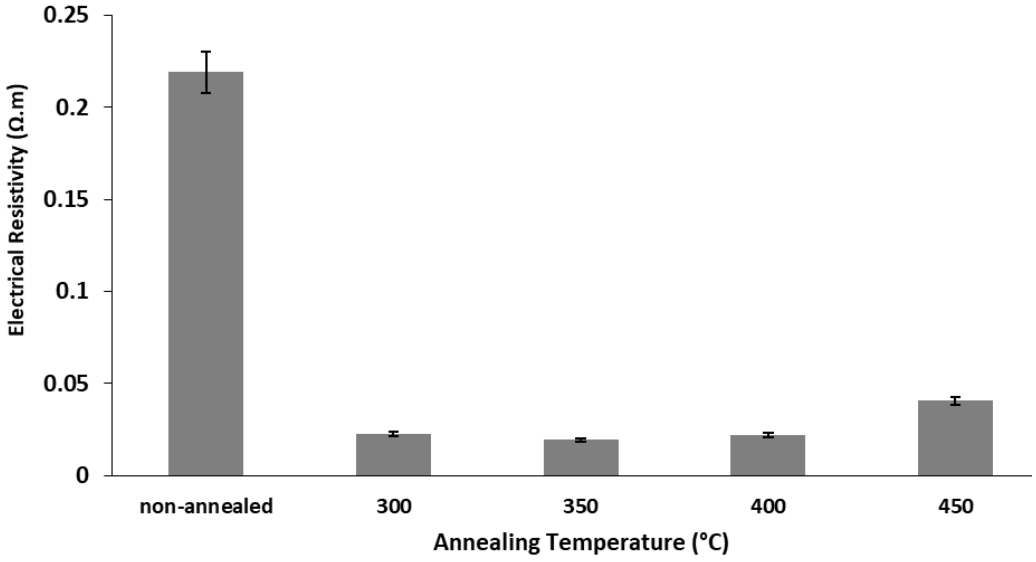


Figure 7- 5: The influence of annealing temperature on the electrical resistivity of RCF-Bi_2S_3 composites.

Figure 7- 6 shows the power factor of RCF-Bi_2S_3 composites as a function of annealing temperatures. The power factor of all annealed RCF-Bi_2S_3 is higher than that of non-annealed RCF-Bi_2S_3 composites owing to improved crystallinity and electron transport properties. The power factor improved significantly by approximately 2600 % at optimum annealing temperature of 400 °C compared to its non-annealed counterpart. Beyond 400°C, the power factor is seen to decrease due to the imbalance in stoichiometry at this extortionate temperature that contributes to impurity scattering and reduction of electrical properties.

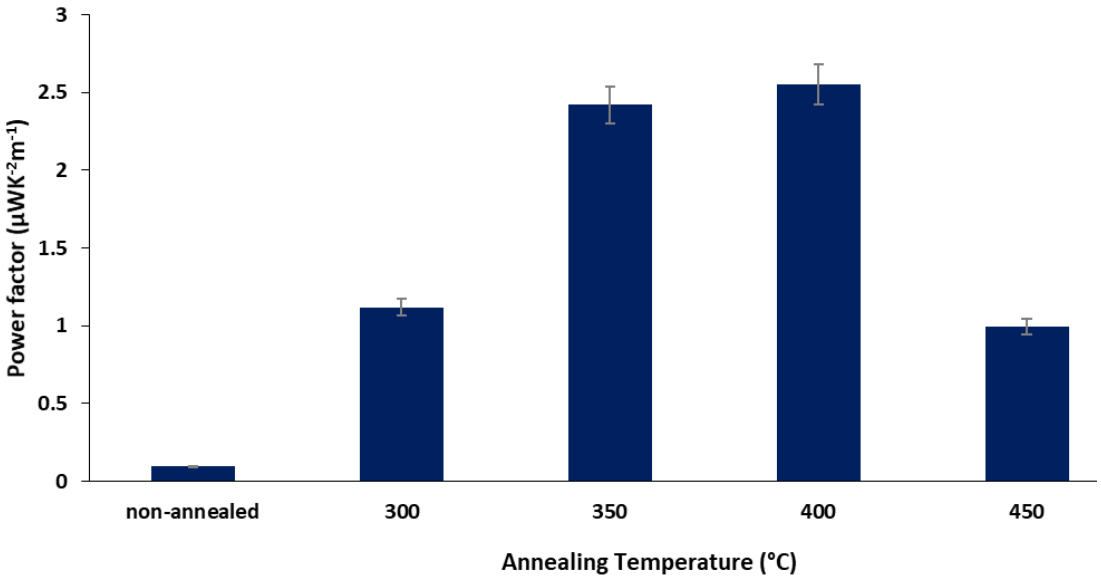


Figure 7- 6: The influence of annealing temperature on the power factor of RCF-Bi_2S_3 composites.

7.2.3 Effect of annealing temperature on the morphology of annealed RCF-Bi_2Te_3 composites

Figure 7- 7 below shows the surface morphology images of RCF-Bi_2Te_3 composites annealed at different temperatures.

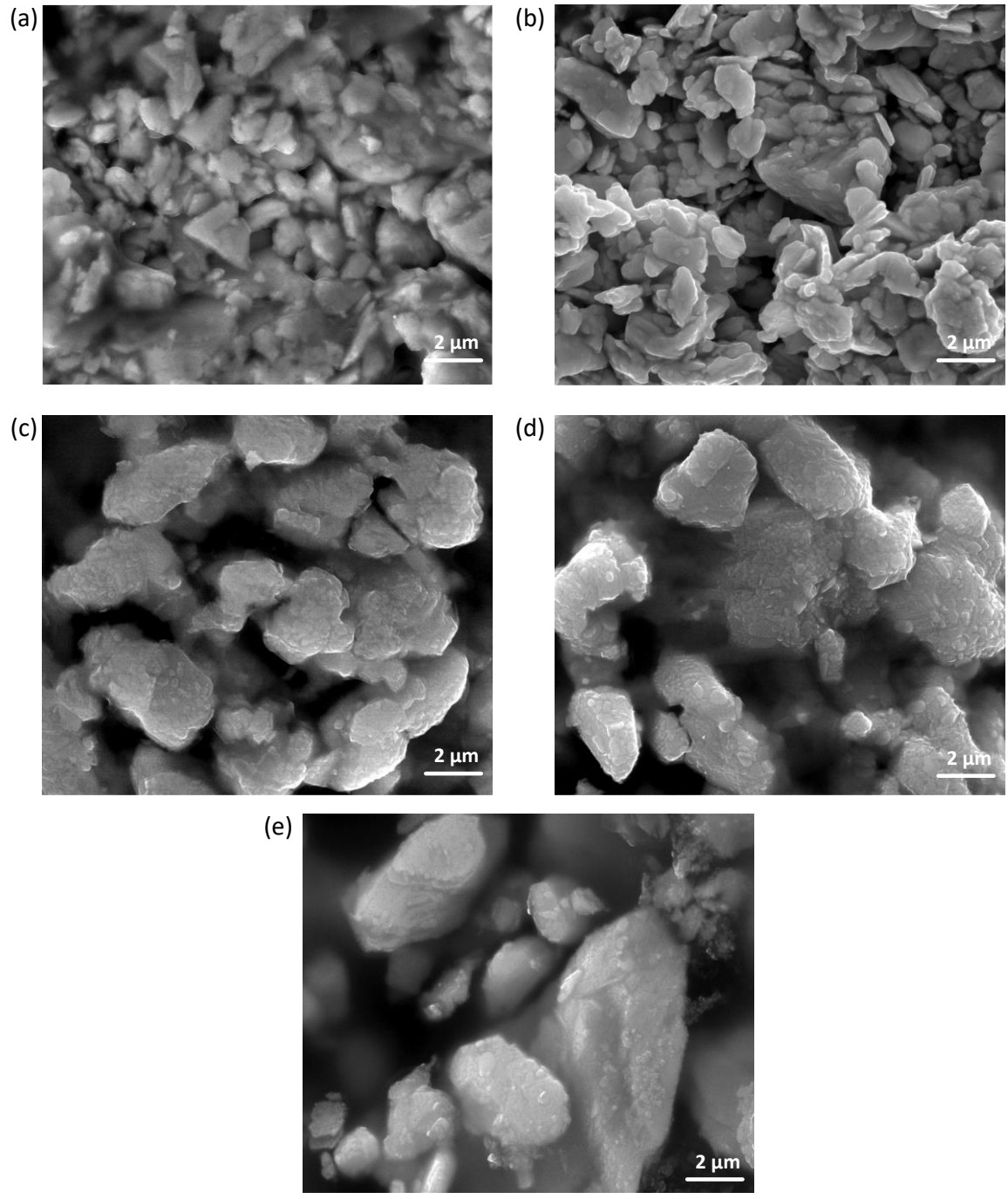


Figure 7- 7: FESEM surface images of RCF-Bi_2Te_3 composites annealed at (a) non-annealed (b) 300 °C (c) 350 °C (d) 400 °C (e) 450 °C.

The increase in thermal energy during annealing led to coalescence of smaller grains that formed larger grains upon annealing as shown in **Figure 7- 7 (b)** as compared to individual small grains observed for the non-annealed sample in **Figure 7- 7 (a)**. The grain size of Bi_2Te_3 particles increased with respect to increase in annealing temperature as shown in **Figure 7- 7 (b)** to **Figure 7- 7 (c).** There were also fewer grain boundaries observed in the FESEM images with the increment in grain size that led to decreased electrical resistivity of the composites upon annealing as shown in **Figure 7- 2**. A similar agglomeration of grains and grain size improvement was also observed by Wang et al. (X. Wang et al., 2013) with annealed sputtered Bi_2Te_3 films and also Rashid et al. (Rashid et al., 2013) with electrodeposited Bi_2Te_3 films that was rapid thermally annealed.

However beyond 350 °C, based on **Figure 7- 7** there was no obvious improvement in grain size as also proven by crystallite size (D) obtained from XRD calculations (which will be discussed further in Section 7.2.5).

7.2.4 Effect of annealing temperature on the morphology of annealed RCF-Bi_2S_3 composites

Figure 7- 8 below shows the surface morphology images of RCF-Bi_2S_3 composites annealed at different temperatures.

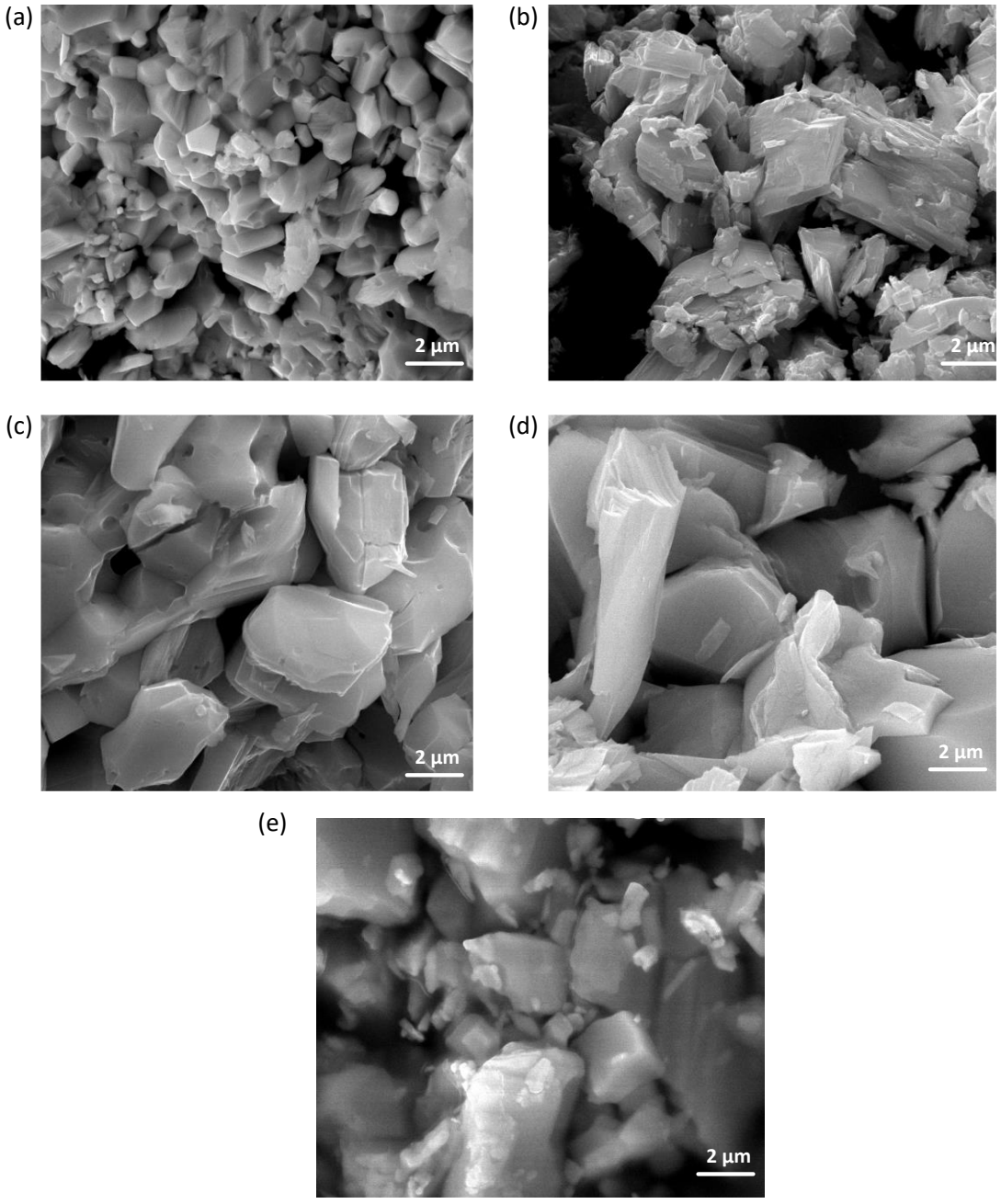


Figure 7- 8: FESEM surface images of RCF-Bi_2S_3 composites annealed at (a) non-annealed (b) 300 °C (c) 350 °C (d) 400 °C (e) 450 °C.

Similar to that of annealed Bi_2Te_3 particles, Bi_2S_3 particles within annealed RCF-Bi_2S_3 composites also depicted an increase in the grain size with respect to annealing temperature as shown in **Figure 7- 8**. The agglomeration of Bi_2S_3 particles to form larger clusters of Bi_2S_3 particles owing to increased thermal energy supplied during annealing is clearly evident in the FESEM micrographs. Due to the coalescence of grains during annealing, there are fewer grain boundaries thus resulting in improved carrier mobility by approximately two orders compared to that of non-annealed sample as shown in **Table 7- 3**. The carrier mobility also led to an almost 90% decrease in electrical resistivity in all annealed samples compared to that of non-annealed sample as shown in **Figure 7- 5**. A similar increase in grain size of Bi_2S_3 particles upon annealing was also observed by A. Hussain et al. (Hussain et al., 2014) in chemically deposited nanostructures of Bi_2S_3 thin films and Riahi et al. (Riahi et al., 2017) in electrochemically deposited Bi_2S_3 thin films.

However a decrease in grain size is observed in samples annealed at 450 °C as shown in **Figure 7- 8 (e)**, perhaps owing to the extensive evaporation of S at this temperature as shown in the EDX analysis in **Table 7- 4** that may have induced a surface defect on the Bi_2S_3 particles. This decrease in grain size also corresponds to the decrease in crystallite size observed from the XRD analysis (which will be discussed further in Section 7.2.6).

7.2.5 Effect of annealing temperature on the XRD analysis of annealed RCF-Bi_2Te_3 composites

X-ray diffraction (XRD) patterns of RCF-Bi_2Te_3 (non-annealed) and annealed RCF-Bi_2Te_3 with respect to different annealing temperatures at a constant annealing time of 2 hours are as shown in **Figure 7- 9**. All XRD patterns shown in **Figure 7- 9** have the following 12 diffraction peaks located at 2θ, 17.59°, 27.78°, 37.93°, 40.42°, 41.27°, 44.64°, 50.37°, 54.00°, 57.17°, 62.31°, 66.04° and 67.17° with orientations of (006), (015), (1010), (0111), (110), (0015), (205), (1016), (0210), (1115), (0120) and (125). These values are in good agreement with standard data of Joint Committee on Powder Diffraction Standards (PDF 00-015-0863) data and the observed peak positions are consistent with the structure of Bi_2Te_3 and observed peak positions are represented by their corresponding Miller indices in the spectra. The most prominent peak is (015) which was used to calculate all XRD related parameters.

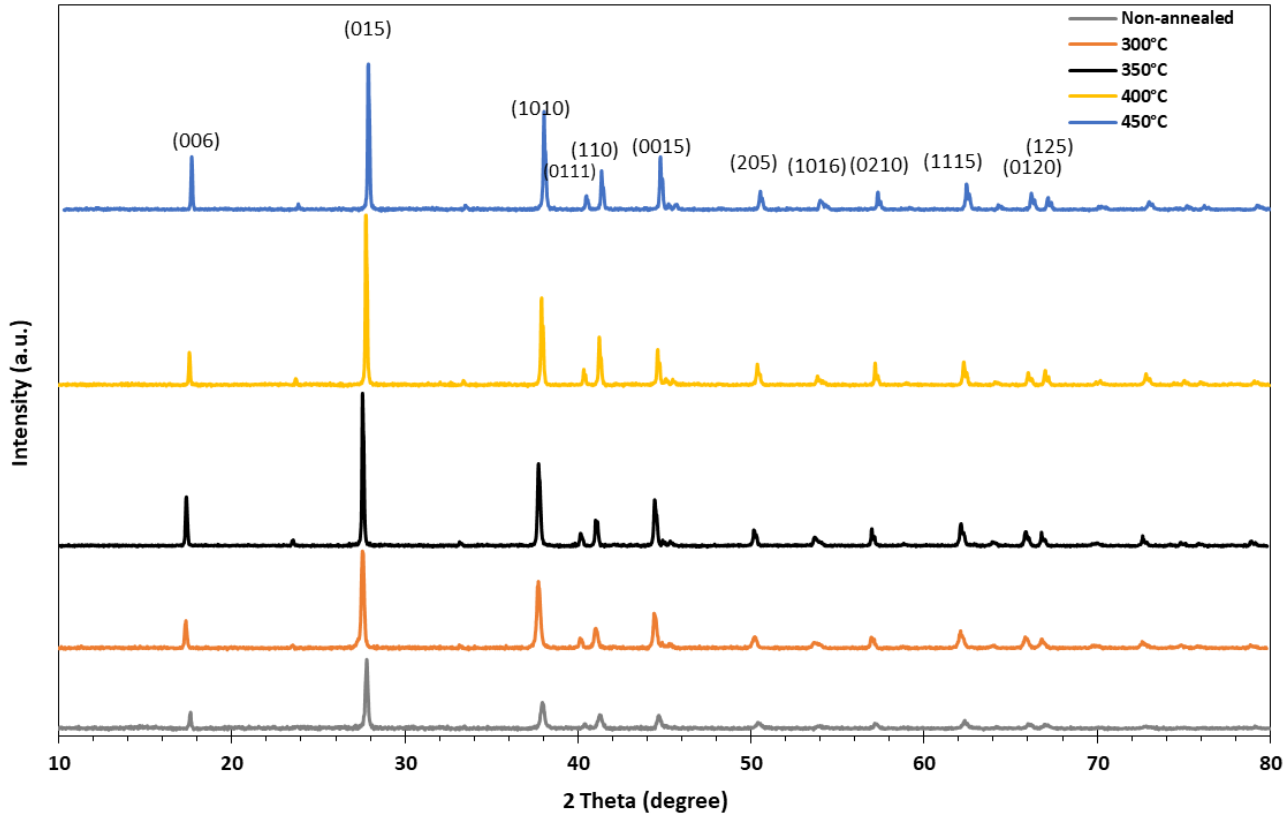


Figure 7- 9: XRD patterns of RCF-Bi_2Te_3 composite annealed at different temperatures for 2 hours.

The D, ε and δ of the RCF-Bi_2Te_3 and annealed RCF-Bi_2Te_3 composites with respect to different annealing temperatures are shown in **Table 7- 5**.

Table 7- 5: FWHM, crystallite size, microstrain and dislocation density of RCF-Bi_2Te_3 annealed at different temperatures.

Annealing Temperature (°C)	FWHM (radian)	Crystallite size, D (nm)	Microstrain (ε x 10^{-3}) (lines^{-2} m^{-4})	Dislocation density (δ x 10^{14}) (lines/m^2)
non-annealed	0.0030	47.01	3.1	4.52
300	0.0026	54.88	2.6	3.32
350	0.0023	61.94	2.3	2.60
400	0.0023	62.88	2.3	2.53
450	0.0024	60.12	2.4	2.76

The crystallization of Bi_2Te_3 particles in the RCF-Bi_2Te_3 composites improved upon annealing which is proven by the increase in the intensity of XRD peaks for all annealed samples as shown in **Figure 7- 9**. Upon annealing, the increase in temperature accelerated the diffusion and agglomeration of the Bi_2Te_3 atoms that led to the above mentioned increase in crystallinity. All of the samples exhibited a polycrystalline nature. This increase in crystallinity upon annealing is also further validated with the decrease in the FWHM values upon annealing as shown in **Table 7- 5**. The FWHM decreased from 0.0030 rad (non-annealed) to 0.0023 rad (400 °C) and increased slightly to 0.0024 rad (450 °C) due to extortionate temperature annealing. A similar increase in the intensity of XRD peaks as a result of improved crystallinity owing to annealing was also observed by (Liu et al., 2016; Singkaselit et al., 2017; Zeng et al., 2013).

Figure 7- 9 also shows a slight shift in the XRD peaks which is in line with the change in Bi and Te content as depicted in **Table 7- 1** upon annealing. The 2θ angle for 015 plane in stoichiometric Bi_2Te_3 (PDF 00-015-0863) with 60 at.% of Te and 40 at.% of Bi is 27.564°. The 015 plane at annealing temperatures of 300 and 350 °C have 2θ at 27.545° that is closest to stoichiometric 2θ at 27.564°. Thus, it is observed in **Figure 7- 9** the XRD peaks shift from left (non-annealed) to right (300 and 350 °C) upon annealing, beyond 350 °C the XRD peaks shift again towards the right side again due to the volatility of Te and subsequent off-stoichiometry content of Bi and Te. The phenomenon of XRD peak shifting as a result of annealing was also observed by Rashid et al. (Rashid et al., 2013).

The crystallite size, D as shown in **Table 7- 5** also increased upon annealing from 47 nm (non-annealed) to 63 nm (400 °C). The increase in D is a result of the agglomeration and enlargement of Bi_2Te_3 grains when annealed. At 450 °C, there is a slight decrease in D to 60 nm perhaps owing to the evaporation of Te and may have induced structural defect that contributed to a smaller crystallite. During the annealing process, the increase in crystal size and reduction in grain boundaries also results in a larger effective mean free path for carriers thus improving its carrier mobility(Huang et al., 2009; Singkaselit et al., 2017). The improved carrier mobility resulted in increased Seebeck coefficient and reduced electrical resistivity as shown in **Figure 7- 1** and **Figure 7- 2** respectively. An increase in crystallite size upon annealing is also observed by Singkaselit et al.(Singkaselit et al., 2017), Rashid et al. (Rashid et al., 2013) and Zeng et al. (Zeng et al., 2013).

The microstrain, ε and dislocation density, δ as shown in **Table 7- 5** was also seen to decrease with respect to increase in annealing temperature. Both ε and δ decreased tremendously from non-annealed to 350 °C, owing to the reduction in lattice imperfection and defects that is commonly attributed by annealing (Huang et al., 2009). Between that of 350 and 400 °C the

parameters almost remained constant and then subsequently increased at 450 °C. The increase in ε and δ at higher annealing temperatures of 400 °C and above, is perhaps attributed to the volatility of Te and imbalance in stoichiometry of Bi_2Te_3 that may have contributed to impurity defects within the structure. The decrease in ε and δ also resulted in a subsequent decrease in the electrical resistivity of the annealed RCF-Bi_2Te_3 composites until 400 °C as shown in **Figure 7- 2**.

7.2.6 Effect of annealing temperature on the XRD analysis of annealed RCF-Bi_2S_3 composites

XRD patterns of RCF-Bi_2S_3 (non-annealed) and annealed RCF-Bi_2S_3 with respect to different annealing temperatures at a constant annealing time of 2 hours are shown in **Figure 7- 10**. All XRD patterns shown in **Figure 7- 10** have the following 27 diffraction peaks located at 2θ, 15.75°, 17.62°, 22.43°,24.99°, 25.23°, 27.49°, 28.65°, 31.84°, 33.04°, 33.96°, 35.65°, 36.68°, 39.09°, 39.95°, 45.60°, 46.51°, 47.05°, 48.48°, 49.21°, 52.63°, 53.86°, 54.77°, 62.68°, 64.57°, 72.04°,73.05° and 76.21° with orientations of (200), (201), (202),(301),(103), (210), (112), (212), (013), (303), (402), (312), (410), (411), (020), (314), (511), (600), (512), (321), (610), (611), (711), (712), (606), (417) and (408). These values are in good agreement with standard data of Joint Committee on Powder Diffraction Standards (PDF 01-074-9437) data and the observed peak positions are consistent with the structure of Bi_2S_3 and observed peak positions are represented by their corresponding Miller indices in the spectra. The most prominent peak is (301) which was used to calculate all XRD related parameters.

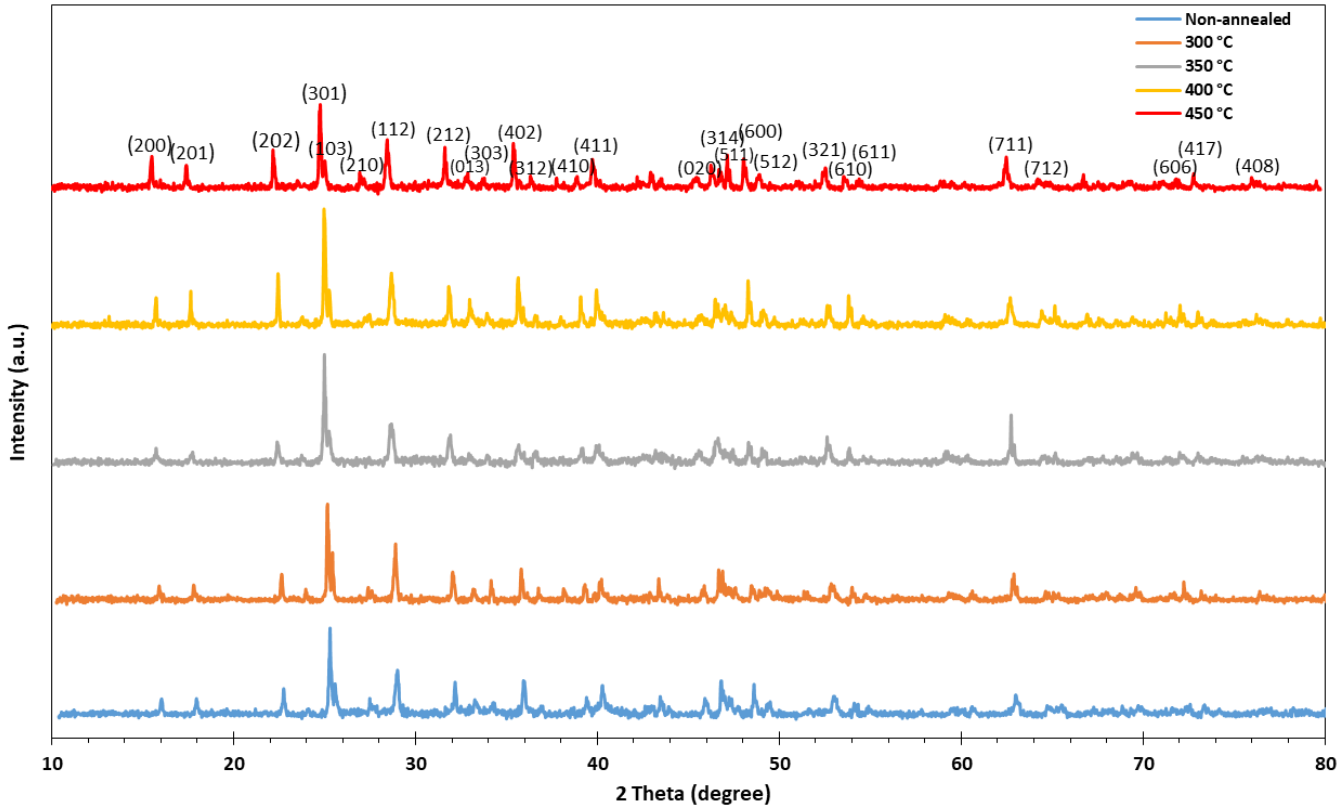


Figure 7- 10: XRD patterns of RCF-Bi_2S_3 composite annealed at different temperatures for 2 hours.

The D, ε and δ of the RCF-Bi_2S_3 and annealed RCF-Bi_2S_3 composites with respect to different annealing temperatures are shown in **Table 7- 6**.

Table 7- 6: FWHM, crystallite size, microstrain and dislocation density of RCF-Bi_2S_3 annealed at different temperatures.

Annealing Temperature (°C)	FWHM (radian)	Crystallite size, D (nm)	Microstrain (ε x 10^{-3}) (lines^{-2} m^{-4})	Dislocation density (δ x 10^{14}) (lines/m^2)
non-annealed	0.0027	52.14	3.08	3.68
300	0.0024	59.36	2.70	2.84
350	0.0021	66.12	2.42	2.29
400	0.0022	65.08	2.46	2.36
450	0.0025	56.49	2.84	3.13

Similar to that of annealed RCF-Bi_2Te_3 composites, Bi_2S_3 particles in annealed RCF-Bi_2S_3 composites also showed improved crystallisation upon annealing. The improved crystallinity is proven with the increase in the intensity of the XRD peaks as shown in **Figure 7- 10** and the decrease of the FWHM values as shown in **Table 7- 6** as compared to that non-annealed. The increase in crystallinity is attributed to the higher thermal energy supplied during the annealing treatment that allow the Bi and S atoms to re-arrange and nucleate to a more ordered and crystalline domain (Chelvanathan et al., 2015). The FWHM decreased from 0.0027 (non-annealed) to approximately 0.0021-0.0022 (350-400 °C); beyond 400 °C due to the possible sublimation of the Bi_2S_3 structure there is an increase in the FWHM value denoting reduced crystallinity. Rincon et al. (Rincón and Nair, 1996) also observed a defect in the Bi_2S_3 structure above 400 °C due to the decomposition of Bi_2S_3 owing to sublimation.

Due to nucleation of the Bi_2S_3 atoms during annealing, there is also a notable increase in the crystallite size upon annealing as shown in **Table 7- 6**. There is an approximate 26% increase in crystallite size from 52.14 nm (non-annealed) to 65-66 nm (350-400 °C), thus resulting in

almost 90% decrease in electrical resistivity as shown in **Figure 7- 5**. The larger grain size indicates lesser grain boundary and a larger mean free path for carriers thus improving the carrier mobility massively by two orders from 6.67×10^{-2} $cm^2V^{-1}s^{-1}$ (non-annealed) to 5.95-6.45×10^{0} $cm^2V^{-1}s^{-1}$ (350-400 °C) as shown in **Table 7- 3**.

Both ε and δ are seen to decrease with increasing annealing temperature as compared to those of non-annealed sample as shown in **Table 7- 6.** Both ε and δ decreased with annealing temperature up to 400 °C, due to the Bi_2S_3 crystal lattice changes that occur during annealing there is a decreased lattice defects that arise from obtaining stoichiometric Bi_2S_3 leading to the reduction in geometric mismatch within the inter-phase boundaries. A similar reduction in ε and δ was also observed in annealed electrodeposited Bi_2S_3 films for optical applications (Riahi et al., 2017) and annealed chemically deposited Bi_2S_3 films (Balasubramanian et al., 2011). However at 450 °C, there is an increase of both ε and δ perhaps due to the change in stoichiometry of Bi_2S_3 at this temperature that is extremely sulphur deficient and inducing distortion in the Bi_2S_3 structure. Native vacancies in the Bi_2S_3 structure is known to induce defects in the band gap thus also reflected in its structural properties when there is sulphur deficiency (Zhan et al., 2014).

In addition to structural parameters, annealing also alters the chemical composition of Bi_2S_3 in annealed RCF-Bi_2S_3 composites. Due to the inevitable change in the composition/stoichiometry of Bi_2S_3 in this study, there is also consequential peak shifting observed in the XRD peaks as shown in **Figure 7- 10** and **Figure 7- 11**. The 2θ angle for (301) plane in stoichiometric Bi_2S_3 (PDF 01-074-9437) with 60 at.% of S and 40 at.% of Bi is 24.983°. The (301) plane at annealing temperatures of 350 and 400 °C have 2θ at 24.987-24.988° that is closest to stoichiometric 2θ at 24.983°.The peak shifting in the XRD patterns of annealed RCF-Bi_2S_3 composites could not be observed clearly in **Figure 7- 10**. Therefore to

highlight this shift better, a zoomed in view on the prominent orientation (301) exhibiting a slight shift to left side from non-annealed to 300 °C as shown in **Figure 7- 11 (a)** indicated by the pink dotted line as the S and Bi content changes from 62.54 and 37.46 at.% (at 0 °C) to 61.67 and 38.33 at.% (300 °C). XRD pattern is also seen to shift further left from 300 °C to 350 °C as shown in **Figure 7- 11 (b)** indicated by the red dotted line as the S and Bi content changes from 61.67 and 38.33 at.% (300 °C) to 60.90 and 39.10 at.% (350 °C) respectively. The XRD pattern of 400 °C is similar to that of 350 °C as there is no significant change in its S and Bi content at this temperature as shown in **Table 7- 4**. At 450 °C, there is a significant shift to the left as the Bi_2S_3 at this temperature is highly off-stoichiometry.

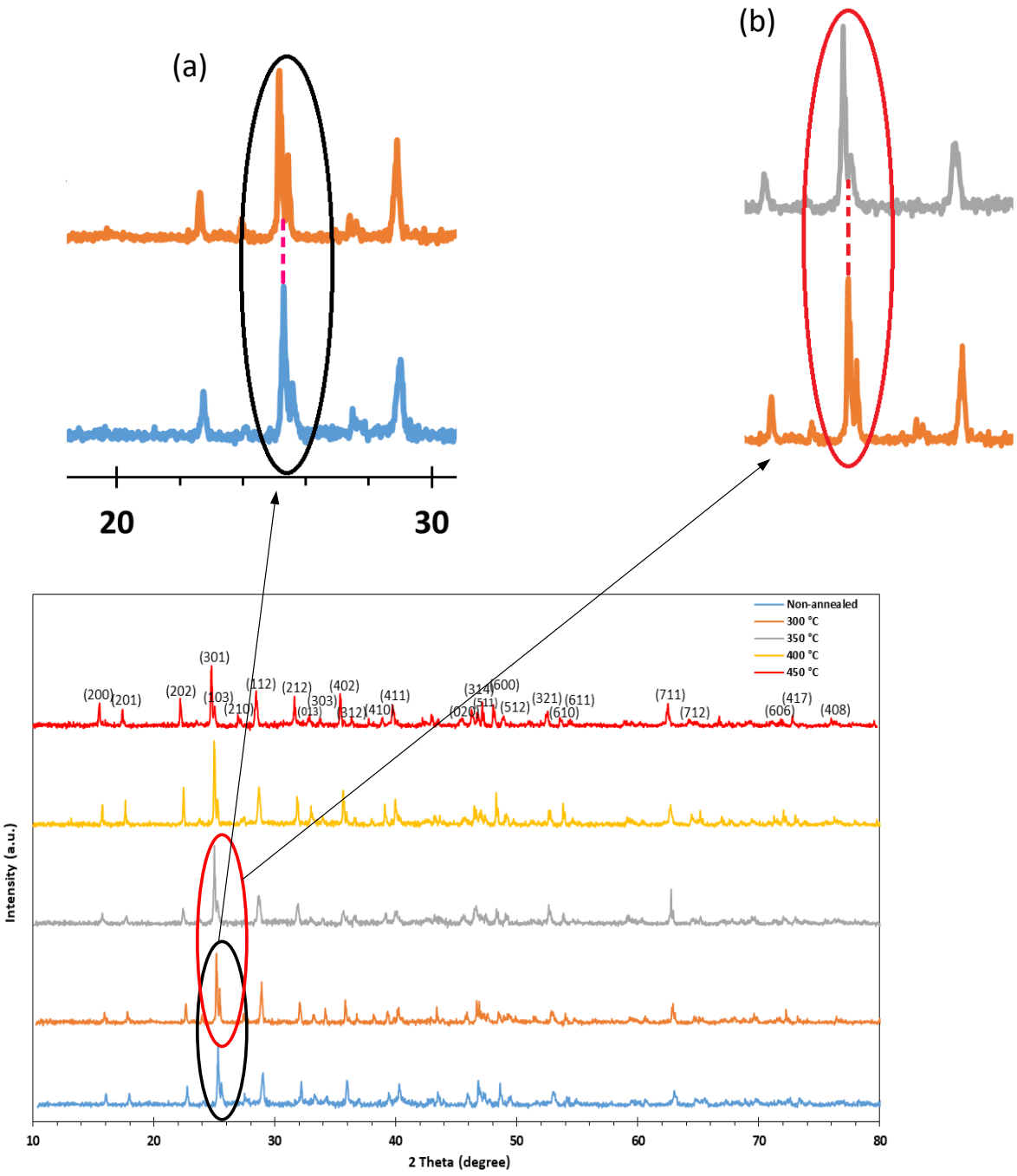


Figure 7- 11: Zoomed in view of XRD patterns of RCF-Bi_2S_3 composite annealed at different temperatures.

7.2.7 Effect of annealing temperature on the thermal stability of annealed RCF-Bi_2Te_3 composites

The thermal stabilities of annealed RCF-Bi_2Te_3 composites were evaluated using thermogravimetric analysis (TGA) and derivative thermogravimetric (DTG) studies. To the best of the author's knowledge, no prior work has studied the thermal stability of Bi_2Te_3 thermoelectric composites with respect to annealing temperatures.

The TGA results for annealed and non-annealed RCF-Bi_2Te_3 composites with respect to annealing temperatures are shown in **Figure 7- 12**.

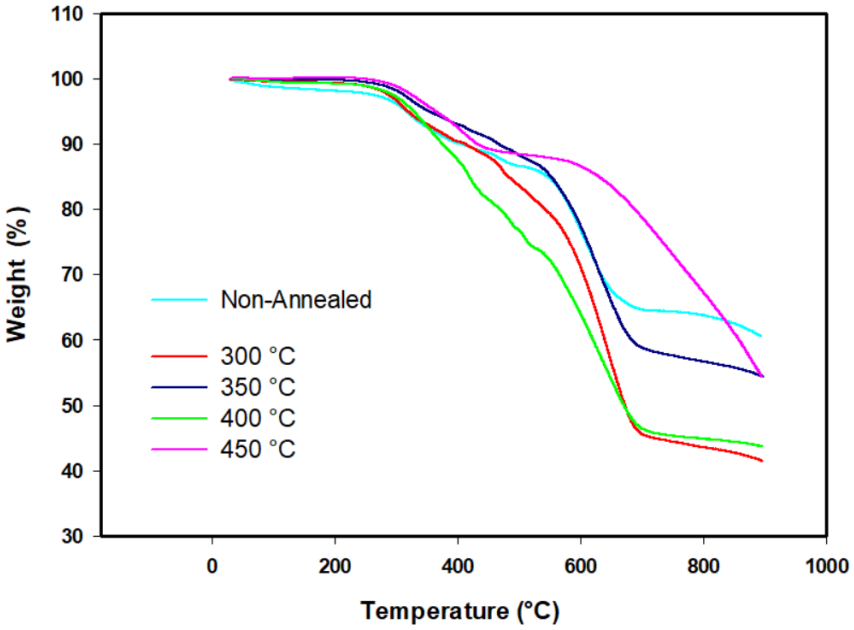


Figure 7- 12: TGA curves of RCF-Bi_2Te_3 composites annealed at different temperatures.

Based on **Figure 7- 12**, annealing improved the onset degradation temperature (T_{onset}) at 5% mass loss in RCF-Bi_2Te_3 composites from 316.2 °C (non-annealed) to 363.83 °C (450 °C). The improvement in T_{onset} may be probable because of the evaporation of volatile and weak bonding after annealing especially for RCF-Bi_2Te_3 composites annealed at higher temperatures. For RCF-Bi_2Te_3 composite annealed at 450 °C, there is a peculiar increase in the T_{onset} plausibly

because most volatile bonds may have evaporated at 400 °C and resulted in the formation of a more thermally stable compound at 450 °C. However this thermally improved structure has adverse thermoelectric properties as shown in **Figure 7- 3**.

The improvement in thermal stability of annealed RCF-Bi_2Te_3 composite is also highlighted in the improvement of the maximum degradation temperature (T_{max}) of the composites upon annealing as shown in **Figure 7- 13**. All annealed DTG curves shifted to the right as compared to the non-annealed curve, denoting an improvement in T_{max}. The T_{max} increased from 602.19 °C (non-annealed) to approximately 630 °C (300,350 and 400 °C). However at 450 °C, there is an extreme shift to the right at which the T_{max} was unable to be obtained due to the limitation of the TGA equipment that has maximum measurement temperature range of up to 1000 °C. Hence, it can be hypothesized that at 450 °C a much thermally stable compound is produced with a marginally larger T_{max} than the rest of the annealed samples. However though thermally more stable, the Bi_2Te_3 structure annealed at 450 °C may have lost elements and bonds responsible for thermoelectric capabilities as proven by its poor thermoelectric performance at this annealing temperature.

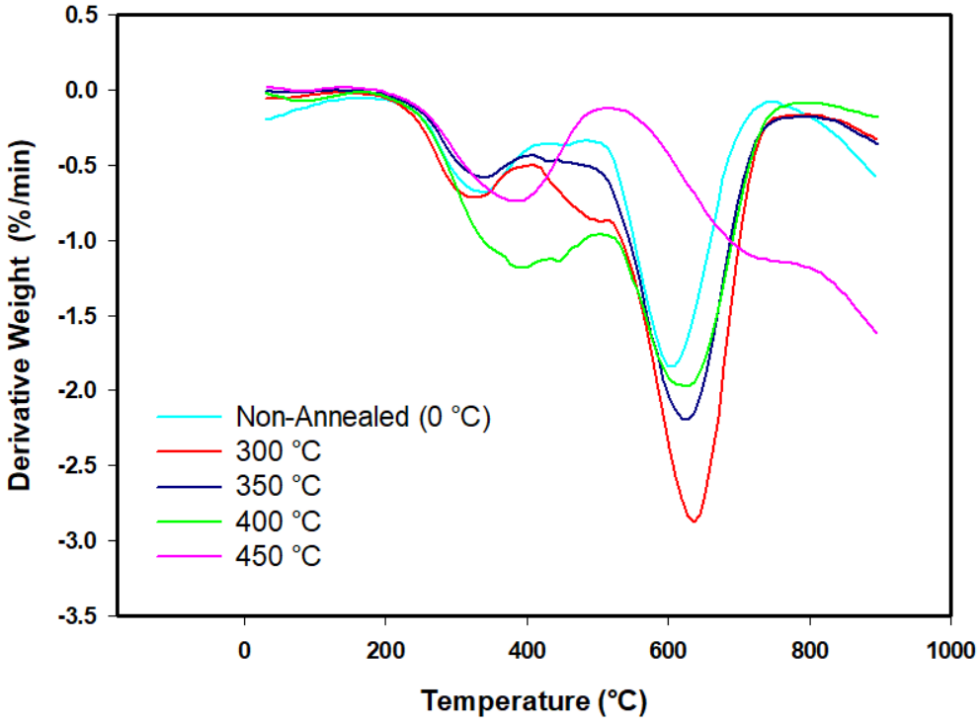


Figure 7- 13: DTG curves of RCF-Bi_2Te_3 composites annealed at various temperatures.

7.2.8 Effect of annealing temperature on the thermal stability of annealed RCF-Bi_2S_3 composites

The thermal stabilities of annealed RCF-Bi_2S_3 composites were evaluated using thermogravimetric analysis (TGA) and derivative thermogravimetric (DTG) studies. To the best of the author's knowledge, no prior work has studied the thermal stability of Bi_2S_3 thermoelectric composites with respect to annealing temperatures.

The TGA results for annealed and non-annealed RCF-Bi_2S_3 composites with respect to annealing temperatures are shown in **Figure 7- 14**.

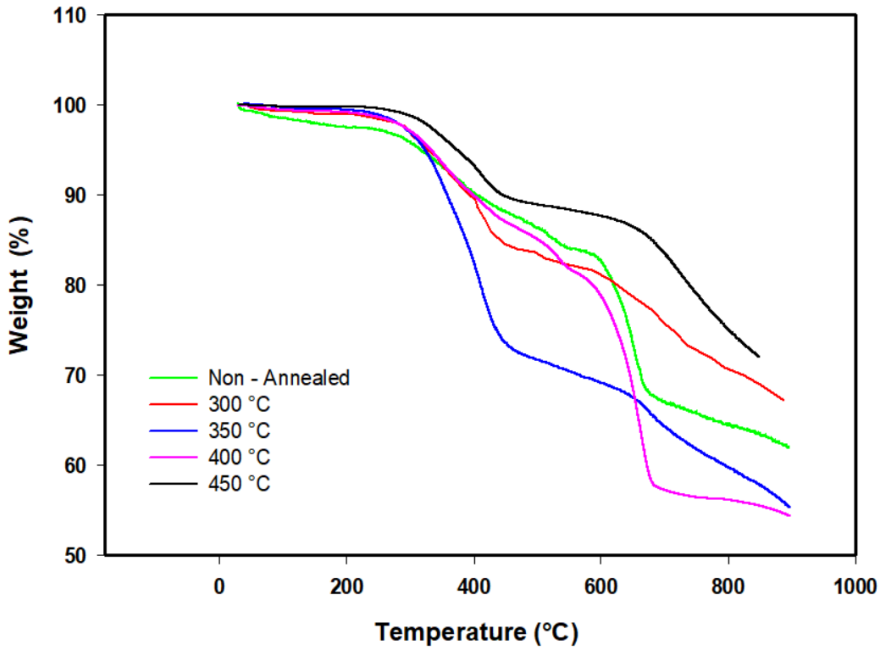


Figure 7- 14: TGA curves of RCF-Bi_2S_3 composites annealed at different temperatures.

Similar to that of annealed RCF-Bi_2Te_3 composites, annealing also improved the onset degradation temperature (T_{onset}) at 5% mass loss in RCF-Bi_2S_3 composites from 316.32 °C (non-annealed) to approximately 328-332 °C (300,350 and 400 °C) as shown in **Figure 7- 14**. The improvement in T_{onset} may be attributed to the evaporation of volatile and weak bonding after annealing.

For RCF-Bi_2S_3 composite annealed at 450 °C, there is a much larger improvement in T_{onset} to 373.94 °C. However though thermally more stable, the Bi_2S_3 structure annealed at 450 °C may have lost elements and bonds responsible for thermoelectric capabilities as proven by its poor thermoelectric performance at this annealing temperature as shown in **Figure 7- 6**.

The improvement in thermal stability of annealed RCF-Bi_2S_3 composite is also highlighted in the improvement of the maximum degradation temperature (T_{max}) of the composites upon annealing as shown in **Figure 7- 15**. The DTG curve exhibits two distinct peaks at which thermal degradation occurs at approximately 400 °C and 638.88 °C. For samples annealed at 300 °C and 350 °C, the T_{max} is at 400 °C, whereas for the rest of the samples the T_{max} is at 638.88 °C. At both degradation peaks, all annealed samples shifted to the right and depicted an improvement in the T_{max} as compared to that of non-annealed sample.

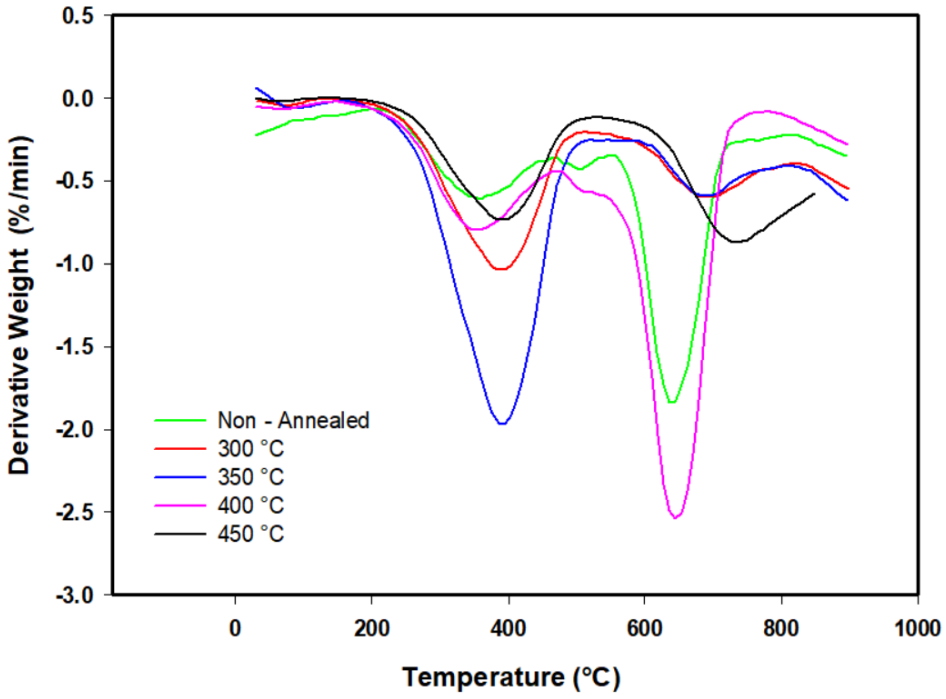


Figure 7- 15: DTG curves of RCF-Bi2S3 composites annealed at various temperatures.

7.2.9 Effect of annealing time on the thermoelectric properties of annealed RCF-Bi_2Te_3

As obtained from Section 7.2.1, the optimum annealing temperature for RCF-Bi_2Te_3 composites is 350 °C. In this section, the effect of varying annealing time at 350 °C will be studied. The Seebeck coefficient, electrical resistivity, and power factor of RCF-Bi_2Te_3 composites annealed at 350 °C subjected to varying annealing time are shown in **Figure 7- 16** to **Figure 7- 18**. The influence of annealing time on the Seebeck coefficient is illustrated in **Figure 7- 16**. The results show that all annealed samples are n-type having a negative Seebeck coefficient. As the annealing time increased, the Seebeck coefficient increased from -39.84 µV/K (non-annealed) to a maximum of -214.27 µV/K (2 hours) denoting a 437% improvement in Seebeck coefficient.

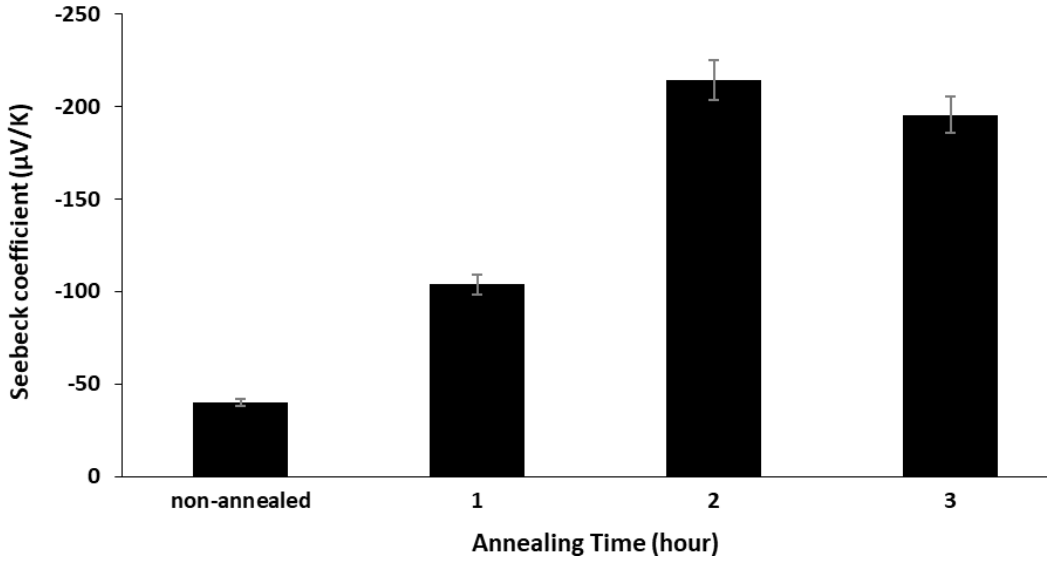


Figure 7- 16: The influence of annealing time on the Seebeck coefficient of RCF-Bi_2Te_3 composites.

Heat energy supplied during annealing allowed for the redistribution and reorganisation of bismuth and tellurium atoms, the tellurium content increased from 58.42 at.% (non-annealed) to 59.46 at.% (2 hours) as shown in **Table 7- 7**. The increase in tellurium content also led to a subsequent decrease in the carrier concentration from 6.01×10^{20} cm^{-3} (non-annealed) to 1.15

$\times 10^{19}$ cm^{-3} (2 hours) as depicted in **Table 7- 8** which resulted in the increased Seebeck coefficient. A similar decrease of carrier concentration was observed for sputtered stoichiometric Bi_2Te_3 and Te-rich Bi_2Te_3 specimens that were subjected to rapid thermal annealing(Kim and Lee, 2006).

Table 7- 7: Effect of annealing time on the Bi and Te content in the RCF-Bi_2Te_3 composites.

Annealing Time (hour)	Te (at %)	Bi (at %)
non-annealed	58.42	41.58
1	59.1	40.9
2	59.46	40.54
3	58.88	41.12

Table 7- 8: Carrier concentration and carrier mobility of RCF-Bi_2Te_3 composites with respect to annealing time.

Annealing Time (hour)	Carrier Concentration (cm^{-3})	Carrier Mobility ($cm^2V^{-1}s^{-1}$)
non-annealed	6.01×10^{20}	1.27×10^{-2}
1	4.91×10^{19}	3.52×10^{-1}
2	1.15×10^{19}	9.28×10^{-1}
3	1.35×10^{19}	9.42×10^{-1}

However, prolonging the annealing duration beyond two hours has a detrimental effect on the Seebeck coefficient of RCF-Bi_2Te_3 composites as displayed in **Figure 7- 16**. The prolonged exposure to heat at 350 °C led to a slight evaporation of Te from 59.46 at.% (2 hours) to 58.88 at.% (3 hours) as shown in **Table 7- 7**. Though Te element tends to sublime out of Bi_2Te_3 at temperatures higher than 400 °C due to its low melting point and high evaporation pressure as previously reported by (Kim and Lee, 2006; J. Lee et al., 2012), however Ohsugi et al. (Ohsugi et al., 2015) has reported the plausibility of Te sublimation at temperatures lower than 400 °C. This is because within the Bi_2Te_3 structure the thermal expansion perpendicular to the Te layers are more prominent than the thermal expansion parallel to the tellurium layers, thus spacing between tellurium layers is increased when subjected to heating. In addition to the thermal expansion, Te easily sublimes out due to the van der Waals bond between neighbouring tellurium layers in the Bi_2Te_3 structure (Liu et al., 2011; Singkaselit et al., 2017). The evaporation Te is also validated by the increase in carrier concentration from 1.15×10^{19} cm^{-3} (2 hours) to 1.35×10^{19} cm^{-3} (3 hours) as shown in **Table 7- 8**. Each tellurium vacancy (V_{Te}) generates two electrons per defect(Liu et al., 2011), thus contributing to the overall increase in carrier concentration and subsequent decrease in Seebeck coefficient at 3 hours.

The influence of annealing time on the electrical resistivity is illustrated in **Figure 7- 17**. The electrical resistivity initially was reduced by approximately 56% from 0.0082 Ω.m (non-annealed) to 0.0036 Ω.m (1 hour). This decrease in resistivity is attributed to the 2671% improvement in carrier mobility from 1.27×10^{-2} $cm^2V^{-1}s^{-1}$ (non-annealed) to 3.52×10^{-1} $cm^2V^{-1}s^{-1}$ (1 hour), though annealing decreased the carrier concentration of Bi_2Te_3 particles, however as the improvement in carrier mobility was larger than the percentage drop in carrier concentration thus decreasing the electrical resistivity as shown in **Table 7- 8**.

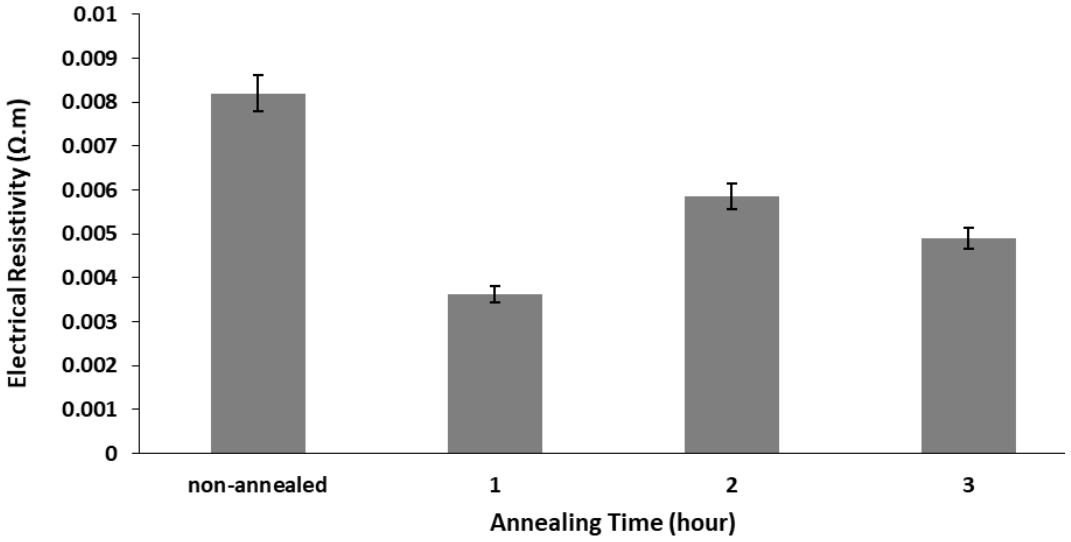


Figure 7- 17: The influence of annealing time on the electrical resistivity of RCF-Bi_2Te_3 composites.

In addition to the carrier transport properties, annealing also improved the bismuth and tellurium content to more stoichiometric proportions from 58.42 at.% of Te (non-annealed) to 59.1 at.% of Te (1 hour) as shown in **Table 7- 7**, resulting in lower carrier trapping and a defect free band gap allowing electrons to transfer efficiently from the valence band to the conduction band. At 2 hours of annealing time, slight increase in resistivity is observed from 0.0036 Ω.m (1 hour) to 0.0059 Ω.m (2 hours), this is due to the continuous decrease in carrier concentration owing to annealing. Prolonged annealing at 350 °C beyond 2 hours results in tellurium evaporation, the tellurium content changes from 59.46 at.% (2 hours) to 58.88 at.% (3 hours) shown in **Table 7- 7**. However as the bismuth content increases in the bismuth telluride alloy owing to evaporation of Te, it depicts a metallic property with a corresponding increase in carrier concentration from 1.15×10^{19} cm^{-3} (2 hours) to 1.35×10^{19} cm^{-3} (3 hours) resulting in reduced electrical resistivity as shown in **Figure 7- 17**.

The influence of annealing time on the power factor is illustrated in **Figure 7- 18**. The power factor increases with respect to annealing duration and reaches a maximum power factor of 7.80-7.83 $\mu WK^{-2}m^{-1}$ within 2-3 hours of duration. All annealed samples exhibited a higher power factor than that of the non-annealed counterpart owing to annealing induced nucleation, grain growth and redistribution of bismuth and tellurium atoms. Therefore, the optimum annealing time for RCF-Bi_2Te_3 composites is 2 hours with a maximum power factor of 7.83 $\mu WK^{-2}m^{-1}$. As annealing beyond two hours leads to tellurium loss and alters the stoichiometry of Bi_2Te_3 which is not favourable for its thermoelectric properties.

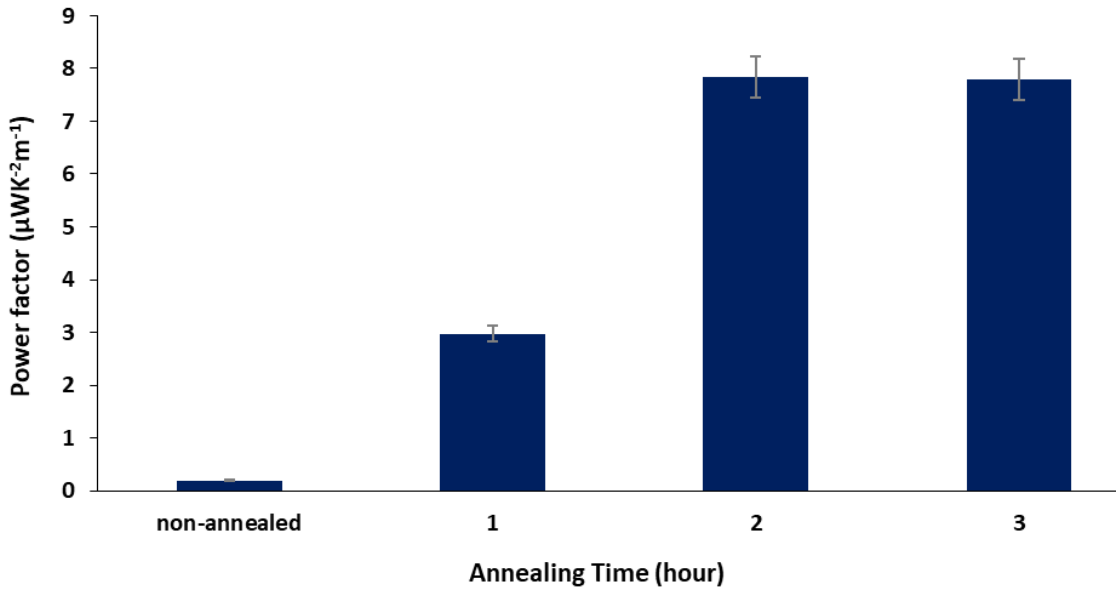


Figure 7- 18: The influence of annealing time on the power factor of RCF-Bi_2Te_3 composites.

7.2.10 Effect of annealing time on the thermoelectric properties of annealed RCF-Bi_2S_3

As obtained from Section 7.2.2, the optimum annealing temperature for RCF-Bi_2S_3 composites is 400 °C. In this section, the effect of varying annealing time at 400 °C will be studied. The Seebeck coefficient, electrical resistivity, and power factor of RCF-Bi_2S_3 composites annealed at 400 °C subjected to varying annealing time are shown in **Figure 7- 19** to **Figure 7- 21**. The influence of annealing time on the Seebeck coefficient is illustrated in **Figure 7- 19**. Similar to that of annealed RCF-Bi_2Te_3 composites, all annealed samples of Bi_2S_3 also exhibited n-type conductivity with negative Seebeck coefficient. With increasing duration of annealing, the Seebeck coefficient increased by approximately 65% from -143.56 µV/K (non-annealed) to a maximum of -236.36 µV/K (2 hours) owing to nucleation and grain growth induced by annealing. The increase in Seebeck coefficient is attributed to the improvement in carrier mobility by two orders as shown in **Table 7- 9** from 6.67×10^{-2} $cm^2V^{-1}s^{-1}$ (non-annealed) to 6.45×10^{0} $cm^2V^{-1}s^{-1}$ (2 hours). The increased grain growth, reduced grain boundaries and reduced crystal lattice deficiencies contributed to the improvement in carrier mobility (Hussain et al., 2014).

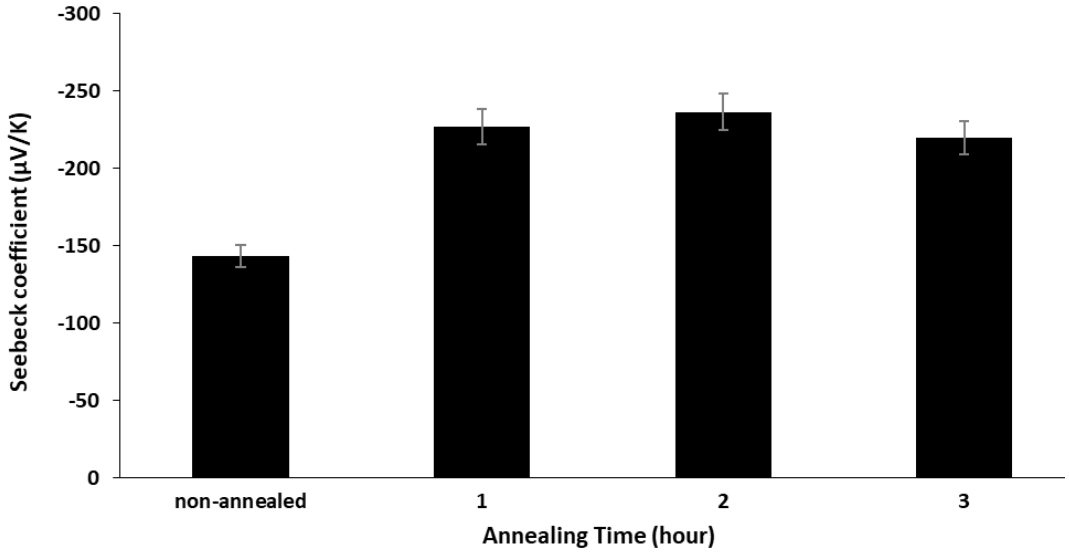


Figure 7- 19: The influence of annealing time on the Seebeck coefficient of RCF-Bi_2S_3 composites.

Table 7- 9: Carrier concentration and carrier mobility of RCF-Bi_2S_3 composites with respect to annealing time.

Annealing Time (hour)	Carrier Concentration (cm^{-3})	Carrier Mobility ($cm^2V^{-1}s^{-1}$)
non-annealed	4.27×10^{18}	6.67×10^{-2}
1	4.95×10^{17}	5.51×10^{0}
2	4.41×10^{17}	6.45×10^{0}
3	5.01×10^{17}	6.39×10^{0}

Table 7- 10: Effect of annealing time on the Bi and S content in the RCF-Bi_2S_3 composites.

Annealing Time (hour)	S (at %)	Bi (at %)
non-annealed	62.54	37.46
1	61.05	38.95
2	60.98	39.02
3	57.07	42.93

The improvement in Seebeck coefficient may also be due to the improvement in the bismuth (Bi) and sulphur (S) content towards more stoichiometric proportions upon annealing. The S content reduced from 62.54 at.% (non-annealed) to 60.98 at.% (2 hours) upon annealing as shown in **Table 7- 10**, tailoring the Bi and S content closer to stoichiometric proportions of 60 at.% of S and 40 at.% of Bi. Stoichiometric specimens are less prone to carrier trapping thus enabling a longer mean free path for carrier transportation leading to improved Seebeck coefficient.

Prolonged annealing beyond 2 hours led to some preliminary sulphur evaporation at 400 °C as shown in **Table 7- 10**, 60.98 at.% of S (2 hours) to 57.07 at.% of S (3 hours). Though

sublimation of Bi_2S_3 is thought to occur at temperatures higher than 400 °C (Rincón and Nair, 1996), however with prolonged annealing it may be possible that Bi_2S_3 powders closer to the walls of the furnace may be subjected to temperatures higher than 400 °C resulting in some loss of sulphur. The enrichment of Bi in the Bi_2S_3 structure upon annealing at 3 hours, have also rendered more metallic behaviours with increased carrier concentrations at 3 hours as shown in **Table 7- 9**. Thus, resulting in decreased Seebeck coefficient at 3 hours as shown in **Figure 7- 19**.

The influence of annealing time on the electrical resistivity is illustrated in **Figure 7- 20**. Annealing reduced the electrical resistivity of RCF-Bi_2S_3 composites by approximately 90% from 0.219 Ω.m (non-annealed) to 0.022 Ω.m (2 hours). The massive decrease in electrical resistivity is due to the two order improvement in carrier mobility from 6.67×10^{-2} $cm^2V^{-1}s^{-1}$ (non-annealed) to a maximum of 6.45×10^{0} $cm^2V^{-1}s^{-1}$ (2 hours) as shown in **Table 7- 9**. The improvement in carrier mobility is attributed to: (i) increase in grain size and reduced grain boundaries due to annealing which will be discussed in Section 7.2.12 (Symeou et al., 2015) and (ii) redistribution of Bi and S atoms towards stoichiometric proportions, the S content decreased from 62.54 at.% (non-annealed), 61.05 at.% (1 hour) and 60.98 at.% (2 hours) as shown in **Table 7- 10**. Thus reducing defects and vacancies in the Bi_2S_3 structure and generating a defect free band gap void of carrier traps (Abdullaev et al., 2001). However, beyond 2 hours the decrease in resistivity is attributed to the concentration of Bi_S antisite defect that is likely to occur due to the sulphur loss which is proven by the increase in carrier concentration from 4.41×10^{17} cm^{-3} (2 hours) to 5.01×10^{17} cm^{-3} (3 hours). A similar increase in carrier concentration was observed by Symeou et al. in annealed $Bi_{0.5}Sb_{1.5}Te_3$ with Bi_{Te} antisite defects(Symeou et al., 2015).

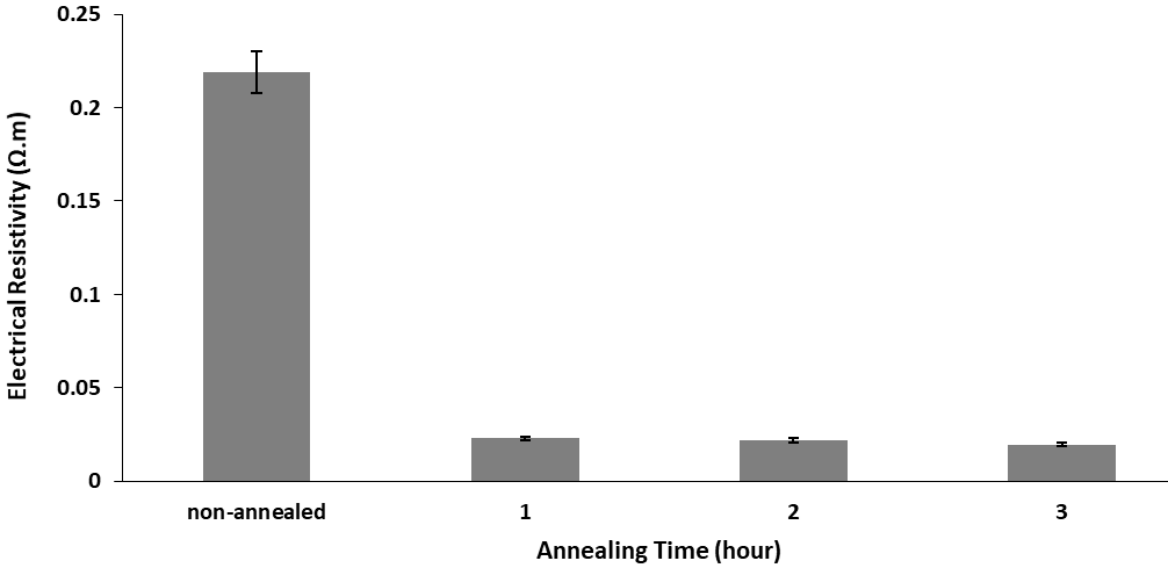


Figure 7- 20: The influence of annealing time on the electrical resistivity of RCF-Bi_2S_3 composites.

The influence of annealing time on the power factor is illustrated in **Figure 7- 21**. The power factor of RCF-Bi_2S_3 composites increased with respect to annealing duration and reached a maximum power factor of 2.551 $\mu WK^{-2}m^{-1}$ at 2 hours. All annealed RCF-Bi_2S_3 composites exhibited power factors 24-27 times higher than that of its non-annealed counterpart. From 3 hours onwards, there is a slight deviation in the stoichiometric composition of Bi_2S_3 perhaps owing to some preliminary sulphur loss at 400 °C, thus resulting in a 3 % decrease in power factor from 2 hours. Therefore, the optimum annealing time for RCF-Bi_2S_3 composites is 2 hours with a maximum power factor of 2.551 $\mu WK^{-2}m^{-1}$. As annealing beyond two hours leads to sulphur loss and alters the stoichiometry of Bi_2S_3 which is not favourable for its thermoelectric properties.

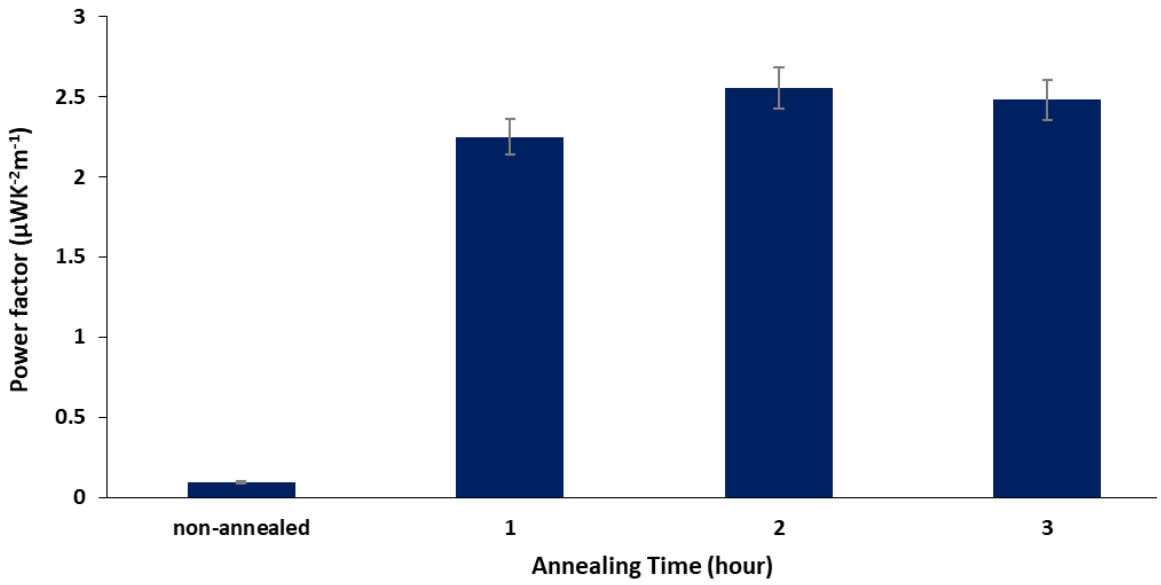


Figure 7- 21: The influence of annealing time on the power factor of RCF-Bi_2S_3 composites.

7.2.11 Effect of annealing time on the morphology of annealed RCF-Bi_2Te_3 composites

Figure 7- 22 below shows the surface morphology images of RCF-Bi_2Te_3 composites annealed at 350 °C with varying annealing duration.

The grain size of all annealed Bi_2Te_3 particles were larger than that of non-annealed sample and grain size also increased with respect to increase in annealing duration as shown in **Figure 7- 22**. The increment in grain size upon annealing led to decreased density of grain boundaries, thus resulting in a one order improvement in carrier mobility for all annealed samples from 1.27×10^{-2} $cm^2V^{-1}s^{-1}$ (non-annealed) to a maximum of 9.42×10^{-1} $cm^2V^{-1}s^{-1}$ (3 hour) as shown in **Table 7- 8**. When there are fewer grain boundaries, there are fewer scattering centres thus requiring lower energy when electrons move from one grain to the other resulting in improved carrier mobility. The improved carrier mobility resulted in a simultaneous increase in both Seebeck coefficient and electrical conductivity as shown in **Figure 7- 16** and **Figure 7- 17**

resulting in higher power factors for annealed RCF-Bi_2Te_3 composites. The optimum annealing duration is 2 hours as there was no significant improvement in grain growth between that of 2 and 3 hours, that was also reflected on its power factor that remained almost constant between this duration as shown in **Figure 7- 18**.

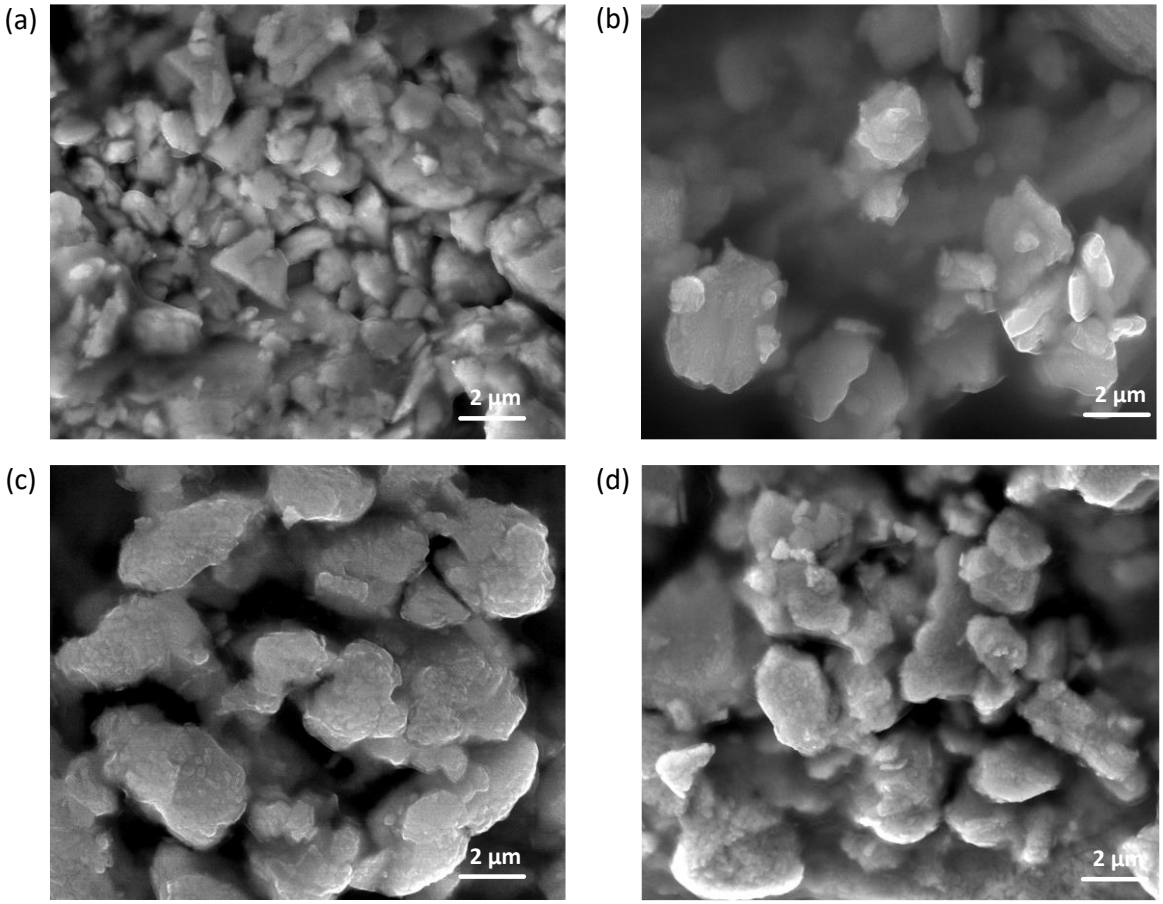


Figure 7- 22: FESEM surface images of RCF-Bi_2Te_3 composites annealed at 350 °C for (a) non-annealed (b) 1 hour (c) 2 hour (d) 3 hour.

7.2.12 Effect of annealing time on the morphology of annealed RCF-Bi_2S_3 composites

Figure 7- 23 below shows the surface morphology images of RCF-Bi_2S_3 composites annealed at 400 °C with varying annealing duration.

Similar to that of annealed RCF-Bi_2Te_3 composites, the grain size of all annealed RCF-Bi_2S_3 composites is visibly larger than that of non-annealed sample as shown in **Figure 7- 23**. The grain growth is owing to grain boundary diffusion of atoms that coalesce small grains to form larger grains in solid state annealing. The grain size of Bi_2S_3 atoms is also seen to increase with annealing duration as shown in **Figure 7- 23 (b-d)** that led to improved carrier mobility in annealed RCF-Bi_2S_3 composites due to decreased grain boundaries. The carrier mobility improved by two orders from 6.67×10^{-2} $cm^2V^{-1}s^{-1}$ (non-annealed) to a maximum of 6.45×10^{0} $cm^2V^{-1}s^{-1}$ (2 hour) as shown in **Table 7- 9**. Between that of 2 and 3 hours, there was no significant grain growth improvement observed, however there was some loss of sulphur observed at 3 hours hence annealing duration beyond 3 hours was not investigated.

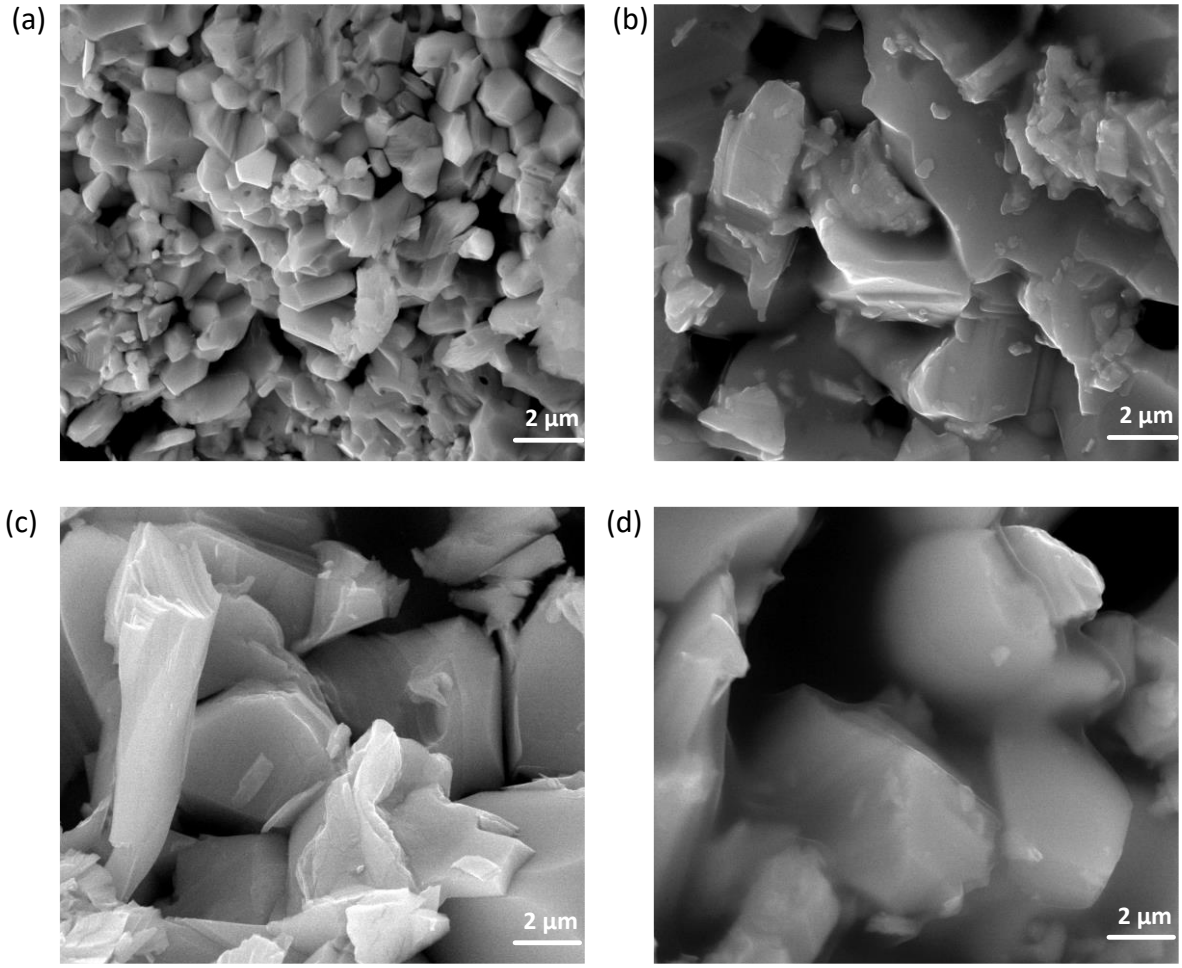


Figure 7- 23: FESEM surface images of RCF-Bi_2S_3 composites annealed at 400 °C for (a) non-annealed (b) 1 hour (c) 2 hour (d) 3 hour.

7.2.13 Effect of annealing time on the XRD analysis of annealed RCF-Bi_2Te_3 composites

X-ray diffraction (XRD) patterns of RCF-Bi_2Te_3 (non-annealed) and annealed RCF-Bi_2Te_3 with respect to different annealing durations at a constant annealing temperature of 350 °C is as shown in **Figure 7- 24**. All XRD patterns shown in **Figure 7- 24** have the following 12 diffraction peaks located at 2θ, 17.59°, 27.78°, 37.93°, 40.42°, 41.27°, 44.64°, 50.37°, 54.00°, 57.17°, 62.31°, 66.04° and 67.17° with orientations of (006), (015), (1010), (0111), (110), (0015), (205), (1016), (0210), (1115), (0120) and (125). These values are in good agreement with standard data of Joint Committee on Powder Diffraction Standards (PDF 00-015-0863) data and the observed peak positions are consistent with the structure of Bi_2Te_3 and observed peak positions are represented by their corresponding Miller indices in the spectra. The most prominent peak is (015) was used to calculate all XRD related parameters.

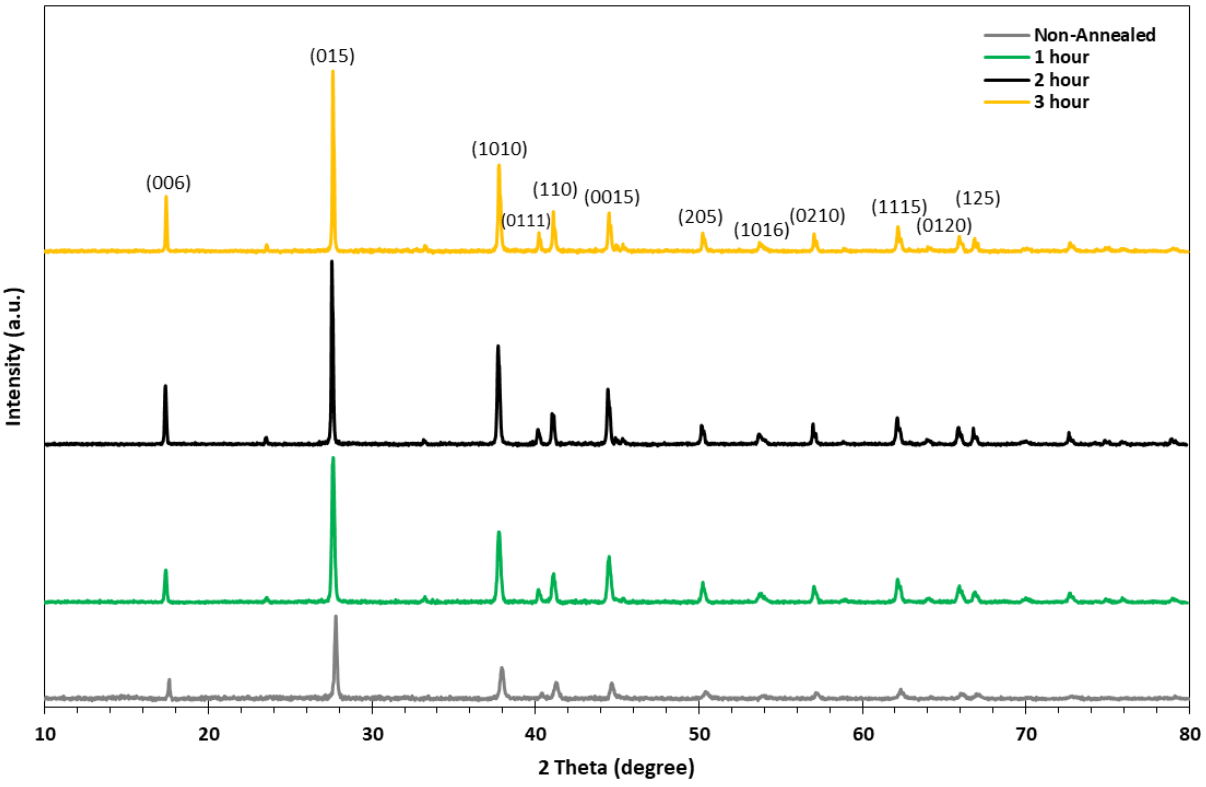


Figure 7- 24: XRD patterns of RCF-Bi_2Te_3 composite annealed at 350 °C for varying durations.

The D, ε and δ of the RCF-Bi_2Te_3 and annealed RCF-Bi_2Te_3 composites with respect to different annealing durations are as shown in **Table 7- 11**.

Table 7- 11: FWHM, crystallite size, microstrain and dislocation density of RCF-Bi_2Te_3 annealed at 350 °C with varying durations.

Annealing Time (hours)	FWHM (radian)	Crystallite size, D (nm)	Microstrain (ε x 10^{-3}) ($lines^{-2}\,m^{-4}$)	Dislocation density (δ x 10^{14}) ($lines/m^2$)
non-annealed	0.0030	47.01	3.1	4.52
1	0.0028	49.56	2.9	4.07
2	0.0023	61.94	2.3	2.60
3	0.0022	63.88	2.3	2.45

All annealed samples exhibited higher peak intensities than that of the non-annealed sample as shown in **Figure 7- 24**. The crystallinity of samples also increased with increasing duration of annealing, which resulted in decreased FWHM values from 0.0030 (non-annealed) to 0.0022 (3 hours) as shown in **Table 7- 11**. The improvement in crystallinity is due to the high thermal energy supplied during annealing that enhanced crystallization of the Bi_2Te_3 particles, leading to sharp and narrower peaks in the XRD pattern and corresponding lower FWHM values. There was only slight improvement in crystallinity in samples annealed at 2 and 3 hours as the FWHM remained at 0.0022-0.0023 as shown in **Table 7- 11**.

The crystallite size, D of all annealed samples was larger than that of the non-annealed sample as shown in **Table 7- 11**. D increased from 47.01 nm (non-annealed) to 63.88 nm (3 hours). The increase in D is a result of the agglomeration and enlargement of Bi_2Te_3 grains when annealed. This is also reflected in the larger grain size of annealed Bi_2Te_3 particles as shown in **Figure 7- 22**. With larger grain sizes, there is a reduction in grain boundaries and larger

effective mean free path for carrier transportation, which is reflected in the improvement in carrier mobility from 1.27×10^{-2} $cm^2V^{-1}s^{-1}$ (non-annealed) to 9.42×10^{-1} $cm^2V^{-1}s^{-1}$ (3 hours) as shown in **Table 7- 8**.

The microstrain, ε and dislocation density, δ as shown in **Table 7- 11** was also seen to decrease with respect to increase in annealing duration. The decrease in ε and δ is due to the reduction in lattice defects upon annealing. Amorphous like materials are known to contain larger amount of defects with higher carrier concentrations (Hamada and Takashiri, 2017), however with annealing as the crystallinity is improved and the amorphous phase is reduced, there will be lower defects within the lattice structure of Bi_2Te_3. However decreasing ε and δ did not reduce the electrical resistivity of annealed RCF-Bi_2Te_3 composites with respect to annealing duration beyond 1 hour as shown in **Figure 7- 17**, the electrical resistivity increased due to the massive decrease in carrier concentration. Despite the increase in electrical resistivity, all annealed RCF-Bi_2Te_3 composites exhibited higher power factor than that of the non-annealed sample as shown in **Figure 7- 18**, due to reduced lattice defects that improved carrier mobility by one order compared to its non-annealed counterpart.

7.2.14 Effect of annealing time on the XRD analysis of annealed RCF-Bi_2S_3 composites

XRD patterns of RCF-Bi_2S_3 (non-annealed) and annealed RCF-Bi_2S_3 with respect to different annealing durations at a constant annealing temperature of 400 °C are shown in **Figure 7- 25**. All XRD patterns shown in **Figure 7- 25** have the following 27 diffraction peaks located at 2θ, 15.75°, 17.62°, 22.43°,24.99°, 25.23°, 27.49°, 28.65°, 31.84°, 33.04°, 33.96°, 35.65°, 36.68°, 39.09°, 39.95°, 45.60°, 46.51°, 47.05°, 48.48°, 49.21°, 52.63°, 53.86°, 54.77°, 62.68°, 64.57°, 72.04°,73.05° and 76.21° with orientations of (200), (201), (202),(301),(103), (210), (112), (212), (013), (303), (402), (312), (410), (411), (020), (314), (511), (600), (512), (321), (610), (611), (711), (712), (606), (417) and (408). These values are in good agreement with standard data of Joint Committee on Powder Diffraction Standards (PDF 01-074-9437) data and the observed peak positions are consistent with the structure of Bi_2S_3 and observed peak positions are represented by their corresponding Miller indices in the spectra. The most prominent peak is (301) was to calculate all XRD related parameters.

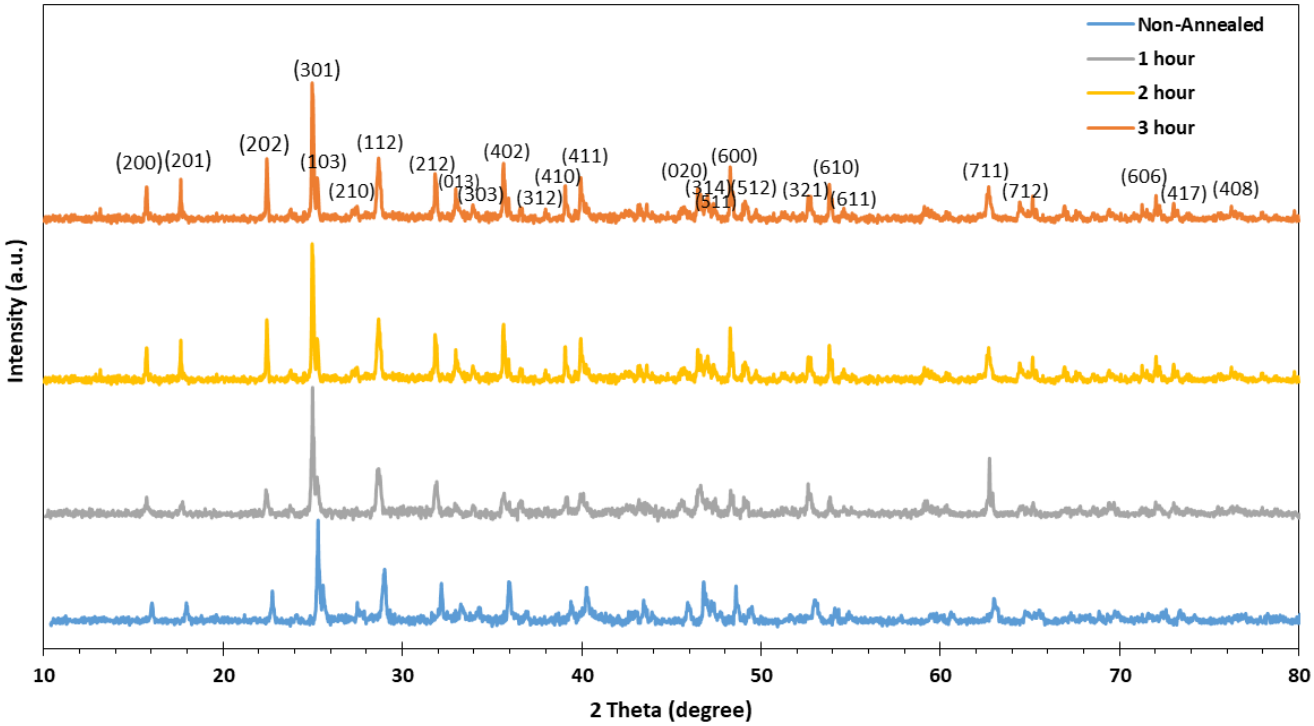


Figure 7- 25: XRD patterns of RCF-Bi_2S_3 composite annealed at 400 °C for varying durations.

The D, ε and δ of the RCF-Bi_2S_3 and annealed RCF-Bi_2S_3 composites with respect to different annealing durations are as shown in **Table 7- 12**.

Table 7- 12: FWHM, crystallite size, microstrain and dislocation density of RCF-Bi_2S_3 annealed at 400 °C with varying durations.

Annealing Time (hours)	FWHM (radian)	Crystallite size, D (nm)	Microstrain (ε x 10^{-3}) ($lines^{-2}\ m^{-4}$)	Dislocation density (δ x 10^{14}) ($lines/m^2$)
non-annealed	0.0027	52.14	3.1	3.68
1	0.0023	62.09	2.6	2.59
2	0.0022	65.07	2.5	2.36
3	0.0021	66.13	2.4	2.29

With increasing annealing duration the peak intensity increased and became narrower indicating an improvement in its crystallinity upon annealing as shown in **Figure 7- 25**. The improvement in crystallinity is also reflected with the decreased FWHM values from 0.0027 (non-annealed) to 0.0021 (3 hour) as shown in **Table 7- 12**. Crystallinity was improved after annealing because of the thermal energy supplied during annealing that promoted the crystallisation and grain coalescence of Bi_2S_3 particles. However, it should be emphasised that there was only slight changes in the FWHM values of annealed samples ranging from 0.0021-0.0023 as shown in **Table 7- 12** with respect to varying annealing duration.

The crystallite size, D of all annealed samples was larger than that of the non-annealed sample as shown in **Table 7- 12**. D increased from 52.14 nm (non-annealed) to 66.13 nm (3 hours). The increase in D is a result of the agglomeration and enlargement of Bi_2S_3 grains when

annealed. This is also reflected in the larger grain size of annealed Bi_2S_3 particles as shown in **Figure 7- 23**. With larger grain sizes, there is a reduction in grain boundaries and larger effective mean free path for carrier transportation, which is reflected in the improvement in carrier mobility by two orders from 6.67×10^{-2} $cm^2V^{-1}s^{-1}$ (non-annealed) to a maximum of 6.45×10^{0} $cm^2V^{-1}s^{-1}$ (2 hours) as shown in **Table 7- 9**. Beyond 2 hours though there is an increase in D, however the carrier mobility drops from 6.45×10^{0} $cm^2V^{-1}s^{-1}$ (2 hours) to 6.39×10^{0} $cm^2V^{-1}s^{-1}$ (3 hours) as shown in **Table 7- 9**, owing to sulphur evaporation and off-stoichiometry of Bi_2S_3 at 3 hours that generates sulphur vacancies which act as scattering centres that deter the mobility of carriers.

The microstrain, ε and dislocation density, δ of annealed samples as shown in **Table 7- 12** was approximately 15-22 % and 29-38 % respectively lower than that of the non-annealed samples. Both ε and δ was also observed to decrease with respect to increasing annealing duration due to the reduction in lattice defects during annealing. The decrease in ε and δ also resulted in a corresponding small decrease in the electrical resistivity of the annealed RCF-Bi_2S_3 composites until 3 hours as shown in **Figure 7- 20**.

7.2.15 Effect of annealing time on the thermal stability of annealed RCF-Bi_2Te_3 composites

The thermal stabilities of RCF-Bi_2Te_3 composites annealed at 350 °C with varying durations were evaluated using thermogravimetric analysis (TGA) and derivative thermogravimetric (DTG) studies.

The TGA results for annealed and non-annealed RCF-Bi_2Te_3 composites with respect to annealing time are shown in **Figure 7- 26**.

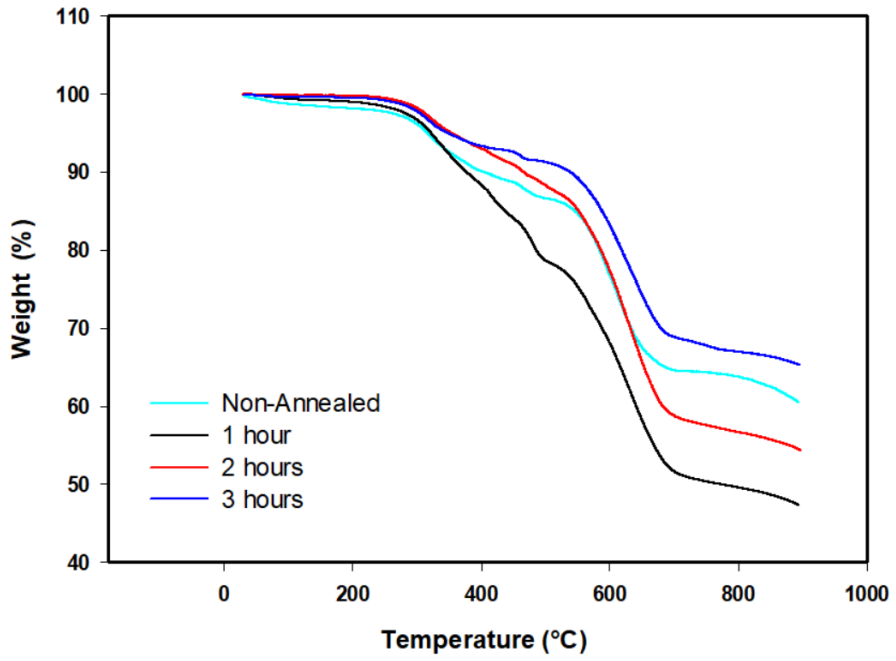


Figure 7- 26: TGA curves of RCF-Bi_2Te_3 composites annealed at different durations.

Based on **Figure 7- 26**, annealing improved the onset degradation temperature (T_{onset}) at 5% mass loss in RCF-Bi_2Te_3 composites from 316.2 °C (non-annealed) to 353.16 °C (2 hours). The improvement in T_{onset} could be attributed to the evaporation of volatile and weakly bonded elements during annealing (heat treatment). After two hours, the T_{onset} slightly decreased from 353.16 °C (2 hours) to 347.94 °C (3 hours).

The improvement in thermal stability of annealed RCF-Bi_2Te_3 composite is also highlighted in the improvement of the maximum degradation temperature (T_{max}) of the composites as shown

in **Figure 7- 27**. All annealed DTG curves shifted to the right as compared to the non-annealed curve, denoting an improvement in T_{max}. The T_{max} increased from 602.19 °C (non-annealed) to approximately 630 °C (1,2 and 3 hours). There was no observable change in T_{max} with varying annealing duration. Both TGA and DTG results indicate that with removal of volatile elements within the Bi_2Te_3 structure during annealing improved the thermal stability of the thermoelectric composites.

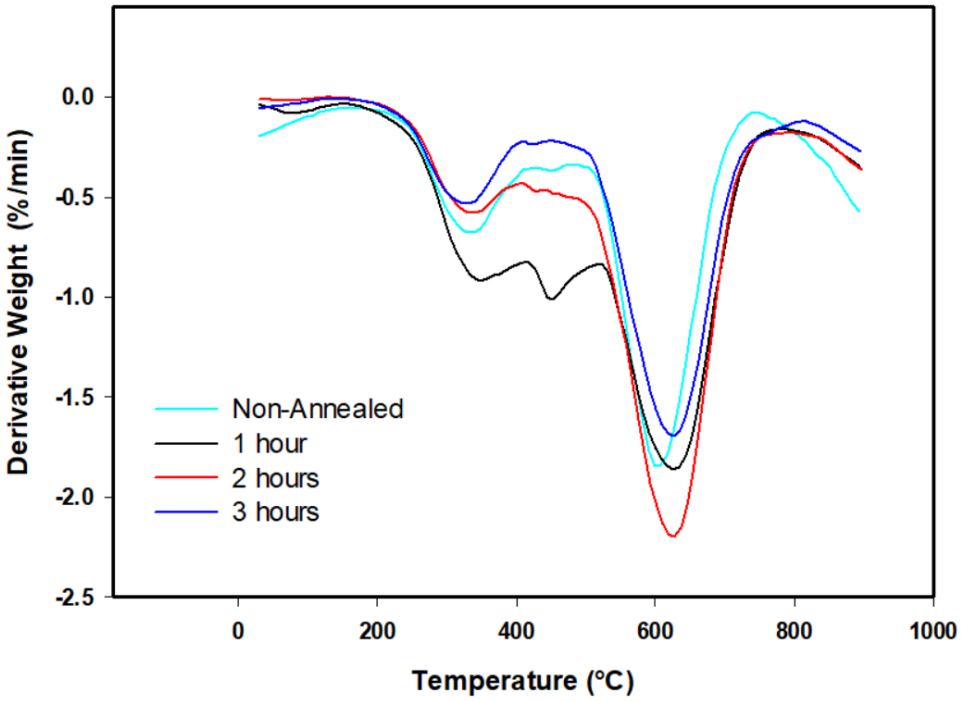


Figure 7- 27: DTG curves of RCF-Bi_2Te_3 composites annealed at various durations.

7.2.16 Effect of annealing time on the thermal stability of annealed RCF-Bi_2S_3 composites

The thermal stabilities of RCF-Bi_2S_3 composites annealed at 400 °C with varying durations were evaluated using thermogravimetric analysis (TGA) and derivative thermogravimetric (DTG) studies.

The TGA results for annealed and non-annealed RCF-Bi_2S_3 composites with respect to annealing time are shown in **Figure 7- 28**.

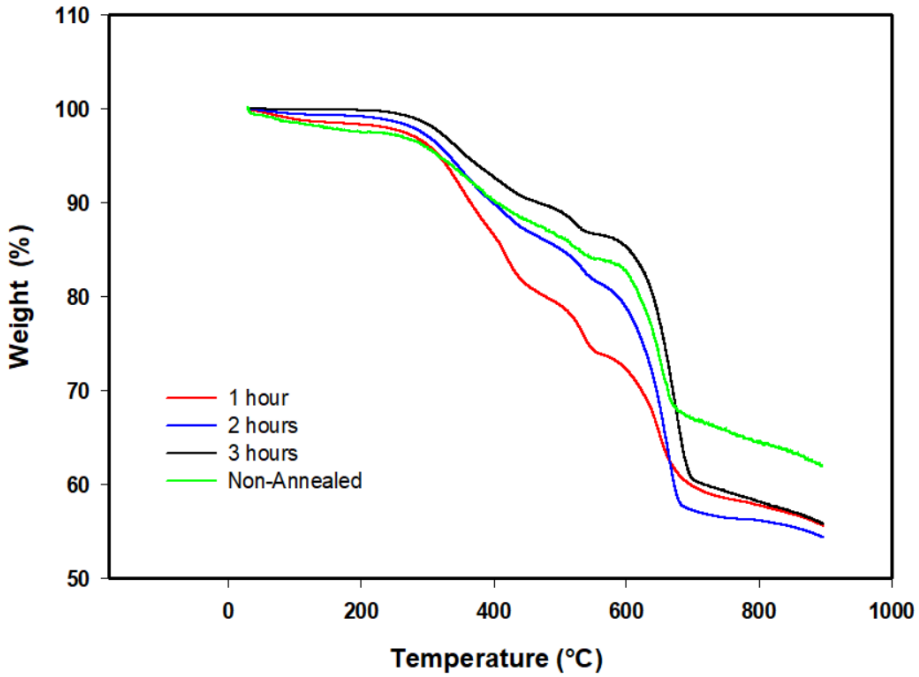


Figure 7- 28: TGA curves of RCF-Bi_2S_3 composites annealed at different durations.

Based on **Figure 7- 28**, annealing improved the onset degradation temperature (T_{onset}) at 5% mass loss in RCF-Bi_2S_3 composites from 316.32 °C (non-annealed) to 359.01°C (3 hours). The improvement in T_{onset} could be attributed to the evaporation of volatile and weakly bonded elements during annealing (heat treatment).

The improvement in thermal stability of annealed RCF-Bi_2S_3 composite is also highlighted in the improvement of the maximum degradation temperature (T_{max}) of the composites as shown in **Figure 7- 29**. All annealed DTG curves shifted very slightly to the right as compared to the non-annealed curve, denoting an improvement in T_{max}. The T_{max} increased from 638.88 °C (non-annealed) to approximately 645.92 °C (1 and 2 hours) and then 663.82 °C (3 hours).Both TGA and DTG results indicate that with removal of volatile elements within the Bi_2S_3 structure during annealing improved the thermal stability of the thermoelectric composites.

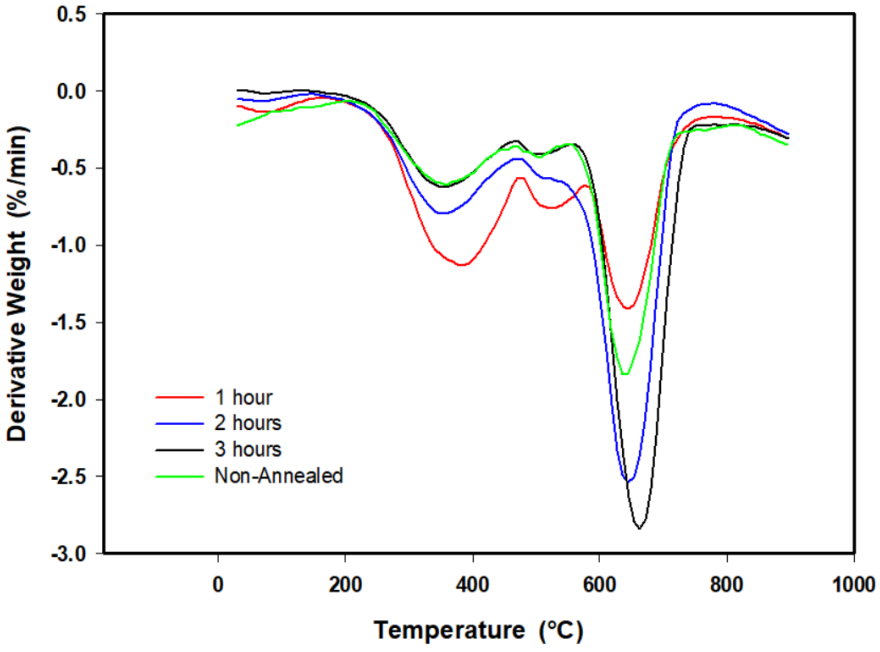


Figure 7- 29: DTG curves of RCF-Bi_2S_3 composites annealed at various durations.

7.3 Summary

In summary, the optimum annealing temperature for Bi_2Te_3 and Bi_2S_3 particles within the RCF composites are 350 and 400 °C respectively. In addition to temperature, the optimum annealing time for both RCF-Bi_2Te_3 and RCF-Bi_2S_3 is 2 hours. At optimum annealing temperature and time, the power factor of RCF-Bi_2Te_3 and RCF-Bi_2S_3 composites are 7.836 and 2.551 $\mu WK^{-2}m^{-1}$ respectively. Both annealed RCF-Bi_2Te_3 and RCF-Bi_2S_3 composites depicted a 4000 and 2600% improvement in power factor as compared to the non-annealed counterparts at optimum annealing temperature and time. Thus, it can be concluded that nucleation and grain growth enlargement during annealing with respect to temperature has brought about tremendous improvement in thermoelectric as well as structural properties in both Bi_2Te_3 and Bi_2S_3 particles.

Chapter 8: Conclusion and future works

8.1 Principal findings

This research work focused on utilising recycled carbon fibre in thermoelectric energy harvesting both as a flexible film and polymer composite. The following principal findings were obtained from this study:

(a) In the first part of this study, flexible thermoelectric films were formed by electrodepositing Bi_2Te_3 on recycled and virgin carbon fibres with varying electrolyte composition. The highest Seebeck coefficient of electrodeposited Bi_2Te_3 on recycled and virgin carbon fibres were -13.99 μV/K and-20.06 μV/K respectively using univariate optimisation. Seebeck coefficient of recycled carbon fibre was comparatively lower than that of virgin fibres in all cases. This could be attributed by the random orientation of recycled fibres, which does not allow uniform adhesion of the coatings on to the fibre. The virgin carbon fibre was merely used as a control to compare the difference in the Seebeck coefficient that arises from its fibre properties. After which, a multivariate optimisation approach using Design of Experiments software was carried out only on recycled fibre. This multivariate optimisation was conducted to determine the optimum electrodeposition parameters such as deposition potential, deposition time, deposition temperature, electrolyte composition and its corresponding effect on Seebeck coefficient. It can be concluded that a multi-parameter interaction yields a 33 % higher optimum response value (-17.25 μV/K) than univariate experimental design (-12.99 μV/K) due to the simultaneous effects of more than one deposition parameter as proven in this study. Even under optimum conditions of 45% lesser than the electrolyte concentration and 50% less deposition time, the Seebeck coefficient of multivariate optimisation (-13.42 μV/K) is still 3.3% higher than

that of univariate optimisation (-12.99 μV/K). The optimum parameters obtained were deposition potential: -0.10 V, deposition time: 0.5 hours, deposition temperature: 25 ºC, and electrolyte composition: 0.240 that yielded a decent Seebeck coefficient of -13.42 μV/K.

(b) The second part of this study focused on the development of a low-cost effective recycled carbon fibre polymer thermoelectric composite using a combination of hot compression and brushing technique. It compared the thermoelectric performance of Bi_2Te_3 to a non-toxic and environmentally friendly chalcogenide Bi_2S_3. The power factor improved by 34 and 17 times upon the incorporation of thermoelectric fillers (Bi_2Te_3 and Bi_2S_3) respectively as compared to that of bare RCF composite. The power factor of RCF composites increased with respect to increasing concentrations of Bi_2Te_3 and Bi_2S_3, however, it reached a maximum of 0.194 $\mu WK^{-2}m^{-1}$ and 0.094 $\mu WK^{-2}m^{-1}$ for RCF-Bi_2Te_3 and RCF-Bi_2S_3 at 45 wt% respectively. The thermoelectric properties of both RCF-Bi_2Te_3 and RCF-Bi_2S_3 were remarkably higher than that of bare RCF composite as proved by the Seebeck coefficient, electrical resistivity, carrier property measurement, FESEM, EDX, XRD and TGA analysis. This is because the presence of the thermoelectric fillers not only suppressed the carrier concentration but also improved the carrier mobility between the gaps of RCF strands, thus enhancing its thermoelectric capabilities. The environmentally friendly RCF-Bi_2S_3 thermoelectric composite is approximately 52% lower in power factor compared to that of RCF-Bi_2Te_3 composites due to its innate material property that has high electrical resistivity.

(c) The third part of the study focused on improving the thermoelectric properties of recycled carbon fibre polymer thermoelectric composite by doping it with MWCNTs. The optimum doping level of MWCNT for RCF-Bi_2Te_3 and RCF-Bi_2S_3 was 0.10 wt% and 0.15 wt% MWCNTs, respectively. At optimum doping level, MWCNTs enhanced the power factors of RCF-Bi_2Te_3 and RCF-Bi_2S_3 composites by approximately 438% and 800%, respectively. With the addition of MWCNT, the difference in power factor between RCF-Bi_2Te_3 and RCF-Bi_2S_3 was approximately 19% whereas the difference in power factor without the addition of MWCNT between RCF-Bi_2Te_3 and RCF-Bi_2S_3 was approximately 52%. This is a validation of the capability of MWCNT to improve the power factor of the environmentally friendly Bi_2S_3 thermoelectric composites to a comparable value with that of Bi_2Te_3. The highest power factor obtained for MWCNT doped RCF-Bi_2Te_3 and RCF-Bi_2S_3 were 1.044 and 0.849 $\mu WK^{-2}m^{-1}$, respectively.

(d) In the fourth part of this study, a thermal treatment known as annealing was used to improve the thermoelectric, electrical transport and crystalline properties of the thermoelectric fillers (Bi_2Te_3 and Bi_2S_3) in the recycled carbon fibre polymer thermoelectric composite. The optimum annealing temperature for Bi_2Te_3 and Bi_2S_3 particles within the RCF composites were 350 and 400 °C respectively. In addition to temperature, the optimum annealing time for both RCF-Bi_2Te_3 and RCF-Bi_2S_3 was 2 hours. At optimum annealing temperature and time, the power factor of RCF-Bi_2Te_3 and RCF-Bi_2S_3 composites were 7.836 and 2.551 $\mu WK^{-2}m^{-1}$ respectively. Both annealed RCF-Bi_2Te_3 and RCF-Bi_2S_3 composites depicted a 4000% and 2600% improvement in power factor at optimum annealing temperature and time as compared to the non-annealed counterparts.

As an overall conclusion, the research work presented in this thesis highlights the plausibility of using recycled materials such as recycled carbon fibre in the forms of films

and composites for thermoelectric applications. This research adds value and also open up a different avenue of application for waste materials such as recycled carbon fibre in energy harvesting applications. From a technological aspect, this research has also highlighted the plausibility of developing a cost effective thermoelectric composite that is capable of emulating both n and p-type nature in a singular module from n-type bismuth chalcogenides and p-type nature of recycled carbon fibre. From the material science aspect, this research is also the first to highlight Bi_2S_3 as a plausible alternative to conventional toxic telluride based thermoelectric materials through the improvement of its thermoelectric properties via MWCNT doping and thermal annealing.

Several works reported in literature utilising carbon fibre for thermoelectric applications and its corresponding thermoelectric properties are summarised in Error! Reference source not found. below. The highest power factor obtained in this research work is 7.84 $\mu WK^{-2}m^{-1}$ and 2.55 $\mu WK^{-2}m^{-1}$ for Bi_2Te_3 and Bi_2S_3 respectively which is remarkably higher by few orders than the works of (Sung et al., 2016), (Kim et al., 2016) and (Pang et al., 2011). However, at the same time its approximately 20 and 5 times lower than the work of (Han and Chung, 2013a) and (Pang et al., 2012) respectively. The difference in performance is coming from the use of pure tellurium fillers in the work of Han and Chung that results in improved thermoelectric performance however is toxic in nature. For the case of Pang et al., though a higher power factor is obtained than the current work however electrodeposition results in films with poor mechanical ruggedness, has a paper like structure that easily tears off and too thin to sustain temperature difference for practical large scale applications as already investigated in Chapter 4 of this thesis. Though, the power factors obtained in this research work are slightly lower than that obtained by the two previous works, it has tremendous potential to be improved by employing the recommendations outlined in section 8.3.

Table 8- 1: Thermoelectric properties of carbon fibre based composites or films.

Composition	Seebeck coefficient (μV/K)	Electrical resistivity (Ω.m)	Power factor ($\mu WK^{-2}m^{-1}$)	Ref
Virgin carbon fibre, epoxy, carbon black, tellurium and Bi_2Te_3 particles	-167.30	0.00023	121.69	(Han and Chung, 2013a)
Virgin carbon fibre, epoxy	+1.80	1.762	1.84×10^{-6}	(Sung et al., 2016)
Virgin carbon fibre, epoxy	+3.34	-	-	(Kim et al., 2016)
Nitric acid intercalated recycled carbon fibre	-18.36	0.000947	0.36	(Pang et al., 2011)
Electrodeposited Bi_2Te_3 on recycled carbon fibre	-48.96	0.0000722	33.2	(Pang et al., 2012)
Recycled carbon fibre composite with annealed Bi_2Te_3 fillers	-214.27	0.0059	7.84	This work
Recycled carbon fibre composite with annealed Bi_2S_3 fillers	-236.36	0.0219	2.55	This work

8.2 Limitations

In order to compute the ZT value of thermoelectric materials, it is important to measure all three parameters (Seebeck coefficient, electrical resistivity and thermal conductivity). However, in this study thermal conductivity measurements were unable to be carried out, as a laser flash thermal conductivity meter was required for this purpose and due to equipment and resource limitation this property could not be measured.

8.3 Recommendation for future works

In light of the work carried out in this thesis, the following future works are recommended in order to fully develop a recycled carbon fibre based thermoelectric composite as a valuable asset in the field of energy harvesting from waste heat.

(a) Incorporating MWCNT into annealed Bi_2Te_3 and Bi_2S_3 fillers and studying the resulting effect on the Seebeck coefficient and electrical resistivity of the RCF composites.

(b) Utilising the multivariate optimisation tool, RSM to simultaneously optimise four experimental parameters such as (i) Bi_2Te_3 and Bi_2S_3 filler concentration (ii) MWCNT concentration, (iii) annealing temperature and (iv) annealing time on the Seebeck coefficient and electrical resistivity of the RCF composites.

(c) Incorporating the use of other binders/thermoplastic polymers that exhibit flexible properties which will result in flexible recycled carbon fibre polymer composites. Flexible thermoelectric composites is hypothesised to have better thermoelectric properties as it enhances thermal contact with heat sources of different geometry and prevent large thermal energy losses.

(d) Doping the flexible binders/thermoplastic polymers with electrically conducting polymers such as polyaniline (PANI), poly(3,4-ethylenedioxythiophene)-poly(styrenesulfonate) (PEDOT:PSS) to improve the electrical conductivity of the composites.

(e) Synthesising nanocomposites of bismuth telluride and bismuth sulphide doped with carbon nanomaterials such as graphene and reduced graphene oxide using hydrothermal technique and comparing its thermoelectric performance with that of physical blending.

(f) Characterisation of thermoelectric properties over a wider range of temperature. This study has only characterised thermoelectric properties of the composites with 10 °C temperature higher than that of ambient due to temperature limitations of the equipment (i.e. Seebeck

coefficient measurement and Hall effect measurement system). As the RCF composites only exhibited thermal degradation at 180 °C, it indicates the plausibility of using these composites for energy harvesting at higher temperature of waste heat (up to 180 °C). Therefore, for future works an advanced model of Hall effect measurement system, HMS ECOPIA 3300 can be used to monitor changes in electrical transport properties from room temperature to 300 °C and also a Seebeck property measurement system will be released soon by Ecopia that is capable of measuring temperature dependent Seebeck coefficient values.

(g) Other non-tellurium and environmentally friendly thermoelectric fillers could also be studied and incorporated into the recycled carbon fibre composites.

REFERENCES

Abad, B., Alda, I., Díaz-Chao, P., Kawakami, H., Almarza, A., Amantia, D., Gutierrez, D., Aubouy, L., Martín-González, M., 2013. Improved power factor of polyaniline nanocomposites with exfoliated graphene nanoplatelets (GNPs). J. Mater. Chem. A 1, 10450–10457. https://doi.org/10.1039/c3ta12105d

Abdullaev, M.A., Magomedova, D.K., Gadzhieva, R.M., Terukov, E.I., Nikolaev, Y.A., Rud, Y. V, Khokhlachev, P.P., 2001. Effect of deviations from stoichiometry on electrical conductivity and photoconductivity of CuInSe2 crystals. Semiconductors 35, 870–872. https://doi.org/10.1134/1.1393017

Agency of Natural Resources and Energy, 2016. The White Paper on Energy Usage. Japan.

Ali, A., Khan, A., Ali, A., Ahmad, M., 2017. Pressure-sensitive properties of carbon nanotubes /bismuth sulfide composite materials. Nanomater. Nanotechnol. 7, 1–9. https://doi.org/10.1177/1847980417707087

Anderson, M.J., Whitcomb, P.J., 2014. Practical Aspects for Designing Statistically Optimal Experiments. J. Stat. Sci. Appl. 2, 85–92.

Arthur, J.R., 1998. Physical and Chemical Methods for Thin-Film Deposition and Epitaxial Growth, in: Czanderna,Alvin W.; Powell,Cedric J; Madey,Theodore E.; Hercules,David M. ;Yates Jr., J.T. (Ed.), Specimen Handling, Preparation, and Treatments in Surface Characterization. pp. 239–293.

Aswal, D.K., Basu, R., Singh, A., 2016. Key issues in development of thermoelectric power generators: High figure-of-merit materials and their highly conducting interfaces with metallic interconnects. Energy Convers. Manag. 114, 50–67. https://doi.org/https://doi.org/10.1016/j.enconman.2016.01.065

Balasubramanian, V., P, N.K., Sengottaiyan, D., Balasubramanian, V., 2015. Effect of the annealing temperature on the current-voltage and Hall effect studies of Bi 2 S 3 thin films grown on glass substrates by using chemical bath deposition. Adv. Appl. Sci. Res. 6, 190–195.

Balasubramanian, V., Suriyanarayanan, N., Prabahar, S., 2011. Effect of Annealing Temperature on Structural and Optical Properties of Chemically Deposited Bismuth Sulphide Thin Films. Chalcogenide Lett. 8, 671–681.

Bark, H., Kim, J.-S., Kim, H., Yim, J.-H., Lee, H., 2013. Effect of multiwalled carbon nanotubes on the thermoelectric properties of a bismuth telluride matrix. Curr. Appl. Phys. 13, S111–S114. https://doi.org/10.1016/j.cap.2013.01.019

Bhardwaj, A., Misra, D.K., Pulikkotil, J.J., Auluck, S., Dhar, A., Budhani, R.C., 2012. Implications of nanostructuring on the thermoelectric properties in half-Heusler alloys. Appl. Phys. Lett. 101. https://doi.org/10.1063/1.4754570

Bharti, M., Singh, A., Samanta, S., Aswal, D.K., 2018. Conductive polymers for thermoelectric power generation. Prog. Mater. Sci. 93, 270–310. https://doi.org/10.1016/j.pmatsci.2017.09.004

Bing Ling, S.K., Tao, L., Huey Hoon, H., Freddy, B., Tianshu, Z., Li, 2014. Waste Energy Harvesting, 1st Editio. ed. Springer, New York. https://doi.org/10.1007/978-3-642-54634-1

Bissessur, R., Kanatzidis, M.G., Schindler, J.L., Kannewurf, C.R., 1993. Encapsulation of polymers into MoS2 and metal to insulator transition in metastable MoS2. J. Chem. Soc. Chem. Commun. 1582. https://doi.org/10.1039/c39930001582

Brostow, W., Datashvili, T., Hagg Lobland, H.E., Hilbig, T., Su, L., Vinado, C., White, J., 2012. Bismuth telluride-based thermoelectric materials: Coatings as protection against thermal cycling effects. J. Mater. Res. 27, 2930–2936. https://doi.org/10.1557/jmr.2012.335

Burton, M.R., Richardson, S.J., Staniec, P.A., Terrill, N.J., Elliott, J.M., Squires, A.M., White, N.M., Nandhakumar, I.S., 2017. A novel route to nanostructured bismuth telluride films by electrodeposition. Electrochem. commun. 76, 71–74. https://doi.org/10.1016/j.elecom.2017.02.004

Cai, Z., Fan, P., Zheng, Z., Liu, P., Chen, T., Cai, X., Luo, J., Liang, G., Zhang, D., 2013. Thermoelectric properties and micro-structure characteristics of annealed N-type bismuth telluride thin film. Appl. Surf. Sci. 280, 225–228. https://doi.org/10.1016/j.apsusc.2013.04.138

Campos, J., Sua, R., 1999. A comparison of the various thermal treatments of chemically deposited bismuth sulfide thin films and the effect on the structural and electrical properties 60, 385–392.

Carmo, J.P., Goncalves, L.M., Wolffenbuttel, R.F., Correia, J.H., 2010. A planar thermoelectric power generator for integration in wearable microsystems. Sensors Actuators, A Phys. 161, 199–204. https://doi.org/10.1016/j.sna.2010.05.010

Chauhan, N.S., Bathula, S., Vishwakarma, A., Bhardwaj, R., Gahtori, B., Srivastava, A.K., Saravanan, M., Dhar, A., 2018. A nanocomposite approach for enhancement of thermoelectric performance in Hafnium-free Half-Heuslers. Materialia. https://doi.org/https://doi.org/10.1016/j.mtla.2018.05.006

Chelvanathan, P., Zakaria, Z., Yusoff, Y., Akhtaruzzaman, M., Alam, M.M., Alghoul, M.A., Sopian, K., Amin, N., 2015. Annealing effect in structural and electrical properties of sputtered Mo thin film. Appl. Surf. Sci. 334, 129–137. https://doi.org/10.1016/j.apsusc.2014.08.154

Chen, G.-X., Kim, H.-S., Park, B.H., Yoon, J.-S., 2006. Multi-walled carbon nanotubes reinforced nylon 6 composites. Polymer (Guildf). 47, 4760–4767. https://doi.org/https://doi.org/10.1016/j.polymer.2006.04.020

Chen, P., Zhou, Z., Jiang, W., Luo, W., Yang, J., Zhu, J., Wang, L., Fan, Y., 2018. Enhancing the thermoelectric performance of filled skutterudite nanocomposites in a wide temperature range via electroless silver plating. Scr. Mater. 146, 136–141. https://doi.org/https://doi.org/10.1016/j.scriptamat.2017.11.019

Chmielowski, R., Péré, D., Bera, C., Opahle, I., Xie, W., Jacob, S., Capet, F., Roussel, P., Weidenkaff, A., Madsen, G.K.H., Dennler, G., 2015. Theoretical and experimental investigations of the thermoelectric properties of Bi2S3. J. Appl. Phys. 117. https://doi.org/10.1063/1.4916528

Chung, D.-Y., Hogan, T., Brazis, P., Rocci-Lane, M., Kannewurf, C., Bastea, M., Uher, C., Kanatzidis, M.G., 2000. CsBi₄Te₆: A High-Performance Thermoelectric Material for Low-Temperature Applications. Science (80-.). 287, 1024 LP-1027.

Chung, D.D.L., 2017. 5 - Polymer-Matrix Composites: Functional Properties, in: Chung, D.D.L.B.T.-C.C. (Second E. (Ed.), . Butterworth-Heinemann, pp. 256–332. https://doi.org/https://doi.org/10.1016/B978-0-12-804459-9.00005-1

Coşkun, M. ibrahi., Karahan, İ.H., Yücel, Y., 2014. Optimized Electrodeposition Concentrations for Hydroxyapatite Coatings on CoCrMo biomedical alloys by computational techniques. Electrochim. Acta 150, 46–54. https://doi.org/10.1016/j.electacta.2014.10.120

Cui, J.L., Mao, L.D., Yang, W., Xu, X.B., Chen, D.Y., Xiu, W.J., 2007. Thermoelectric properties of Cu-

doped n-type (Bi2Te3)0.9–(Bi2−xCuxSe3)0.1(x=0–0.2) alloys. J. Solid State Chem. 180, 3583–3587. https://doi.org/https://doi.org/10.1016/j.jssc.2007.10.013

Dachraoui, O., Merino, J.M., Mami, A., León, M., Caballero, R., Maghraoui-Meherzi, H., 2018. Annealing study and thermal investigation on bismuth sulfide thin films prepared by chemical bath deposition in basic medium. Appl. Phys. A Mater. Sci. Process. 124, 0. https://doi.org/10.1007/s00339-018-1584-7

Danine, A., Termentzidis, K., Schaefer, S., Li, S., Ensinger, W., Boulanger, C., Lacroix, D., Stein, N., 2018. Synthesis of bismuth telluride nanotubes and their simulated thermal properties. Superlattices Microstruct. https://doi.org/https://doi.org/10.1016/j.spmi.2018.06.042

Del Frari, D., Diliberto, S., Stein, N., Boulanger, C., Lecuire, J.-M., 2005. Comparative study of the electrochemical preparation of Bi2Te3, Sb2Te3, and (BixSb1−x)2Te3 films. Thin Solid Films 483, 44–49. https://doi.org/10.1016/j.tsf.2004.12.015

Delaire, O., Ma, J., Marty, K., May, A.F., McGuire, M.A., Du, M.-H., Singh, D.J., Podlesnyak, A., Ehlers, G., Lumsden, M.D., Sales, B.C., 2011. Giant anharmonic phonon scattering in PbTe. Nat. Mater. 10, 614.

Deng, J., Zhao, Z.Y., 2018. Electronic structure and optical properties of bismuth chalcogenides Bi2Q3(Q = O, S, Se, Te) by first-principles calculations. Comput. Mater. Sci. 142, 312–319. https://doi.org/10.1016/j.commatsci.2017.10.032

Desale, D.J., Shaikh, S., Siddiqui, F., Birajdar, R., Late, R., Ghule, A., Sharma, R., 2013. Enhancement of photosensitivity by annealing in Bi2S3thin films grown using SILAR method. Compos. Part B Eng. 46, 1–6. https://doi.org/10.1016/j.compositesb.2012.11.011

Ding, L.C., Akbarzadeh, A., Tan, L., 2018. A review of power generation with thermoelectric system and its alternative with solar ponds. Renew. Sustain. Energy Rev. 81, 799–812. https://doi.org/https://doi.org/10.1016/j.rser.2017.08.010

Dresselhaus, M.S., Chen, G., Tang, M.Y., Yang, R., Lee, H., Wang, D., Ren, Z., Fleurial, J.P., Gogna, P., 2007. New directions for low-dimensional thermoelectric materials. Adv. Mater. 19, 1043–1053. https://doi.org/10.1002/adma.200600527

Du, X., Cai, F., Wang, X., 2014. Enhanced thermoelectric performance of chloride doped bismuth sulfide prepared by mechanical alloying and spark plasma sintering. J. Alloys Compd. 587, 6–9. https://doi.org/10.1016/j.jallcom.2013.10.185

Du, Y., Cai, K.F., Chen, S., Cizek, P., Lin, T., 2014. Facile Preparation and Thermoelectric Properties of Bi2Te3 Based Alloy Nanosheet/PEDOT:PSS Composite Films. ACS Appl. Mater. Interfaces 6, 5735–5743. https://doi.org/10.1021/am5002772

Du, Y., Shen, S.Z., Cai, K., Casey, P.S., 2012a. Research progress on polymer-inorganic thermoelectric nanocomposite materials. Prog. Polym. Sci. 37, 820–841. https://doi.org/10.1016/j.progpolymsci.2011.11.003

Du, Y., Shen, S.Z., Yang, W., Donelson, R., Cai, K., Casey, P.S., 2012b. Simultaneous increase in conductivity and Seebeck coefficient in a polyaniline/graphene nanosheets thermoelectric nanocomposite. Synth. Met. 161, 2688–2692. https://doi.org/10.1016/j.synthmet.2011.09.044

Dughaish, Z.H., 2002. Lead telluride as a thermoelectric material for thermoelectric power generation. Phys. B Condens. Matter 322, 205–223. https://doi.org/https://doi.org/10.1016/S0921-4526(02)01187-0

Ebbesen, T.W., Lezec, H.J., Hiura, H., Bennett, J.W., Ghaemi, H.F., Thio, T., 1996. Electrical conductivity of individual carbon nanotubes. Nature 382, 54.

Enerdata, 2018. Global Energy Statistical Yearbook 2018 [WWW Document]. URL https://yearbook.enerdata.net/total-energy/world-consumption-statistics.html (accessed 7.16.18).

F.Keuch, T., 2015. Thin Films and Epitaxy: Basic Techniques, and Materials, Processes, and Technology. Elsevier, Oxford.

Feng, B., Li, G., Pan, Z., Hou, Y., Zhang, C., Jiang, C., Hu, J., Xiang, Q., Li, Y., He, Z., Fan, X., 2018. Effect of Ba and Pb dual doping on the thermoelectric properties of BiCuSeO ceramics. Mater. Lett. 217, 189–193. https://doi.org/https://doi.org/10.1016/j.matlet.2018.01.074

Gautier, P., Vallee, A., Sinito, C., Etcheberry, A., Simon, N., 2016. Diamond & Related Materials Effect of growth temperature on the electrodeposition of zinc oxide layers on diamond surfaces. Diam. Relat. Mater. 62, 1–6. https://doi.org/10.1016/j.diamond.2015.12.005

Ge, Z.-H., Qin, P., He, D., Chong, X., Feng, D., Ji, Y.-H., Feng, J., He, J., 2017. Highly Enhanced Thermoelectric Properties of Bi/Bi $_2$ S $_3$ Nanocomposites. ACS Appl. Mater. Interfaces 9, 4828–4834. https://doi.org/10.1021/acsami.6b14803

Glatz, W., Durrer, L., Schwyter, E., Hierold, C., 2008. Novel mixed method for the electrochemical deposition of thick layers of Bi2+xTe3-x with controlled stoichiometry. Electrochim. Acta 54, 755–762. https://doi.org/10.1016/j.electacta.2008.06.065

Goldsmid, H.J., 2017. The Seebeck and Peltier effects. Phys. Thermoelectr. Energy Convers. https://doi.org/10.1088/978-1-6817-4641-8ch1

Goldsmid, H.J., 2016. The Improvement of a Specific Material—Bismuth Telluride BT - Introduction to Thermoelectricity, in: Goldsmid, H.J. (Ed.), . Springer Berlin Heidelberg, Berlin, Heidelberg, pp. 85–107. https://doi.org/10.1007/978-3-662-49256-7_6

Goldsmid, H.J., Douglas, R.W., 1954. The use of semiconductors in thermoelectric refrigeration. Br. J. Appl. Phys. 5, 458–458. https://doi.org/10.1088/0508-3443/5/12/513

Golia, S., Arora, M., Sharma, R.K., Rastogi, a. C., 2003. Electrochemically deposited bismuth telluride thin films. Curr. Appl. Phys. 3, 195–197. https://doi.org/10.1016/S1567-1739(02)00200-6

Gong, C., Shi, Z., Zhang, Y., Chen, Y., Hu, J., Gou, J., Qin, M., Gao, F., 2018. Fabrication and thermoelectric properties of Ca-Co-O ceramics with negative Seebeck coefficient. Results Phys. 9, 1233–1238. https://doi.org/https://doi.org/10.1016/j.rinp.2018.04.044

Goto, M., Sasaki, M., Xu, Y., Zhan, T., Isoda, Y., Shinohara, Y., 2017. Control of p-type and n-type thermoelectric properties of bismuth telluride thin films by combinatorial sputter coating technology. Appl. Surf. Sci. 407, 405–411. https://doi.org/10.1016/j.apsusc.2017.02.187

Goux, A., Pauport, T., Chivot, J., Lincot, D., 2005. Temperature effects on ZnO electrodeposition 50, 2239–2248. https://doi.org/10.1016/j.electacta.2004.10.007

Grasso, S., Tsujii, N., Jiang, Q., Khaliq, J., Maruyama, S., Miranda, M., Simpson, K., Mori, T., Reece, M.J., 2013. Ultra low thermal conductivity of disordered layered p-type bismuth telluride. J. Mater. Chem. C 1, 2362. https://doi.org/10.1039/c3tc30152d

Haken, W., 1910. No Title. Ann. Phys., Lpz. 32, 319.

Hamada, J., Takashiri, M., 2017. Structural changes in nanocrystalline Bi2Te3/Bi2Se3multilayer thin

films caused by thermal annealing. J. Cryst. Growth 468, 188–193. https://doi.org/10.1016/j.jcrysgro.2016.11.130

Han, S., Chung, D.D.L., 2013a. Carbon fiber polymer-matrix structural composites exhibiting greatly enhanced through-thickness thermoelectric figure of merit. Compos. Part A Appl. Sci. Manuf. 48, 162–170. https://doi.org/10.1016/j.compositesa.2013.01.008

Han, S., Chung, D.D.L., 2013b. Through-thickness thermoelectric power of a carbon fiber/epoxy composite and decoupled contributions from a lamina and an interlaminar interface. Carbon N. Y. 52, 30–39. https://doi.org/10.1016/j.carbon.2012.08.071

Hasan, B.A., Shallal, I.H., 2014. Structural and Optical Properties of SnS Thin Films. J. Nanotechnol. Adv. Mater. 2, 43–49. https://doi.org/10.1080/17458080.2013.788226

He, J., Kanatzidis, M.G., Dravid, V.P., 2013. High performance bulk thermoelectrics via a panoscopic approach. Mater. Today 16, 166–176. https://doi.org/10.1016/j.mattod.2013.05.004

Hewitt, C.A., Carroll, D.L., 2014. Carbon nanotube-based polymer composite thermoelectric generators. ACS Symp. Ser. 1161, 191–211. https://doi.org/10.1021/bk-2014-1161.ch009

Hewitt, C.A., Kaiser, A.B., Craps, M., Czerw, R., Roth, S., Carroll, D.L., 2013. Temperature dependent thermoelectric properties of freestanding few layer graphene/polyvinylidene fluoride composite thin films. Synth. Met. 165, 56–59. https://doi.org/10.1016/j.synthmet.2013.01.009

Huang, H., Luan, W., Tu, S., 2009. Influence of annealing on thermoelectric properties of bismuth telluride films grown via radio frequency magnetron sputtering. Thin Solid Films 517, 3731–3734. https://doi.org/10.1016/j.tsf.2009.01.015

Hussain, A., Begum, A., Rahman, A., 2014. Effects of annealing on nanocrystalline Bi2S3 thin films prepared by chemical bath deposition. Mater. Sci. Semicond. Process. 21, 74–81. https://doi.org/10.1016/j.mssp.2014.01.029

Investorintel, 2014. Rarer than rare earths, the trials and tribulations of tellurium [WWW Document]. URL https://investorintel.com/sectors/technology-metals/technology-metals-intel/tellurium-trials-tribulations/ (accessed 6.27.18).

Iversen, B.B., Palmqvist, A.E.C., Cox, D.E., Nolas, G.S., Stucky, G.D., Blake, N.P., Metiu, H., 2000. Why are Clathrates Good Candidates for Thermoelectric Materials? J. Solid State Chem. 149, 455–458. https://doi.org/https://doi.org/10.1006/jssc.1999.8534

Jagadish, P.R., Li, L.P., Chan, A., Khalid, M., 2016. Effect of Annealing on Virgin and Recycled Carbon Fiber Electrochemically Deposited with N-type Bismuth Telluride and Bismuth Sulfide. Mater. Manuf. Process. 31, 1223–1231. https://doi.org/10.1080/10426914.2015.1090590

Jariwala, B., Shah, D., Ravindra, N.M., 2015. Influence of doping on structural and optical properties of Bi 2 Te 3 thin films. Thin Solid Films 589, 396–402. https://doi.org/10.1016/j.tsf.2015.05.020

Jeon, S., Oh, M., Jeon, H., Hyun, S., Lee, H., 2011. Effects of post-annealing on thermoelectric properties of bismuth–tellurium thin films deposited by co-sputtering. Microelectron. Eng. 88, 541–544. https://doi.org/10.1016/j.mee.2010.06.036

Jin, Y., Wang, W., 2010. Effect of Substrate on the Structure and Thermoelectric Properties of n-Type Bi2Te3−y Se y Thin Films Prepared by Electrodeposition. J. Electron. Mater. 39, 1469–1475. https://doi.org/10.1007/s11664-010-1306-1

Jun, S., Lee, K., Oh, T., 2006. Effects of Hydrogen Annealing on the Thermoelectric Properties of Electrodeposited Bi 2 Te 3 for Nanowire Applications 48, 1708–1712.

Kaganj, A.B., Rashidi, A.M., Arasteh, R., Taghipoor, S., 2009. Crystallisation behaviour and morphological characteristics of poly(propylene)/multi-walled carbon nanotube nanocomposites. J. Exp. Nanosci. 4, 21–34. https://doi.org/10.1080/17458080802688427

Kasap, S., 2001. Thermoelectric Effects in Metals. Dep. Electr. Eng. Univ. Saskatchewan, Canada 1–11.

Khalfallah, M., Abbès, B., Abbès, F., Guo, Y.Q., Marcel, V., Duval, A., Vanfleteren, F., Rousseau, F., 2014. Innovative flax tapes reinforced Acrodur biocomposites: A new alternative for automotive applications. Mater. Des. 64, 116–126. https://doi.org/10.1016/j.matdes.2014.07.029

Khalili, P., Tshai, K.Y., Hui, D., Kong, I., 2017. Synergistic of ammonium polyphosphate and alumina trihydrate as fire retardants for natural fiber reinforced epoxy composite. Compos. Part B Eng. 114, 101–110. https://doi.org/10.1016/j.compositesb.2017.01.049

Kim, D.-H., Lee, G.-H., 2006. Effect of rapid thermal annealing on thermoelectric properties of bismuth telluride films grown by co-sputtering. Mater. Sci. Eng. B 131, 106–110. https://doi.org/10.1016/j.mseb.2006.03.034

Kim, D.H., Kwon, I.H., Kim, C., Han, B., Im, H.J., Kim, H., 2013. Tellurium-evaporation-annealing for p-type bismuth-antimony-telluride thermoelectric materials. J. Alloys Compd. 548, 126–132. https://doi.org/10.1016/j.jallcom.2012.08.130

Kim, J.-H., Okamoto, N.L., Kishida, K., Tanaka, K., Inui, H., 2006. High thermoelectric performance of type-III clathrate compounds of the Ba–Ge–Ga system. Acta Mater. 54, 2057–2062. https://doi.org/https://doi.org/10.1016/j.actamat.2005.12.032

Kim, J., Choi, J., Bae, J., Kim, M., Oh, T., 2013. Thermoelectric Characteristics of n-Type Bi2Te3 and p-Type Sb2Te3 Thin Films Prepared by Co-Evaporation and Annealing for Thermopile Sensor Applications 54, 618–625. https://doi.org/10.2320/matertrans.M2013010

Kim, K.T., Choi, S.Y., Shin, E.H., Moon, K.S., Koo, H.Y., Lee, G.-G., Ha, G.H., 2013. The influence of CNTs on the thermoelectric properties of a CNT/Bi2Te3 composite. Carbon N. Y. 52, 541–549. https://doi.org/10.1016/j.carbon.2012.10.008

Kim, K.T., Eom, Y.S., Son, I., 2015a. Fabrication Process and Thermoelectric Properties of CNT/Bi2(Se,Te)3Composites. J. Nanomater. 2015, 1–6. https://doi.org/10.1155/2015/202415

Kim, K.T., Eom, Y.S., Son, I., 2015b. Fabrication Process and Thermoelectric Properties of CNT / Bi 2 (Se , Te) 3 Composites. J. Nanomater. Article ID. https://doi.org/10.1155/2015/202415

Kim, M., Oh, T., Kim, J., 2007a. Annealing Behavior of Bi 2 Te 3 Thermoelectric Semiconductor Electrodeposited for Nanowire Applications 50, 670–676.

Kim, M., Oh, T., Kim, J., Min-Young, M.-Y., Tae-Sung, T.-S., Jin-Sang, J.-S., 2007b. Annealing Behavior of Bi2Te3 Thermoelectric Semiconductor Electrodeposited for Nanowire Applications. J. Korean Phys. Soc. 50, 670. https://doi.org/10.3938/jkps.50.670

Kim, M., Sung, D.H., Kong, K., Kim, N., Kim, B.J., Park, H.W., Park, Y. Bin, Jung, M., Lee, S.H., Kim, S.G., 2016. Characterization of resistive heating and thermoelectric behavior of discontinuous carbon fiber-epoxy composites. Compos. Part B Eng. 90, 37–44. https://doi.org/10.1016/j.compositesb.2015.11.037

Kim, M.Y., Oh, T.S., 2009. Electrodeposition and thermoelectric characteristics of Bi 2Te 3 and Sb 2Te 3 films for thermopile sensor applications. J. Electron. Mater. 38, 1176–1181.

https://doi.org/10.1007/s11664-008-0653-7

Kim, S.J., We, J.H., Cho, B.J., 2014. A wearable thermoelectric generator fabricated on a glass fabric. Energy Environ. Sci. 7, 1959. https://doi.org/10.1039/c4ee00242c

Kioupakis, E., Tiago, M.L., Louie, S.G., 2010. Quasiparticle electronic structure of bismuth telluride in the GW approximation. Phys. Rev. B - Condens. Matter Mater. Phys. 82, 1–4. https://doi.org/10.1103/PhysRevB.82.245203

Kleinke, H., 2010. New bulk Materials for Thermoelectric Power Generation: Clathrates and Complex Antimonides. Chem. Mater. 22, 604–611. https://doi.org/10.1021/cm901591d

Kotkata, M.F., Kandil, K.M., 1987. A study of the electrical conductivity of amorphous-crystalline selenium mixtures. Mater. Sci. Eng. 95, 287–293. https://doi.org/10.1016/0025-5416(87)90521-0

Kumar, S., Chaudhary, D., Kumar Dhawan, P., Yadav, R.R., Khare, N., 2017. Bi2Te3-MWCNT nanocomposite: An efficient thermoelectric material. Ceram. Int. 43, 14976–14982. https://doi.org/10.1016/j.ceramint.2017.08.017

Kunadian, I., Andrews, R., Pinar Mengüç, M., Qian, D., 2009. Thermoelectric power generation using doped MWCNTs. Carbon N. Y. 47, 589–601. https://doi.org/https://doi.org/10.1016/j.carbon.2008.10.043

Kusagaya, K., Takashiri, M., 2015. Investigation of the effects of compressive and tensile strain on n-type bismuth telluride and p-type antimony telluride nanocrystalline thin films for use in flexible thermoelectric generators. J. Alloys Compd. 653, 480–485. https://doi.org/10.1016/j.jallcom.2015.09.039

Lee, H.J., Hyun, S., Park, H.S., Han, S.W., 2011. Thermoelectric properties of n-type Bi-Te thin films with various compositions. Microelectron. Eng. 88, 593–596. https://doi.org/10.1016/j.mee.2010.06.019

Lee, J., Kim, J., Moon, W., Berger, A., Lee, J., 2012. Enhanced Seebeck Coe ffi cients of Thermoelectric Bi 2 Te 3 Nanowires as a Result of an Optimized Annealing Process 19512–19516.

Lee, P.-J., Chao, L.-S., 2010. High-temperature thermoelectric properties of Ti0.5(ZrHf)0.5−xNbxNi0.9Pd0.1Sn0.98Sb0.02 half-Heusler alloys. J. Alloys Compd. 504, 192–196. https://doi.org/https://doi.org/10.1016/j.jallcom.2010.05.086

Lee, S., Bock, J.A., Trolier-McKinstry, S., Randall, C.A., 2012. Ferroelectric-thermoelectricity and Mott transition of ferroelectric oxides with high electronic conductivity. J. Eur. Ceram. Soc. 32, 3971–3988. https://doi.org/10.1016/j.jeurceramsoc.2012.06.007

Lee, S., Lee, K.H., Kim, Y.-M., Kim, H.S., Snyder, G.J., Baik, S., Kim, S.W., 2018. Simple and efficient synthesis of nanograin structured single phase filled skutterudite for high thermoelectric performance. Acta Mater. 142, 8–17. https://doi.org/https://doi.org/10.1016/j.actamat.2017.09.044

Lee, W., Hong, C.T., Kwon, O.H., Yoo, Y., Kang, Y.H., Lee, J.Y., Cho, S.Y., Jang, K.S., 2015. Enhanced thermoelectric performance of bar-coated SWCNT/P3HT thin films. ACS Appl. Mater. Interfaces 7, 6550–6556. https://doi.org/10.1021/acsami.5b00626

Lévesque, I., Bertrand, P.O., Blouin, N., Leclerc, M., Zecchin, S., Zotti, G., Ratcliffe, C.I., Klug, D.D., Gao, X., Gao, F., Tse, J.S., 2007. Synthesis and thermoelectric properties of polycarbazole, polyindolocarbazole, and polydiindolocarbazole derivatives. Chem. Mater. 19, 2128–2138.

https://doi.org/10.1021/cm070063h

Li, C., Jiang, F., Liu, C., Wang, W., Li, X., Wang, T., Xu, J., 2017. A simple thermoelectric device based on inorganic/organic composite thin film for energy harvesting. Chem. Eng. J. 320, 201–210. https://doi.org/10.1016/j.cej.2017.03.023

Li, D., Sun, R.R., Qin, X.Y., 2011. Improving thermoelectric properties of p-type Bi2Te3-based alloys by spark plasma sintering. Prog. Nat. Sci. Mater. Int. 21, 336–340. https://doi.org/10.1016/S1002-0071(12)60066-5

Li, J., Tang, X., Li, H., Yan, Y., Zhang, Q., 2010. Synthesis and thermoelectric properties of hydrochloric acid-doped polyaniline. Synth. Met. 160, 1153–1158. https://doi.org/https://doi.org/10.1016/j.synthmet.2010.03.001

Li, S., Soliman, H.M. a., Zhou, J., Toprak, M.S., Muhammed, M., Platzek, D., Ziolkowski, P., Müller, E., 2008. Effects of Annealing and Doping on Nanostructured Bismuth Telluride Thick Films. Chem. Mater. 20, 4403–4410. https://doi.org/10.1021/cm800696h

Lim, Y.S., Song, M., Lee, S., An, T.H., Park, C., Seo, W.S., 2016. Enhanced thermoelectric properties and their controllability in p-type (BiSb)2Te3compounds through simultaneous adjustment of charge and thermal transports by Cu incorporation. J. Alloys Compd. 687, 320–325. https://doi.org/10.1016/j.jallcom.2016.06.144

Lin, J., Chen, Y., Lin, C., 2013. Annealing Effect on the Thermoelectric Properties of Bi2Te3 Thin Films Prepared by Thermal Evaporation Method 2013.

Lin, J., Chen, Y., Lin, C., Chien, H., Wen, C., Chang, J., Zhan, Z., 2015. Annealing effects on the thermoelectric properties of silver-doped bismuth telluride thin films. Mee 148, 51–54. https://doi.org/10.1016/j.mee.2015.08.008

Liu, B., Ma, H., Huo, D., Liu, H., Liu, B., Chen, J., Jia, X., 2018. Thermoelectric properties of In-substituted Ge-based clathrates prepared by HPHT. J. Mater. 4, 68–74. https://doi.org/https://doi.org/10.1016/j.jmat.2017.11.001

Liu, H., Wang, J., Hu, X., Boughton, R.I., Zhao, S., Li, Q., Jiang, M., 2002. Structure and electronic transport properties of polyaniline/NaFe4P12 composite. Chem. Phys. Lett. 352, 185–190. https://doi.org/https://doi.org/10.1016/S0009-2614(01)01389-6

Liu, S., Liu, F., Zhu, X.Q., Bai, Y., Ma, D.Y., Ma, F., Xu, K.W., 2016. Limited grain growth in multilayered Bi/Te thin films and the influence on the thermal and electrical conductivity. Vacuum 127, 88–95. https://doi.org/10.1016/j.vacuum.2016.02.013

Liu, W., Yan, X., Chen, G., Ren, Z., 2012. Recent advances in thermoelectric nanocomposites. Nano Energy 1, 42–56. https://doi.org/10.1016/j.nanoen.2011.10.001

Liu, W.S., Zhang, Q., Lan, Y., Chen, S., Yan, X., Zhang, Q., Wang, H., Wang, D., Chen, G., Ren, Z., 2011. Thermoelectric property studies on Cu-doped n-type Cu xBi 2Te 2.7Se 0.3 nanocomposites. Adv. Energy Mater. 1, 577–587. https://doi.org/10.1002/aenm.201100149

Liufu, S.C., Chen, L.D., Yao, Q., Wang, C.F., 2007. Assembly of one-dimensional nanorods into Bi2S3 films with enhanced thermoelectric transport properties. Appl. Phys. Lett. 90, 1–4. https://doi.org/10.1063/1.2712504

Lognone, Q., Gascoin, F., 2015. On the effect of carbon nanotubes on the thermoelectric properties of n-Bi2Te2.4Se0.6 made by mechanical alloying. J. Alloys Compd. 635, 107–111. https://doi.org/10.1016/j.jallcom.2015.02.055

Luo, T.Y., Liang, T.X., Li, C.S., 2004. Addition of carbon nanotubes during the preparation of zirconia nanoparticles: Influence on structure and phase composition. Powder Technol. 139, 118–122. https://doi.org/10.1016/j.powtec.2003.12.001

Ma, R., Liu, G., Li, J., Li, Y., Chen, K., Han, Y., Zhou, M., Li, L., 2017. Effect of secondary phases on thermoelectric properties of Cu2SnSe3. Ceram. Int. 43, 7002–7010. https://doi.org/https://doi.org/10.1016/j.ceramint.2017.02.126

Ma, Y., Ahlberg, E., Sun, Y., Iversen, B.B., Palmqvist, A.E.C., 2012. Thermoelectric Characteristics of Electrochemically Deposited Bi2Te3 and Sb2Te3 Thin Films of Relevance to Multilayer Preparation. J. Electrochem. Soc. 159, D50. https://doi.org/10.1149/2.033202jes

Ma, Y., Ahlberg, E., Sun, Y., Iversen, B.B., Palmqvist, A.E.C., 2011. Thermoelectric properties of thin films of bismuth telluride electrochemically deposited on stainless steel substrates. Electrochim. Acta 56, 4216–4223. https://doi.org/10.1016/j.electacta.2011.01.093

Ma, Y., Johansson, A., Ahlberg, E., Palmqvist, A.E.C., 2010. A mechanistic study of electrodeposition of bismuth telluride on stainless steel substrates. Electrochim. Acta 55, 4610–4617. https://doi.org/10.1016/j.electacta.2010.03.018

Madre, M.A., Costa, F.M., Ferreira, N.M., Sotelo, A., Torres, M.A., Constantinescu, G., Rasekh, S., Diez, J.C., 2013. Preparation of high-performance Ca3Co4O9 thermoelectric ceramics produced by a new two-step method. J. Eur. Ceram. Soc. 33, 1747–1754. https://doi.org/https://doi.org/10.1016/j.jeurceramsoc.2013.01.029

Magri, P., Boulanger, C., Lecuire, J.-M., 1996. Synthesis, properties and performances of electrodeposited bismuth telluride films. J. Mater. Chem. 6, 773. https://doi.org/10.1039/jm9960600773

Majumdar, A., 2004. Thermoelectricity in Semiconductor Nanostructures. Science (80-.). 303, 777 LP-778.

Manohari, A.G., Dhanapandian, S., Manoharan, C., Kumar, K.S., Mahalingam, T., 2014. Effect of doping concentration on the properties of bismuth doped tin sulfide thin films prepared by spray pyrolysis. Mater. Sci. Semicond. Process. 17, 138–142. https://doi.org/10.1016/j.mssp.2013.09.012

Martín-González, M.S., Prieto, A.L., Gronsky, R., Sands, T., Stacy, A.M., 2002. Insights into the Electrodeposition of Bi[sub 2]Te[sub 3]. J. Electrochem. Soc. 149, C546. https://doi.org/10.1149/1.1509459

McConnell, V.P., 2010. Launching the carbon fibre recycling industry. Reinf. Plast. 54, 33–37. https://doi.org/10.1016/S0034-3617(10)70063-1

McGrail, B.T., Sehirlioglu, A., Pentzer, E., 2015. Polymer composites for thermoelectric applications. Angew. Chemie - Int. Ed. 54, 1710–1723. https://doi.org/10.1002/anie.201408431

Mele, P., Saini, S., Honda, H., Matsumoto, K., Miyazaki, K., Hagino, H., Ichinose, a., 2013. Effect of substrate on thermoelectric properties of Al-doped ZnO thin films. Appl. Phys. Lett. 102. https://doi.org/10.1063/1.4812401

Memon, A.A., Patil, S.A., Sun, K.C., Mengal, N., Arbab, A.A., Sahito, I.A., Jeong, S.H., kim, H.S., 2018. Carbonous metallic framework of multi-walled carbon Nanotubes/Bi 2 S 3 nanorods as heterostructure composite films for efficient quasi-solid state DSSCs. Electrochim. Acta. https://doi.org/10.1016/j.electacta.2018.04.131

Mengistie, D.A., Chen, C.H., Boopathi, K.M., Pranoto, F.W., Li, L.J., Chu, C.W., 2015. Enhanced thermoelectric performance of PEDOT:PSS flexible bulky papers by treatment with secondary dopants. ACS Appl. Mater. Interfaces 7, 94–100. https://doi.org/10.1021/am507032e

Michel, S., Diliberto, S., Boulanger, C., Bolle, B., 2006. Effect of electrochemical deposition conditions on the crystallographic texture of bismuth telluride alloys. J. Cryst. Growth 296, 227–233. https://doi.org/10.1016/j.jcrysgro.2006.08.036

Michel, S., Diliberto, S., Boulanger, C., Stein, N., Lecuire, J.M., 2005. Galvanostatic and potentiostatic deposition of bismuth telluride films from nitric acid solution: Effect of chemical and electrochemical parameters. J. Cryst. Growth 277, 274–283. https://doi.org/10.1016/j.jcrysgro.2004.12.164

Miyazaki, Y., Kajitani, T., 2001. Preparation of Bi 2 Te 3 films by electrodeposition 229, 542–546.

Mizoguchi, H., Hosono, H., Ueda, N., Kawazoe, H., 1995. Preparation and electrical properties of Bi2S3 whiskers. J. Appl. Phys. 78, 1376–1378. https://doi.org/10.1063/1.360315

Moriarty, G.P., Wheeler, J.N., Yu, C., Grunlan, J.C., 2012. Increasing the thermoelectric power factor of polymer composites using a semiconducting stabilizer for carbon nanotubes. Carbon N. Y. 50, 885–895. https://doi.org/10.1016/j.carbon.2011.09.050

Morin, C., Loppinet-Serani, A., 2012. Near-and supercritical solvolysis of carbon fibre reinforced polymers (CFRPs) for recycling carbon fibers as a valuable resource: State of the art. J. Supercrit. Fluids 232–240.

Narducci, D., Selezneva, E., Cerofolini, G., Frabboni, S., Ottaviani, G., 2012. Impact of energy filtering and carrier localization on the thermoelectric properties of granular semiconductors. J. Solid State Chem. 193, 19–25. https://doi.org/10.1016/j.jssc.2012.03.032

Nath, C., Kumar, A., Kuo, Y.K., Okram, G.S., 2014. High thermoelectric figure of merit in nanocrystalline polyaniline at low temperatures. Appl. Phys. Lett. 105. https://doi.org/10.1063/1.4897146

Ni, J., Zhao, Y., Liu, T., Zheng, H., Gao, L., Yan, C., Li, L., 2014. Strongly coupled Bi2S3@CNT hybrids for robust lithium storage. Adv. Energy Mater. 4, 1–5. https://doi.org/10.1002/aenm.201400798

Nolas, G.S., Kaeser, M., Littleton IV, R.T., Tritt, T.M., 2000. file:///C:/Users/User/Downloads/S1359645417308108.ris. Appl. Phys. Lett. 77, 1855–1857. https://doi.org/10.1063/1.1311597

Nolas, G.S., Morelli, D.T., Tritt, T.M., 1999. SKUTTERUDITES: A Phonon-Glass-Electron Crystal Approach to Advanced Thermoelectric Energy Conversion Applications. Annu. Rev. Mater. Sci. 29, 89–116. https://doi.org/10.1146/annurev.matsci.29.1.89

Ohsugi, I.J., Tokunaga, D., Kato, M., Yoneda, S., Isoda, Y., 2015. Dissociation and sublimation of tellurium from the thermoelectric tellurides. Mater. Res. Innov. 19, S5-301-S5-303. https://doi.org/10.1179/1432891714Z.0000000001097

Ohta, H., 2018. 18 - Thermoelectrics based on metal oxide thin films A2 - Pryds, Nini, in: Esposito, V.B.T.-M.O.-B.T.F.S. (Ed.), Metal Oxides. Elsevier, pp. 441–464. https://doi.org/https://doi.org/10.1016/B978-0-12-811166-6.00018-2

Pang, E.J.X., Chan, A., Pickering, S.J., 2011. Thermoelectrical properties of intercalated recycled carbon fibre composite. Compos. Part A Appl. Sci. Manuf. 42, 1406–1411.

https://doi.org/10.1016/j.compositesa.2011.06.004

Pang, E.J.X., Pickering, S.J., Chan, a., Wong, K.H., Lau, P.L., 2012. N-type thermoelectric recycled carbon fibre sheet with electrochemically deposited Bi2Te3. J. Solid State Chem. 193, 147–153. https://doi.org/10.1016/j.jssc.2012.04.046

Pang, H., Piao, Y.Y., Tan, Y.Q., Jiang, G.Y., Wang, J.H., Li, Z.M., 2013. Thermoelectric behaviour of segregated conductive polymer composites with hybrid fillers of carbon nanotube and bismuth telluride. Mater. Lett. 107, 150–153. https://doi.org/10.1016/j.matlet.2013.06.008

Patil, D.S., Arakerimath, R.R., Walke, P. V, 2018. Thermoelectric materials and heat exchangers for power generation – A review. Renew. Sustain. Energy Rev. 95, 1–22. https://doi.org/https://doi.org/10.1016/j.rser.2018.07.003

Paunovic, Milan;Schlesinger, M., 2006. FUNDAMENTALS OF ELECTROCHEMICAL DEPOSITION, Second. ed. John Wiley & Sons Inc Publication, Hoboken.

Pundir, S.K., Singh, S., Sivaiah, B., Kumar, R., Dhar, A., 2016. Study of ball milled bismuth telluride composites reinforced with MWCNTs for thermoelectric behaviour. Adv. Mater. Lett. 7, 549–554. https://doi.org/10.5185/amlett.2016.6112

Qiu, L., Zhou, J., Cheng, X., Ahuja, R., 2010. Electrochemical deposition of Bi2Te3-based thin films. J. Phys. Chem. Solids 71, 1131–1136. https://doi.org/10.1016/j.jpcs.2010.03.020

Rahman, A.A.A., Ali Umar, A., Othman, M.H.U., 2015. Effect of bismuth telluride concentration on the thermoelectric properties of PEDOT:PSS-glycerol organic films. Phys. E Low-Dimensional Syst. Nanostructures 66, 293–298. https://doi.org/10.1016/j.physe.2014.10.032

Raissi, S., Farsani, R.-E., 2009. Statistical process optimization through multi-response surface methodology. World Acad. Sci. Eng. Technol. 51, 267–271.

Rakhshani, A.E., Varghese, J., 1988. The Effect of Temperature on Electrodeposition of Cuprous Oxide. Phys. Stat. Sol. 105, 183–188.

Rashid, M.M., Cho, K.H., Chung, G.-S., 2013. Rapid thermal annealing effects on the microstructure and the thermoelectric properties of electrodeposited Bi2Te3 film. Appl. Surf. Sci. 279, 23–30. https://doi.org/10.1016/j.apsusc.2013.03.112

Ren, F., Wang, H., Menchhofer, P.A., Kiggans, J.O., 2013. Thermoelectric and mechanical properties of multi-walled carbon nanotube doped Bi0.4Sb1.6Te3 thermoelectric material. Appl. Phys. Lett. 103, 0–5. https://doi.org/10.1063/1.4834700

Riahi, M., Martínez-Tomás, C., Agouram, S., Boukhachem, A., Maghraoui-Meherzi, H., 2017. The effects of thermal treatment on structural, morphological and optical properties of electrochemically deposited Bi2S3 thin films. Thin Solid Films 626, 9–16. https://doi.org/10.1016/j.tsf.2017.02.022

Rincbn, M.E., 1996. KINETICS OF ELECTRICAL CONDUCTIVITY ENHANCEMENT IN BISMUTH SULPHIDE THIN FILMS . PART II : OPTOELECTRONIC PROPERTIES (FILM) AND PHASE TRANSFORMATIONS (POWDER) UNDER OXYGEN ANNEALING 57, 1947–1955.

Rincón, M.E., Nair, P.K., 1996. Kinetics of electrical conductivity enhancement in bismuth sulphide thin films. Part I: Argon and hydrogen annealing. J. Phys. Chem. Solids 57, 1937–1945. https://doi.org/10.1016/S0022-3697(96)00072-8

Romanjek, K., Vesin, S., Aixala, L., Baffie, T., Bernard-Granger, G., Dufourcq, J., 2015. High-Performance Silicon–Germanium-Based Thermoelectric Modules for Gas Exhaust Energy

Scavenging. J. Electron. Mater. 44, 2192–2202. https://doi.org/10.1007/s11664-015-3761-1

Rowe, D., 1995. Introduction, in: CRC Handbook of Thermoelectrics. CRC Press, Boca Raton. https://doi.org/doi:10.1201/9781420049718.ch1

Sanchez, S., Levy-Clement, C., Ivanova, V., 2012. Electrochemical Deposition of ZnO Thin Films and Nanowires for Photovoltaic Applications. J. Electrochem. Soc. 159, D705–D712. https://doi.org/10.1149/2.024212jes

Saramat, A., Svensson, G., Palmqvist, A.E.C., Stiewe, C., Mueller, E., Platzek, D., Williams, S.G.K., Rowe, D.M., Bryan, J.D., Stucky, G.D., 2006. Large thermoelectric figure of merit at high temperature in Czochralski-grown clathrate Ba8Ga16Ge30. J. Appl. Phys. 99. https://doi.org/10.1063/1.2163979

Seeking Alpha, 2017. Tellurium - Take Advantage Of Growing Demand For This Rare Metal [WWW Document]. URL https://seekingalpha.com/article/4035194-tellurium-take-advantage-growing-demand-rare-metal (accessed 6.27.18).

Shang, H., Gu, H., Zhong, Y., Ding, F., Li, G., Qu, F., Zhang, H., Dong, Z., Zhang, H., Zhou, W., 2017. Synergetic combination of Te content and deposition temperature to optimize thermoelectric properties using sputtered bismuth telluride films. J. Alloys Compd. 690, 851–855. https://doi.org/10.1016/j.jallcom.2016.08.162

Shuai, L., Fei, L., Xiaoqi, Z., Yu, B., Dayan, M., Fei, M., Kewei, X., 2015. Elemental Ratio Controlled Semiconductor Type of Bismuth Telluride Alloy Thin Films. Rare Met. Mater. Eng. 44, 3041–3044. https://doi.org/10.1016/S1875-5372(16)60047-4

Shutoh, N., Sakurada, S., 2005. Thermoelectric properties of the TiX(Zr0.5Hf0.5)1−XNiSn half-Heusler compounds. J. Alloys Compd. 389, 204–208. https://doi.org/https://doi.org/10.1016/j.jallcom.2004.05.078

Singkaselit, K., Sakulkalavek, A., Sakdanuphab, R., 2017. Effects of annealing temperature on the structural, mechanical and electrical properties of flexible bismuth telluride thin films prepared by high-pressure RF magnetron sputtering. Adv. Nat. Sci. Nanosci. Nanotechnol. 8. https://doi.org/10.1088/2043-6254/aa7222

Sootsman, J.R., Chung, D.Y., Kanatzidis, M.G., 2009. New and old concepts in thermoelectric materials. Angew. Chemie - Int. Ed. 48, 8616–8639. https://doi.org/10.1002/anie.200900598

Sugiyama, K.I. and H.U. and M.S. and T.T. and S., 2005. Fabrication of flexible thermopile generator. J. Micromechanics Microengineering 15, S233. https://doi.org/10.1088/0960-1317/15/9/S10

Sung, D.H., Kang, G.H., Kong, K., Kim, M., Park, H.W., Park, Y. Bin, 2016. Characterization of thermoelectric properties of multifunctional multiscale composites and fiber-reinforced composites for thermal energy harvesting. Compos. Part B Eng. 92, 202–209. https://doi.org/10.1016/j.compositesb.2016.02.050

Symeou, E., Pervolaraki, M., Mihailescu, C.N., Athanasopoulos, G.I., Papageorgiou, C., Kyratsi, T., Giapintzakis, J., 2015. Thermoelectric properties of Bi0.5Sb1.5Te3thin films grown by pulsed laser deposition. Appl. Surf. Sci. 336, 138–142. https://doi.org/10.1016/j.apsusc.2014.10.038

Szymczak, J., Legeai, S., Michel, S., Diliberto, S., Stein, N., Boulanger, C., 2014. Electrodeposition of stoichiometric bismuth telluride Bi2Te 3 using a piperidinium ionic liquid binary mixture. Electrochim. Acta 137, 586–594. https://doi.org/10.1016/j.electacta.2014.06.036

Takahashi, M., 1993. Electrodeposition of Bi-Te Alloy Films. J. Electrochem. Soc. 140, 2550.

https://doi.org/10.1149/1.2220860

Takashiri, M., Hamada, J., 2016. Bismuth antimony telluride thin films with unique crystal orientation by two-step method. J. Alloys Compd. 683, 276–281. https://doi.org/10.1016/j.jallcom.2016.05.058

Takashiri, M., Shirakawa, T., Miyazaki, K., Tsukamoto, H., 2007. Fabrication and characterization of bismuth–telluride-based alloy thin film thermoelectric generators by flash evaporation method. Sensors Actuators A Phys. 138, 329–334. https://doi.org/10.1016/j.sna.2007.05.030

Tang, X., Li, P., Deng, S., Zhang, Q., 2008. High temperature thermoelectric transport properties of double-atom-filled clathrate compounds YbxBa8-xGa16Ge30. J. Appl. Phys. 104, 1–7. https://doi.org/10.1063/1.2951888

Toshima, N., 2017. Recent progress of organic and hybrid thermoelectric materials. Synth. Met. 225, 3–21. https://doi.org/https://doi.org/10.1016/j.synthmet.2016.12.017

Toshima, N., Imai, M., Ichikawa, S., 2011. Organic-inorganic nanohybrids as novel thermoelectric materials: Hybrids of polyaniline and bismuth(III) telluride nanoparticles. J. Electron. Mater. 40, 898–902. https://doi.org/10.1007/s11664-010-1403-1

Trawiński, B., Bochentyn, B., Gostkowska, N., Łapiński, M., Miruszewski, T., Kusz, B., 2018. Structure and thermoelectric properties of bismuth telluride—Carbon composites. Mater. Res. Bull. 99, 10–17. https://doi.org/10.1016/j.materresbull.2017.10.043

Triefenbach, F., 2008. Design of experiments: the D-optimal approach and its implementation as a computer algorithm. Bachelor's Thesis Inf. Commun. ….

Tritt, T.M., 2001. Preface, in: Tritt, T.M.B.T.-S. and S. (Ed.), Recent Trends in Thermoelectric Materials Research II. Elsevier, pp. ix–xiv. https://doi.org/https://doi.org/10.1016/S0080-8784(01)80133-2

Venkatasubramanian, R., Siivola, E., Colpitts, T., O'quinn, B., 2001. Thin-film thermoelectric devices with high room-temperature figures of merit. Nature 597–602.

Wang, D., Su, Y., Chen, D., Wang, L., Xiang, X., Zhu, D., 2015. Preparation and characterization of poly(3-octylthiophene)/carbon fiber thermoelectric composite materials. Compos. Part B Eng. 69, 467–471. https://doi.org/10.1016/j.compositesb.2014.10.007

Wang, J., Cai, K., Shen, S., Yin, J., 2014. Preparation and thermoelectric properties of multi-walled carbon nanotubes/polypyrrole compositesfile:///C:/Users/User/Google Drive/Aug 15 Phd Works/Journals/CF as TE Modules/CF TE/CNT Bi2Te3/CNT and Polymer Only/Simultaneous increase in conductivity and . Synth. Met. 195, 132–136. https://doi.org/10.1016/j.synthmet.2014.06.003

Wang, L., Jia, X., Wang, D., Zhu, G., Li, J., 2013. Preparation and thermoelectric properties of polythiophene/multiwalled carbon nanotube composites. Synth. Met. 181, 79–85. https://doi.org/10.1016/j.synthmet.2013.08.011

Wang, S., Chung, D.D.L., 1999. Carbon fiber polymer-matrix composite interfaces as thermocouple junctions. Compos. Interfaces 6, 512–513. https://doi.org/10.1163/156855499X00198

Wang, S., Lü, Q., Li, L., Fu, G., Liu, F., Dai, S., Yu, W., Wang, J., 2013. High-temperature thermoelectric properties of Cd1−xPrxO ceramics, Scripta Materialia. https://doi.org/10.1016/j.scriptamat.2013.06.018

Wang, W.-L.L., Wan, C.-C.C., Wang, Y.-Y.Y., 2007. Composition-dependent characterization and

optimal control of electrodeposited Bi2Te3 films for thermoelectric application. Electrochim. Acta 52, 6502–6508. https://doi.org/10.1016/j.electacta.2007.04.037

Wang, X., He, H., Wang, N., Miao, L., 2013. Effects of annealing temperature on thermoelectric properties of Bi 2 Te 3 films prepared by co-sputtering. Appl. Surf. Sci. 276, 539–542. https://doi.org/10.1016/j.apsusc.2013.03.130

Wang, X., Meng, F., Wang, T., Li, C., Tang, H., Gao, Z., Li, S., Jiang, F., Xu, J., 2018. High performance of PEDOT:PSS/SiC-NWs hybrid thermoelectric thin film for energy harvesting. J. Alloys Compd. 734, 121–129. https://doi.org/https://doi.org/10.1016/j.jallcom.2017.11.013

Wang, Y.Y., Cai, K.F., Yin, J.L., An, B.J., Du, Y., Yao, X., 2011. In situ fabrication and thermoelectric properties of PbTe - Polyaniline composite nanostructures. J. Nanoparticle Res. 13, 533–539. https://doi.org/10.1007/s11051-010-0043-y

Wong, D.P., Chien, W.-L., Huang, C.-Y., Chang, C., Ganguly, A., Lyu, L.-M., Hwang, J.-S., Chen, L.-C., Chen, K.-H., 2016. Enhanced thermoelectric performance in a percolated bismuth sulfide composite. RSC Adv. 6, 98952–98955. https://doi.org/10.1039/C6RA21418E

Xu, H., Wang, W., 2013a. Electrodeposition of MWNT/Bi2Te3 composite thermoelectric films. J. Electron. Mater. 42, 1936–1945. https://doi.org/10.1007/s11664-013-2479-1

Xu, H., Wang, W., 2013b. Synthesis and Characterization of CNTs / Bi 2 Te 3 Thermoelectric Nanocomposites. Int. J. Electrochem. Sci. 8, 6686–6691.

Yan, H., Sada, N., Toshima, N., 2002. Thermal transporting properties of electrically conductive polyaniline films as organic thermoelectric materials. J. Therm. Anal. Calorim. 69, 881–887. https://doi.org/10.1023/A:1020612123826

Yang, J., Chen, R., Fan, X., Bao, S., Zhu, W., 2006. Thermoelectric properties of silver-doped n-type Bi2Te 3-based material prepared by mechanical alloying and subsequent hot pressing. J. Alloys Compd. 407, 330–333. https://doi.org/10.1016/j.jallcom.2005.06.041

Yang, Q., Hu, C., Wang, S., Xi, Y., Zhang, K., 2013. Tunable Synthesis and Thermoelectric Property of Bi 2 S 3 Nanowires. J. Phys. Chem. C 117, 5515–5520. https://doi.org/10.1021/jp307742s

Yang, W., Wang, H., Liu, T., Gao, L., 2016. A Bi2S3@CNT nanocomposite as anode material for sodium ion batteries. Mater. Lett. 167, 102–105. https://doi.org/10.1016/j.matlet.2015.12.108

Yao, W., Xia, Q., 2014. Preparation and thermoelectric properties of bismuth telluride-carbon fiber reinforced cement composites. Gongneng Cailiao/Journal Funct. Mater. 45, 15134–15137and 15142. https://doi.org/10.3969/j.issn.1001-9731.2014.15.029

Yeo, Y.H., Oh, T.S., 2014. Thermoelectric properties of p-type (Bi,Sb)2Te3 nanocomposites dispersed with multiwall carbon nanotubes. Mater. Res. Bull. 58, 54–58. https://doi.org/10.1016/j.materresbull.2014.04.046

Yoo, B.Y., Huang, C.-K., Lim, J.R., Herman, J., Ryan, M. a., Fleurial, J.-P., Myung, N.V., 2005. Electrochemically deposited thermoelectric n-type Bi2Te3 thin films. Electrochim. Acta 50, 4371–4377. https://doi.org/10.1016/j.electacta.2005.02.016

Yoo, I.-J.J., Myung, N. V., Lim, D.C., Song, Y., Jeong, Y.-K.K., Kim, Y. Do, Lee, K.H., Lim, J.-H.H., 2013. Electrodeposition of BixTey thin films for thermoelectric application. Thin Solid Films 546, 48–52. https://doi.org/10.1016/j.tsf.2013.05.036

Yu, C., Kim, Y.S., Kim, D., Grunlan, J.C., 2008. Thermoelectric behavior of segregated-network polymer nanocomposites. Nano Lett. 8, 4428–4432. https://doi.org/10.1021/nl802345s

Yu, Y.Q., Zhang, B.P., Ge, Z.H., Shang, P.P., Chen, Y.X., 2011. Thermoelectric properties of Ag-doped bismuth sulfide polycrystals prepared by mechanical alloying and spark plasma sintering. Mater. Chem. Phys. 131, 216–222. https://doi.org/10.1016/j.matchemphys.2011.09.010

Yücel, E., Yücel, Y., 2017a. Fabrication and characterization of Sr-doped PbS thin films grown by CBD. Ceram. Int. 43, 407–413. https://doi.org/10.1016/j.ceramint.2016.09.173

Yücel, E., Yücel, Y., 2017b. Effect of doping concentration on the structural, morphological and optical properties of Ca-doped PbS thin films grown by CBD. Opt. - Int. J. Light Electron Opt. 142, 82–89. https://doi.org/https://doi.org/10.1016/j.ijleo.2017.04.104

Yucheng, L., Jerome, M.A., Gang, C., Zhifeng, R., 2010. Enhancement of Thermoelectric Figure-of-Merit by a Bulk Nanostructuring Approach. Adv. Funct. Mater. 20, 357–376. https://doi.org/10.1002/adfm.200901512

Zeng, Z., Yang, P., Hu, Z., 2013. Temperature and size effects on electrical properties and thermoelectric power of Bismuth Telluride thin films deposited by co-sputtering. Appl. Surf. Sci. 268, 472–476. https://doi.org/10.1016/j.apsusc.2012.12.134

Zhan, S., Wan, H., Xu, L., Huang, W., Huang, G., Long, J., Peng, P., 2014. Native vacancy defects in bismuth sulfide. Int. J. Mod. Phys. B 28, 1–13. https://doi.org/10.1142/S0217979214501501

Zhang, Q., Xu, L., Zhou, Z., Wang, L., Jiang, W., Chen, L., 2017. Constructing nanoporous carbon nanotubes/Bi2Te3composite for synchronous regulation of the electrical and thermal performances. J. Appl. Phys. 121. https://doi.org/10.1063/1.4975467

Zhang, S., Li, A., Sun, K., 2017. Thermoelectric properties of Graphene/Mn0.7Zn0.3Fe2O4 composites. Ceram. Int. 43, 8643–8647. https://doi.org/https://doi.org/10.1016/j.ceramint.2017.03.183

Zhang, Y., Wang, X.L., Yeoh, W.K., Zheng, R.K., Zhang, C., 2012. Electrical and thermoelectric properties of single-wall carbon nanotube doped Bi2Te3. Appl. Phys. Lett. 101, 031909. https://doi.org/10.1063/1.4737898

Zhang, Z., Chen, G., Wang, H., Zhai, W., 2015. Enhanced thermoelectric property by the construction of a nanocomposite 3D interconnected architecture consisting of graphene nanolayers sandwiched by polypyrrole nanowires. J. Mater. Chem. C 3, 1649–1654. https://doi.org/10.1039/c4tc02471k

Zhao, L.-D., Zhang, B.-P., Liu, W.-S., Zhang, H.-L., Li, J.-F., 2008. Enhanced thermoelectric properties of bismuth sulfide polycrystals prepared by mechanical alloying and spark plasma sintering. J. Solid State Chem. 181, 3278–3282. https://doi.org/10.1016/j.jssc.2008.08.022

Zhao, X.B., Ji, X.H., Zhang, Y.H., Zhu, T.J., Tu, J.P., Zhang, X.B., 2005. Bismuth telluride nanotubes and the effects on the thermoelectric properties of nanotube-containing nanocomposites. Appl. Phys. Lett. 86, 1–3. https://doi.org/10.1063/1.1863440

Zhao, Y., Liu, T., Xia, H., Zhang, L., Jiang, J., Shen, M., Ni, J., Gao, L., 2014. Branch-structured Bi 2 S 3 – CNT hybrids with improved lithium storage capability. J. Mater. Chem. A 2, 13854–13858. https://doi.org/10.1039/C4TA02717E

Zheng, Z., Fan, P., Liang, G., Zhang, D., Cai, X., Chen, T., 2010. Annealing temperature influence on electrical properties of ion beam sputtered Bi2Te3 thin films. J. Phys. Chem. Solids 71, 1713–1716. https://doi.org/10.1016/j.jpcs.2010.09.012

Zhu, T., Chong, M.N., Phuan, Y.W., Ocon, J.D., Chan, E.S., 2016. Effects of electrodeposition synthesis

parameters on the photoactivity of nanostructured tungsten trioxide thin films: Optimisation study using response surface methodology. J. Taiwan Inst. Chem. Eng. 61, 196–204. https://doi.org/10.1016/j.jtice.2015.12.010

Zhu, W., Deng, Y., Wang, Y., Luo, B., Cao, L., 2014. Preferential growth transformation of Bi0.5Sb1.5Te3films induced by facile post-annealing process: Enhanced thermoelectric performance with layered structure. Thin Solid Films 556, 270–276. https://doi.org/10.1016/j.tsf.2014.02.041

Zhu, Z., Iyemperumal, S.K., Kushnir, K., Carl, A.D., Zhou, L., Brodeur, D.R., Grimm, R.L., Titova, L. V., Deskins, N.A., Rao, P.M., 2017. Enhancing the solar energy conversion efficiency of solution-deposited Bi_2S_3 thin films by annealing in sulfur vapor at elevated temperature. Sustain. Energy Fuels. https://doi.org/10.1039/C7SE00398F

Zou, H., Rowe, D.M., Min, G., 2001. Growth of p- and n-type bismuth telluride thin films by 222, 82–87.